METABOLIC CHANGES IN THE SALIVARY GLAND FOLLOWING RADIATION TREATMENT

by

Lauren Buss

A Dissertation Submitted to the Faculty of the

SCHOOL OF NUTRITONAL SCIENCES AND WELLNESS

In Partial Fulfillment of the Requirements

For the Degree of

DOCTOR OF PHILOSOPHY

In the Graduate College

THE UNIVERSITY OF ARIZONA

2023

THE UNIVERSITY OF ARIZONA
GRADUATE COLLEGE

As members of the Dissertation Committee, we certify that we have read the dissertation prepared by: Lauren G. Buss
titled: Metabolic Changes in the Salivary Gland Following Radiation Treatment

and recommend that it be accepted as fulfilling the dissertation requirement for the Degree of Doctor of Philosophy.

Kirsten H Limesand
Kirsten Limesand — Date: Apr 13, 2023

Floyd H. Chilton
Floyd H. Chilton (Apr 13, 2023 10:09 PDT)
Floyd H. Chilton — Date: Apr 13, 2023

Jessica A. Martinez (Apr 19, 2023 12:57 PDT)
Jessica A. Martinez — Date: Apr 19, 2023

Ningning Zhao
Ningning Zhao — Date: Apr 13, 2023

Final approval and acceptance of this dissertation is contingent upon the candidate's submission of the final copies of the dissertation to the Graduate College.

I hereby certify that I have read this dissertation prepared under my direction and recommend that it be accepted as fulfilling the dissertation requirement.

Kirsten H Limesand
Kirsten Limesand — Date: Apr 13, 2023
Nutritional Sciences and Wellness

ACKNOWLEDGMENTS

I would like to thank my mentor, Dr. Kirsten Limesand, for her mentoring over the past 5 years. From her, I learned to think critically and independently and now I am trained for a career as a scientist. I'd like to acknowledge my committee members, Dr. Ski Chilton, Dr. Jessica Martinez, and Dr. Ningning Zhao for the knowledge they have imparted to me in the design of my research studies and the interpretation of data. I am grateful for working with Dr. Megha Padi and Diogo Oliveira de Pessoa on my first and second projects as they created the data integration pipeline and performed the bioinformatics analysis. Dr. Justin Snider helped us process and interpret the metabolomics data for our second project. Dr. Rick Schnellmann allowed us to use his Seahorse analyzer for the experiments in my third project, and his former graduate student Dr. Kristin Campbell and Agilent field application specialist Anup Srivastava helped me optimize the assays for our model.

I would like to thank my lab team, who helped train and motivate me to complete this degree. Former PhD student Dr. Kristy Gilman and former lab manager Dr. Partha Samadder trained me during my first 3 years and helped me complete experiments and interpret data. Our current lab manager Dr. Brenna Rheinheimer has helped out with my experiments over the past 2 years. Current graduate student Jordan Gunning has survived the past 5 years of our PhD program together with me and has been a helpful teammate. I thank all of you for your support as you have endured the good and the bad with me over the past 5 years and I will miss working with you all.

I am grateful to the Nutritional Sciences and Wellness graduate program, to all of the faculty that I have had the privilege of knowing and learning from and the other graduate students. Dr. Richard Simpson and Peggy Rupert lead our program as the director and coordinator, and I am grateful for their commitment and support to us. I'd also like to thank our building manager, Tait Hansen, for helping our lab with every technology-related problem and building-related problem.

Lastly, I would like to thank my family and friends for their love and support. You have each played an important role in helping me through this challenging degree.

LAND ACKNOWLEDGEMENT

We respectfully acknowledge the University of Arizona is on the land and territories of Indigenous peoples. Today, Arizona is home to 22 federally recognized tribes, with Tucson being home to the O'odham and the Yaqui. Committed to diversity and inclusion, the University strives to build sustainable relationships with sovereign Native Nations and Indigenous communities through education offerings, partnerships, and community service.

DEDICATION

This dissertation is dedicated to my grandfather, Kenneth Meeks, who passed away on August 4^{th}, 2022. It was his desire to see me graduate and become the first doctor in the family before he passed.

TABLE OF CONTENTS

List of Figures and Tables

Abstract

Over 54,000 new cases of head and neck cancer (HNC) are estimated for 2022 in the Unites States and the current treatment involves surgery and radiotherapy. Due to the proximity of the salivary glands to HNC tumors, they are indirectly damaged by radiotherapy and lose secretory function due to their high level of radiation sensitivity. Salivary gland hypofunction leads to xerostomia and other deleterious conditions, such as malnutrition, dental caries, and periodontal disease. Salivary hypofunction treatments include topical agents and saliva stimulants, which temporarily treat the symptoms without regenerating the tissue to restore function for HNC patients who experience chronic xerostomia following radiotherapy. Progress has been made in identifying the mechanisms driving the radiation-damage response, but the metabolic reprogramming that facilitates these mechanisms in the salivary gland is not understood.

Metabolomics analysis has been useful for identifying biomarkers of radiation damage in tissues using animal models and in urine and serum of humans. By incorporating additional “omics” data with metabolomics data, more accurate metabolic reactions can be mapped to identify biological networks affected by radiation. To investigate the metabolic phenotype of radiation-induced damage in the salivary gland, we integrated transcriptomic and metabolomic data analysis to identify significant gene-metabolite interactions (Chapter II). Altered metabolites and transcripts significantly converged on a specific region in the metabolic reaction network in parotid tissue glands of mice collected 5 days following radiation treatment. Both integrative pathway enrichment using rank-based statistics and network analysis highlighted significantly coordinated changes in glutathione metabolism, energy metabolism (TCA cycle and thermogenesis), peroxisomal lipid metabolism, and bile acid production with radiation. Integrated changes observed in energy metabolism suggest that radiation induces a mitochondrial

dysfunction phenotype. These findings validated previous pathways involved in the radiation-damage response, such as altered energy metabolism, and identified robust signatures in the salivary gland, such as reduced glutathione metabolism, that may be driving salivary gland dysfunction.

The aforementioned study identified metabolic changes at 5 days after radiation treatment in the salivary gland, which is the time point when compensatory proliferation begins in the gland in an attempt to heal the damaged tissue. However, the cells are not differentiating properly and becoming fully functional as assessed by decreased amylase levels in the cells. Additionally, decreases in apical and basolateral polarity markers begin at 5 days post-radiation, contributing to the loss of function in the gland. Day 5 denotes the transition between the acute phase of the radiation-damage response marked by increased DNA damage, apoptosis, and reactive oxygen species (ROS) production leading to loss of salivary gland function at 3 days post-radiation, to the chronic phase where increased ROS production continues as well as increased compensatory proliferation and decreased differentiation markers. Due to the complexity of the radiation-damage response over time, we sought to delineate metabolic changes at the acute, intermediate, and chronic radiation-damage response stages in the salivary glands of mice following a single 5 Gy dose (Chapter III). Ultra-high performance liquid chromatography-mass spectrometry was performed on parotid salivary gland tissue collected at 3, 14, and 30 days following radiation treatment. Pathway enrichment analysis, network analysis based on metabolite structural information, and weighted-gene correlation network analysis were used to incorporate both metabolite levels and structural annotation into the analysis for robust results. The greatest number of enriched pathways was observed at 3 days following radiation and the lowest at 30 days following radiation, and various amino acid metabolism pathways were significantly enriched at all three radiation time points as well as glutathione metabolism and central carbon metabolism in cancer. This study identified the temporal changes in pathways underlying the radiation damage response in the salivary gland to aid in the development of precision therapy for different stages of radiation-induced salivary gland dysfunction.

Due to the changes observed in energy metabolism by integrating transcripts and metabolites at day 5 following radiation in the salivary gland, we decided to pursue a deeper investigation of the effects of radiation on energy metabolism in the salivary gland (Chapter IV). The reprogramming of energy metabolism has been observed in cancer and wound healing models to provide the necessary fuel for cell proliferation, but the reprogramming of energy metabolism in the salivary gland in response to radiation has not been investigated. We hypothesized that glycolytic flux increases to fuel compensatory proliferation while oxidative phosphorylation decreases due to mitochondrial dysfunction following radiation. We measured the oxygen consumption rate (OCR) and extracellular acidification rate (ECAR) of irradiated primary acinar cells to assess glycolytic flux and oxidative phosphorylation and ATP production produced from each pathway. We measured protein levels and enzymatic activity of the rate-limiting enzymes in glycolysis and measured lactate concentrations in irradiated parotid gland tissue. To assess mitochondrial function, we measured protein levels of complex I and III subunits of the electron transport chain and measured mitochondrial DNA (mtDNA) copy number and spare respiratory capacity. Lastly, we tested fuel dependency and flexibility of irradiated acinar cells. Our results showed an increase in OCR, ECAR, and ATP production rate at 24 hours and 5 days post-radiation with a subsequent decrease at chronic time points. Hexokinase protein levels and activity increased at 3 days post-IR and lactate concentration increased at days 5 and 14 post-radiation. Complex I and III subunit protein levels decreased at days 3 and 5 post-radiation while mitochondrial DNA copy number increased chronically post-radiation. Primary acinar cells became more dependent on long-chain fatty acids for fuel at day 5 post-radiation. These results elucidated the reprogramming of energy metabolism in the salivary gland in response to radiation over time, which may contribute to the radiosensitivity of the gland and aid in identifying therapeutic targets for restoring function.

I. Literature Review

Clinical significance

Over 54,000 new cases of head and neck cancer (HNC) are estimated in 2022 in the Unites States with over 11,000 estimated deaths attributed to HNC [1]. Squamous cell carcinomas are the most common types of HNC arising in the oral cavity, the sinonasal cavity, the larynx and pharynx, and the salivary glands [2]. Older males who regularly consume tobacco and alcohol, two of the most historical risk factors for HNC, are the population most commonly diagnosed with HNC, however the incidence rate has decreased in recent decades due to decreased tobacco consumption in the United States [2], [3]. Currently, the most common risk factor for HNC is infection with human papillomavirus (HPV) [4]. An increased incidence in HPV-related HNC is observed over the past several decades in younger adults, as the percentage of HPV-related HNC cases increased from 41% in 2000 to 72% by 2009 and has already surpassed the number of HPV-related cervical cancers by 2020 [5]. Additionally, an increase in the number of survivors of HNC is increasing, with over 249,330 male survivors in the United States identified by the American Cancer Society and the National Cancer Institute in 2019 with a projected 5% increase by 2030 [6].

Treatment for head and neck cancer

Surgery is considered the standard of care for oral cavity cancers, whether by endoscopic or robotic surgery, while radiation therapy in combination with chemotherapy is used for areas outside of the oral cavity for treatment [7]. Treatment choice for HNC patients is determined by tumor size, type, and location, patient factors such as smoking and age, and patient preference [7]. Radiation therapy is commonly used in the management of HNC because tumor progression is typically local and can therefore be controlled with radiation treatment [8]. A longitudinal study of patients from 1975-2001 with glottic carcinomas receiving exclusively radiation treatment (65 Gray in 44 days) resulted in 75% survival with laryngeal preservation observed in 85% of the group, demonstrating that radiotherapy is an effective disease management treatment [9]. Not only is radiation an effective treatment, but improvements in radiation delivery, specifically with intensity-modulated radiotherapy (IMRT) using targeted photon beams to conform to the shape of the tumor, have reduced the amount of toxic radiation damage to tissues surrounding the tumor [10]. Unfortunately, limiting properties of the photon beam still result in radiation exposure to the surrounding healthy tissues leading to acute and chronic damage [10].

The three major salivary glands (parotid, submandibular, and sublingual) are a set of tissues located within the head and neck region that is typically within the field of radiation exposure when HNC patients undergo radiotherapy. The salivary glands are radiosensitive, which is surprising considering they are a slowly proliferating tissue that is highly differentiated [11]. Radiation exposure results in salivary gland hypofunction, which can lead to hyposalivation, mucositis, a persistent dry-mouth sensation (xerostomia), oral infections, malnutrition, and dysphagia [11]. Within 1 week of radiation treatment, unstimulated and stimulated saliva flow rates decrease sharply (50-60%) and continue decreasing throughout the course of treatment, resulting in impaired saliva production chronically that can persist for over 2 years following radiotherapy [12 13]. Acute salivary gland dysfunction is predictive of chronic dysfunction (lasting at least six months following radiotherapy), and loss of functional acini with fibrosis development contributes to chronic dysfunction of the gland [13]. Salivary gland hypofunction and xerostomia have been reported in over 80% of HNC patients [14], [13] and thus negatively affect the quality of life of most HNC survivors. This is a serious concern as many HNC patients are elderly and immunocompromised and may experience poor survival outcomes.

Radiation dosing strategies

Conventional radiation therapy for HNC patients delivers a total of 60-70 Gray (Gy) with the goal of curing the cancer, and the administration of radiation is divided into approximately 2 Gy doses per day, five days a week [15]. This division of the radiation dose into smaller fractions is called fractionated radiation therapy, and it has been in use since the 1920's in 50% of cancer treatments and 40% of cancer cures [16]. Fractionated radiotherapy is advantageous because it increases tumor radiosensitivity by allowing reoxygenation and cell cycle redistribution between fractions, and in surrounding normal tissue it allows time for DNA repair mechanisms to reduce toxic effects [16]. The parotid salivary gland, the largest of the salivary glands in humans, is more radiosensitive compared to the submandibular salivary gland, and radiologists have concluded that a 23 Gy total dose to the parotid gland and a 42 Gy total dose to the submandibular gland is ideal for preserving salivary gland function when administered in fractionated doses [17], [18]. Experimentation with conventional fractionated radiotherapy to reduce toxic side effects to normal tissues has utilized administering 1-2 Gy twice a day instead of once per day to reduce the occurrence of late toxicity, reduce total treatment time, and allow for higher total dosing to be administered compared to conventional fractionation [19]. An updated meta-analysis of radiotherapy in squamous cell carcinomas of head and neck (MARCH) compared hyperfractionation radiotherapy (twice per day fractions) to conventional fractionation radiotherapy and discovered that hyperfractionation radiotherapy was associated with a 3.1% increase in HNC patient survival at 5 years post treatment and local tumor control was improved with hyperfractionation radiotherapy [19]. Although benefits have been observed using hyperfractionation radiotherapy compared to conventional radiotherapy, logistical issues prevent hyperfractionation radiotherapy from becoming the standard of care due to difficulty scheduling patients twice a day, patient management between the daily doses, and cost [19]. Additionally, reports of chronic toxic effects (occur 90 days or more after hyperfractionation radiotherapy) have been reported in HNC patients, such as aspiration pneumonia, esophageal narrowing, and osteoradionecrosis [20]. Due to the costs outweighing the benefit for hyperfractionation radiotherapy, conventional fractionated radiotherapy remains the standard of care for HNC.

Conformal radiation therapy (CRT)

CRT was a popular radiation therapy modality in the 1960's and 1970's that directs single-intensity photon radiation beams to the tumor using x-rays to image the target area [21]. Two types of CRT exist: two-dimensional (2D)-CRT and three-dimensional (3D)-CRT, with 3D-CRT developing when computed tomography (CT), magnetic resonance imaging (MRI), and positron emission tomography (PET) scans were invented for 3D imaging. 2D-CRT uses one to four lateral boxes to direct the radiation beam while 3D-CRT incorporates axial anatomy that can accommodate irregular shapes [22]. Although 3D-CRT improved delivery of radiation to tumors compared to 2D-CRT, the photon beam damages surrounding healthy tissues due to the uniform dose administration [21]. The limitations associated with 3D-CRT, specifically damage to surrounding tissue often preventing target dosing volume to the tumor, led to the development of intensity modulated radiation therapy (IMRT).

Intensity modulated radiation therapy (IMRT)

IMRT emerged in the 1980's as the newest radiation therapy modality and was advantageous due to its targeted delivery of high radiation doses reaching the target volume to the tumor, thereby delivering a more concentrated radiation dose to the tumor for eradication

[20]. Additionally, due to the tight dose gradients used in IMRT, normal tissues surrounding the tumor are spared to a greater extent than when using conventional radiotherapy with beams of uniform intensity [20]. Advances in volumetric imaging using CT, MRI, and PET scans led to the development of IMRT due to the geometry of the tumor and surrounding healthy tissues being detected with three-dimensional (3D) imaging, which opened the door to the idea of modulating the radiation intensity based on the spatial arrangement of the tissues to deliver conformal dose distributions [23]. Advances in computer software for calculating dose distribution provide a standardized approach for choosing every beam angle and treatment volume, thereby reducing the amount of time it takes clinicians to calculate accurate radiation dosing using IMRT [22]. A study compared treatment outcomes in nasopharyngeal carcinoma patients receiving either 2D-CRT, 3D-CRT, or IMRT and the results showed better 5-year overall survival for the patients receiving 3D-CRT and IMRT (74% and 77%, respectively) compared to 2D-CRT (60%) [24]. In a group of patients with advanced primary tumors, IMRT significantly improved 5-year overall survival compared to both 2D-CRT and 3D-CRT [24]. In addition to improving overall survival, IMRT has been demonstrated to improve local tumor control and improve salivary function by sparing the parotid glands in clinical trials [25], [26], [27]. Although IMRT has been shown to improve salivary function as assessed by salivary flow rate, xerostomia has not always been reported as improved by patients following IMRT and still remains a clinical problem [28], [29].

Volumetric modulated arc therapy (VMAT)

VMAT was a radiation modality introduced in 2007 to overcome the limitation of the fixed field used in IMRT [30]. VMAT delivers radiation in a continuous rotation that allows the patient to be treated from a full 360° beam angle, and during the rotation the clinician can adjust rotation speed, treatment aperture shape, and dose rate [30]. Two advantages of VMAT over IMRT is that treatment time is reduced, and the number of monitor units (MU) used is reduced, which decreases the amount of low-dose radiation exposed to the rest of the body [30], [31]. However, the algorithm design for VMAT is a larger and more challenging problem compared to IMRT and is still in the optimization stages for different cancer types [32]. A study compared VMAT to IMRT using varying radiation doses to ten patients with oropharynx or nasopharynx carcinoma and observed 100% coverage of the planned target volume of 95-100% using VMAT while 96-100% coverage was observed using IMRT, demonstrating that both plans are clinically acceptable with slightly higher coverage achieved with IMRT [33]. Both VMAT and IMRT demonstrated sparing of the spinal cord and brainstem while VMAT was superior to IMRT in parotid gland sparing [33]. A similar study comparing VMAT and IMRT found no significant difference in coverage of the planned target volume (96% average for both treatment plans), but it confirmed the previous study in demonstrating superior tissue sparing of the parotid gland using VMAT compared to IMRT [34]. A recent study published in 2022 evaluated the clinical efficacy and late toxicity of VMAT in 86 patients with nasopharyngeal carcinoma and observed an average 85.9% disease-free survival rate, 100% locoregional control at 12 months, and 96.2% locoregional control at 24 months [35]. Although local tumor control was excellent using VMAT treatment, 10% of the patients presented with distant metastases, demonstrating the importance of combining chemotherapy with radiotherapy to improve disease-free survival [35]. The effect of VMAT treatment on xerostomia in thirty squamous cell cancer of unknown primary (SCCUP) HNC patients was evaluated and grade 2 + xerostomia incidence decreased from 6 months (55.5%) to 12 months (7.7%), with no patients reporting xerostomia at 24 months post-treatment [36]. Based on these results, VMAT is an improved mode of radiation delivery for sparing healthy salivary glands to preserve tissue function in HNC patients compared to IMRT and conventional radiotherapy.

Intensity modulated proton therapy (IMPT)

The newest radiotherapy technique for HNC patients is intensity modulated proton therapy, which replaces the photons used in IMRT with protons. The use of protons for radiotherapy was first introduced in 1946 by Robert Wilson due to the unique dose distribution of protons, which delivers a maximal radiation dose to a designated tissue depth with no observed exit dose [37]. This is advantageous as protons can administer high dose radiation to tumor sites with practically no collateral damage to surrounding normal tissue, and several studies have demonstrated decreased radiation exposure to surrounding healthy tissue in HNC patients receiving IMPT compared to IMRT [38], [39], [40]. A recent study compared the effects of IMPT and IMRT on xerostomia in 532 oropharyngeal cancer patients and observed at 18-36 months post-treatment fewer cases of moderate-severe xerostomia in IMPT patients (6%) compared to IMRT patients (20%), suggesting that improved parotid gland sparing is reducing xerostomia in oropharyngeal cancer patients receiving IMPT [41]. Even with the observed dosimetric and clinical advantages of IMPT over IMRT, technological limitations with this new technique exist [37]. IMPT displays high sensitivity to changes in patient positioning, therefore frequent imaging is required throughout treatment for adaptive planning, which is estimated to occur in 16-38% of treatment plans [42]. Currently, the development of linear energy transfer-guided optimization is being researched for implementation in the clinic to improve the technology [43].

The choice of which radiotherapy treatment plan to use is individualized to the HNC patient based on tumor type, stage, and location, and with improvements in dose delivery and tissue sparing, less damage to the surrounding salivary glands is observed [44]. Yet even with the recent technological advancements in radiotherapy, HNC patients still report xerostomia, demonstrating the necessity of investigating mechanisms underlying radiation-induced salivary gland dysfunction in order to identify therapeutic targets to restore tissue function [13].

Chemotherapy and Immunotherapy

If the tumor in a HNC patient is considered high risk for surgical removal, such as a high risk of developing blood clots, the chemotherapy agent cisplatin (100 mg/m^2 every 3 weeks) combined with radiotherapy is a standard non-surgical treatment strategy [44]. For advanced tumors, concurrent chemotherapy using platinum agents that bind to the DNA of cancer cells and induce cell death combined with radiotherapy results in a 10-20% overall survival benefit at 3 years post-treatment compared to radiotherapy alone [45]. The two primary platinum agents used to treat HNC are cisplatin and carboplatin, and even though cisplatin is the more widely used agent, carboplatin results in less adverse side effects compared to cisplatin [45]. A study compared the effect of cisplatin versus carboplatin on overall survival in head and neck squamous cell carcinoma (HNSCC) patients and found no significant differences between the two chemotherapy agents, suggesting that carboplatin-based chemotherapy may be a viable alternate treatment for patients who do not tolerate cisplatin, such as those with underlying renal damage [45].

Cetuximab was approved in 2006 by the United States Food and Drug Administration (FDA) as an immunotherapy treatment for HNC, and it is an immunoglobulin G1 (IgG1) monoclonal antibody that binds to the epidermal growth factor receptor (EGFR) on epithelial cancer cells and inhibits signaling, which sensitizes the cancer cells to radiation treatment [46]. Although cetuximab in conjunction with radiotherapy has been demonstrated to improve HNC patient overall survival compared to radiotherapy alone [46], [47], studies have demonstrated decreased overall survival for chemoradiotherapy with cetuximab compared to chemoradiotherapy with cisplatin in HPV-positive oropharyngeal carcinoma [48], [49]. Therefore, combination platinum-based chemotherapy with cetuximab was investigated to determine if combination chemotherapy with immunotherapy can further improve HNC patient survival. A study compared the effects of cisplatin or carboplatin with cetuximab and 5-fluorouracil, which is a pyrimidine analog that inhibits DNA synthesis by inhibiting the thymidylate synthase enzyme involved in pyrimidine biosynthesis [50]. The addition of cetuximab and 5-fluorouracil to platinum-based chemotherapy improved overall survival from 7.4 months to 10.1 months in HNC patients with recurrent or metastatic cancer [50]. Additional studies have corroborated these results, leading to platinum chemotherapy plus cetuximab plus 5-fluorouracil becoming the standard first-line treatment for recurrent or metastatic HNC [51], [52]. Although combination chemotherapy with immunotherapy is effective in improving overall survival, it often results in toxic effects such as anemia, neutropenia, and thrombocytopenia that further decrease the quality of life of HNC patients and can result in early treatment cessation [50].

More recently, immunomodulatory drugs that target immune-suppressive pathways have been approved for HNC treatment. The mechanism of action of these drugs is to target the programmed cell death protein 1 (PD-1) and the programmed cell death ligand 1 (PD-L1) pathways. The PD-1/PD-L1 axis blocks T cell activation, proliferation, and survival within cancer cells and inhibits the immune response, thus enhancing survival of the cancer against the anti-tumor immune response [53]. PD-1 and PD-L1 are both expressed on tumor-specific T cells, which allows anti-PD-1/PD-L1 agents to enhance the anti-tumor immune response by blocking the tumor's immunosuppressive signaling through PD-1/PD-L1 [53]. Pembrolizumab is an immune checkpoint inhibitor (IgG4 antibody) that targets PD-1/PD-L1 and is FDA approved for treating HNC [54]. A recent phase III clinical study compared the effects of pembrolizumab alone, pembrolizumab plus platinum chemotherapy and 5-fluorouracil, and cetuximab plus platinum chemotherapy and 5-fluorouracil on overall survival and progression-free survival [55]. The results showed improved overall survival with the pembrolizumab plus chemotherapy treatment compared to the cetuximab plus chemotherapy treatment, with no significant differences in progression-free survival between the groups, thus supporting the use of pembrolizumab as a first-line treatment for recurrent or metastatic HNC [55]. Nivolumab is another anti-PD-1/PD-L1 agent that is FDA approved for treating HNC, and a phase III clinical trial compared nivolumab treatment to cetuximab treatment on overall survival in recurrent HNC patients six months following platinum chemotherapy [56]. Overall survival was improved with nivolumab compared to cetuximab (36% versus 16.6%), suggesting that nivolumab is a successful agent for improving survival in platinum refractory HNC patients [56]. Durvalumab and tremelimumab are additional anti-PD-1/PD-L1 agents that demonstrated acceptable safety profiles and clear antitumor activity in head and neck squamous cell carcinoma patients in a phase I study, which shows promise for these immunomodulatory drugs to also become utilized in HNC treatment [57]. Although advances in chemotherapy and immunotherapy for HNC improve patient survival, radiation is still the standard of care for early-stage tumors and is used in conjunction with surgery and chemo/immunotherapy for advanced-stage tumors [44]. Therefore, xerostomia is still a significant clinical problem in HNC patients receiving treatment.

Clinical management of xerostomia

Several treatment options are available for radiation-induced salivary gland hypofunction in HNC patients, yet they are limited in their effect on prevention and recovery of salivary gland function. The approved treatment options exhibit transient beneficial effects and certain drugs are associated with unpleasant side effects. Current treatments for salivary gland hypofunction will be presented in this section, followed by research identifying possible therapeutic targets for restoring salivary gland function.

Preventative therapies

To date, amifostine is the only FDA-approved radioprotective drug used during chemoradiotherapy for xerostomia prevention in HNC patients. Amifostine was originally developed for use by the U.S. army, and upon declassification of the drug it was subsequently used for medical experiments [58]. Animal experiments in the 1970's-90's supported the radioprotective activity of amifostine in mice exposed to radiation in a variety of normal tissues, including the parotid gland [59], [60], [61]. Amifostine exerts radioprotective effects to normal tissues by its activated thiol group scavenging free radicals produced by radiation and by preventing radiation-induced DNA single and double-strand breaks [62]. Additionally, the drug exerts chemoprotective effects to normal tissues by preventing cisplatin-DNA adducts [63]. The selectivity of amifostine into non-tumor cells is based on a few factors. One factor is the higher concentration of the enzyme alkaline phosphatase on the membrane of non-tumor cells compared to malignant cells [64]. Alkaline phosphatase is the enzyme that dephosphorylates the prodrug form of amifostine into its activated thiol form that can freely diffuse into cells [64]. Another factor contributing to the selectivity of amifostine is the acidic environment of the tumor lowering the dephosphorylation rate of amifostine into the active free thiol form [65].

Additionally, poor tumor vascularization is hypothesized to reduce delivery of amifostine to the tumor and contribute to the drug's cytoprotective selectivity [58].

Clinical trials investigating the use of amifostine in reducing radiation side effects in HNC patients demonstrate conflicting results. Amifostine has been shown to decrease both acute and chronic xerostomia with the use of chemotherapy or radiation, although over half of the HNC patients experienced unpleasant side effects that included nausea, vomiting, and hypotension [66], [67]. In other clinical trials, amifostine treatment during chemoradiotherapy showed no significant reduction in acute or chronic xerostomia in HNC patients [68], [69], with 28% of the patients discontinuing amifostine treatment before the end of radiotherapy due to unpleasant side effects (nausea and vomiting) and ineffectiveness of amifostine on reducing xerostomia development [68]. A clinical trial investigating the toxic side effects of amifostine on HNC patients undergoing chemoradiotherapy observed 41% of their patients discontinue amifostine treatment due to hypotension, vomiting, or allergic reactions [70]. The authors further compiled their results with previous literature on amifostine toxic effects, and they observed 78% discontinuation in patients receiving concurrent chemotherapy and 24% discontinuation in patients receiving only concurrent radiotherapy, suggesting that amifostine might be better tolerated in HNC patients receiving only radiotherapy as treatment [70]. Although amifostine has been FDA-approved for nearly 20 years, it is not routinely used clinically due to the toxic side effects, drug cost, and additionally, the increased use of IMRT and IMPT reduce the need for the radioprotective agent [71].

A prosthetic device utilized during radiation treatment to prevent radiation-induced salivary gland damage is an intraoral radiation stent (IRS). The concept of an IRS is that it can diminish the radiation dose delivered to surrounding healthy tissues by increasing the distance of the healthy tissue from the radiation beam [72]. Positioning stents are the type of IRS commonly used in the clinic for photon and proton radiation delivered to HNC patients, and they are effective in decreasing radiation delivery to the salivary gland by depressing the mandible [72]. One of the first clinical studies to evaluate the effect of positioning stents on xerostomia, mucositis, and salivary changes tested the stents on lingual carcinoma patients [73]. After a 60-day evaluation period, the experimental group that used positional stents during radiotherapy reported significantly decreased xerostomia, mucositis, and changes in saliva compared to the control group that did not use positional stents [73]. Another study investigated the effect of a personalized IRS on late xerostomia and dental cavity development in six patients with early-stage lip cancer and observed no signs of late xerostomia or dental cavity development at 39-months following treatment [74]. Although these devices are used in the clinic due to their efficacy at decreasing radiation-induced side effects in HNC patients, their use is not routine due to the expertise and time required to fabricate the IRS [72].

Alternative therapies

Acupuncture has been tested clinically to alleviate radiation-induced xerostomia, but the incorporation of the method as a component of standard care remains controversial due to the lack of mechanistic knowledge regarding the effect of acupuncture on xerostomia and variability in current acupuncture treatment protocols [75]. Several clinical trials demonstrated that true acupuncture compared to sham acupuncture may alleviate radiation-induced xerostomia in HNC patients by improving self-reported xerostomia scores acutely and chronically following 6-8 weeks of acupuncture treatment [76], [77], [78]. However, significant improvements in salivary flow with acupuncture treatment following radiotherapy remain to be established in clinical trials. To investigate which areas of the brain are stimulated with acupuncture for xerostomia treatment, twenty healthy subjects received true and sham acupuncture at the LI-2 acupoint of the non-dominant hand as this acupoint has been reported to improve radiation-induced xerostomia in HNC patients [79]. Functional magnetic resonance imaging (fMRI) scans showed that true acupuncture stimulated areas of the brain related to salivation/gustation while sham acupuncture did not stimulate these areas [79]. Additionally, saliva production was significantly higher in the true acupuncture group compared to sham acupuncture, suggesting a possible mechanism by which LI-2 acupuncture stimulates increased saliva production [79]. This mechanism remains to be investigated in HNC patients receiving radiotherapy.

Hyperbaric oxygen therapy (HBOT) is a technique that has been utilized for decades to treat radiation injury and is used as an adjuvant to surgery for osteoradionecrosis in HNC patients [80]. HBOT increases oxygen delivery to tissues by the person breathing 100% oxygen in a sealed chamber containing higher atmospheric pressure (2-3 atmospheres absolute (ATA), which translates to 200-300 kilopascals) [81]. The increased oxygen concentration in radiation-damaged tissues promotes wound healing through angiogenesis [80]. A prospective study tested the effects of HBOT on xerostomia in HNC patients following radiotherapy and discovered after thirty 90-minute sessions of HBOT over a period of 6 weeks, both saliva volume and xerostomia scores significantly improved at the end of the treatment period [82]. A systematic review was performed to determine if HBOT improves xerostomia in HNC patients and observed improvements in saliva viscosity and xerostomia scores across seven studies [83]. However, the majority of the studies were prospective, demonstrating the need for more randomized controlled clinical trials to strengthen the effectiveness of HBOT treatment for improving xerostomia in the clinic.

Palliative therapies

Treatments for radiation-induced xerostomia manage the dry-mouth sensation by lubricating the oral cavity or stimulating saliva production from the remaining functional gland. Physicians often recommend sipping water and over-the-counter agents to their HNC patients post-radiotherapy to alleviate xerostomia symptoms, such as mouthwashes, sugar-free gums, and moisturizing gels, specifically Biotène® products as they have demonstrated clinical efficacy in alleviating oral discomfort following radiotherapy [84]. The formulation of oral lubricants/saliva substitutes includes hydrophilic compounds, such as mucin, xanthan gum, hydroxyethylcellulose, and glycerine, and sometimes immunologically active compounds are incorporated as well [85], [86]. Due to the variety of available saliva substitutes, a study investigated the saliva substitute preferences of HNC patients with xerostomia following radiotherapy and discovered that product flavor and consistency were the most influential factors in deciding which saliva substitute they preferred to use since the duration of effect was short for each agent, ranging from 20 minutes to 2 hours depending on the patient [87]. Due to the transient efficacy of current saliva substitutes, studies are investigating an alternative strategy whereby the endogenous mucins in the patient's mouth are enhanced to improve oral lubrication rather than relying on exogenous compounds to lubricate the oral cavity [88], [89]. One such study tested the effects of the mucoadhesive chitosan on recruiting glycoproteins in the saliva of a Sjögren's syndrome patient to increase the lubricant properties of the saliva using an *ex vivo* tongue-enamel friction system and discovered over a 7-fold increase in duration of lubricant effect compared to buffer control [88]. Another study tested the safety and efficacy of preactivated chitosan covalently linked to mercaptonicotinic acid (MNA) on HNC squamous cells and observed no cell toxicity from the compound and a 1.3-fold improvement in mucoadhesion compared to unmodified chitosan, suggesting that preactivated chitosan may be a promising mucoadhesive for improving xerostomia symptom relief and duration [90], but more research is needed before this compound can reach clinical trial testing.

Pilocarpine is an FDA-approved drug for treating xerostomia that acts as a muscarinic acetylcholine agonist in acinar cells to stimulate saliva secretion [91]. The efficacy of pilocarpine in improving radiation-induced xerostomia in HNC patients has been demonstrated in multiple clinical trials [92],[93], [94], but unfortunately adverse systemic effects are commonly observed. These adverse effects include excessive sweating, lacrimation, nausea, vomiting, and chest pain in a dose-dependent manner, which lead to decreased adherence to the drug treatment [95]. Recent research has focused on topical administration of pilocarpine as a mouthwash to reduce the adverse side effects associated with the drug. A clinical trial compared the effects of 1% and 2% pilocarpine mouthwash on salivary flow and adverse side effects in subjects with xerostomia and discovered after two weeks of treatment significantly higher salivary flow in the 1% and 2% pilocarpine mouthwash groups compared to the placebo mouthwash, with the 2% pilocarpine group displaying significantly higher salivary flow compared to the 1% pilocarpine group [96]. No adverse side effects were reported by any of the 48 subjects, which may increase patient adherence to the treatment [96]. It is important to note that none of the subjects exhibited radiation-induced xerostomia, therefore the effects of this study may be different based on various etiologies (such as radiation damage compared to Sjögren's syndrome) [96]. Cevimeline is another FDA-approved muscarinic acetylcholine agonist for saliva stimulation that has demonstrated efficacy clinically for improving radiation-induced xerostomia in HNC patients, but it is also associated with adverse side effects, the most common one being excessive sweating [97], [98]. A study compared the efficacy and adverse side effects of pilocarpine and cevimeline and discovered that the two drugs exhibit similar improvements in salivary secretion and similar adverse side effects in xerostomia patients [99]. Bromhexine, nizatidine, and cisapride are additional drugs that have demonstrated the ability to increase saliva secretion by mucolytic action and cholinergic stimulation, but the research is limited investigating their effects on radiation-induced xerostomia [100], [101]. Even though topical administration of pilocarpine appears promising for alleviating xerostomia, it is still only a temporary solution for treating radiation-induced salivary gland damage.

Mechanisms of radiation-induced salivary gland damage

Salivary gland structure

The three major salivary glands (parotid, submandibular, and sublingual) contribute to over 90% of saliva production [17] and serve particular functions based on their structural composition. The parotid gland is mainly composed of acinar cells that secrete saliva and are responsible for the majority of stimulated saliva production in addition to ductal cells that deliver saliva to the mouth [102], [11]. The submandibular gland is composed of ductal cells and a mixed acinar cell population with both saliva and mucous secretion functions and is responsible for the majority of unstimulated saliva production [103], [11]. The sublingual gland is also composed of a mixture of ductal and acinar cells, but the acinar cells contain 10-fold higher levels of mucins compared to acinar cells in the submandibular gland and therefore the sublingual gland is responsible for the majority of mucous secretion [104], [17]. Thus, investigating individual cellular compartments within the major salivary glands is necessary to investigate the different functions of salivary glands collectively.

DNA damage, inadequate DNA repair, cell cycle arrest

It is well established that radiation (IR) directly and indirectly damages intracellular DNA, and in the salivary gland the typically-observed DNA damage types are oxidative damage to the sugars and bases, clustered DNA damage, and DNA single- and double-stranded breaks (SSBs/DSBs) [105], [106], [107]. One study demonstrated in parotid salivary gland tissue extracted from mice exposed to a single 5 Gy IR dose a 3.3-times increase in DNA DSBs compared to untreated tissue within 15 minutes of exposure [108]. This same study demonstrated inadequate DNA repair in irradiated parotid tissue by measuring Sirtuin-1 (SirT-1) protein levels, as SirT-1 is recruited to DNA damage sites and deacetylates p53 and Forkhead box class O (FOXO) transcription factors, which suppresses apoptosis and promotes DNA damage repair [109]. SirT-1 protein levels were significantly reduced in irradiated parotid tissue compared to untreated, which is correlated with inadequate DNA DSB repair [108]. The study also measured phosphorylation of the histone H2A variant H2AX at Ser139 (known as γ-H2AX), which is reflective of DNA repair, and compared it to irradiated mice pretreated with insulin-like growth factor-1 (IGF-1) [108]. Phosphorylated γ-H2AX protein levels were about 50% lower in the irradiated mice pretreated with IGF-1 compared to irradiated only mice, indicating that IGF-1 enhances DNA DSBs repair resolution after IR treatment [108]. Furthermore, it was demonstrated that SirT-1 activity is necessary for IGF-1 mediated DNA repair in irradiated parotid acinar cells as pretreatment with the SirT-1 specific inhibitor EX 527 and IGF-1 resulted in DSBs comparable to that of non-irradiated controls [108]. IGF-1 pretreatment has been shown to preserve salivary gland function in mice at 30 and 90 days post-fractionated IR treatment [110], therefore SirT-1-dependent IGF-1 DNA repair may be one of the mechanisms facilitating the preservation of salivary gland function following IR.

DNA damage checkpoints are essential for halting the cell cycle to allow DNA repair to occur before proceeding through mitosis to ensure cell viability [111]. It has been demonstrated in acinar cells from parotid glands exposed to 5 Gy IR that the percentage of cells in the G2/M phase checkpoint is not significantly different from untreated cells, but when mice are pretreated with IGF-1 and exposed to IR, the percentage of cells in G2/M increases fourfold compared to untreated and irradiated only groups [112]. Expression levels of the cell cycle arrest gene *p21* and phosphorylated cyclin-dependent kinase *cdc2* levels were significantly higher in the groups pretreated with IGF-1 compared to untreated and irradiated only groups, suggesting IGF-1-induced G2/M cell cycle arrest is promoted through p21 and its inhibitory action on *cdc2* [112]. It was further demonstrated that IGF-1 pretreatment reduces the binding of ΔNp63 (a truncated p63 isoform lacking a transactivation domain) to the p21 promoter after irradiation, which corroborates the increase in p21 expression observed with IGF-1 pretreatment [112]. Additionally, irradiated mice pretreated with IGF-1 displayed decreased phosphorylated and total p53 protein levels at 8- and 24-hours following IR compared to irradiated only mice, suggesting that p53 is involved in IR-induced cell cycle arrest [112]. To confirm the involvement of p53, parotid tissue from irradiated p53 knockout ($^{-/-}$) mice with or without IGF-1 pretreatment was stained for proliferating cell nuclear antigen (PCNA) and the percentage of PCNA-positive acinar cells increased significantly in the p53$^{-/-}$ mice pretreated with IGF-1 compared to wild-type controls, showing that p53 is necessary to induce cell cycle arrest following IR and prevent proliferation [112]. Another study tested the effects of a cyclin-dependent kinase inhibitor, Roscovitine, on cell cycle arrest following 5 Gy IR treatment and discovered that pretreatment of mice with Roscovitine significantly increased the percentage of cells in the G2/M phase checkpoint and upregulated p21 expression at 6 hours post treatment compared to IR plus vehicle group [113]. Roscovitine pretreatment preserved salivary gland function at days 3, 14, and 30 following IR treatment compared to radiation plus vehicle group [110], suggesting that the increase in G2/M cell cycle arrest underlies preserved salivary gland function after IR treatment.

Apoptosis, autophagy, and cellular senescence

Apoptosis has been shown to increase acutely following radiation in salivary acinar cells of mice, beginning at 8 hours, peaking at 24 hours, and diminishing after 72 hours [114], [115], [116], [117]. To investigate the apoptotic mechanism, the role of Akt in suppressing apoptosis following (0.25-5 Gy) IR treatment was tested using transgenic mice expressing a constitutively activated mutant of Akt1, myr-Akt1 [114]. Akt phosphorylates MDM2 (murine double minute clone 2), which stimulates translocation of MDM2 from the cytoplasm to the nucleus where it binds p53 to target it for degradation [118]. In addition to the role of p53 in signaling cell cycle arrest in response to DNA damage, it can also induce apoptosis when DNA repair is ineffective [119]. At 8 and 24 hours post-IR treatment (single 5 Gy dose), the percent of activated caspase-3 positive cells was significantly lower in acinar cells from the irradiated myr-Akt mice compared to the irradiated control mice, which supports the role of Akt in suppressing radiation-induced apoptosis in salivary acinar cells [114]. Additionally, levels of phosphorylated p53 at serine^{18} and total p53 protein levels significantly decreased in acinar cells from irradiated myr-Akt mice compared to irradiated control mice [114]. To test the role of MDM2 in the Akt/p53 pathway of apoptotic suppression, the researchers used short interfering RNA (siRNA) to knockdown MDM2 in myr-Akt derived acinar cells and discovered increased total p53 protein levels at 48 and 72 hours post-transfection and increased susceptibility to etoposide-induced apoptosis in the siRNA transfected myr-Akt derived acinar cells compared to the lipid transfection control myr-Akt derived acinar cells [114]. Thus, these results support the role of the Akt/MDM2/p53 pathway suppressing apoptosis in irradiated salivary acinar cells.

Another study confirmed p53-dependent apoptosis following IR in the salivary gland using a p53$^{-/-}$ mouse model [115]. A dose-dependent increase in transcription of pro-apoptotic genes (PUMA and Bax) was observed at 4 hours post-(1, 2, or 5 Gy) IR treatment in the parotid glands of $p53^{+/+}$ and $p53^{+/-}$, and this increase was attenuated in the $p53^{-/-}$ group [115]. Additionally, salivary flow rate did not significantly change in the $p53^{-/-}$ group following IR at both acute and chronic time points while salivary flow rate significantly decreased in the $p53^{+/+}$ and $p53^{+/-}$ groups chronically, which further supports the role of p53-dependent apoptosis contributing to loss of function of the salivary gland following IR treatment [115].

Further research has corroborated p53-dependent apoptosis underlying IR-induced salivary gland dysfunction using human parotid epithelial cells (hPECs) [120]. This study investigated the mechanistic effect of keratinocyte growth factor-1 (KGF-1) on radioprotection in hPECs, as KGF-1 has been shown to regenerate damaged epithelial cells in other tissues (lung, oral mucosa, and gastrointestinal tract) [120]. KGF-1 was administered to the cells directly after 10 or 20 Gy IR and the results of the TUNEL assay that detects fragmented DNA revealed a significant decrease in TUNEL-positive apoptotic cells in the treatment group compared to irradiated-only control cells [120]. The researchers investigated the anti-apoptotic mechanism by measuring protein levels of pro-apoptotic proteins p53, Bax, PUMA, cleaved caspase-9 and -3, and Bcl-2 and again observed a significant decrease in the pro-apoptotic protein levels in the treatment group compared to irradiated-only control cells [120]. To study the role of KGF-1 p53-dependent apoptosis inhibition in conferring radioprotection of the salivary gland, the researchers locally delivered KGF-1 to the salivary glands in rats and observed a significant improvement in salivary flow rates at 2 and 16 weeks post-15 Gy IR compared to the control group that received radiation only plus phosphate buffered saline (PBS) vehicle, which suggests the radioprotective effect of KGF-1 in the salivary gland is associated with regulation of p53-dependent apoptosis [120]. Thus, targeting p53-dependent apoptosis may be a promising mechanism for restoring IR-induced salivary gland dysfunction.

In addition to p53-dependent apoptosis contributing to IR-induced salivary gland dysfunction, protein kinase C delta (PKCδ) is a pro-apoptotic isoenzyme that has also been demonstrated to play a role in salivary gland dysfunction following IR. PKCδ is cleaved by caspase-3 following IR stimuli to induce apoptosis and PKCδ knockdown was demonstrated to protect parotid salivary glands *in vivo* from radiation-induced apoptosis compared to wild-type littermates at 24 hours following radiation [121]. This study tested if p53 is inactivated when PKCδ is knocked down and discovered no significant differences in phosphorylated p53 levels between PKCδ$^{-/-}$ and PKCδ$^{+/+}$ cells exposed to the apoptotic inducer etoposide, demonstrating that PKCδ is downstream of p53-induced apoptotic signaling [121]. The study also showed that PKCδ activates c-Jun amino-terminal kinase (JNK) since JNK phosphorylation was significantly decreased in the PKCδ$^{-/-}$ cells exposed to the apoptotic inducer etoposide compared to the PKCδ$^{+/+}$ cells exposed to etoposide [121]. A different study tested the effect of PKCδ on IR-induced salivary gland dysfunction using tyrosine kinase inhibitors to prevent phosphorylation and activation of PKCδ [122]. Dasatinib is a broad-spectrum tyrosine kinase inhibitor and significantly abrogated phosphorylation of PKCδ at Tyr-64 and Tyr-155 in pretreated ParC5 (rat parotid acinar) cells compared to untreated ParC5 cells [122]. The researchers administered dasatinib orally to mice 1 hour before and 3 hours after 10 Gy IR treatment and harvested parotid tissue at 24 hours post treatment to analyze apoptosis using caspase-3 staining [122]. Dasatinib treatment reduced activated caspase 3 in the irradiated parotid tissue by over 60% compared to the irradiated only parotid tissue group [122], suggesting that targeting PKCδ activation may provide another mechanism for preventing apoptosis-dependent IR damage in the salivary gland.

Autophagy is a mechanism by which cellular components are degraded and recycled, and activation of this mechanism has been linked to apoptosis following damage but the relationship between the two mechanisms is not fully elucidated [123]. The role of autophagy in IR-induced salivary gland damage was investigated by measuring the conversion of LC3-I to LC3-II, p62 phosphorylation levels, Atg5, and Atg 7 levels in the parotid tissue of irradiated mice as these are markers of autophagy induction [124]. At 4, 6, and 8 hours following 5 Gy IR treatment, autophagy was not significantly induced [124], so the researchers tested if IGF-1 pretreatment would induce autophagy and preserve salivary gland function after IR treatment since IGF-1 has previously been shown to decrease apoptosis and preserve salivary gland function [110]. At 6 and 8 hours post IR, autophagy was induced in the IGF-1 pretreated irradiated mice compared to the irradiated only control group, as demonstrated by increased Atg5 and Atg7 protein levels, increased LC3-II levels, and decreased phosphorylated p62 levels [124]. To confirm that autophagy is a mechanism by which IGF-1 preserves salivary gland function following IR, autophagy-deficient mice (*Atg5*$^{f/f}$*;Aqp5-Cre*) received IGF-1 treatment prior to 5 Gy IR and when saliva was collected at acute, intermediate, and chronic IR time points, the salivary flow rate was significantly lower in the autophagy-deficient mice compared to *Atg5*$^{+/+}$*;Aqp5-Cre* wild-type mice, demonstrating the importance of autophagy for IGF-1-mediated salivary gland preservation after IR [124]. Interestingly, the study observed a significant increase in apoptosis at 24 and 48 hours post-IR in the autophagy-deficient mice compared to the wild-type mice, suggesting an inverse relationship exists between apoptosis and autophagy in the parotid gland following IR [124].

Based on the previous research, autophagy induction may be a therapeutic mechanism for restoring IR-induced damage in the salivary gland. A pharmacological autophagy inducer, the rapalogue CCI-779, was given 4-8 days following 5 Gy IR treatment in FVB mice and salivary flow rates were restored to untreated levels compared to the irradiated-only group at chronic time points following IR [125], suggesting rapalogues may be useful in the clinic for the management of IR-induced xerostomia in HNC patients. Recently, a 3D organoid system was used to investigate the role of autophagy in the self-renewal capability of salivary gland stem cells and found that pharmacological stimulation of autophagy promoted self-renewal in both mouse and human salivary gland stem cells [126], which provides a promising mechanism to investigate for permanent restoration of function following IR damage in the salivary gland.

Cellular senescence has been observed to occur following IR in the salivary gland of different model organisms [127], [128], [129]. One study used a mouse model to investigate senescence induction in the salivary gland following 15 Gy IR exposure and observed persistent DNA damage at 48 hours to 8 weeks following IR (measured by increased γH2AX and p53 binding protein-1 (53BP1) phosphorylation in response to DNA DSBs), and an increase in senescence-associated markers SA-βgal, p19ARF, and DcR2, PAI-1 and inflammatory cytokine interleukin (IL)-6 at 2 and 8 weeks following IR treatment [127]. The study further demonstrated the significance of IL-6 in senescence induction following IR in the salivary gland by using an IL-6 knockout (IL-$6^{-/-}$) mouse and observed a significant reduction in the aforementioned senescence-associated markers, and they further supported this point by pretreating wild-type mice with local IL-6 administration before IR treatment and observed a reduction in the senescence-associated markers as well as increased saliva production compared to irradiated-only control wild-type mice at 8 weeks post-IR [127]. Another group used a swine model and observed a significant decrease in expression of the anti-senescence marker vascular endothelial growth factor (VEGF) in salivary gland epithelial cells at 1 and 5 weeks post-20 Gy IR treatment, and they were able to reverse this decrease through Hedgehog activation in resident parotid gland macrophages to reduce epithelial cell senescence [128]. These findings were corroborated in a follow-up study where the researchers observed that transient Sonic Hedgehog (Shh) activation in the submandibular glands of mice via adenoviral delivery at day 3 following 15 Gy IR treatment reduced cellular senescence (Gdf15 gene expression) and oxidative stress while promoting DNA repair (increased expression of survivin and miR-21 genes) [130]. Thus, inhibiting cellular senescence may be a therapeutic mechanism for restoring IR-induced dysfunction in the salivary gland.

Reactive oxygen species production

It is well-established that IR increases reactive oxygen species (ROS) production, and this effect has been demonstrated to alter mitochondrial function in salivary submandibular cells by contributing to destruction of mitochondrial membrane structures, decreased mitochondrial membrane potential, and increased cytochrome c release [131]. The role of mitochondrial ROS production in IR-induced salivary gland dysfunction was demonstrated in a study where mice received MitoTEMPO treatment 10 minutes before, 24 hours after, and 48 hours after 15 Gy IR treatment [132]. MitoTEMPO is a pharmacological mitochondrially targeted ROS scavenger, and MitoTEMPO treatment attenuated the initial IR-induced increase at 24-72 hours in mitochondrial ROS and it rescued the decrease in salivary flow rate observed in irradiated mice at 30 and 60 days post-IR treatment [132]. Thus, the acute increase in mitochondrial ROS after IR contributes to chronic salivary gland dysfunction and inhibiting this initial increase is beneficial in managing chronic damage. Another group developed an ROS scavenger, HL-003, with the goal of achieving superior antioxidant potential compared to amifostine [133]. Mice received an injection of either HL-003 or amifostine 30 minutes prior to 15 Gy IR and salivary gland tissue was collected 2 weeks after treatment, and pretreatment with both HL-003 and amifostine rescued salivary flow rate compared to irradiated only mice, with the HL-003 IR group displaying a slightly higher improvement compared to the amifostine IR group [133]. This study demonstrated that HL-003 protects the salivary epithelium from IR damage as the expression of the salivary epithelial marker, AQP-5, was preserved with HL-003 pretreatment in irradiated mice, and that HL-003 decreases oxidative damage as total antioxidant capacity levels were rescued to untreated control levels in the HL-003 pretreated IR mice [133]. A separate study investigated salidroside, the main ingredient of a Chinese herb, and discovered that submandibular acinar cells pretreated with salidroside for 24 hours prior to 15 Gy IR had decreased mitochondrial ROS production, rescued mitochondrial damage, and significantly increased levels of the antioxidants superoxide dismutase (SOD), catalase (CAT), and reduced glutathione (GSH) compared to irradiated only cells at 24, 48, and 72 hours post-IR [134]. Based on these studies, pharmacological agents that scavenge free radicals and inhibit their production are promising for preserving salivary gland function following IR and possibly decreasing the adverse side effects associated with amifostine treatment.

Inflammatory response

Inflammation is an essential phase of wound healing and unresolved inflammation may underlie IR-induced salivary gland dysfunction. It has been shown that expression levels of inflammatory cytokine interleukin (IL)-6 increase at 3 hours post-13 Gy IR treatment, decrease at 6 hours, and increase again at day 14 post-IR in the salivary glands of mice [127]. Since IL-6 is a proinflammatory cytokine, the role of this cytokine in IR-induced salivary gland dysfunction needs to be further studied [13]. The P2X7 receptor (P2X7R) is an extracellular ATP (eATP)-gated ion channel that upon activation by eATP released from damaged cells promotes proinflammatory signaling of cytokines (including IL-6), tumor necrosis factor-α (TNF-α), and the eicosanoid prostaglandin E_2 (PGE_2) [135]. A study investigated the role of P2X7R in salivary gland damage post-IR using P2X7R knockout (P2X7R$^{-/-}$) mice and observed significantly decreased PGE_2 release in the primary parotid cells of P2X7R$^{-/-}$ mice compared to wild-type mice following 5 Gy IR at 24, 48, and 72 hours [135]. Importantly, the study demonstrated that P2X7R deletion using the knockout mice and antagonism using P2X7R antagonist (A438079) pretreatment 1 hour prior to IR significantly restored saliva flow rate at both 3 and 30 days following IR compared to irradiated wild-type and irradiated wild-type plus vehicle controls [135]. P2X7R was shown to play a role in salivary gland dysfunction following IR that may be mediated by PGE_2 secretion, and it was further demonstrated that the effect of P2X7R is independent of apoptosis as apoptotic levels were similar in parotid cells of P2X7R knockout mice and wild-type mice at 24-72 hour following IR [135]. To further elucidate the role of PGE_2 secretion in IR-induced salivary gland dysfunction, the researchers treated FVB and C57B6/6J mice with indomethacin at days 3, 5, and 7 post 5 Gy IR and observed restoration of salivary flow rate at days 10 and 30 post-IR compared to the irradiated plus vehicle control [136]. Indomethacin is a non-steroidal anti-inflammatory drug (NSAID) that decreases PGE_2 secretion by preferentially blocking cyclooxygenase-1 (COX-1) in parotid acinar cells, and the study confirmed that indomethacin treatment significantly decreased both COX-1 activity and PGE_2 secretion at 24 hour post 5 Gy IR [136]. The researchers further investigated the mechanism of PGE_2 secretion in salivary gland damage post-IR and discovered decreased JNK activity at day 8 following IR and decreased proliferation and increased amylase levels at day 30 post-IR in mice receiving post-IR indomethacin treatment compared to irradiated plus vehicle control mice, suggesting JNK signaling via PGE_2 secretion contributes to salivary gland damage and loss of function following IR [136].

Neuronal and vascular changes

Parasympathetic innervation is essential for normal function of the salivary glands as denervation results in irreversible salivary gland atrophy [137]. More specifically, parasympathetic ganglion removal in mouse explant organ culture significantly decreased keratin 5-positive ($K5^+$) epithelial progenitor cells, and these cells are necessary for organogenesis to occur when they are in an undifferentiated state [138]. Knox et al. tested the importance of parasympathetic innervation in the IR damage response by exposing fetal submandibular explant cultures from transgenic mice expressing fluorescent progenitor cells ($K5^+$) to 5 Gy IR [139]. At days 5 and 7 following IR, the progenitor cells ($K5^+$) survived but parasympathetic function was impaired as evidenced by decreased end bud number, and neurturin expression was reduced, which increased neuronal apoptosis [139]. Neurturin is a neurotrophic factor produced by the submandibular gland during development and is important for normal parasympathetic signaling [139], [140]. The researchers treated the submandibular explant cultures with neurturin and it rescued the parasympathetic function that was diminished with IR as well as increased epithelial regeneration, suggesting that neurturin protects parasympathetic innervation and may restore salivary gland function following IR [139]. *In vivo* adenoviral delivery of neurturin to mouse salivary glands 24 hours prior to 5 Gy IR treatment restored salivary flow rates to untreated levels at 60 days following IR, and using *ex vivo* fetal salivary gland cultures they demonstrated that neurturin adenovirus improved salivary gland growth after IR by increasing parasympathetic innervation [141], thus supporting the role of neurturin in protecting the salivary gland from IR-induced dysfunction by increasing parasympathetic innervation. To improve delivery of the neurturin gene for clinical use, an adeno-associated virus serotype 2 (AAV2) vector was used to reduce the number of immune side effects associated with the adenovirus serotype 5 vector used in the previous study [142]. This follow-up study delivered an AAV2-based vector encoding human neurturin (CERE-120) to the salivary glands of minipigs 10 days prior to fractionated IR (6 x 5 Gy) and observed restoration of salivary flow rates at 90, 120, and 300 days post-IR and RNA sequencing (RNA-seq) analysis revealed a decrease in expression of genes involved in IR-induced fibrosis and the innate and adaptive humoral immune responses with CERE-120 pretreatment [142]. Not only does neurturin appear to increase parasympathetic innervation to restore IR-induced salivary gland dysfunction, but it also appears to affect the immune and fibrotic responses, suggesting that neurturin exerts multi-faceted effects on salivary gland restoration.

While the acinar cells have been the main focus for investigating IR-induced salivary gland damage, the microvascular endothelial cells are also involved in IR damage, and this was first demonstrated in the gastrointestinal (GI) tract of mice [143]. A group investigated the effect of 15 Gy IR on the microvasculature of the salivary glands of mice and discovered an approximate 45% decrease in the microvessel density (MVD) of irradiated mice compared to unirradiated controls [144]. VEGF and basic fibroblast growth factors (bFGF) were previously shown to protect the GI tract of mice, so the researchers used adenoviral delivery of VEGF and bFGF to the salivary glands of mice 48 hours prior to 15 Gy IR treatment and observed restoration of MVD to non-irradiated control levels at 4 hours post-IR as well as restoration of salivary flow rate at 8 weeks post-IR compared to non-irradiated controls [144]. Another study sought to investigate the mechanism by which IR-induced microvascular damage contributes to salivary gland dysfunction and tested the role of ROS by pretreating mice with TEMPOL, the ROS scavenger, 10 minutes prior to 15 Gy IR [145]. Pretreatment with TEMPOL significantly restored MVD levels to non-irradiated control levels at 4 hours post-IR, suggesting that IR-induced microvascular damage is mediated by increased ROS production, which contributes to loss of salivary gland tissue function [145]. A different approach was used by a group to investigate if bone marrow-derived cells (BMCs) mobilized with cytokine agents (granulocyte colony-stimulating factor (G-CSF) or the combination of FMS-like tyrosine kinase-3 ligand, stem cell factor, and G-CSF (termed F/S/G)) can regenerate IR-damaged salivary glands [146]. The F/S/G post-IR treatment was more effective compared to the G-CSF treatment as the F/S/G treatment increased the amount of mobilized BMCs by 10-fold and resulted in significantly reduced damage to submandibular blood vessels and BMC-derived vessels, suggesting that combination cytokine treatment can increase the efficacy of BMCs regenerating IR-damaged salivary glands [146].

Cell structure alterations

Adherens junctions are important in the formation of new cell-cell contacts during wound healing and are essential for acinar cell differentiation in embryonic submandibular gland development [147]. A complex interplay exists between adherens junctions and the actin cytoskeleton in response to injury to regulate cell shape, and a study investigated how 5 Gy IR affects both adherens junctions (the E-cadherin/β-catenin complex) and actin in the parotid salivary glands of mice and observed a significant decrease in E-cadherin/β-catenin binding at days 4, 7, and 30 post-IR and disrupted F-actin organization at days 7 and 30 post-IR [148]. The researchers further elucidated the mechanism of E-cadherin/β-catenin disassociation following IR and discovered that phosphorylated Rho-associated coiled-coil containing kinase 1 (ROCK1) increases at day 7 post-IR, and activated ROCK regulates the myosin regulatory light chain (MLC) that controls actin filament movement, suggesting that IR induces a ROCK-mediated E-cadherin/β-catenin disassociation that results in disrupted F-actin organization and contributes to loss of tissue function [148]. In addition to adherens junctions, tight junctions between cells maintain the cellular polarity and following 20 Gy IR targeted to the submandibular glands of rats, tight junction width decreased at 1 and 12 weeks post-IR, and both secretory function and tight junction width were restored when pilocarpine was administered 1 hour prior to IR and for 6 consecutive days post-IR, which supports the importance of tight junction function for preserving IR-induced salivary gland dysfunction [149]. Cellular polarity was demonstrated to be disrupted following IR as decreased levels of the apical polarity marker, protein kinase C zeta (PKCζ), were observed at days 5, 7, and 30 post-5 Gy IR in mouse parotid salivary glands [150]. The researchers observed increased levels of Jun N-terminal kinase (JNK), a kinase that increases cell proliferation, at day 5 post-IR, and discovered using PKCζ knockdown *in vivo* and inhibition *in vitro* that PKCζ suppression increases JNK activation, leading to compensatory proliferation in the irradiated salivary gland [150]. Thus, IR-induced apical-basolateral polarity disruption is correlated with increased compensatory proliferation in the salivary gland, which contributes to chronic loss of function.

Compensatory proliferation

Increased cell proliferation in response to tissue damage, termed compensatory proliferation, has been observed to occur in the salivary gland following IR, beginning acutely in the intercalated duct and starting at 5-6 days post-IR in the acinar cells and granular convoluted tubule cells of the parotid and submandibular glands [151], [152], [153]. Although the number of cells is increasing to re-populate the tissue, measured using antigen KI-67 (Ki67) positive cells as a proliferation marker, they are not differentiating properly to restore function to the salivary gland tissue, as evidenced by reduced levels of the acinar cell differentiation marker salivary amylase and decreased salivary flow rates chronically following IR [154], [155]. Various pharmacological agents have been tested to inhibit compensatory proliferation in the salivary gland and see if the inhibition correlates with loss of tissue function. The agonist monoclonal antibody mAbEDAR1 activates the signaling of the ectodermal signaling molecule ectodysplasin-A1 (EDA)/EDA receptor (EDAR), which initiates development of teeth, hair follicles, and salivary glands [156]. Administration of mAbEDAR1 to mice 4 days following 5 Gy IR resulted in restoration of salivary gland function to unirradiated vehicle control levels at day 14 and chronically post-IR [157]. Proliferating cell nuclear antigen (PCNA) staining revealed a significant decrease in the number of PCNA-positive acinar cells in the post-IR mAbEDAR1 treatment group compared to the irradiated plus vehicle group as well as restoration of amylase positive area to unirradiated vehicle control levels, demonstrating that mAbEDAR1 decreases cell proliferation and increases differentiation following IR in the salivary gland, which is correlated with restored salivary gland function [157]. The rapalogue CCI-779 was previously shown to induce autophagy in a mouse model following 5 Gy IR and restore salivary flow rates chronically, and in the same study CCI-779 administered post-IR restored PCNA levels and amylase area to untreated control levels, which further supports the role of compensatory proliferation contributing to IR-induced salivary gland dysfunction [125]. Additionally, IGF-1 administered 4-8 days post-5 Gy IR reduced the percentage of PCNA positive acinar cells at day 9 post-IR and chronically compared to irradiated control mice and restored amylase area and salivary flow rates to untreated levels chronically [154].

Chibly et al. used a mouse model to demonstrate that inactivation of atypical protein kinase C zeta (aPKCζ) is correlated with the initiation of compensatory proliferation in progenitor cells, identified as label-retaining cells (LRCs), in the acinar compartment of the salivary gland at 5-7 days post-IR [153]. Upon administration of IGF-1 post-5 Gy IR, the percentage of aPKCζ positive LRCs as well as salivary flow rates were restored to untreated levels at day 30 post-IR, and using a $Prkcz^{-/-}$ mouse model the study showed that aPKCζ is required for IGF-1-induced restoration of salivary gland function following IR [153]. Interestingly, $Prkcz^{-/-}$ mice display significantly higher baseline proliferation, assessed by percentage of Ki67-positive acinar cells, compared to wild-type mice, and 5 Gy IR does not alter proliferation levels over time in the $Prkcz^{-/-}$ mice, further supporting the observation that PKCζ is modulated by IR and correlated with increased cell proliferation at day 5 and 30 post-IR [150]. Thus, PKCζ may be a therapeutic target to reduce proliferation post-IR in the salivary gland and restore function due to its role in regulating both cellular polarity and compensatory proliferation.

Stem/progenitor cells and tissue regeneration

The reactivation of endogenous adult stem cells in the salivary gland is a promising therapeutic mechanism for restoration of IR-induced dysfunction. Initiating cells that aid in tissue reconstruction following injury are defined as progenitor cells since their differentiation capabilities are limited compared to multipotent stem cells [158]. A hinderance to this research is the limited knowledge regarding the identity of the salivary gland stem and progenitor cell (SPC) population in the salivary gland, especially since cellular differences exist across the three major glands [153], [158], [159]. More specifically, the identity of adult SPCs that contribute to acinar cell formation during wound healing is unclear and is needed to restore secretory function following IR damage [160]. One view is that SPCs in the adult ductal compartment give rise to both ductal and acinar cells [161], however, a lack of definitive lineage tracing experiments has led to this hypothesis not demonstrating the contribution of ductal cell replacement to salivary gland function [162]. An older study identified the transcriptional regulator *Mist1* exclusively expressed in salivary acinar cells across all three major pairs of salivary glands [163], paving the way for a more recent study to investigate acinar cell replacement using a genetic pulse-chase experiment [162]. Using a tamoxifen-inducible Cre reporter for *Mist1* gene expression in the *Rosa26*$^{\text{Brainbow2.1}}$ (*R26*)$^{\text{Brainbow2.1}}$ reporter mouse strain, the researchers were able to trace the proliferating acinar cells through the expression of fluorescent reporter proteins and observed clonal expansion of the acinar cells after a 6-month chase in submandibular and parotid glands [162]. The researchers further demonstrated that acinar cells are replaced by clonal expansion of differentiated acinar cells rather than unlabeled stem cells following injury by performing ductal ligation and observed clonal expansion of the acinar cells following de-ligation [162]. Another group demonstrated that $SOX2^+$ is a marker for salivary gland progenitor cells that differentiate into acinar cells using a similar genetic lineage tracing design as the previous study and demonstrated that $SOX2^+$ is necessary for proper acinar cell function as SOX2 ablation in $SOX2^+$ cells resulted in atrophic cells and decreased total number of acinar cells in the salivary gland [160]. Furthermore, the researchers tested the effect of 10 Gy IR on SOX2-mediated acinar cell replenishment in the sublingual gland of their genetic lineage tracing mouse model and discovered 14 days post-IR replacement of acinar cells by $SOX2^+$ cells, which they further demonstrated can be activated by post-IR treatment with the acetylcholine mimetic carbachol [160]. Thus, $SOX2^+$ cells may be a therapeutic target to restore the functional acinar compartment of the salivary gland following IR damage.

A different model for identification of salivary gland SPCs uses a label retention assay, which is a pulse-chase assay utilizing bromodeoxyuridine (BrdU) or 5-Ethynyl-2′-deoxyuridine (EdU) injections in a pup mouse model that incorporates into the DNA of actively dividing cells and detects label retaining cells (LRCs) in the salivary glands of the adult mice [164], [165],

[166]. One study administered BrdU or EdU to 10-day old mice and chased them to 8 weeks when the salivary glands are fully developed and observed the presence of LRCs in both the acinar and ductal compartments of parotid and submandibular glands [165]. Putative salivary SPC markers Keratin 5 (K5), Keratin 14 (K14) and c-kit co-localized with the LRCs in various gland compartments and structures, suggesting that the salivary LRCs are a heterogeneous population [165]. The researchers further demonstrated that LRCs are progenitor cells as the LRCs were able to proliferate to form primary and secondary spheres that co-localized with the proliferation marker Ki67 and matured to produce amylase, which provides support for the regenerative capacity of LRCs to restore salivary gland function [165]. Importantly, the effect of 5 Gy IR on salivary LRCs was tested and a similar percentage of LRCs was observed in both acinar and ductal compartments in the irradiated mice compared to the untreated mice, and no apoptosis was observed in the LRC population 24 hours post-IR as no co-localization of caspase-3 and Edu was observed [165]. These results suggest that an endogenous, heterogeneous LRC population remains in the salivary gland following IR damage and could be stimulated to regenerate the gland. A different investigation observed salispheres generated from Edu-labeled LRCs in the parotid glands of mice exposed to 5 Gy IR and noticed a significant decrease in the number and size of spheres formed compared to salispheres from non-irradiated mice [167]. Additionally, post-IR treatment with the growth factor fetal bovine serum (FBS) or IGF-1 restored salisphere numbers and size from irradiated glands to those from non-irradiated glands, suggesting that certain growth factors can stimulate salivary LRCs to proliferate *ex vivo* following IR damage [167].

Calcium signaling dysregulation

Salivary gland secretion is controlled by store-operated Ca^{2+} entry (SOCE) signaling in acinar cells [168]. The calcium-permeable channel, transient potential melastatin-like 2 (TRPM2), was activated by 15 Gy exposure in mouse submandibular acinar cells as evidenced by a high Ca^{2+} influx 24 hours post-IR [169]. Interestingly, salivary flow was restored in both TRPM2 knockout mice and wild-type mice receiving the ROS scavenger TEMPOL or the poly [ADP-ribose] polymerase 1 (PARP1) inhibitor 3-aminobenzamide at 30 days post-IR treatment, demonstrating that TRPM2-induced loss of salivary function following IR is mediated by both PARP1 and ROS activity [169]. A follow-up study investigated the mechanism by which TRPM2 activation mediates loss of salivary gland function and using TRPM2 knockout mice observed that 15 Gy IR decreases the endoplasmic reticulum (ER)-$Ca2^{+}$ sensor protein, stromal interaction molecule 1 (STIM1), and SOCE in submandibular acinar cells starting at 48 hours post-IR [170]. The researchers observed a significant increase in caspase-3 activation at 3 and 10 days post-IR in the wild-type mice compared to the TRPM2 knockout mice, demonstrating the role of TRPM2 stimulating caspase-3 cleavage of STIM1, resulting in decreased levels of the protein that initiates SOCE following IR [170]. Adenoviral delivery of STIM1 to the salivary glands of mice 15 days post 15 Gy IR resulted in a twofold increase in SOCE in the acinar cells and in saliva secretion at 30 days post-IR compared to irradiated control virus mice, further illustrating that STIM1 depletion following IR treatment in the salivary gland decreases saliva secretion by decreasing SOCE [170]. Thus, calcium signaling dysregulation contributes to loss of salivary gland function after IR treatment and TRPM2 and STIM1 are promising therapeutic targets for restoring tissue function.

Metabolomics Analysis

Background and Methods

Metabolomics is the study of metabolites, which are the substrates and products of metabolic reactions that drive cellular functions essential for life. Metabolites are involved in a plethora of biochemical actions, such as energy production and storage, apoptosis, post-translational modification regulation, epigenetic regulation, embryonic stem cell pluripotency, and signal transduction through their interaction with proteins [171], [172], [173], [174], [175]. Metabolites modulate both gene and protein activity and reflect environmental changes, thus metabolites and their activity reflect the phenotype of the biological system [176].

Metabolomic studies are untargeted or targeted depending on the research question. Untargeted studies are hypothesis-generating investigations aimed at acquiring as much data as possible, annotating the metabolites, and identifying metabolite changes as relative levels to each other to provide an overview of metabolic changes [177]. Targeted studies are hypothesis-driven investigations using internal standards to identify and quantify a select number of known metabolites, typically metabolites of interest from untargeted studies [177]. The two major analytical methods used in metabolomics are separation techniques coupled to mass spectrometry (MS) and nuclear magnetic resonance (NMR) spectroscopy. Liquid chromatography coupled to MS (LC-MS) and gas chromatography coupled to MS (GC-MS) are used to separate the compounds through elution or gas gradients, with the choice of method depending on the sample composition [178]. High performance liquid chromatography (HPLC) is a commonly-used separation technique as it is capable of separating compounds of a wide polarity range [178]. Within the mass spectrometer, the ion source converts the molecules within samples into ions, the mass analyzer resolves the ions in an electromagnetic field or time-of-flight tube, and then the detector measures the ions [178]. Electrospray ionization (ESI) is a popular ion source and is termed “soft ionization” as many of the detected molecular ions remain intact through the conversion process [178]. MS-based metabolomics approaches have several advantages, such as high detection sensitivity and a large output of detected metabolites, but sample preparation is more technical than in NMR spectroscopy as different chromatography techniques are required for different classes of metabolites and the sample is destroyed through the analysis [179]. NMR spectroscopy is a more simplified workflow compared to MS approaches, where alterations in the electromagnetic waves emitted by the nuclei of the sample are detected and analyzed to form spectral data [179]. NMR spectroscopy is an advantageous technique due to its high reproducibility and it can also be used for *in vivo* studies using ^{1}H magnetic resonance spectroscopy [179]. Although a full review of metabolomics methodology is beyond the scope of this literature review, an overview of the methods used in the following research studies is presented here for context.

Metabolic biomarker discovery

Due to the ability of metabolites to distinguish phenotypes, identifying metabolic signatures that are biomarkers of disease is helpful for prediction, diagnosis, and early treatment. One of the earliest metabolic biomarkers discovered for tumors is an increase in glycolysis in the presence of oxygen, termed the “Warburg effect”, which increases the rate of ATP production for sustained malignant cell proliferation [180]. Since this discovery, the metabolic reprogramming of cancer cells has been further elucidated and is quite complex, involving many pathways that interact with glucose and glutamine synthesis for energy production, such as mutations in Kreb’s cycle enzymes corresponding to the intermediates isocitrate, succinate, and fumarate [181]. Isocitrate dehydrogenase (IDH) gain-of-function mutations are present in several cancers, such as glioma and acute myeloid leukemia, and targeted inhibitors of IDH1 and IDH2 inhibited malignant cell proliferation and induced cell differentiation *in vitro* and *in vivo*, and early clinical trials confirm the efficacy of the inhibitors for suppressing cancer growth in hematological cancers [182]. Thus, metabolic biomarker discovery for diseases can identify therapeutic targets for disease treatment. Metabolomics studies extend across many disease and damage phenotypes for biomarker discovery and targeted therapy, including but not limited to different cancer models, cardiovascular disease, diabetes, liver disease, ischemia–reperfusion injury, and radiation (IR) damage [183], [184], [185].

Metabolic biomarkers of radiation damage: rodent model biofluids

Much research has focused on utilizing metabolomics to rapidly identify individuals exposed to IR, through accidental exposure or a nuclear event, as a biodosimetric method for treatment of acute radiation syndrome (ARS). Easily accessible biofluids are the preferred analysis medium for humans and include urine, serum, and saliva. Therefore, many animal studies utilize these biofluids for assessing IR-induced metabolic biomarkers.

The utility of urine for biodosimetric research has been supported by numerous studies using various model systems [186], [187], [188], [189]. Tyburski et al. used a mouse model (C57BL/6-N) to investigate the effects of low-IR doses at different time points on the urinary metabolic profile [186]. Mice were exposed to single doses of 0 (sham), 1, 2, or 3 Gy radiation (whole-body) and urine was collected in 24-hours intervals at day 1, 3, 5, 7, and 9 after IR exposure [186]. Urine samples were analyzed using ultra-performance liquid chromatography coupled to time-of-flight mass spectrometry (UPLC-TOFMS) and revealed elevated levels of deaminated purine and pyrimidine derivatives thymidine, 2′-deoxyuridine, 2′-deoxyxanthosine, xanthine and xanthosine at day 1 following 1-3 Gy IR with a decrease in metabolite levels observed with increasing time post-IR compared to sham irradiated controls [186]. These deaminated purine and pyrimidine derivatives reached peak levels at 8-12 hours post-IR and returned to baseline levels at 36 hours post-IR, revealing a time-dependent excretion [186]. The authors hypothesized that IR induces nitrosative deamination of 2'-deoxycytidine and 2'-deoxyguanosine acutely, which leads to increased production of thymidine, xanthine and xanthosine in the urine [186]. Thus, urinary levels of deaminated purine and pyrimidine derivatives may aid in identifying the time course of low-IR exposure dose response for appropriate treatment to be administered. A different group investigated the effect of a range of IR doses (0.5 to 10 Gy IR) at different time points on the urinary metabolic prolife using a rat model [187]. UPLC-TOFMS of urine samples at 6-72 hours post-IR revealed a dose- and time-dependent decrease in urine metabolite excretion as thymidine and creatine levels increased and citrate levels decreased compared to sham irradiated controls [187]. These results in a rat model are similar to IR-induced metabolic biomarkers observed in the mouse model.

The effects of higher-IR dose (8 Gy IR exposure to whole-body) on the urinary metabolite profile of mice was investigated using nuclear magnetic resonance (NMR) spectroscopy and the samples were analyzed for a 6 hour period on days 1 through 7 post-IR [190]. Creatine, succinate, methylamine, citrate, 2-oxoglutarate, taurine, N-methyl-nicotinamide, hippurate, and choline were dysregulated post-IR, displaying a decreasing trend through days 3 and 4 followed by an increasing trend through day 7 with levels closely restored to sham irradiated control levels [191]. These metabolites are associated with the Kreb’s cycle, amine metabolism, lipid metabolism, amino acid metabolism, and nucleotide metabolism, suggesting time-dependent alterations in a variety of metabolic pathways in response to 8 Gy IR [190]. Another group used NMR spectroscopy (untargeted metabolomics analysis) to identify biomarkers that differentiate between whole-body IR exposure and partial-body IR exposure in a mouse model [192]. Mice received 10 Gy radiation to the whole body or targeted to the thoracic, abdominal, or hind limb region and urine samples were collected 24 hours post-IR [192]. Energy, gut flora, and taurine metabolism were common to whole-body and partial-body IR, but distinct metabolic profiles were observed in the urine between the whole body, thoracic, abdominal, and hind limb IR groups [192]. Taurine, creatine, and trimethylamine-N-oxide (TMAO) were most significantly upregulated in the hind limb IR group [192]. These results demonstrate that urinary metabolic markers are able to acutely distinguish whole-body from partial-body IR exposure. A follow-up study aimed to assess the reproducibility of urinary metabolite markers of IR exposure using NMR spectroscopy (untargeted metabolomics) and a logistic regression model using a mouse model [193]. Mice received whole-body 7.5 Gy IR and urine was collected 24 hours post-IR [193]. Tri-carboxylic acid (TCA) cycle, taurine and hypotaurine metabolism, and primary bile acid biosynthesis were the most significantly altered pathways with IR exposure compared to sham irradiated controls, and the logistic regression model predicted taurine, citrate, alpha-ketoglutarate, and fumarate as biomarkers with high sensitivity (1.00) and specificity (0.964) [193]. This study was able to validate previously identified biomarkers of IR exposure using a prediction model, which supports the use of these metabolites for IR exposure screening.

A more comprehensive urinary metabolic profiling of radiation exposure was performed by integrating liquid chromatography coupled to mass spectrometry (LC-MS) and NMR spectroscopy (both untargeted metabolomics analysis) [194]. Mice were exposed to 5 or 7.5 Gy radiation to the whole body and urine was collected 24 hours post-IR [194]. Taurine, creatine, citrate, and 2-oxoglutarate were elevated at both IR doses and enhanced coverage of metabolites and correlation networks in energy, taurine, gut flora, L-carnitine, and nucleotide metabolism was observed at both IR doses compared to sham irradiated controls [194]. This study demonstrated a similar urinary metabolic signature in response to both 5 and 7.5 Gy IR and improved metabolic profiling depth by combining the analysis of two independent metabolomics analysis techniques.

In addition to urine, saliva has been demonstrated to be a useful medium for assessing IR-induced metabolic changes. In a pilot study, mice were exposed to 0.5, 3, or 8 Gy (very low, low, or high dose) radiation to the whole body and saliva was collected on day 1 and 7 post-IR [195]. UHPLC-MS (untargeted metabolomics) analysis identified amino acids, fatty acids, and intermediates of nicotinate and nicotinamide metabolism as dysregulated at day 1 in saliva of each IR dose group, and at day 7 only the 8 Gy IR group displayed metabolic changes [195]. Based on these results, acute collection of saliva following IR exposure is needed to capture the complete metabolic effects, unless the dose is high enough to induce long-term effects as was observed with the 8 Gy IR dose.

Metabolic biomarkers of radiation damage: rodent model tissues

Although using biofluids to assess metabolic signatures of IR damage is convenient due to the non-invasive method of collection, biofluid metabolic profiles reflect the effect of IR on multiple organs and are therefore not useful for identifying tissue-specific mechanisms induced by IR exposure. A group investigated the effect of IR on cardiotoxicity by targeting 0.2 or 2 Gy IR to the heart tissue of mice and collecting the tissue at 48 hours and 20 weeks post-IR [185]. NMR spectroscopy (untargeted metabolomics analysis) revealed elevated levels of pantothenate and glutamate and decreased levels of alanine, malonate, acetylcarnitine, glycine, and adenosine at 48 hours post-2 Gy IR compared to sham irradiated controls [185]. Amino acid and amine derivatives were dysregulated between the 48-hour and 20-week time points in the groups exposed to 2 Gy IR [185]. Interestingly, histological analysis of the heart tissue did not reveal significant differences in collagen content or apoptosis between the two IR doses at the two time points compared to sham irradiated control, indicating that metabolomics analysis is a more sensitive method for detecting IR-induced effects in heart tissue compared to histological analysis [185]. Other researchers investigated metabolic changes in testicular tissue of mice exposed to 2 Gy whole-body IR and tissue was harvested at 24 hours, 3 weeks, and 5 weeks post-IR [196]. NMR spectroscopy (untargeted metabolomics analysis) identified changes in energy metabolism, osmolytes, and membrane metabolism acutely at 24 hours and some of these changes persisted chronically compared to sham irradiated controls [196]. Importantly, trichostatin A administration at 1 hour and 24 hours post-IR reversed the observed metabolic changes in testicular tissue and morphological and functional properties of sperm were restored [196], suggesting that reversing IR-induced metabolic changes may ameliorate IR-induced damage and restore tissue function.

The effects of IR, both whole-body and targeted, on liver metabolism have been investigated using *in vivo* mouse models. The effects of different types of whole-body radiation, γ (3.0 and 7.8 Gy) or proton (3.0 Gy), on liver metabolism at days 4 and 11 post-IR in mice was tested using NMR spectroscopy (untargeted metabolomics analysis) [197]. Distinct metabolic profiles were observed for each IR source and IR dose in liver tissue compared to sham irradiated controls [197]. However, across the different IR sources, seven metabolites were significantly increased (including glutathione, creatinine, and glutamine) and choline, O-phosphocholine, and trimethylamine N-oxide levels were significantly decreased at days 4 and 11 post-IR [197]. Another group compared the effects of whole-body IR and targeted IR to the liver on metabolic reprogramming by analyzing both liver tissue and plasma [198]. Mice received 10 or 50 Gy IR targeted to the liver or 10 Gy whole-body IR, and using LC-MS and GC-MS (untargeted metabolomics analysis) at 24 hours post-IR, purine and pyrimidine metabolites were associated with both liver and plasma samples from the 50 Gy IR targeted to the liver group [198]. The results from this study suggest that plasma may be useful for identifying biomarkers of IR-induced liver toxicity since common metabolites were altered in both the liver and plasma samples [198]. The effect of IR on intestinal metabolism was investigated by applying targeted 2 or 20 Gy IR to the abdomen of mice and harvesting the intestinal tissue 24 hours post-IR for GC-MS (untargeted metabolomics analysis) [199]. Elevated levels of amino acids, carbohydrates, organic acids, and sugars were observed in the tissue compared to sham irradiated controls [199], and the authors hypothesized that the increased amino acid levels are associated with increased oxidative stress.

In addition to research investigating IR exposure in the context of a nuclear event, other researchers are investigating radiation exposure in the context of space travel. Space radiation consists of protons, γ-rays, neutrons, and heavy ions mixed together, which is a health risk for astronauts on long-term space missions [200]. A study investigated the effects of three different low-dose IR exposures (γ-rays, ^{16}O, and ^{56}Fe) on splenic metabolism in mice at 1, 2, and 4 months post-IR, which is similar to the accumulated IR exposure astronauts would encounter on a long duration space flight [201]. UHPLC-MS (untargeted metabolomics analysis) of spleen tissue showed different metabolite profiles between the 3 different IR sources, but purine metabolism, Krebs cycle, fatty acids, acylcarnitines, and amino acid metabolism were altered with IR across the different sources at different time points [201]. Metabolite alterations were more significant at 1-month post-IR in the γ IR group whereas the alterations were more significant at 4 months post-IR in the ^{16}O and ^{56}Fe IR groups [201]. Due to the involvement of purine metabolism in DNA repair, the authors speculate that metabolic dysregulation of purine metabolism in the spleen may contribute to increased DNA damage and inflammation previously observed in the blood of astronauts on long-term missions [201].

Metabolic biomarkers of radiation damage: nonhuman primate model

Due to the closer genetic similarity of nonhuman primates (NHPs) to humans over other animal models, many studies have utilized NHP models, usually rhesus monkeys or macaques, to improve the translation of murine IR biomarkers to humans. Additionally, NHP models minimize the genetic differences observed in human studies, which is useful for identifying metabolic IR signatures [188]. However, limited studies have examined tissues of NHP for mechanistic responses to IR damage, and those studies focus on histological analysis and not metabolic perturbations [202], [203], [204]. Thus, metabolomic profiling of biofluids is the standard for investigating metabolic IR signatures in NHPs. To identify IR biomarkers in NHPs and compare them to those previously identified in rodent models, urine was collected from NHPs exposed to 1.0, 3.5, 6.5 or 8.5 Gy whole-body IR at 12-hour intervals up to 3 days post-IR [205]. UPLC-TOFMS (untargeted metabolomics analysis) revealed the greatest increase in the urinary biomarkers taurine, hypoxanthine, adipic acid, and tyramine sulfate at 24 hours post 8.5 Gy IR with a subsequent decrease at 48 and 72 hours post-IR [205]. To compare radiation biomarkers in NHPs to those previously identified in rodents, targeted metabolomics of xanthosine, thymidine, 2′-deoxyuridine, N-hexanoylglycine, tyrosine, and tyramine was performed and interestingly, the concentrations of these metabolites did not significantly change with IR in NHP urine, demonstrating that inter-species differences exist in metabolic IR signatures [205]. A different group investigated radiation biomarker differences between NHPs exposed to 5.8 and 7.2 Gy whole-body IR and mice exposed to 14 and 9.6 Gy whole-body IR by combining NMR spectroscopy and LC-MS untargeted metabolomics analysis [206]. Mouse serum was collected at 5 hours and days 1-4 post-IR while NHP serum was collected at 8 hours, days 2, 3, 7, and 8 post-IR and glucose metabolism, phospholipid biosynthesis, and nucleotide metabolism were commonly altered temporally across the two species [206]. Carnitine was the only significantly dysregulated metabolite shared between the two species, and it was decreased over time in the mouse model and contrastingly increased over time in the NHP model [206]. Thus, the direction of metabolite alterations in response to IR differs across species.

A study desired to investigate the metabolic radiation signature at 7 days post IR (2, 4, 6, 7 and 10 Gy whole-body IR) in the urine of NHPs since previous studies were performed acutely (24 hours post-IR) [189]. Alterations in fatty acid β oxidation, tryptophan metabolism, purine catabolism, taurine metabolism, and steroid hormone biosynthesis were observed while males excreted significantly higher levels of L-carnitine, L-acetylcarnitine, xanthine and xanthosine compared to females using UPLC-TOFMS (untargeted metabolomics analysis) [189]. This study was useful for identifying sex differences in the metabolic response to radiation that may be translatable to humans. Another study observed the temporal effects of a single IR dose (7.2 Gy whole-body IR) in the serum of NHPs [207]. UPLC-TOFMS (untargeted metabolomics) at 24, 36, 48 and 96 hours post-IR revealed increased carnitine, propionylcarnitine, and acetylcarnitine at 24 hours that subsequently decreased to 96 hours post-IR in the serum [207]. The researchers also measured cytokine levels and observed increases in proinflammatory cytokines that correlated with temporal changes in amino acids, lipids, and deaminated purines, which supports a relationship between the metabolome and the immune response that is altered upon IR exposure in the serum [207]. To further investigate temporal effects of a single IR dose, a group administered a lower IR dose (4 Gy whole-body IR) to NHPs and collected serum and urine for metabolomics analysis on days 1-60 post-IR [208]. UHPLC-MS untargeted metabolomics analysis revealed the highest enrichment of protein metabolism, fatty acid β oxidation, DNA base deamination, and energy metabolism at day 1 post-IR in urine and at days 1-21 in serum [208]. These results suggest that urinary biomarkers are more useful for identifying IR exposure acutely while serum biomarkers are useful for identifying IR exposure at later time points.

Other studies have used serum to identify radiation metabolic signatures in NHPs. The effects of 2-10 Gy whole-body IR on the serum metabolic profile of NHPs at day 7 post-IR were investigated using UHPLC-MS untargeted metabolomics and lipidomics analysis [209]. Diacylglycerols (DGs) and short chain triacylglycerols (TGs) were decreased in the serum at 7 days post-IR [209]. IR dose-dependent changes in levels of the serum biomarkers valine, hypoxanthine, L-carnitine, proline, uridine, tyrosine, and taurine were observed [209]. This study was useful for identifying specific metabolomic as well as lipidomic IR exposure signatures in the serum of NHPs.

Recently, a group investigated metabolic changes in IR-induced multiple-organ injury in NHPs to identify tissue biomarkers of radiation exposure [210]. NHPs were exposed to 12 Gy partial body IR to spare the bone marrow and kidney, liver, lung, heart, and jejunum tissues were harvested over a period of 3 weeks for LC-MS (untargeted metabolomics analysis) [210]. The results showed temporal changes in both citrulline and branched chain amino acids in all tissue types, with changes in fatty acid oxidation observed across the tissue types in response to radiation, suggesting a conserved metabolic damage response across different tissue types [210].

Metabolic biomarkers of radiation damage: human model

Few studies utilize human models to identify metabolic biomarkers of IR exposure due to the limited subject selection, which are those who have been exposed to IR either through medical treatment or a nuclear event. One study used patients diagnosed with leukemia, non-Hodgkin's lymphoma, myelodysplastic syndrome, or essential thrombocytosis and collected urine samples at 4-6 hours following a single IR dose (1.25 Gy whole-body IR) and at 24 hours following three fractions of 1.25 Gy IR [188] to identify a metabolic IR signature in humans. UPLC-TOFMS (untargeted metabolomics analysis) showed increased excretion of decanoylcarnitine and decreased excretion of octanoylcarnitine at 24 hours post-IR in the urine of both male and female patients [188]. However, sex differences were observed in hypoxanthine, xanthine, and uric acid alterations at 24 hours post-IR [188]. This group observed a higher amount of noise in the dataset than they had observed in previous animal studies, as variables such as age, diet, race, and genetics influence the metabolic phenotype and make it difficult to draw conclusions correlating IR exposure to specific metabolic biomarkers, especially since the patients had various types of cancer [188].

A different group used the serum of human patients with head and neck squamous cell carcinoma (HNSCC) to identify metabolic biomarkers of acute radiation damage that leads to weight loss [211]. The patients were of different tumor stages and received different radiation treatment plans that ranged from 51-72 Gy total IR dose delivered in fractions over a period of 5-7 weeks and serum was collected weekly during the treatment period [211]. NMR spectroscopy untargeted metabolomics analysis showed that ketone bodies (D-3-hydroxybutyrate (3HB), acetoacetate (AcAc), and acetone) significantly increased as weight loss increased following IR in the serum, starting at 2 weeks after treatment initiation [211]. N-acetyl containing glycoproteins (NAGs), choline, propylene glycol, and acetate increased in the serum as IR treatment duration increased [211]. Thus, the researchers identified IR-induced metabolic biomarkers associated with weight loss that may help stratify patients for individualized treatment. The same group sought to identify serum metabolic markers reflective of IR exposure to tumors in HNSCC patients using NMR spectroscopy [212]. These patients with various tumor stages received one of four IR techniques: 1) conventional fractionation- 2 Gy per fraction, 35 fractions over 7 weeks, 2) continuous accelerated irradiation- 1.8 Gy per fraction, 40 fractions over 6 weeks, 3) accelerated hypofractionated irradiation-3 Gy per fraction, 17 fractions over 3.5 weeks, or 4) accelerated irradiation with simultaneous integrated boost-2.2 Gy per fraction, 30 fractions over 6 weeks [212]. Serum was collected weekly during the treatment period for metabolomics analysis [212]. Across the IR treatment protocols, N-acetyl-glycoprotein (NAG), N-acetylcysteine, glycerol, glycolate, and lipid species were significantly altered starting at 3 weeks since treatment initiation and continuing through the rest of treatment, which corroborates the data from their previous study [212]. IR tissue volume was positively correlated with inflammatory markers and creatinine while negatively correlated with lymphocyte count [212]. In addition to the previously mentioned variables affecting human metabolic phenotypes, these results also identified drugs taken by patients and inconsistencies in blood sampling as affecting the data, again adding to the difficulty of correlating targeted IR exposure to specific biomarkers in human serum [212].

Metabolic biomarkers of radiation damage: saliva

The use of saliva for identifying IR metabolic biomarkers is relatively emergent compared to the use of urine, serum, and tissues. The use of saliva is attractive and has been shown to increase compliance, especially in studies with children, due to the ease of sample collection and storage compared to blood [213]. However, limitations exist with using saliva for biomarker identification, such as the lower concentration of molecules in saliva compared to blood and the influence of lifestyle factors (smoking, diet, etc.) on saliva composition [214]. Saliva has been utilized to identify biomarkers of cancer, including systemic biomarkers for lung, breast, pancreas, and pelvic tumors, as well as other diseases such as cardiovascular disease and diabetes [215], [216]. One of the first published studies to investigate biomarkers of IR exposure in saliva of cancer patients exposed to whole-body IR performed proteomics analysis on the saliva at 2, 4, and 24 hours post each IR fraction (1.5, 1.65, or 2 Gy) [217]. Using a targeted assay, the study observed responses of monocyte chemo-attractant protein 1 (MCP-1), interleukin 8 (IL8), and intercellular adhesion molecule 1 (ICAM-1) to IR, which may influence the metabolomic response to IR as well [217].

A pilot study investigating the metabolic response to IR in saliva was performed with a mouse model exposed to 0.5, 3 and 8 Gy whole-body IR [195]. Saliva was collected on day 1 and 7 post-IR and UHPLC-MS untargeted metabolomics analysis identified enrichment of amino acids, fatty acids, and intermediates of nicotinate and nicotinamide metabolism across all 3 IR doses at day 1 post-IR in saliva [195]. At day 7 post-IR, only 8 Gy IR induced significant metabolic alterations in dodecanedioic acid, proline, and nicotinic acid [195]. These results successfully identified a metabolic IR signature in mice that required further validation. The same research group performed a follow-up study to validate their results observed in mice using a NHP model. NHPs received 4 Gy whole-body IR and saliva was collected over time between day 1 and 60 post-IR [218]. UPLC-TOFMS untargeted metabolomics analysis revealed enrichment of amino acids and nucleotides from day 1 to day 60 post-IR in saliva and the metabolic profile of the day 60 IR group separated the most from the pre-treatment control metabolic profile [218]. This study corroborated the results observed in the mouse model with amino acid enrichment observed in saliva post IR and it displayed chronic salivary IR metabolic signatures following acute IR exposure.

Metabolomics analysis related to the salivary gland

Salivary gland metabolism has mainly been studied in the context of the salivary gland autoimmune disorder, Sjögren's syndrome (SS), oral cancers and diseases, and aging models [219], [220], [221]. A group analyzed the saliva of primary SS (pSS) patients using NMR spectroscopy untargeted metabolomics analysis and observed significant increases in choline, taurine, and alanine over a 20-week collection period compared to healthy controls [219]. Interestingly, the researchers observed large variations between subjects for glycine, choline, and alanine levels in saliva of pSS patients [219], which suggests that using salivary metabolite biomarkers for pSS diagnosis may be challenging. Another group analyzed the saliva of pSS patients using GC-MS untargeted metabolomics analysis and observed decreased levels of glycine, tyrosine, uric acid and fucose in saliva of pSS patients compared to healthy controls [222]. An interesting find was that the salivary metabolite profile of pSS patients was less diverse compared to healthy controls [222], suggesting that metabolic diversity is beneficial for healthy salivary gland function. A different group used LC-MS untargeted metabolomics to analyze the saliva of pSS patients and observed significant dysregulation of tryptophan metabolism, tyrosine metabolism, carbon fixation, and aspartate and asparagine metabolism in saliva of pSS patients [223]. Using a machine-learning algorithm, phenylalanine was found to be a good predictor of pSS [223]. Collectively, these findings suggest that various amino acids may serve as biomarkers of pSS in saliva for diagnostic purposes.

Salivary and serum metabolic biomarkers have been explored as diagnostic tools of salivary gland tumors, periodontitis, and oral cancer. A group collected serum from human patients with salivary gland tumors and performed UHPLC-MS and NMR spectroscopy untargeted metabolomics analysis and discovered significant enrichment of valine, leucine and isoleucine biosynthesis, aminoacyl-tRNA biosynthesis, and alanine, aspartate and glutamate metabolism in the serum of salivary gland tumor patients compared to healthy controls [224]. The researchers also observed that serine and lactic acid serum levels increased in patients with benign salivary gland tumors as they transformed into malignant tumors [224]. Another group collected saliva from a human cohort to identify metabolic biomarkers of periodontitis [225]. Using UHPLC-MS untargeted metabolomics, they identified a significant association between the bacterial metabolite phenylacetate and periodontal variables in saliva [225]. Interestingly, the researchers observed a difference in the salivary metabolite profile between adults 20-59 years old and adults 60 years old and older, with the older adults displaying increased levels of creatine, lactate, propionylcarnitine, glycerophosphorylcholine, and adenosine 5′-monophophate that are associated with missing teeth [225]. Several studies have investigated salivary biomarkers of oral cancer. One group tested the effect of saliva collection timing on metabolic biomarker detection of oral cancer in human patients [220]. Saliva was collected at 12 hours after dinner, 1.5 hours after breakfast, and 3.5 hours after breakfast for capillary electrophoresis time-of-flight mass spectrometry (CE-TOFMS) analysis [220]. The results showed 12-hour fasting after dinner resulted in a higher number of significantly altered metabolites in saliva of oral cancer patients compared to the other collection time points, and at all collection time points N,N-dimethylglycine, trimethylamine N-oxide, isopropanolamine, guanosine, cystine and hypotaurine were significantly elevated in the saliva of oral cancer patients compared to healthy controls [220]. A different group compared the salivary metabolic biomarkers between different developmental stages of oral cancer: Oral squamous cell carcinoma (OSCC), oral epithelial dysplasia (OED), and persistent suspicious oral mucosal lesions (PSOML) [191]. Using CE-TOFMS untargeted metabolomics analysis on saliva collected from human patients, the researchers observed 6 metabolites that were significantly decreased in the saliva of OSCC and OED patients compared to PSOML patients, and they discovered decreased ornithine, o-hydroxybenzoate, and ribose 5-phosphate levels in saliva were predictive of OSCC and OED and discriminated against PSOML using a logistic regression model [191]. Thus, these results demonstrate that the salivary metabolic profile may be useful for diagnosing early stages of OSCC. Other researchers used the salivary metabolome to differentiate between OSCC and oral lichen planus (OLP), an inflammatory condition affecting the mucous membranes in the mouth [226]. Saliva was collected from human patients with OSCC and OLP and CE-TOFMS untargeted metabolomics analysis identified enrichment of indole-3-acetate and ethanolamine phosphate levels in the saliva of OSCC compared to OLP patients [226]. The researchers also observed 14 metabolites (mainly amino acid and amide derivatives) that were differentially expressed in the saliva of OSCC compared to OLP patients [226]. These results provide useful salivary metabolic biomarkers to distinguish OSCC from OLP for clinical diagnosis.

As salivary gland function deteriorates with aging, research has investigated the effect of aging on the salivary metabolome to identify therapeutic targets for restoring function. A group used an extensive aging mouse model, SAMP1/Klotho$^{-/-}$ mice, and performed CE-TOFMS untargeted metabolomics on salivary gland tissue to identify mechanistic changes within the gland [221]. The results revealed that acetylcholine levels and mRNA and protein expression of choline acetyltransferase (ChAT) were significantly decreased in the salivary glands of

SAMP1/Klotho$^{-/-}$ mice compared to wild-type controls [221]. The researchers manipulated ChAT levels using adenoviral delivery of ChAT *in vivo* to SAMP1/ Klotho$^{-/-}$ mice, which resulted in restored salivary secretion to wild-type control levels [221]. The researchers also observed disruption of ascorbic acid biosynthesis, which they further investigated in a follow-up study [227]. The researchers again performed CE-TOFMS untargeted metabolomics analysis on salivary tissue from the SAMP1/Klotho$^{-/-}$ mice and observed decreased levels of UDP-glucuronic acid, D-glucuronic acid, and L-ascorbic acid compared to wild-type mice [227]. Supplementation with ascorbic acid treatment for 18 days increased saliva secretion in SAMP1/Klotho$^{-/-}$ mice, and they observed that ascorbic acid treatment restored expression of muscarinic receptors M1 (M1AchR) and M3 (M3AchR) in SAMP1/Klotho$^{-/-}$ mice to levels observed in the wild-type controls [227]. Collectively, these studies demonstrate the efficacy of targeting choline acetyltransferase and ascorbic acid to improve salivary gland function in a mouse aging model.

Multi-omics analysis of radiation damage/disease

Radiation damage and resistance models

While metabolomics is a useful platform of high-dimensional data for identifying phenotypes of IR damage and disease models, the integration of multiple data platforms can provide even more mechanistic insight to improve precision medicine. Multi-omics refers to the use of more than one "omics" platform, including but not limited to genomics, transcriptomics, epigenetics, proteomics, metabolomics, and microbiome research [228]. A major advantage of multi-omics approaches is the identification of network-level relationships between genes, proteins, metabolites, and gut bacteria that are driving the observed phenotype. A few studies have incorporated multi-omics analysis of the IR damage response using mouse models to better understand the relationship between gut microbiota and their metabolites as gut microbiota dysbiosis has been demonstrated to play a role in IR-induced intestinal damage [229]. One group was interested in the gut microbiota/metabolite signatures of mice that survive high-dose IR exposure to create a targeted therapeutic for IR resistance [230]. Using specific pathogen-free (SPF) C57BL/6 mice to control for metabolites produced from gut microbiota, mice were exposed to 9.2 Gy whole-body IR and 5-15% of the mice survived up to 600 days post-IR [230]. Feces was collected from the mice that survived long-term, called "elite survivors", at 290 days post-IR and high-throughput gene-sequencing analysis of 16S ribosomal RNA (rRNA) in fecal bacterial DNA was performed to identify the gut microbiome profile and UHPLC-MS untargeted metabolomics analysis to identify the metabolomic profile conferring radiation resistance [230]. Bacterial taxa *Lachnospiraceae* and *Enterococcaceae* were elevated in the feces of surviving mice as well as tryptophan metabolites and short-chain fatty acids acetate, butyrate, and propionate at 290 days post-IR and were demonstrated to protect mice from radiation-induced death [230]. Using a gut microbiome-metabolome network approach, the researchers were able to identify the microbiota taxa and the metabolites they produce that confer IR resistance in mice. Another group investigated radiation enteritis by combining gut microbiota and lipidomic analysis in the colorectal tissue of mice exposed to 18 Gy IR targeted to the abdomen [231]. *Dubosiella* and *Alistipes* bacteria were the most highly correlated with differentially expressed glycerophospholipid metabolites in the colon, and the correlation was the strongest acutely at 1-week post-IR compared to chronically at 6 weeks post-IR [231]. The results from this study elucidated the relationship between specific bacterial taxa and their metabolites that are correlated with IR damage in the colon.

Multi-omics research has also investigated IR resistance in tumors. Using The Cancer Genome Atlas (TCGA) and metabolic Flux Balance Analysis (FBS) models generated from the

TCGA genomic and transcriptomic datasets, a group developed a machine learning algorithm to differentiate metabolic biomarkers of radiation-resistant and radiation-sensitive tumors and then experimentally validated the metabolic biomarkers in radio-sensitive and radio-resistant cell lines using LC-MS [232]. Increased levels of fatty acid and cholesterol metabolites were associated with tumor radiation resistance while central carbon, lipid, and nucleotide metabolism were biomarkers of radiation sensitivity [232].

Cancer models

Multi-omics analysis is becoming increasingly utilized in cancer studies for discovering greater mechanistic insight. A study used prostate cancer tissue and adjacent non-cancerous tissue from human subjects and performed integrated RNA-sequencing and UHPLC-MS untargeted metabolomics to identify metabolic pathways altered in prostate cancer [233]. In the pathway analysis, cysteine and methionine metabolism, nicotinamide adenine dinucleotide metabolism, and hexosamine biosynthesis were altered at both the transcript and metabolite level in prostate cancer tissue compared to non-cancerous adjacent tissue [233]. At the metabolite level, sphingosine showed high specificity and sensitivity for differentiating prostate cancer from non-cancerous prostatic hyperplasia [233]. A different group investigated prostate cancer mechanisms by integrating transcriptomics data, GC-MS and LC-MS untargeted metabolomics data, and protein level data using human prostate cancer tissue [234]. Integrated analysis showed dysregulation of fatty acid, sphingolipid, and polyamine metabolism in prostate cancer, which provided additional pathway-level alterations compared to the previous study [234]. Fatty acid oxidation was altered in the clinically used pathologic variable, *TMPRSS2-ERG* (*ERG*) translocation positive prostate cancer samples, and *ERG* translocation was negatively correlated with gluconic acid and maltotriose in prostate cancer [234]. These results were able to demonstrate the effect of *ERG* translocation on the metabolomic profile of prostate cancer patients by integrating multi-omics analysis. In addition to prostate cancer, integrated analysis has identified the relationship between the adipokine chemerin and the metabolic profile in clear cell renal cell carcinoma (ccRCC) [235]. Combining RNA-sequencing and UHPLC-MS untargeted metabolomics and lipidomics using human ccRCC samples and plasma, 4 cell lines, and a xenograft mouse model of ccRCC, the researchers observed obesity-dependent elevations of the adipokine chemerin in ccRCC tissue samples and plasma compared to healthy controls [235]. The multi-omics analysis showed that chemerin suppressed fatty acid oxidation, prevented ferroptosis, and maintained fatty acid levels in ccRCC [235]. Furthermore, monoclonal antibody treatment targeting chemerin decreased lipid levels and tumor growth [235], demonstrating the relationship between chemerin and the metabolome in ccRCC. Multi-omics analysis has also been used to investigate triple-negative breast cancer (TNBC) mechanisms. RNA-sequencing and UHPLC-MS untargeted metabolomics were combined to analyze *in vitro* and *in vivo* mouse and human models of TNBC and discovered differences in ferroptosis-related metabolites and pathways compared to healthy controls [236]. Additionally, oxidized phosphatidylethanolamines and glutathione metabolism (GPX4) levels were increased in the luminal androgen receptor (LAR) subtype, and GPX4 inhibition induced tumor ferroptosis and improved antitumor immunity in TNBC LAR subtype tumors [236]. Thus, integrated multi-omics analysis identified ferroptosis induction as a type of immunotherapy for TNBC LAR subtype tumors.

Spaceflight damage models

An interesting application of combining multi-omics approaches was used to investigate the effects of spaceflight on human physiology, as many of the molecular mechanisms underlying spaceflight effects, such as bone loss and immune dysfunction, are unknown [237].

This group collected urine and blood from human astronauts and performed transcriptomics, proteomics, and UHPLC-MS untargeted metabolomics and observed significant enrichment of mitochondrial processes, innate immunity, chronic inflammation, cell cycle, circadian rhythm, and olfactory functions during spaceflight compared to controls [237]. The results also showed evidence of DNA damage in blood and urine samples of astronauts in spaceflight [237]. Collectively, these results suggest mitochondrial dysfunction plays a role in the physiological effects associated with spaceflight. For additional study details, view Table 1.1.

Table 1.1. Metabolomics analysis of radiation exposure in different models, metabolomics analysis related to the salivary gland, and multi-omics analysis of radiation damage/disease in various models.

Model system	Methodology	IR	Tissue/bio fluid sample	Major findings	Ref
Metabolic biomarkers of radiation damage: rodent model biofluids					
Dose- and time-dependent IR exposure in C57BL/6N mice	UPLC-TOFMS untargeted metabolomics	1-3 Gy	Urine	• Thymidine, 2′-deoxyuridine, 2′-deoxyxanthosine, xan-thine and xanthosine were elevated in the urine 24 hours post-1-3 Gy IR. • The elevated deaminated purine and pyrimidine derivatives peaked at 8-12 hours post IR and returned to baseline levels by 36 hours post-IR.	[186]
IR exposure in C57BL/6mice	NMR spectroscopy untargeted metabolomics	8 Gy to whole body	Urine	• Creatine, succinate, methylamine, citrate, 2-oxoglutarate, taurine, N-methyl-nicotinamide, hippurate, and choline were urinary biomarkers at 7 days post-IR. • Temporal analysis showed a decrease in citrate, taurine, 2-oxoglutarate, and hippurate at days 3 and 4 post-IR.	[190]
Total body vs. partial body IR in C57BL/6J mice	NMR spectroscopy untargeted metabolomics	10 Gy to whole body, abdomen, thoracic cavity, or hind limb	Urine	• Energy, gut flora, and taurine metabolism were common to whole body and partial body IR at 24 hours post-exposure. • Distinct metabolic signatures were	[192]

				observed in each IR group compared to each other and control group. • Taurine, creatine, and trimethylamine-N-oxide (TMAO) were the most significantly upregulated in the hind limb IR group.	
Prediction model of IR exposure in C57BL/6J mice	NMR spectroscopy untargeted metabolomics and logistic regression model	7.5 Gy to whole body	Urine	• Tri-carboxylic acid (TCA) cycle, taurine and hypotaurine metabolism, and primary bile acid biosynthesis were the most significantly altered pathways in IR exposure at 24 hours. • The prediction model resulted in high sensitivity, specificity, and accuracy for taurine, citrate, alpha-ketoglutarate, and fumarate as biomarkers of IR exposure in urine.	[193]
IR exposure in C57BL/6J mice	Integrated NMR spectroscopy and UHPLC-MS untargeted metabolomics	5 Gy or 7.5 Gy to whole body	Urine	• Taurine, creatine, citrate, and 2-oxoglutarate were dose-dependent biomarkers of IR exposure at 24 hours. • Integrated analysis showed enrichment of energy, taurine, gut flora, L-carnitine, and nucleotide metabolism with IR.	[194]
Dose- and time-dependent IR exposure in Sprague Dawley rats	UHPLC-MS untargeted metabolomics	0.5-10 Gy to whole body	Urine	• A dose- and time-dependent decrease in urine metabolite excretion was observed from 6 to 72 hours post-IR.	[187]

				• Carnitine, uric acid, cytosine, isocitrate, thymidine, and creatine were biomarkers of 2.5 Gy IR exposure across time.	
Metabolic biomarkers of radiation damage: rodent model tissues					
IR cardiotoxicity in C57Bl/6NCrl mice	NMR spectroscopy untargeted metabolomics	0.2 or 2 Gy to heart tissue	Heart tissue	• Elevated levels of pantothenate and glutamate and decreased levels of alanine, malonate, acetylcarnitine, glycine and adenosine were observed 48 hours post-2 Gy IR. • Decreased levels of glutamine and acetylcarnitine were observed 20 weeks post-2 Gy IR. • 0.2 Gy IR did not induce significant changes.	[185]
IR testicular toxicity in C57BL/6 mice	NMR spectroscopy untargeted metabolomics	2 Gy to whole body	Testicular tissue	• Changes in energy, osmolytes, and membrane metabolism occurred acutely at 24 hours and some of the changes persisted through weeks 3 and 5 post-IR in testicular tissue. • Trichostatin A administration at 1 hour and 24 hours post-IR reversed the observed metabolic changes in testicular tissue and morphological and functional properties of sperm were restored.	[196]
IR liver toxicity in C57BL/6 mice	NMR spectroscopy untargeted metabolomics	3 or 7.8 Gy to whole body	Liver tissue	• 3 Gy proton and 3 Gy gamma IR resulted in different metabolic	[197]

				profiles in the liver at days 4 and 11 post-IR. • Choline, O-phosphocholine, and trimethylamine N-oxide levels were significantly decreased post-IR. • Glutamine, glutathione, malate, creatinine, phosphate, betaine and 4-hydroxyphenylacetate were significantly increased post-IR.	
IR liver toxicity in C57BL/6 mice	GC-MS and LC-MS untargeted metabolomics	10 or 50 Gy to liver or 10 Gy to whole body	Liver tissue and plasma	• Liver metabolites enriched with targeted 50 Gy IR were pentose phosphate, purine, and pyrimidine metabolites. • Liver metabolites commonly enriched in targeted and whole-body IR were amino acids, sugars, fumarate, lineolate, n-hexadecanoic acid, and uridine. • Plasma biomarkers commonly enriched in targeted and whole-body IR were 3 indoxyl sulfate, indole-3-lactic acid, phenyllactic acid, pipecolic acid, hippuric acid, and 2-deoxyuridine.	[198]
IR intestinal toxicity in C57BL/6 mice	GC-MS untargeted metabolomics	2 Gy or 20 Gy targeted to the abdomen	Intestinal tissue	• Elevated levels of amino acids, carbohydrates, organic acids, and sugars were observed in intestinal tissue in a dose-dependent manner. • The authors hypothesize that	[199]

				increased amino acids are correlated with increased oxidative stress contributing to damage.	
IR splenic toxicity in C57BL/6 mice	UHPLC-MS untargeted metabolomics	0.2 Gy of ^{16}O, 0.2 Gy of ^{56}Fe, or 1 Gy of ^{137}Cs	Spleen tissue	• Purine metabolism, tricarboxylic acid cycle, fatty acids, acylcarnitines, and amino acids are altered with IR in the spleen. • Purine degradation and fatty acid metabolism increased over time post-IR (1, 2, and 4 months) in the spleen. • More metabolic alterations were observed at 1 month post-IR in the γ-radiation group compared to the high energy particle IR groups where more alterations were observed at 4 months post-IR.	[201]
Biomarkers of radiation damage: nonhuman primate model					
IR exposure in nonhuman primates	UPLC-TOFMS untargeted metabolomics	2-10 Gy to whole body	Urine	• Males excreted significantly higher levels of l-carnitine, l-acetylcarnitine, xanthine, and xanthosine compared to females 7 days post-IR exposure. • Fatty acid β oxidation, tryptophan metabolism, purine catabolism, taurine metabolism and steroid hormone biosynthesis were altered with IR.	[189]
IR exposure in nonhuman primates	UHPLC-MS untargeted	1-8.5 Gy to whole body	Urine	• Temporal analysis of the urinary biomarkers taurine, hypoxanthine,	[205]

	and targeted metabolomics			adipic acid, and tyramine sulfate showed an increase at 24 hours post-8.5 Gy IR with a subsequent decrease at 48 and 72 hours post-IR. • Targeted metabolomics on previously identified rodent biomarkers (xanthosine, thymidine, 2′-deoxyuridine, and N-hexanoylglycine) in nonhuman primate urine showed no significant changes in metabolite concentration with IR.	
Temporal IR exposure in nonhuman primates	UPLC-TOFMS untargeted metabolomics	7.2 Gy to whole body	Serum	• Carnitine, propionylcarnitine, and acetylcarnitine increased at 24 hours post-IR and decreased to 96 hours post-IR in serum. • Arginine and betaine decreased at 48- and 96-hours post-IR in serum. • Temporal changes were observed in pro-inflammatory cytokines, deaminated purines, and lipids post-IR in serum.	[207]
Temporal IR exposure in nonhuman primates	UHPLC-MS untargeted metabolomics	4 Gy to whole body	Serum and urine	• Protein metabolism, fatty acid β oxidation, DNA base deamination, and energy metabolism were enriched the most at day 1 post-IR in urine and at days 1-21 in serum. • Using a training and validation cohort,	[208]

				urinary acetylcarnitine and serum carnitine displayed high sensitivity and specificity as biomarkers of IR in nonhuman primates.	
IR exposure in nonhuman primates	UHPLC-MS untargeted metabolomics and lipidomics	2-10 Gy to whole body	Serum	• Diacylglycerols (DGs) and short chain triacylglycerols (TGs) were decreased in the serum at 7 days post-IR. • Valine biosynthesis/degradation was enriched at all IR doses. • IR dose-dependent changes in levels of the serum biomarkers valine, hypoxanthine, L-carnitine, proline, uridine, tyrosine, and taurine were observed.	[209]
IR exposure across mouse (CD2F1) and nonhuman primates	NMR spectroscopy and LC–MS untargeted metabolomics	14 and 9.6 Gy to whole body of mouse groups, 5.8 and 7.2 Gy to whole body of nonhuman primates	Serum	• Across the 2 species, glucose metabolism, phospholipid biosynthesis, and nucleotide metabolism were altered temporally (8 hours to 8 days post-IR). • L-carnitine was the only common metabolite altered by IR across the 2 species. • Amifostine pre-treatment corrected the IR-induced alterations in metabolic pathways by day 7 post-IR.	[206]
IR multiple-organ injury in nonhuman primates	LC–MS untargeted metabolomics	12 Gy partial body IR sparing	Kidney, lung, liver, heart, and	• Temporal changes in both citrulline and branched chain amino acids occurred in all	[210]

		the bone marrow	jejunum tissue	tissue types over a 3-week period. • Changes in fatty acid oxidation were observed across all tissue types, suggesting a conserved metabolic IR damage response.	
Biomarkers of radiation damage: human model					
IR exposure in humans using patients diagnosed with leukemia, non-Hodgkin's lymphoma, myelodysplastic syndrome, or essential thrombocytosis	UHPLC-MS untargeted metabolomics	3 fractions of 1.25 Gy to whole body with a 4-6 hour interval between fractions	Urine	• Increased excretion of decanoylcarnitine and decreased excretion of octanoylcarnitine was observed at 24 hours post-IR in both males and females. • Hypoxanthine, xanthine, and uric acid were significantly altered 24 hours post-IR and sex differences were observed in the alterations.	[188]
IR treatment of head and neck squamous cell carcinoma (HNSCC) patients	NMR spectroscopy untargeted metabolomics	Targeted IR to tumor location: 51-72 Gy delivered in fractions over 5-7 weeks	Serum	• Ketone bodies (D-3-hydroxybutyrate (3HB), acetoacetate (AcAc), and acetone) significantly increased as weight loss increased following IR in the serum. • N-acetyl containing glycoproteins (NAGs), choline, propylene glycol, and acetate increased in the serum as IR treatment duration increased.	[211]
IR treatment of head and neck squamous cell carcinoma	NMR spectroscopy untargeted metabolomics	Targeted IR to tumor location: A. 2 Gy per	Serum	• Across the IR treatments, N-acetyl-glycoprotein (NAG), N-acetylcysteine, glycerol, glycolate, and	[212]

(HNSCC) patients		fraction, 35 fractions B. 1.8 Gy per fraction, 40 fractions C. 3 Gy per fraction, 17 fractions D. 2.2 Gy per fraction, 30 fractions		lipid species were significantly altered. • IR tissue volume was correlated with inflammatory markers, creatinine, and lymphocyte count.	
Metabolic biomarkers of radiation damage: saliva					
IR exposure in C57BL/6 mice	UHPLC-MS untargeted metabolomics	0.5, 3, or 8 Gy to whole body	Saliva	• Amino acids, fatty acids, and intermediates of nicotinate and nicotinamide metabolism were enriched with all 3 IR doses at 1 day post-IR in saliva. • At 7 days post-IR only 8 Gy IR induced significant metabolic alterations (dodecanedioic acid, proline, and nicotinic acid).	[195]
IR exposure in nonhuman primates	UPLC-TOFMS untargeted metabolomics	4 Gy to whole body	Saliva	• Amino acids and nucleotides were enriched from day 1 to day 60 post-IR in saliva. • Adenine, tyrosine, and leucine were decreased at all time points post-IR in saliva.	[218]

				• The metabolite profile of the day 60 IR group displayed the clearest separation from the pretreatment control.	
Metabolomics analysis related to the salivary gland					
Model system	Damage/disease phenotype	Methodology	Tissue/ biofluid sample	Major findings	Ref
Human primary Sjögren's syndrome (pSS) patients	Primary Sjögren's syndrome (pSS)	NMR spectroscopy untargeted metabolomics	Saliva	• Choline, taurine, and alanine were significantly increased in the saliva of pSS patients over a 20-week collection period. • Large inter-individual variation was observed for glycine, choline, and alanine in saliva of pSS patients.	[219]
Human primary Sjögren's syndrome (pSS) patients	Primary Sjögren's syndrome (pSS)	GC-MS untargeted metabolomics	Saliva	• Glycine, tyrosine, uric acid and fucose levels were decreased in saliva of pSS patients. • The salivary metabolite profile of pSS patients was less diverse compared to healthy controls.	[222]
Human primary Sjögren's syndrome (pSS) patients	Primary Sjögren's syndrome (pSS)	LC-MS untargeted metabolomics	Saliva	• Tryptophan metabolism, tyrosine metabolism, carbon fixation, and aspartate and asparagine metabolism were significantly dysregulated in saliva of pSS patients. • Using a machine-learning algorithm, phenylalanine was found to be a good predictor of pSS.	[223]
Human patients with	Salivary gland tumors (SGT)	UHPLC-MS and NMR spectroscopy	Serum	• Valine, leucine and isoleucine biosynthesis, aminoacyl-tRNA	[224]

salivary gland tumors		untargeted metabolomics		biosynthesis, and alanine, aspartate and glutamate metabolism were significantly enriched in SGT patient serum. • Serine and lactic acid serum levels increased from healthy controls, to benign SGTs, to malignant SGTs.	
Study of Health in Pomerania human cohort, nondiabetic	Periodontitis	UHPLC-MS untargeted metabolomics	Saliva	• The bacterial metabolite phenylacetate was significantly associated with periodontal variables in saliva. • Phenylalanine and tyrosine metabolites (phenylacetate, phenyllactate, 3-phenylpropionate, and 3-[4-hydroxyphenyl]propionate), N6-acetyllysine, pipecolate, isovalerate, isocaproate, and ω-6 fatty acid dihomo-linolenate were associated with periodontal variables in saliva of adults 20-59 years old. • Increased levels of creatine, lactate, propionylcarnitine, glycerophosphorylcholine, and adenosine 5′-monophophate were associated with missing teeth in saliva of adults 60 years old and older.	[225]
Human oral cancer patients	Oral cancer	CE-TOFMS untargeted metabolomics	Saliva	• 12-hour fasting after dinner resulted in a higher number of significantly altered	[220]

				metabolites in saliva of oral cancer patients compared to both 1.5 and 3.5-hour fasts after breakfast. • N,N-dimethylglycine, trimethylamine N-oxide, isopropanolamine, guanosine, cystine and hypotaurine were significantly elevated in the saliva of oral cancer patients compared to healthy controls at all fasting time points.	
Human oral squamous cell carcinoma (OSCC), oral epithelial dysplasia (OED), and persistent suspicious oral mucosal lesions (PSOML) patients	Oral squamous cell carcinoma (OSCC), oral epithelial dysplasia (OED), and persistent suspicious oral mucosal lesions (PSOML)	CE-TOFMS untargeted metabolomics	Saliva	• 6 metabolites were significantly decreased in the saliva of OSCC and OED patients compared to PSOML patients. • Decreased ornithine, o-hydroxybenzoate, and ribose 5-phosphate levels in saliva were predictive of OSCC and OED and discriminate against PSOML.	[191]
Human oral squamous cell carcinoma (OSCC) and oral lichen planus (OLP) patients	Oral squamous cell carcinoma (OSCC) and oral lichen planus (OLP)	CE-TOFMS untargeted metabolomics	Saliva	• Indole-3-acetate and ethanolamine phosphate levels were enriched in the saliva of OSCC patients compared to OLP patients. • 14 metabolites (mainly amino acid and amide derivatives) were differentially expressed in the saliva of OSCC patients compared to OLP patients.	[226]

Mouse model of accelerated aging (SAMP1/Klotho -/-)	Age-associated loss of salivary gland function	CE-TOFMS untargeted metabolomics	Salivary gland tissue	• Acetylcholine levels and mRNA and protein expression of choline acetyltransferase (ChAT) were significantly decreased in the salivary glands of SAMP1/Klotho-/- mice compared to wild-type controls. • Adenoviral delivery of ChAT *in vivo* to SAMP1/Klotho-/- mice restored salivary secretion to wild-type control levels.	[221]
Mouse model of accelerated aging (SAMP1/Klotho -/-)	Age-associated loss of salivary gland function	CE-TOFMS untargeted metabolomics	Salivary gland tissue	• UDP-glucuronic acid, D-glucuronic acid, and L-ascorbic acid levels were decreased in the salivary glands of SAMP1/Klotho-/- mice compared to wild-type controls. • Expression of muscarinic receptors M1 (M1AchR) and M3 (M3AchR) was restored in SAMP1/Klotho-/- mice to wild-type control levels with ascorbic acid treatment. • Ascorbic acid treatment increased saliva secretion in SAMP1/Klotho-/- mice.	[227]
Multi-omics analysis of damage/disease					
Model system	Damage/disease phenotype	Methodology	Tissue/ biofluid sample	Major findings	Ref
Specific pathogen free (SPF) C57BL/6	IR- 9.2 Gy to whole body	High-throughput 16S rDNA sequencing	Feces	• Bacterial taxa *Lachnospiraceae* and *Enterococcaceae* were elevated in the feces of	[230]

		and UHPLC-MS global metabolomics		surviving mice at 290 days post-IR and protected mice from radiation-induced death. • Tryptophan metabolites and short-chain fatty acids acetate, butyrate, and propionate were elevated in the surviving mice at 290 days post-IR and protected mice from radiation-induced death.	
C57BL/6 mice	IR- 18 Gy to abdomen	High-throughput 16S rDNA sequencing and UHPLC-MS global lipidomics	Colorectal tissue	• *Dubosiella* and *Alistipes* bacteria were the most highly correlated with differentially expressed lipid metabolites in the colon at 1 week post-IR. • Glycerophospholipids were the most prevalent and significant biomarker of IR enteritis at 24 hours post-exposure.	[231]
The Cancer Genome Atlas (TCGA) human patients, radio-resistant and radio-sensitive cell lines	IR- human patients in TCGA previously received radiotherapy	Integrated RNA-seq gene expression data from TCGA patients with LC–MS untargeted metabolomics from radio-resistant and radio-sensitive cell lines	TCGA tumors across multiple cancer and radio-resistant and radio-sensitive cells	• A machine-learning algorithm was developed that predicted metabolic biomarkers of radiation-resistant and radiation-sensitive tumors and validated the biomarkers with high accuracy and sensitivity by integrating experimental metabolomics data with training RNA-seq data. • Increased levels of fatty acid and cholesterol	[232]

				metabolites were associated with tumor radiation resistance. • Central carbon, lipid, and nucleotide metabolism were biomarkers of radiation sensitivity.	
Human prostate cancer patients	Prostate cancer	Integrated RNA-seq gene expression and UHPLC-MS untargeted metabolomics	Prostate cancer tissue and adjacent non-cancerous tissue	• Cysteine and methionine metabolism, nicotinamide adenine dinucleotide metabolism, and hexosamine biosynthesis were altered at the transcript and metabolite level in prostate cancer tissue. • Sphingosine showed high specificity and sensitivity for differentiating prostate cancer from non-cancerous prostatic hyperplasia.	[233]
Human prostate cancer patients	Prostate cancer	GC-MS, LC-MS untargeted metabolomics, gene expression, and protein levels	Prostate cancer tissue	• Integrated analysis showed dysregulation of fatty acid, sphingolipid, and polyamine metabolism in prostate cancer. • Fatty acid oxidation was altered in *ERG* translocation positive prostate cancer samples. • *ERG* translocation was negatively correlated with gluconic acid and maltotriose in prostate cancer.	[234]
4 cell lines, xenograft mouse model, and	Clear cell renal cell carcinoma (ccRCC)	RNA-sequencing and UHPLC-MS	Human ccRCC samples and	• Obesity-dependent elevations of the adipokine chemerin were observed in	[235]

human clear cell renal cell carcinoma (ccRCC) patients		untargeted metabolomics and lipidomics	plasma, 4 cell lines, and xenograft mouse model of ccRCC	ccRCC tissue samples and plasma. • Multi-omics analysis showed that chemerin suppressed fatty acid oxidation, prevented ferroptosis, and maintained fatty acid levels. • Monoclonal antibody targeting chemerin decreased lipid levels and tumor growth.	
14 cell lines, xenograft mouse model, and human triple-negative breast cancer patients (TNBC)	Triple-negative breast cancer (TNBC)	RNA-sequencing and UHPLC-MS untargeted metabolomics	human triple-negative breast cancer tissue samples, 14 cell lines, xenograft mouse model of TNBC	• Differences in ferroptosis-related metabolites and pathways were observed in TNBC subtypes. • Oxidized phosphatidylethanolamines and glutathione metabolism (GPX4) levels were increased in the luminal androgen receptor (LAR) subtype. • GPX4 inhibition induced tumor ferroptosis and improved antitumor immunity in TNBC LAR tumors.	[236]
Human astronauts, 4 human cell models, 13 different tissues (11 mouse and 2 human), and 2 mouse strains (C57BL/6 and BALB/C)	Spaceflight effects	Transcriptomics, proteomics, and UHPLC-MS untargeted metabolomics	Urine and blood of astronauts, 4 human cell models, 13 different tissues (11	• Significant enrichment of mitochondrial processes, innate immunity, chronic inflammation, cell cycle, circadian rhythm, and olfactory functions was observed in spaceflight. • DNA damage was evidenced in blood and urine samples of	[237]

			mouse and 2 human), and 2 mouse strains (C57BL/6 and BALB/C)	astronauts in spaceflight. • Lipid metabolism was upregulated in the liver and kidneys and downregulated in the eyes and adrenal gland in spaceflight.	

Future directions in metabolomics/multi-omics and radiation damage research

The presented studies demonstrate the significant effect of radiation exposure on the metabolic profile, whether it is analyzed in urine, serum, saliva, or tissue. Urine, serum, and saliva metabolic biomarkers of acute radiation syndrome (ARS) have been identified and validated using machine-learning algorithms and multiple cohorts. Salivary biomarkers associated with Sjögren's syndrome, oral cancers, and salivary gland aging are useful for clinical diagnosis. However, more mechanistic studies are required to correlate the biomarker perturbations with the physiological effects of radiation exposure or disease to discover more metabolic and signaling pathways that can be used as therapeutic targets for prevention or treatment.

The use of multi-omics approaches to identify network-level relationships between genes, metabolites, proteins, and gut microbiota is highly valuable data for uncovering complex dynamic relationships that regulate radiation resistance and cancer. Multi-omics approaches have become utilized for investigating the physiological effects of low-dose radiation experienced during spaceflight on astronauts, and more research in this field is expected as the number of long-term spaceflights is increasing. As the data analysis pipelines for integrating the different “omics” platforms is still in the developmental stages, more publications will emerge with novel pipelines for integrating multi-omics data using different model systems investigating radiation damage. Multi-omics analysis of radiation damage in various tissues is necessary for identifying tissue-specific metabolic pathway perturbations underlying loss of function.

Gaps in Knowledge

The presented research illustrates the necessity for investigating the metabolic response to radiation damage in salivary gland tissue. Although metabolomics analysis has been performed on biofluids collected from whole-body radiation exposure using *in vivo* animal models across multiple species as well as in human patients, metabolomics analysis on irradiated salivary gland tissue has not been published. Additionally, multi-omics analyses of genes and metabolites altered with radiation damage in salivary gland tissue have not been published, which would provide greater insight into the metabolic reactions altered in response to radiation. Acquiring untargeted metabolomics data will open the door to validation studies of metabolic pathways of interest altered in response to radiation in the salivary gland, with the goal of correlating the data with previously identified mechanisms underlying radiation-induced salivary gland dysfunction to identify additional druggable targets for functional salivary gland tissue restoration after radiation exposure.

II. [1]Integration of metabolomics and transcriptomics reveals convergent pathways driving radiation-induced salivary gland dysfunction

Authors: Lauren Meeks[1], Diogo De Oliveira Pessoa[2], Jessica A Martinez[1,3], Kirsten H Limesand[1,3] and Megha Padi[2,3,4*]

Affiliations:
[1]Department of Nutritional Sciences, University of Arizona, Tucson, AZ, United States of America
[2] Bioinformatics Shared Resource, Arizona Cancer Center, University of Arizona, Tucson, AZ, United States of America
[3]University of Arizona Cancer Center, Tucson, AZ, United States of America
[4]Department of Molecular and Cellular Biology, University of Arizona, Tucson, AZ, United States of America

* Corresponding Author
Megha Padi
1515 North Campbell Avenue, Room 4943
Tucson, AZ 85724
mpadi@email.arizona.edu
(520) 626-8003

Keywords: γ-radiation, data integration, metabolomics, transcriptomics, salivary gland

Funding: This work was supported in part by NIH R01 grants DE023534 and DE029166 to KHL.

Conflict of interests: No conflicts of interest, financial or otherwise, were declared by the authors.

[1] Note: The contents of this chapter were previously published in Physiological Genomics.

Meeks L, De Oliveira Pessoa D, Martinez JA, Limesand KH, Padi M. Integration of metabolomics and transcriptomics reveals convergent pathways driving radiation-induced salivary gland dysfunction. Physiol Genomics 2021;53(3):85-98 doi:10.1152/physiolgenomics.00127.2020.

Introduction

The American Cancer Society estimates over 53,000 new cases of head and neck cancer reported each year in the United States [238]. Radiation therapy is part of the standard of care for these types of cancers, but unfortunately it causes irreversible damage to the surrounding salivary glands resulting in a significant loss of physiological function [239]. This damage leads to chronic hyposalivation and xerostomia, diminishing the quality of life of these cancer patients [240], [241]. Prevention and treatment options for xerostomia, such as anti-inflammatory cytokine drugs and topical analgesics, only provide symptom control and do not restore endogenous production of saliva [12], [242].

In order to capture the systemic damage caused by radiation, metabolomics analyses have been conducted of saliva, serum, and urine to identify biomarkers of whole-body radiation exposure in mouse models [195], [218], [243]. At the tissue level, radiotherapy (2 Gy γ-radiation) has been shown to alter energy and membrane metabolism in testicular tissue of mice at acute (24 hour) and chronic (5 week) time points post-radiation [196]. Interestingly, trichostatin A administration (an epigenetic regulator) reversed the observed radiation-induced metabolic alterations and testicular dysfunction [196]. This research demonstrates that a therapeutic intervention can restore tissue-specific function following radiotherapy. To our knowledge, no study has investigated the metabolic alterations caused by radiation-induced damage in the salivary gland.

Although metabolomic profiling technologies have become increasingly powerful, metabolite levels alone may not specifically determine which reactions are altered by irradiation, and other ‘omics data can help fill this gap. Integration of transcriptomic and metabolomic data can identify significant associations between enzymes and metabolites that drive the phenotype under study. A common approach for interpreting ‘omics data is to evaluate the differentially expressed genes or metabolites for known pathways, but this analysis will necessarily limit the scope to a small subset of features. Gene set enrichment analysis (GSEA) [244] is a popular alternative approach that uses the full range of p-values across all genes to identify pathways ranked higher than expected by chance. GSEA and metabolite set enrichment analysis (MSEA) [245] can be combined to find pathways that are significant across both modalities. However, changes in metabolic state cannot always be neatly confined to pre-defined pathways, and these analysis strategies cannot discover new disease pathways. Overlaying gene and/or metabolite data on networks of known interactions can reveal “active modules” that provide mechanistic insight without being limited to pre-defined pathways [246].

The purpose of this study was to integrate genes and metabolites altered in response to irradiation in the salivary gland and integrate their function using network- and pathway-based enrichment analysis. One key finding is that radiation treatment leads to coordinated changes in a statistically significant region of the metabolic network. Integrated enriched pathways include glutathione metabolism, energy metabolism (TCA cycle and thermogenesis), peroxisomal lipid metabolism, and bile acid production. Manual curation of metabolites not annotated to KEGG and HMDB databases correspond to increased synthesis of glycosyl ceramides and increased sphingosine levels, highlighting additional metabolic pathways involved in the radiation-damage response that cannot, by definition, be captured using conventional pathway enrichment. Both our manual curation and our automated network integration analyses revealed new metabolic facets of previously observed radiation-induced salivary gland phenotypes. These metabolic alterations potentially explain the exquisite sensitivity of salivary gland tissue to radiation.

Materials and Methods

Mice and radiation treatment

Mice were housed and treated following protocols approved by the University of Arizona Institutional Animal Care and Use Committee (IACUC). All experiments were conducted using female FVB mice obtained from Jackson Laboratories (Bar Harbor, ME). At 4-6 weeks of age, mice were treated with one 5 Gy radiation dose using a ^{60}Cobalt Teletherapy Instrument from Atomic Energy of Canada Ltd Theratron (80-cm distance from source). Prior to radiation treatment, mice were anesthetized with an intramuscular injection of ketamine/xylazine (70 mg/kg-10 mg/mL) and placed in a 50 mL conical tube. To target the head and neck region for radiation treatment, the rest of the body was shielded with >6mm thick lead during radiation exposure.

Tissue preparation and metabolomics processing

Parotid salivary glands were extracted from mice five days post-radiation treatment (N=4) and from untreated mice (N=4). Tissue was snap frozen and shipped to Metabolon, Inc., for metabolomic profiling. Samples were prepared by precipitating proteins with methanol containing standards for reporting extraction efficiency. The resulting supernatant was analyzed on three platforms, split into equal parts. The instrument settings, data procurement, and software for data management were previously described in detail [247], [248]. The samples were desiccated under a vacuum for at least 24 hours followed by nitrogen derivatization using bistrimethyl-silyl-trifluoroacetamide. Electron impact ionization was used to analyze the samples on a Thermo-Finnigan Trace DSQ fast-scanning single-quadrupole mass spectrometer (Thermo Fisher Scientific Inc.). A Waters Acquity UPLC (Waters Corporation) coupled to a linear trap quadrupole MS (Thermo Fisher Scientific Inc.) equipped with an electrospray ionization source was used to perform ultra-performance liquid chromatography (UPLC)/MS-MS2 on the samples. From each sample, one injection (5 μL) was optimized for positive ions and a second for negative ions. Identification of metabolites was performed by automated comparison of the ion features in the samples to an in-house reference library. The reference library contains over 2,400 reliable chemical standard entries that incorporate retention time, molecular weight (m/z), preferred adducts, and in-source fragments with their associated MS-MS2 spectra. Fast identification of metabolites in the samples was achieved with high confidence utilizing this reference library. The median relative standard deviation (RSD) for the internal standards used for each sample run was calculated to assess instrument variability and was found to be 3%. To assess total process variability, the RSD for all endogenous biochemicals in the technical replicates was calculated and found to be 7%.

Metabolomics statistical analysis

Metabolon data was processed using MetaboAnalyst (MetaboAnalyst 4.0) [249]. Metabolites with missing values in at least 50% of samples were removed; remaining missing values were imputed with half of the minimum positive value in the original data based on the assumption that the values were below the instrument detection sensitivity limits. The data were then normalized using log-transformation and Pareto scaling as previously described for metabolomics studies [250]. Sample distribution of metabolite data was assessed by Principal Component Analysis (PCA), using the package prcomp from R [251], and Orthogonal partial least squares discriminant analysis (OPLS-DA), using the package ropls from R [252]. Both PCA and OPLS-DA results were visualized with the ggplot2 package from [253]. A significant-features plot (S-plot) was generated that visualized the variable influence in the OPLS-DA model. Metabolites with p1 between -20 and -10 were considered important metabolites upregulated in response to radiation, and metabolites with p1 between 10 and 20 were considered important metabolites downregulated in response to radiation. The metabolites identified as important from the S-plot that are not annotated to Human Metabolome Database (HMDB) IDs were assigned corresponding pathway(s) and enzymes using MetaCyc [254], [255]. For metabolites not identified by MetaCyc, corresponding pathways(s) and enzymes were curated manually using PubChem and KEGG when available [256].

Metabolite Differential Intensity Analysis

Normalized metabolite data were compared between untreated and irradiated conditions using the R package *limma* [257]. A significance threshold of $P_{adj} < 0.25$ (p-values adjusted using Benjamin-Hochberg method) was used and differentially expressed metabolites visualized with the pheatmap package from R [258]. Metabolite pathway enrichment was performed by Metabolite Set Enrichment Analysis (MSEA), using the R package *fgsea* with the pre-ranked option. Metabolites were ranked by their $(-log_{10}[p\text{-}value])$*sign($log_2$(fold change)) value and tested for enrichment against the metabolite Consensus Pathways Database (CPDB).

RNA Isolation, NGS Library Preparation and Sequencing

Parotid salivary glands were extracted from a separate set of mice five days post-radiation treatment (N = 3) and from untreated mice (N = 3) for transcriptomic profiling. Tissue was snap frozen and shipped to the University of Arizona Genomics Core for RNA-seq analysis. RNA was isolated with TRIzol reagent using the manufacturer's protocol (Thermo Fisher Scientific Inc.), then treated with RNase-free DNase. Presence of residual genomic DNA (gDNA) was assessed by PCR. The degree of RNA degradation was assessed by microfluidic electrophoresis. cDNA libraries were prepared with the Illumina TruSeq™ Stranded Total RNA Library Prep Kit and

Illumina RNA single indexing following the manufacturer's protocol with an input of 2,000ng of template. Prepared cDNA libraries were quantified with and sequenced using the HiSeq 2500 platform in the Rapid Run configuration (2x100 paired-end sequencing) and the base calling software BCL2Fastq from Illumina.

RNA-seq data preprocessing and analysis

Raw reads were trimmed using Trimmomatic 0.32 [259] and quality was assessed using FastQC 0.1 [260]. Reads were aligned to mouse reference genome GRCm38 using HISAT2 [261] Gene-level counts were determined using HTSeq-count 0.6.1 [262]. Genes with zero read counts in all six samples were removed from further analysis. Counts data were normalized using the variance stabilizing transformation method from DESeq2 [263]. Principal Component Analysis (PCA) was carried out in R. Differential expression analysis was performed with default parameters in DESeq2, and genes with an adjusted p-value < 0.05 were visualized with the ComplexHeatmap package from R [264]. Pathway enrichment was determined by Gene Set Enrichment Analysis (GSEA), as implemented in the R package *fgsea*, using the pre-ranked genes option. Genes were ranked by their ($-log_{10}[p\text{-}value]$)*sign($log_2$(fold change)) value, and were tested for enrichment in Gene Ontology (GO) biological process gene sets from MSigDB.

Pathway enrichment

Integrated pathway analysis was conducted by first performing gene and metabolite pathway enrichment separately by pre-ranked Gene Set Enrichment Analysis (GSEA), as implemented in the R package *fgsea*. Genes and metabolites were ranked by their ($-log_{10}[p\text{-}value]$)*sign($log_2$(fold change)) value, and were tested for enrichment against the Consensus Pathways Database (CPDB) - downloaded from the CPDB website on 11 Jun 2020 12:13 - GMT-0700. Joint pathway enrichment analysis was carried out according to Cavill [265], where metabolite and gene set enrichment analysis results were combined, and only pathways with enrichment estimates for both genes and metabolites were selected. For each pathway i, the joint p-value (p-joint) was calculated by the product $pm_i * pg_i$, where pm_i is the metabolite enrichment p-value and pg_i is the gene enrichment p-value for pathway i determined via *fgsea*. P-value adjustment for joint p-values was then calculated according to the Benjamini & Hochberg method [266]. Pathways considered as significant were selected based on the criteria of having $pm_i < 0.05$, $pg_i < 0.05$ and FDR < 0.05.

Network analysis of significant metabolites and genes

STITCH: All human chemical-protein interactions were downloaded from STITCH (stitch.embl.de) on Feb 9 2020. Note that this graph is bipartite, as edges exist only between proteins and chemicals. A radiation-associated subgraph of STITCH was created by restricting to genes with $P_{adj} < 0.05$ and metabolites with $P < 0.05$, where P is the unadjusted p-value. This subgraph had 61 metabolites and 91 genes and 298 edges between them. To test the significance of the subgraph, we selected 1000 random sets of matched metabolites and genes from the set of all measured genes and metabolites in our platforms. We then computed the number of unique STITCH interactions and total edge weight for each matched random subgraph. An empirical p-value was computed by summing the number of times the random subgraph had a larger number of unique interactions or total edge weight than the observed radiation-associated subgraph. To visualize the subgraph, we used the R package *condor* to identify bipartite network communities, MetaboAnalyst to identify enriched pathways (parameters on web-based application: “Joint pathway enrichment” with no fold changes, KEGG or HMDB metabolite IDs used depending on which had better coverage, enrichment run against “All pathways” not just metabolic, Fisher’s exact test with, “Combine queries” option), and Cytoscape v3.7.2 to create the final network image [267]. Recon3d: The Recon3d reactions and annotations were downloaded from https://www.vmh.life on 13-May-2020. Genes and metabolites were restricted using the same p-value thresholds as above for STITCH. Edges were drawn between every differential gene and metabolite (mapping to a KEGG ID) that participated in a common reaction according to Recon3d. The network was visualized using Cytoscape v3.7.2. Meta-network: Meta-networks were created by adding the scores of the STITCH interactions between all measured members of the two pathways, or only the GSEA leading edge genes and metabolites in the two pathways. The total STITCH score was then used as the final edge weight connecting two pathway nodes in the meta-network.

Active module analysis

jActiveModules: Active modules were identified using jActiveModules plugin in [246]. Cytoscape 3.7.2. The input network was the STITCH subnetwork consisting of all genes and metabolites that were measured in our dataset (by Metabolon or by RNA-sequencing). Unadjusted differential expression p-values were used to score all nodes. Module search was carried out using default settings. “Max depth from start nodes” was set to the default value of 2. Genes and Metabolites app (GAM) [268]: Unadjusted p-values and $\log_2$(fold change) values were input for all measured genes and all measured metabolites with KEGG identifiers. Whenever multiple transcripts mapped to the same gene, the transcript with the lowest p-value was chosen to represent that gene. GAM was run using the R Shiny app (https://artyomovlab.wustl.edu/shiny/gam/) with default parameters.

Data availability

The RNA-sequencing data can be accessed in the Gene Expression Omnibus (GEO) with accession number GSE155902 (https://www.ncbi.nlm.nih.gov/geo/query/acc.cgi?acc=GSE155902). All supplemental data, including raw metabolomics data, can be accessed using the following link to Zenodo; https://doi.org/10.5281/zenodo.4391402.

Results

Metabolomic and transcriptomic profiling of irradiated salivary glands

Compensatory proliferation in the parotid salivary gland and loss of tissue function at 5 days post-radiation treatment has been previously demonstrated and is reflective of the radiation-damage response [117], [153], [11]. There were 749 total metabolites identified by the metabolomics analysis. At this timepoint, a clear distinction was observed between the metabolite profiles of the irradiated and untreated (control) group in the principal component analysis (PCA; Fig. 2.1.A) and orthogonal partial least squares discriminant analysis (OPLS-DA; Fig. 2.1.B). From the OPLS-DA S-plot (Fig. 2.1.C), we identified 34 metabolites of importance that were upregulated (between -20 to -10 p1) and 20 that were downregulated (between 10 to 20 p1) in response to irradiation (Supplemental Table S1; for all supplemental material, use the Zenodo link provided in the Data Accessibility section of the Methods). The upregulated metabolites included amino acid derivatives, bile acids, and ceramides, whereas many downregulated metabolites fell into glutathione and glycerol families. Out of the 54 metabolites identified from the S-plot, 5 were not annotated to KEGG, HMDB, or PubChem: 1-dihomo-linolenylglycerol (20:3), 1-heptadecenoylglycerol (17:1), equol sulfate, glycosyl ceramide d18:1/20:0, d16:1/22:0, and glycosyl ceramide (d18:2/24:1, d18:1/24:2) (Supplemental Table S1). Therefore, these 5 metabolites could not be included in GSEA, MSEA, joint pathway enrichment, or network analysis and were manually annotated to pathways.

Differential intensity analysis showed 7 metabolites with $P_{\mathrm{adj}} < 0.1$, and 30 metabolites with unadjusted $P < 0.01$ between the irradiated and untreated conditions, out of the 749 total identified metabolites (Supplemental Table S2). The top 25 most significant differentially expressed metabolites are shown in the heatmap (Fig. 2.1.D). Using Metabolite Set Enrichment

Analysis (MSEA) we found that altered metabolites are enriched for amino acid metabolism, sphingolipid metabolism, and nucleotide metabolism (the full list of significant pathways is provided in Supplemental Table S3).

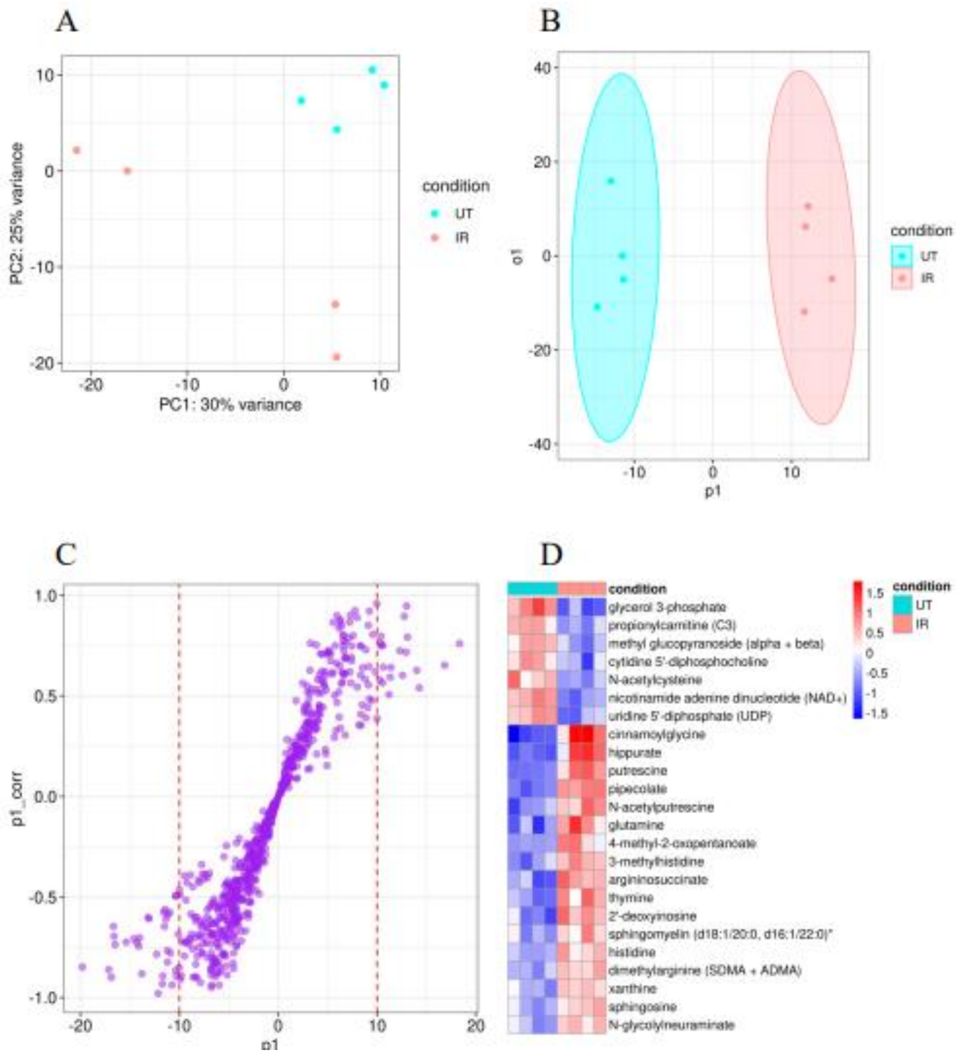

Figure 2.1. Metabolite profile differences between irradiated (IR) (N=4) and untreated (UT) (N=4) parotid salivary gland tissue in female mice.

(A) Principal component analysis (PCA) scores of normalized metabolite data separated by condition with principal component 1 (PC1) accounting for 30% of the variance and principal component 2 (PC2) accounting for 25% of the variance between conditions. (B) Orthogonal partial least squares discriminant analysis (OPLS-DA) scores of normalized metabolite data separated by condition (p1 is the predictive component displaying variation between conditions and o1 is the orthogonal component displaying variation within conditions). (C) OPLS-DA loadings significant features (S-plot) shows the contribution (p1) and the reliability (p1_corr) of the predictive component separating the metabolites by condition. (D) Heatmap of top 25 differentially expressed metabolites with a significance threshold of $P_{adj} < 0.25$ in irradiated versus untreated samples. Color key denotes the Z-score by row.

To profile the transcriptome, we performed RNA-sequencing of untreated and irradiated salivary glands. The PCA plot showed separation between irradiated and control samples (Fig. 2.2A). Differential expression analysis resulted in 155 genes with $P_{adj} < 0.05$ annotated to mouse, out of which 135 have an associated human ortholog gene symbol (Fig. 2.2B, Supplemental Table S4). Furthermore, pre-ranked gene set enrichment analysis against the Gene Ontology database for biological processes mainly showed perturbation in pathways associated with immune response, cell adhesion, and protein targeting (Supplemental Table S5). Six genes that are annotated to enzyme commission (EC) metabolic enzymes were differentially expressed; these included carbonic anhydrase 6 (CA6), ceramide glucosyltransferase (UGCG), the phosphatase INPP4B, and the phosphodiesterase ENPP2. The lack of GO term enrichment in metabolic pathways, coupled with the relative scarcity of differentially expressed enzymes, prompted us to move to a more integrative approach that would help interpret the transcriptomic profiles in the context of the metabolic network.

A

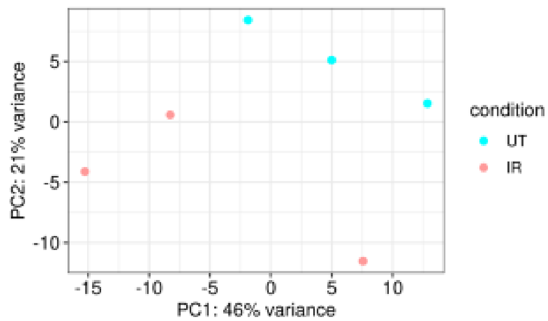

B

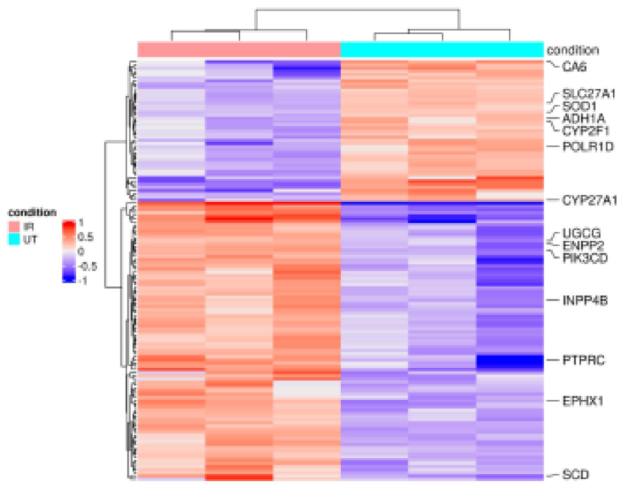

Figure 2.2. Transcriptome profile differences between irradiated (IR) (N=4) and untreated (UT) (N=4) parotid salivary gland tissue in female mice.

(A) Principal Component Analysis (PCA) plot of RNA sequencing data. (B) Heatmap of 155 differentially expressed genes with $P_{adj} < 0.05$ in irradiated and untreated samples. Pre-ranked gene set enrichment analysis against the Gene Ontology database for biological processes shows significant upregulation for ceramide glucosyltransferase activity, lipid binding and phosphatidylinositol trisphosphate phosphatase activity, and protein kinase binding and phosphatase activity; significant downregulation is observed for oxidoreductase activity, long-chain fatty acid-CoA ligase activity, and carbonate dehydratase activity in response to radiation.

Integration of metabolomic and transcriptomic data through rank-based statistics

Separate analysis of metabolomic and transcriptomic data revealed some common pathways (such as DNA replication), but most of the enriched processes were distinct. Furthermore, only a handful of enzymes and metabolites were significantly different between irradiated and control samples after applying the standard differential expression pipeline. Therefore, we decided to use rank-based enrichment tests similar to Gene Set Enrichment Analysis (GSEA) to integrate the two datasets (see methods section and Supplemental Table S6). Based on this analysis, we discovered 103 pathways that have a joint FDR < 0.05 and also have nominally significant enrichment in the genes and the metabolites separately, showing that they are supported by alterations in both data types (Figure 2.3A, Supplemental Table S7). The highest ranked enriched pathways include the TCA cycle and respiratory electron transport, thermogenesis, and the cell cycle.

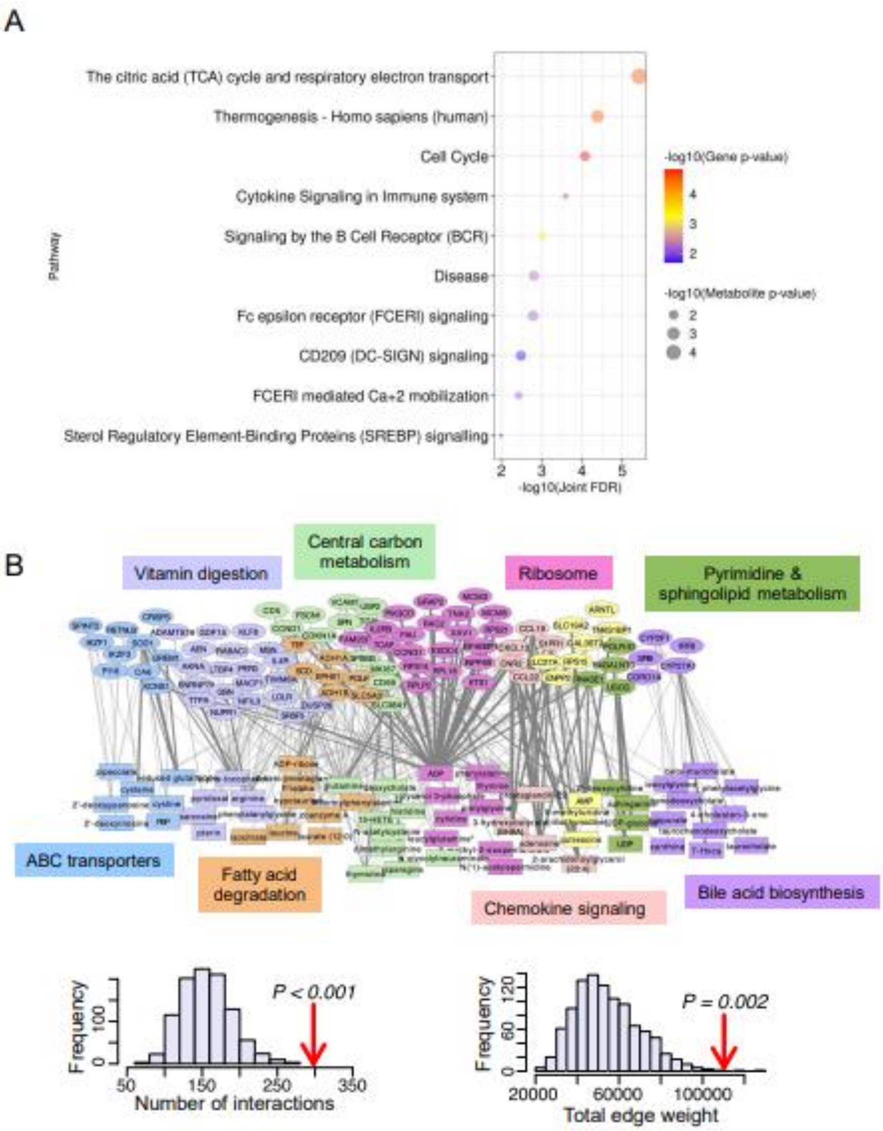

Figure 2.3. Integration of metabolomic and transcriptomic data through pathway enrichment and network analysis.

(A) Joint pathway enrichment p-values were calculated by the product of each metabolite and gene enrichment p-value against the Consesus Path Database. Adjusted p-values were then estimated according to the Benjamini & Hochberg method. Bubble plot shows the top 10 enriched pathways ranked by (-log10(joint adjusted p-value) * leading edge number of enzymes * leading edge number of transcription factors) / total number of leading edge genes. (B) (Above) Network shows all STITCH interactions between nominally significant metabolites (P < 0.05; rectangles) and statistically significant genes (P_{adj} < 0.05; ellipses), with the edge thickness proportional to the interaction score in the STITCH database. Nodes are colored according to community membership and significantly enriched pathways are indicated in the matching color. Note that yellow genes/metabolites were not statistically enriched for any KEGG pathway. (Below) Histograms show how the observed number of STITCH interactions (left) or total STITCH interaction score (right) among the irradiation-altered genes and metabolites (P_{adj} < 0.05 and P < 0.05, respectively) compares with 1000 randomly chosen matched sets of genes and metabolites measured by our transcriptomic and metabolomic platforms.

Identifying key gene-metabolite interactions through network analysis

Using the human orthologs determined earlier, we overlaid our expression and metabolite data in the context of human metabolic networks assembled in publicly available resources (STITCH and Recon3d) [269], [270]. We observed that the 475 genes with P < 0.01 and the 134 metabolites with P < 0.05 interact more strongly with each other in the STITCH chemical-protein network than expected by chance (P < 0.001; permutation test). This interaction demonstrates that our two profiling experiments converge on a common metabolic subnetwork that underlies the response of the salivary gland to radiation. Using network community detection, we found that the network of altered genes and metabolites fall in clusters enriched for distinct metabolic pathways including bile acid biosynthesis, fatty acid degradation, central carbon metabolism, and sphingolipid metabolism (Figure 2.3B). Likewise, overlaying altered genes and metabolites on the Recon3d network of reconstructed metabolic reactions (https://www.vmh.life/#reconmaps) highlights key interactions, including the regulation of reduced glutathione by GPX4; an increase in the amino acid transporter SLC38A1 associated with higher levels of glutamine, arginine, and other amino acids; and the catalysis of the reaction creating phosphoenolpyruvate (PEP) by the enolase ENO3 (Supplemental Figure S1).

Next, we sought to expand the subnetworks of altered genes and metabolites through nodes that are not themselves altered by irradiation, but which are implicated by their close proximity to differentially expressed nodes using jActiveModules [246] and the Genes and Metabolites web application (GAM) [268]. The top-scoring module from jActiveModules involved amino acid metabolism, bile acids (taurochenodeoxycholate), peroxisomal lipid metabolism (ACOT1/2) and glutathione (Figure 2.4A). GAM also led to a network module that centered on glutamate and glutathione metabolism and connected with amino acids and putrescine (Figure 2.4B). Overall, overlaying the data on the metabolic network highlighted the central role of glutathione in connecting the observed changes in amino acid metabolism, lipid metabolism, and bile acids.

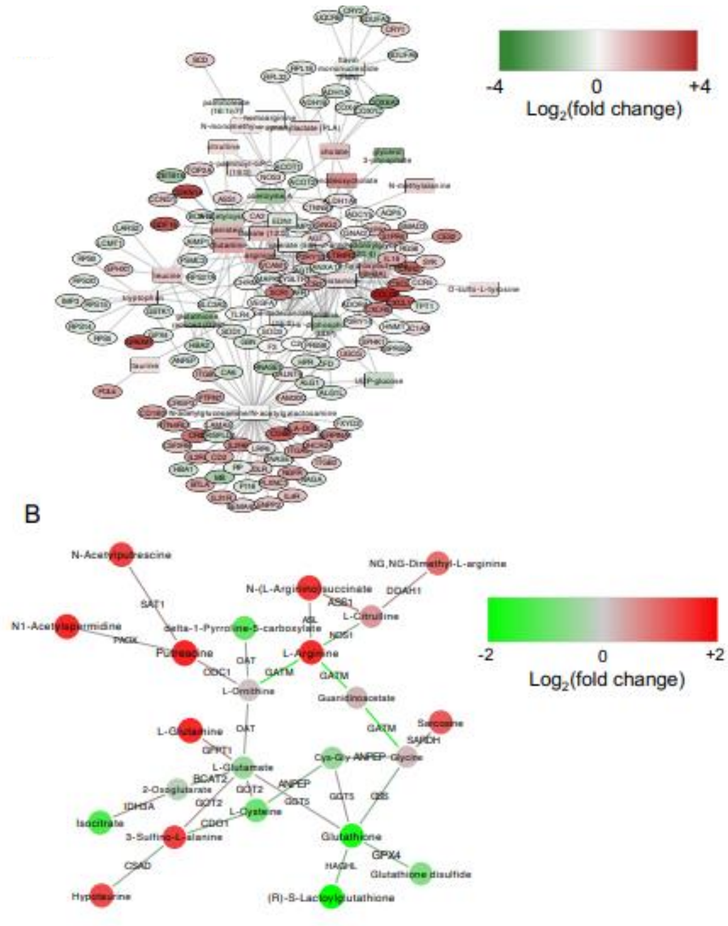

Figure 2.4. Active module analysis.

(A) Top-scoring module from jActiveModules analysis in Cytoscape. Rectangles indicate metabolites and ovals indicate genes. (B) Active module found by the Shiny app Genes And Metabolites (GAM). Circles represent metabolites and edges are labeled by genes that help catalyze the metabolic reactions between those metabolites.

Integrated view of how radiation alters cellular metabolism in salivary glands

From the list of significantly enriched pathways from GSEA, we manually removed cell cycle and cell proliferation pathways (which are commonly observed in the radiation damage response [117]) and manually selected twelve representative metabolic pathways from the remaining results. To visualize how these pathways feed into each other, we constructed two meta-networks, where each pathway is represented as a single node. In the first "unperturbed" meta-network, edges represent the total weight of STITCH interactions between all pathway members that were measured using our 'omics platforms; in the second "IR-perturbed" version, the edges represent the total weight of interactions between only the GSEA "leading edge" genes and metabolites that were altered five days after irradiation. The first meta-network (Fig. 2.5A) shows that the baseline pathway definitions cause strong interactions between TCA cycle, thermogenesis, and peroxisomal lipid metabolism. Comparing with the IR-perturbed meta-network (Fig. 2.5B), we see that irradiation causes a major shift towards interactions among protein digestion, glutathione metabolism, nucleotide metabolism, and cellular respiration.

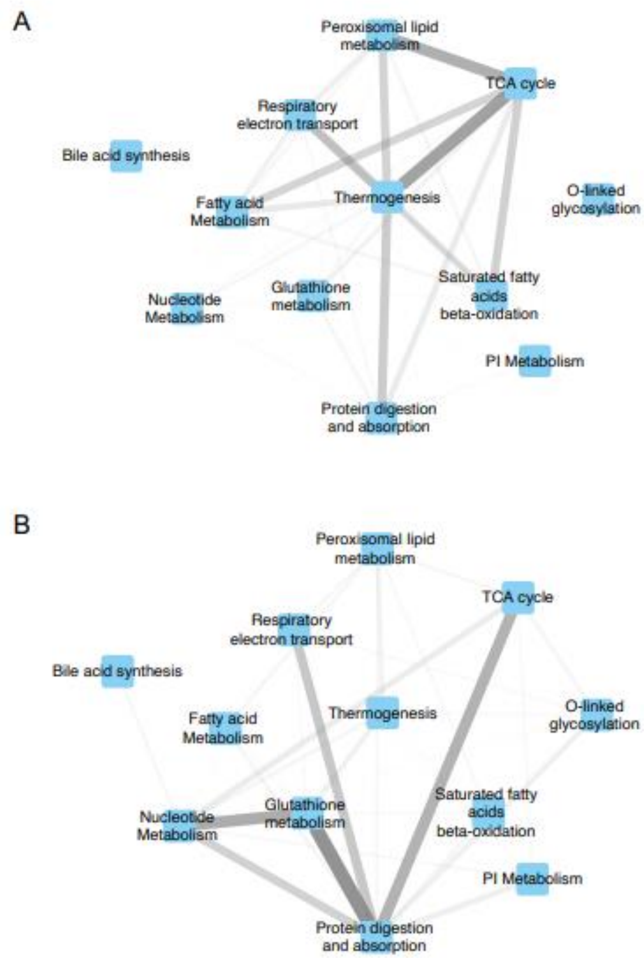

Figure 2.5. Meta-network showing interactions between pathways.

Nodes represent manually selected set of twelve significantly enriched metabolic pathways. Edge weights between pathways correspond to the total strength of protein-chemical interactions from the STITCH database between members of those pathways. Edge width and transparency are both proportional to edge weight. (A) Baseline network: All measured genes and metabolites in each pathway are included. (B) Perturbed network: Only the leading edge genes and metabolites (i.e. those most altered by irradiation) are included from each pathway.

Next, we mapped out in greater detail the metabolic reactions in these pathways and the cellular compartments in which they take place (Fig. 2.6). We identified leading edge genes and metabolites from the GSEA and MSEA analyses within the mapped metabolic pathways and denoted them as upregulated or downregulated in response to radiation. Most genes involved in phosphatidylinositol (PI) signaling increase with radiation treatment. In contrast, most metabolites annotated to PI signaling do not show significant changes or are not detected, but we do see a significant decrease in 2-arachidonylglycerol (2-AG) levels from the differential expression analysis, which can be annotated to PI signaling or endocannabinoid metabolism. Several leading edge amino acids that map to glutathione metabolism increase with radiation treatment, including elevation in the levels of glutamine, a precursor in glutathione synthesis, and the glutamine transporter gene *SLC38A1*. Further down the glutathione metabolism pathway, reduced glutathione (GSH) and *GPX4* (gene that encodes the enzyme glutathione peroxidase which converts GSH to the oxidized form, GSSG) both decrease post-radiation. Peroxisomal lipid metabolism displays reductions at both the transcript and metabolite levels. Interestingly, there is a significant increase from the differential expression analysis in the levels of at least 4 secondary bile acids and at least 5 acyl-amino acids, which can both be synthesized in the peroxisome. Mitochondrial fatty acid beta-oxidation is also downregulated at both the transcript and metabolite level. A decrease is seen in the transcript levels of the enzyme acyl-CoA thioesterase 1 that hydrolyzes acyl-CoA into coenzyme A and free fatty acids, and additionally in the metabolite coenzyme A. Mitochondrial oxidative phosphorylation is downregulated at the transcript level, specifically within complex I, III, IV, and the ATP synthase complex. Within the sphingolipid metabolism pathway, we observe an increase in the levels of four sphingomyelin species and two glycosyl ceramide species from differential intensity analysis. The expression of *UGCG* that encodes the enzyme which converts ceramide to glycosyl ceramide is upregulated, corresponding with an increase in glycosyl ceramide biosynthesis in response to radiation treatment. The lipolysis regulation pathway contains decreases in a few genes and metabolites, most notably *ADRB3* that encodes for a beta-adrenergic receptor family member and *LIPE*, a lipase involved in free fatty acid production. This manual curation of metabolites to metabolic pathways reveals an additional layer of detail that, when combined with the integrated networks, creates a more holistic representation of irradiation-induced changes in a metabolic context within the salivary gland.

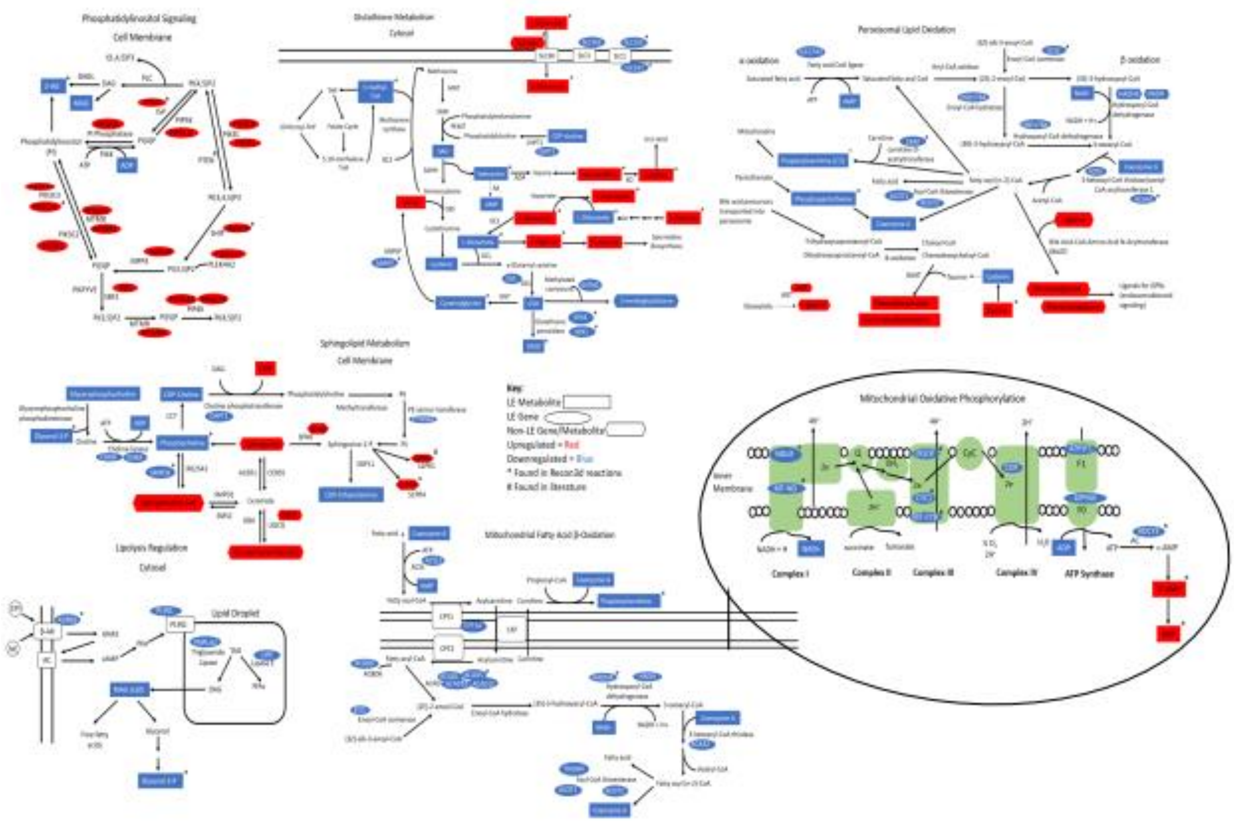

Figure 2.6. Integrative visualization of enriched pathways in metabolic reaction diagram.

Map of the metabolic pathways and the cellular compartments in which they take place with upregulated and downregulated transcripts and metabolites observed in response to irradiation. Rectangles correspond to MSEA leading edge (LE) metabolites, ovals correspond to GSEA LE transcripts. Red denotes upregulated transcripts/metabolites and blue denotes downregulated transcripts/metabolites. Non-LE metabolites that are statistically significant ($P_{adj} < 0.05$) from differential intensity analysis are denoted by the rectangular shape with the rounded edges.

Asterisks denote transcripts/metabolites found in Recon3d reactions. Pound sign denotes the transcript/metabolite is found in radiation-damage response literature.

Discussion

Radiation-induced salivary gland dysfunction and xerostomia continue to be significant problems for head and neck cancer patients due to a lack of mechanistic understanding of salivary gland damage. Here we have conducted a pathway and network analysis of metabolomic and transcriptomic profiles of the irradiated salivary gland compared to control. Our results support previous work that suggests involvement of glutathione and PI metabolism [271], [272], [273]; and suggest novel interactions including sphingolipid/ceramide metabolism, peroxisomal metabolism dysregulation, and mitochondrial dysfunction.

Radiation induces the production of reactive oxygen species (ROS) such as hydrogen peroxide, resulting in DNA damage and lipid damage (lipid peroxidation) [274]. Glutathione is one of the most abundant antioxidants produced to neutralize ROS and prevent radiation-induced damage [275]. Our data shows a significant decrease in reduced glutathione (GSH) and the transcript *GPX4* that encodes glutathione peroxidase involved in the synthesis of oxidized glutathione (GSSG), suggesting that the decreased GSH levels following radiation treatment could be driving the sensitivity to radiation that results in the loss of tissue function. Previous metabolomics research showed decreased levels of GSH in non-cancerous bone marrow tissue and increased levels in non-cancerous liver tissue in response to 6 Gy radiation [271]. In different model systems, GSH administration has produced mixed results in terms of protection from radiation damage [275]. In our data, both the jActiveModules and the GAM network analyses highlight GSH as a central node connecting different facets of cellular response to irradiation. Our meta-network analysis also revealed strong interactions between genes and metabolites within glutathione metabolism and members of several other pathways (TCA cycle/electron transport chain and protein digestion/absorption) that could be involved in regulating radiation-induced loss of function. An interaction of interest from the Recon metabolic reconstruction (https://www.vmh.life/#reconmaps) involves downregulated cysteine in glutathione metabolism concurrent with increased alanine and asparagine and decreased *SLC1A5* expression in protein digestion/absorption. *SLC1A5* encodes a neutral amino acid transporter that can facilitate the sodium-dependent exchange of alanine and asparagine as well as cysteine (https://www.vmh.life/#reconmaps). Targeting *SLC1A5* may increase cysteine import and increase glutathione synthesis and metabolism to mitigate radiation-induced damage.

Our RNA-seq and network analysis detected significant upregulation of a majority of transcripts involved in PI signaling following radiation, but most metabolites associated with PI signaling were not detected. This is in line with a previous study in an irradiated 3D skin model where the phosphatidylinositol-4,5 diphosphate pathway was significantly upregulated at the transcriptomic and proteomic levels but not at the metabolomic level [273]. The PI metabolism pathway is involved in the regulation of diverse cellular functions including proliferation, cell motility, and glycolysis [276]. The PI 5-phosphatases have been demonstrated to play a role in polarity and cell motility of cancer cells [277]. Cellular communication from irradiated cells via the PI3K pathway may lead to distinct transcriptional activation in bystander cells [278]. In a model of acute pancreatitis, loss of phosphoinositide 3-kinase-gamma (PI3K gamma) led to enhanced survival due in part to reductions in cell death and neutrophil infiltration [279]. Collectively, PI signaling plays a critical, yet complex role during damage and repair responses.

Radiation-induced changes in sphingolipid metabolism may play a role in the apoptosis-induced compensatory proliferation response or the inflammatory response in the salivary gland. Acidic sphingomyelinase (ASMase) converts sphingomyelin to ceramide; in the plasma membrane, ceramide acts as a secondary messenger capable of triggering several pathways to execute apoptosis, such as by direct interaction with phospholipase A2 and cathepsin D [280]. Acute increases in ceramide production and apoptosis lead to the switch from apoptotic signaling to increased cell proliferation [280]. In this study we observed significantly increased expression of the transcript *UGCG* that encodes the enzyme ceramide glucosyltransferase in the irradiated salivary glands compared to control, as well as significantly increased levels of glycosyl ceramide (d18:1/20:0, d16:1/22:0) and glycosyl ceramide (d18:2/24:1, d18:1/24:2). In response to radiation treatment, increased apoptosis is observed in parotid salivary gland that peaks at 24 hours following radiation treatment [115], [154], [113] and is followed by a compensatory proliferation response that begins five days after treatment that continues for at least 90 days [153], [150]. Thus, understanding the role of glycosyl ceramides in the induction and chronic upregulation of compensatory proliferation may reveal new targets that could restore function to the salivary gland following radiation.

In this study, significantly increased levels of sphingosine and the transcript *SPHK1* were observed in the irradiated salivary glands compared to control. *SPHK1* encodes the enzyme involved in sphingosine-1-phosphate (S1P) synthesis [281]. S1P is a bioactive sphingolipid derived from sphingosine that has been shown to increase prostaglandin E_2 (PGE_2) levels in human granulosa cells as part of regulating the reproductive system [282]. We have previously demonstrated that radiation induces an inflammatory response through PGE_2 release and that deletion in the P2X7 receptor ($P2X7R^{-/-}$) exhibited reductions in PGE_2 release and preserved saliva flow following radiation treatment [135]. Additionally, the transcripts *S1PR1* and *S1PR4* that encode S1PR1 and S1PR4, respectively, were significantly upregulated following radiation in our dataset. Binding of S1P to these receptors has been associated with mediation of inflammatory signaling to enhance cell survival, migration, angiogenesis, proliferation, and differentiation depending on tissue and type of injury [281], [283]. S1P treatment in human granulosa cells has been shown to activate yes-associated protein (Yap) via S1P1R and S1P3R during follicular development [153]. Our lab has previously shown that radiation-induced loss of apical-basolateral polarity leads to Yap activation at five days post-radiation, which is the same time point as the current study [153]. Interestingly, in a model that restores salivary gland function following radiation treatment (using injections of insulin-like growth factor 1), apical-basolateral polarity is restored and Yap activation is reduced [153]. Here, according to the STITCH interaction database (http://stitch.embl.de/), *S1PR4* interacts with glutamate in glutathione metabolism and adenosine in selenoamino acid metabolism, highlighting the complexity of the role of sphingolipid signaling in the radiation response due to interactions with multiple metabolic pathways. Overall, this suggests that radiation may increase the activation of inflammatory signaling mechanisms associated with S1PR1 and S1PR4 in the salivary gland that integrates with the compensatory proliferation response. Future studies inhibiting the sphingolipid receptors should shed light on the downstream mechanisms mediating the radiation phenotype.

We observed downregulated levels of both propionylcarnitine (peroxisomal lipid metabolism) and the transcript *HADHA*, which encodes the enzyme hydroxyacyl-CoA dehydrogenase (mitochondrial fatty acid beta-oxidation). Propionylcarnitine is known to interact with HADHA [284]. Previous reports have also shown that peroxisomal and mitochondrial metabolism are tightly synchronized to coordinate the effects on lipid oxidation [284], [285]. Interestingly, *HADHA* is expressed at higher levels in the salivary gland as compared with other tissues throughout the body [286]. In a metabolomics analysis of mouse serum, whole-body 6 Gy radiation resulted in enrichment of branched chain fatty acids (BCFAs) and very-long chain fatty acids (VLCFAs), implying dysregulated peroxisomal fatty acid beta-oxidation [271]. BCFA and VLCFA substrates are specifically transported into peroxisomes and not mitochondria for oxidation [287]. Conversely, in the irradiated salivary glands we observed lower expression of the *ABCD1* transcript which encodes the ABCD1 transporter responsible for the import of VLCFAs into the peroxisome [287]; this suggests decreased peroxisomal fatty acid oxidation in response to radiation.

Since the joint pathway enrichment analysis identified peroxisomal lipid metabolism as significantly downregulated in response to radiation, this prompted us to investigate if other metabolic processes associated with the peroxisome are also dysregulated. Dysregulation of bile acid synthesis, acyl glycine conjugation, and glyoxylate metabolism, processes that occur in the peroxisome, are observed following radiation. Increased levels of bile acids and their conjugates (e.g. chenodeoxycholate and taurochenodeoxycholate), acyl glycine conjugates (e.g. phenylalanylglycine and cinnamoylglycine), as well as increased expression of the *ABCD3* transcript that encodes the ABCD3 transporter responsible for import of bile acid intermediates into the peroxisome are observed following radiation. The bile acid and acyl glycine conjugated products may be involved in cell signaling that functions in the radiation-damage response [288]. Additionally, increased peroxisomal glyoxylate metabolism occurs in response to radiation. The AGT enzyme converts glyoxylate to glycine specifically in the peroxisome, and a significant increase in *AGT* transcript expression as well as glycine levels are observed in the salivary gland. The transcripts involved in glyoxylate metabolism in the cytosol and mitochondria are downregulated in response to radiation (*LDHA* and *GRHPR*, respectively). These results imply that radiation increases glyoxylate detoxification via the conversion to glycine specifically in the peroxisome in the salivary gland. Results from the Recon metabolic reconstruction (https://www.vmh.life/#reconmaps) further support the connection between these various peroxisomal metabolic pathways by identifying a connection between the reaction facilitated by the *SLC27A2* transcript in peroxisomal alpha-oxidation and the synthesis of the bile acid chenodeoxycholate, supporting the evidence for peroxisomal-specific bile acid synthesis. Collectively, these results demonstrate unique peroxisomal metabolic changes in response to radiation that deserve further investigation to understand the specific roles that each alteration plays in the radiation-damage response.

Alterations in thermogenesis and beta-oxidation pathways (Figure 2.5a,b), along with significant reductions in genes within mitochondria (Figure 2.6), suggest that radiation may induce a mitochondrial dysfunction phenotype. Many studies have described a loss or inefficiencies in electron transport chain (ETC) function as a hallmark of mitochondrial dysfunction [289], [290], [291]. Within the results depicted in this study, reductions in NAD+, UQCR, NDUF, COX, ATP5, and MT-ND family members are most notably related to reduced ETC capacity. The products of these genes function within complexes I, III, IV, and V and are largely encoded within mitochondrial DNA (mtDNA) [292]. In contrast to nuclear DNA, mtDNA is not associated with histones and has been shown to be more sensitive to genotoxic stress [292]. In addition, reductions in propionylcarnitine (C3) were observed (Figure 2.6) that may lead to increases in free radicals and lipid peroxidation [293]. The direct and indirect effects of radiation treatment along with potential inefficiencies in translation of these mtDNA products [290], [292] may explain the global reductions observed in these genes.

The reductions in NAD+ may also be an indication of inefficiencies in NADH transport across mitochondrial membranes. Under conditions where glycolytic intermediates are diverted to secondary pathways (pentose phosphate pathway, etc.), the glycerol-3-phosphate and malate–

aspartate shuttles provide a mechanism for NADH utilization by the ETC in order to maintain glycolysis by increasing NAD+ availability [294]. Following radiation treatment, glycerol-3-phosphate levels are decreased that likely impact the efficiency of the glycerol-3-phosphate shuttle to transport NADH. In addition, increases in lipid peroxidation due to reductions in C3 can lead to ferroptosis where mitochondria exhibit structural alterations [293], further exacerbating the mitochondrial dysfunction phenotype.

By integrating metabolomic and transcriptomic data, we showed that the genes and metabolites altered by irradiation of the salivary gland converge on a statistically significant metabolic network that involves glutathione metabolism, energy metabolism (TCA cycle and thermogenesis), peroxisomal lipid metabolism, and bile acid production. Manual curation of the metabolite data not annotated to KEGG or HMDB identified sphingolipid metabolism to also be an important pathway in the damage response. These findings provide specific metabolic signatures of irradiation damage in the salivary gland as well as plausible signaling interactions that drive radiation-induced salivary gland dysfunction.

III. [2]Temporal Metabolomics Analysis of Pathways Underlying Radiation-Induced Salivary Gland Dysfunction

Authors: Lauren Meeks[1], Diogo De Oliveira Pessoa[2], Justin M. Snider[1], Megha Padi[2,3,4], Kirsten H. Limesand[1,3*], Jessica A. Martinez[1,3]

Affiliations:
[1]School of Nutritional Sciences and Wellness, University of Arizona, Tucson, AZ, United States of America
[2]Biostatistics and Bioinformatics Shared Resource, Arizona Cancer Center, University of Arizona, Tucson, AZ,
United States of America
[3]University of Arizona Cancer Center, Tucson, AZ, United States of America
[4]Department of Molecular and Cellular Biology, University of Arizona, Tucson, AZ, United States of America

* Corresponding Author
Kirsten H. Limesand
1177 E 4th St, Shantz Building Room 421
Tucson, AZ 85719
limesank@arizona.edu
(520) 626-4517

Keywords: metabolomics, salivary gland, γ-radiation, amino acid metabolism

Funding: This work was supported in part by NIH R01 grants DE023534 and DE029166 to KHL and NIH F31 grant DE030663-01 to LM.

Conflict of interests: No conflicts of interest, financial or otherwise, were declared by the authors.

[2] Note: The contents of this chapter are currently submitted to *PLOS One* and awaiting editorial decision.

Introduction

Annually, over 54,000 new cases of head and neck cancer (HNC) are estimated in the United States by the American Cancer Society, with approximately 5% of these cases resulting in death [295]. Radiotherapy, combined with chemotherapy and surgery, is the dominant treatment for HNC and is effective in eliminating tumors and preventing cancer recurrence [296], [45]. Due to the proximity of the salivary glands to HNC tumors, they are indirectly damaged by radiotherapy and lose secretory function due to their high level of radiation sensitivity [297], [12], [13]. Acutely, oral mucositis and loss of saliva production begins to occur within the first week of radiotherapy as loss of acinar cells and glandular shrinkage occurs [13], [298]. Hyposalivation continues to persist chronically in over 80% of HNC patients [11], [14], [299]. Failure of the acinar cells to functionally repair and regenerate contributes to chronic salivary gland dysfunction, with the level of acute damage reflecting the level of chronic complications, such as dental caries, periodontitis, and nutritional deficiencies [300], [301], [302], [303]. The underlying mechanisms regulating chronic radiation-induced salivary gland dysfunction are unknown [13]. Current treatments to temporarily relieve symptoms include sialagogues without restoring function to the damaged salivary gland, and are associated with unpleasant side effects and inconsistent results [304], [305]. Therefore, the underlying mechanisms of radiation-induced salivary gland damage need to be discovered to identify methods for restoring function to the damaged gland.

Metabolomics is a powerful platform that reflects the effects of disease or damage in cells, tissues, or biological fluids since the metabolic phenotype is the interaction of multiple environmental factors in combination with genetic factors [306], [307], [308], [309]. Small changes in gene expression or protein levels are magnified at the metabolite level, which suggests that changes in metabolite profiles may provide a clearer reflection of an organism's phenotype compared to changes at the gene and protein level [310]. Metabolomics is a useful tool for discovering biomarkers of disease and has been utilized to identify metabolite biomarkers in many disease states, including head and neck cancers and Sjögren's syndrome (SS) [310], [311]. SS is an autoimmune disease that disrupts normal function of the salivary and tear glands, resulting in a comparable phenotype observed in radiation-induced salivary gland dysfunction [312]. In an untargeted metabolomics study of SS patient serum using machine learning, 21 significant metabolites were correlated with lipid and amino acid metabolic pathways, suggesting that these pathways are biomarkers of SS [313]. To understand the mechanisms underlying dry mouth conditions, Hynne and colleagues incorporated both SS patients and HNC patients after receiving radiation treatment (50-70 Gy total dose delivered over 6 weeks in 2 Gy fractions) and performed saliva metabolomics on both groups compared to healthy controls [314]. Although distinct metabolic profiles were observed between the SS patients, the radiation-treated HNC patients, and the controls, pyrimidine nucleotides and nucleosides were elevated in both patient groups compared to control groups and amino acid metabolism was dysregulated in both patient groups, suggesting that these metabolites may be useful in the diagnostics of these two dry mouth conditions [314].

Metabolomics has also been used to identify mechanisms underlying the radiation-damage response in multiple tissue types. The effects of different radiation dosages (0, 2, and 20 Gy) on the intestinal tissue metabolite profile in C57BL/6 mice revealed increases in amino acid levels that correlated with increased radiation dosage, which the authors suggest might be reflective of oxidative stress and pose amino acid metabolism as a possible therapeutic target mechanism to alleviate radiation-induced intestinal toxicity [199]. The effect of 12 Gy partial body radiation on liver, kidney, heart, lung, and small intestinal tissue of non-human primates at acute and intermediate damage time points revealed temporal changes in both citrulline and branched chain amino acids in all tissue types [210]. Our previous work integrated metabolites and transcripts altered in response to radiation treatment at five days post-IR in mouse parotid salivary gland tissue and identified joint pathway enrichment for glutathione metabolism, energy metabolism (TCA cycle and thermogenesis), bile acid production, and peroxisomal lipid metabolism [315]. Decreases in apical/basolateral polarity and increases in compensatory proliferation in the acinar cell compartment have been demonstrated at five days post-IR, with continued increases in compensatory proliferation correlated with chronic loss of secretory function [153], [117]. Since loss of secretory function has been previously demonstrated to begin as early as three days post-IR and continue for at least 90 days, these data suggest that the aforementioned metabolic pathways may drive salivary gland dysfunction [117], [153], [154], [315]. The purpose of this study is to perform a temporal analysis and identify metabolic changes that occur in the salivary gland due to radiation treatment at acute, intermediate, and chronic damage time points. We can then articulate the metabolic changes that are correlated with the different stages of the radiation-induced damage response and place them in a biological context through network analysis.

Materials and Methods

Mice

Mice were housed and treated following protocols approved by the University of Arizona Institutional Animal Care and Use Committee (IACUC). All experiments were conducted using 4-6 week old female FVB/NJ mice obtained from Jackson Laboratories (Bar Harbor, ME).

Radiation treatment

Mice were treated with a single five Gy radiation dose using a ^{60}Cobalt Teletherapy Instrument from Atomic Energy of Canada Ltd Theratron (80-cm distance from source). Prior to radiation treatment, mice were anesthetized with an intraperitoneal injection of ketamine/xylazine (70mg/kg-10 mg/mL) and placed in a 50 mL conical tube. To target the head and neck region for radiation treatment, the rest of the body was shielded with >6mm thick lead during radiation exposure.

Tissue preparation and metabolomics processing

Parotid salivary glands were extracted from mice at 3 days post-IR (N=8), 14 days post-IR (N=8), 30 days post-IR (N=8), and from untreated mice (N=4). 10-20mg of parotid salivary gland tissue sample was subjected to a methanol (1mL) extraction of both polar and nonpolar metabolites. Samples were homogenized in a MPbio FastPrep 24 bead beater utilizing 2mL homogenization tubes, Glass beads (Sigma 425-600µm acid washed, G8772-100G), and 1mL methanol spiked with internal standard mix (10µL Deuterated Amino Mix, 10µL of SPLASH LipidoMIX Internal standard mixture, Avanti, Al; Product number 330707) for additional semiquantitative analysis. Sample were homogenized under the following Fast prep conditions: twice at 6.5m/s for 20Sec. Tissue precipitant was pelleted through centrifugation (10 min, 10,000

RPM, 4°C), supernatant was transferred and dried under nitrogen and further stored at -20°C until resuspended in 100μL methanol/0.1% formic acid.

Ultra-high performance liquid chromatography-mass spectrometry (UHPLC-MS) analysis

One μL of sample extract was injected onto a Thermo Vanquish Duo UHPLC system in randomized order and separated using a Thermo Scientific Accucore 150-Amide-HILIC (250 x 2.1mm 2.6μ) and Hypersil GOLD (150 x 2.1mm 1.9μ) columns for hydrophilic interaction liquid chromatography (HILIC) and reverse phase (RP) chromatography, respectively, as described by Najdekr et al. [316]. The HILIC solvent system included a gradient from solvent A (95% acetonitrile/ 5% water with 10 mM ammonium acetate and 0.1% formic acid) to solvent B (50% acetonitrile/ 50% water with 10 mM ammonium acetate and 0.1% acetic acid) over 12 mins at 500μL/min, and column re-equilibration occurs during RP analysis. The RP chromatography included a gradient from solvent A (0.1% formic acid in water) to solvent B (0.1% formic acid in methanol) over 12 minutes at 300μL/min, and column re-equilibration occurs during HILIC analysis. Column temperatures were maintained at 50°C. Mass spectrometry (MS) detection was performed using a state-of-the-art Thermo Exploris 480, utilizing default lipidomic and metabolomic acquisition settings optimized by Thermo unless otherwise stated. These settings include: 3.4kV spray voltage in positive ion mode, 45AU sheath gas, 10AU auxiliary gas, and 325°C ion transfer tube, 350 °C vaporizer temperature. The Orbitrap mass analyzer scanned from 67-1000 m/z at 120,000 resolution for full scans and 15,000 for MS/MS scans. Samples were run in MS mode only, while Pooled QC's were run in MS/MS mode. HCD was utilized for fragmentation in Data-dependent acquisition (20 scans) and dynamic exclusion was set to 8 sec. Thermo AquireX platform was utilized on the pooled QC sample to achieve optimal feature annotation.

Metabolite ID annotation

Compound Discoverer version 3.3 provided Compound Names, SMILES IDs and KEGG IDs for a portion of the detected metabolites as part of its output. A single Pooled QC was created as a composited from all sample groups (aliquots were combined post extraction) and run between every 15 samples during LC/MS analysis, then utilized post processing to remove features with greater that 30% variation in the QC samples. The QC sample was also utilized for peak area and retention time normalization over the entire run. Annotations were assigned in Compound Discoverer utilizing the following data bases: MZcloud, Metabolika, ChemSpider, and MassList. Features with predicted formulas (only) based on accurate mass were also exported as part of the output. PubChem ID annotation was carried out by querying the PubChem database primarily from compound names and secondarily from compound formulas using the function *get_cid* from the *webchem* package. KEGG IDs that were not supplied by Compound Discoverer were annotated primarily by querying the Chemical Translation Service (CTS) database from compound names using the *cts_convert* function from the *webchem* package and secondarily by querying the KEGG database from compound formulas using the *keggFind* function from the *KEGGREST* package. SMILES IDs that were not supplied by compound discoverer were annotated by querying the PubChem database from PubChem IDs using the *pc_prop* function from the *webchem* package. In HILIC mode, 1,540 compounds were detected, and 598 metabolites (39%) were annotated at each timepoint. In RP mode, 2,852 compounds were detected, and 1,172 metabolites (41%) were annotated at each time point.

Metabolite class annotation

Metabolite class annotation was performed using the Human Metabolome Database (HMDB) (HMDB Version 5.0) first, and if the compound was not identified in HMDB then the PubChem database (National Library of Medicine) was used. The compound names were entered into the metabolite search engine and when the correct metabolite was identified, the class information was found under "Chemical Taxonomy" in the HMDB database or under the description of the metabolite in the PubChem database. If the metabolite could not be identified, "NA" was recorded.

Metabolomics statistical analysis

HILIC and RP peak files were obtained through the Compound Discoverer software version 3.3 and analyzed using the R statistical computing environment. Metabolite intensity counts were loaded with the *Read.TextData* function. Data quality assessment was carried out with the *SanityCheckData* function, followed by quality control via *ContainMissing* and the *ReplaceMin* functions. Data was normalized with the *Normalization* function (parameters: rowNorm = "NULL", transNorm ="LogNorm", scaleNorm = "ParetoNorm", ratio = FALSE, ratioNum = 20). All metabolite data processing steps were carried out using the *MetaboAnalystR* package. Principal components for PLS-DA with the *opls* function from the ropls package. Normalized metabolite data distribution was visualized with PSL-DA using the *ggplot2* package. Differentially expressed metabolites with $P_{adj} < 0.05$ were defined as significant.

Pathway enrichment analysis

Metabolite set enrichment analysis was carried out with *fora* (over representation analysis) and *fgsea* (pre-ranked set enrichment analysis) functions from the *fgsea* package (parameters: minimal metabolite set size 5, maximal metabolite set size 500). Pathway enrichment was performed against KEGGpathways from the ConsensusPathDB (CPDB) database for metabolites. Enriched pathways with P_{adj} <0.25 were defined as significant.

Network analysis

Metabolite PubChem and SMILES IDs were annotated primarily from compound names and secondarily from compound formulas. The metabolite annotation was used as input to obtain the structural data file (sdf) information and compute the metabolite structural similarity network, done with the Metamapp package. The generated network files (sif) were used to detect communities with the Louvain algorithm, and overrepresentation analysis (ORA) was applied to each detected cluster with more than 50 metabolites to identify enriched pathways. Enrichment analysis was carried out with the *fora* function from the *fgsea* package (parameters: minimal metabolite set size 5, maximal metabolite set size 500) using all KEGG pathways from the ConsensusPathDB (CPDB) database for metabolites. Metabolites clusters (communities) with hypergeometric p-value cutoff of 0.05 were defined as significant.

Weighted gene correlation network analysis (WGCNA)

Normalized metabolite levels were used for assessing correlation patterns using weighed gene co-expression analysis (WGCNA). Briefly, the scale free topology fit R^2 was computed and the smallest value above a 0.9 threshold was used. The adjacency matrix was then computed using the established R^2 value and used to obtain the Topological Overlap Matrix (TOM). The corresponding dissimilarity matrix (1 - TOM) values were hierarchically clustered, and modules detected using the criteria of a tree height of 0.995 and a minimum of 50 metabolites. Pathway enrichment overrepresentation analysis (ORA) was applied to each detected module, using the fora function from the fgsea package and CPDB KEGG pathways as described above. Enriched pathways with $P_{adj} < 0.25$ were defined as significant.

Data availability

All supplemental data, including raw metabolomics data and R code, can be accessed using the following link to Zenodo; https://doi.org/10.5281/zenodo.7775482.

Results

The IR time points chosen for this study reflect the acute, intermediate, and chronic damage responses in the salivary gland to identify kinetic changes in metabolites (Figure 3.1). Selection of radiation dose (5 Gy) was based on consideration of the clinical exposure in patients (2 Gy/day), comparison to other papers in the field (10-40 Gy), and data from our previous studies (2-10 Gy) [37], [116], [317] , [318], [113], [319]. Apoptosis of salivary acinar cells has been reported between 8-72 hours following radiation with peak in levels around 24 hours post-treatment [114], [320]. Increased levels of reactive oxygen species (ROS) have been detected as early as 24 hours post-IR and persist for at least ten days [170]. Loss of secretory function has been reported as early as three days post-IR [321], [154]. Therefore, three days post-IR was chosen as a representative acute damage time point. At five days post-IR, increases in compensatory proliferation and decreases in apical/basolateral polarity in the acinar cellular compartment begins and persistent increases in compensatory proliferation is correlated with chronic loss of secretory function [153], [157] , [154], [125]. Decreases in acinar cell differentiation markers (e.g. amylase) have been reported as early as ten days post-IR and persist for at least 90 days post-treatment [136], [157], [154], [125]. Fourteen days post-IR was selected as a representative intermediate damage time point as it exhibits increased compensatory proliferation, decreased differentiation and decreased function and we hypothesize may be a pivotal time point in the wound healing response [322]. We have previously demonstrated that radiation-induced loss of secretory function at 30 days post-treatment is similar at 60 and 90 day post-treatment [154]. Therefore 30 days was chosen as a representative chronic damage time point as it exhibits increased compensatory proliferation, decreased differentiation and decreased function.

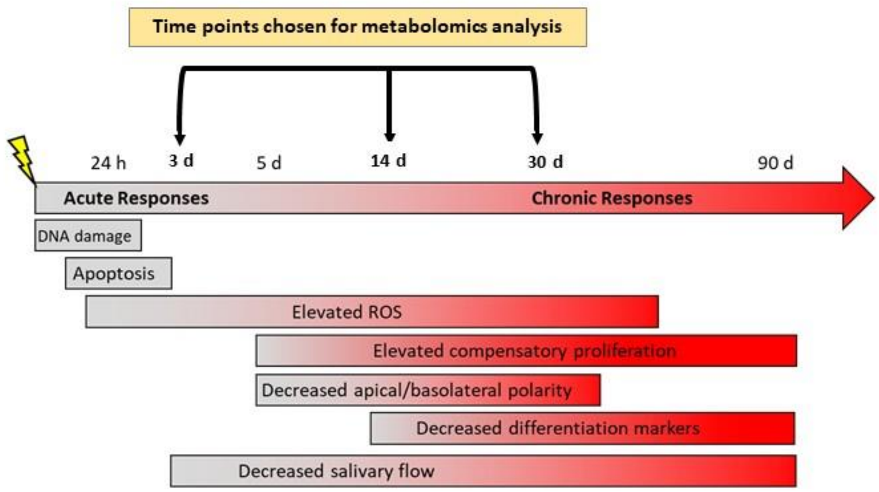

Figure 3.1. Summary of previously identified mechanisms underlying the radiation damage response in the salivary gland over time following exposure to a single 5 Gy dose.

Abbreviations: h=hours, d=days, DNA=deoxyribonucleic acid, ROS=reactive oxygen species.

Metabolomic profiling reveals separation between all radiation time points

Metabolomic profiles in each phase were compared between treated and untreated groups at days 3, 14 and 30 post-IR to determine temporal differences. HILIC chromatography was used to separate hydrophilic metabolites while RP chromatography was used to separate polar and aromatic metabolites as well as organic acids, thus improving the scope of metabolites detected [316]. The number of detected features in HILIC phase was 4,600 and the number of detected features in RP phase was 8,525. There were 1,534 metabolites identified by Compound Discoverer in HILIC phase at day 3 IR (Table S1; for all supplemental material, use the Zenodo link provided in the Data Accessibility section of the Methods), 1,531 at day 14 IR (Table S2), and 1,535 at day 30 IR (Table S3). There were 2,844 metabolites identified in RP phase at day 3 IR (Table S1), 2,840 at day 14 IR (Table S2), and 2,841 at day 30 IR (Table S3). The partial least squares discriminant analysis reveals distinct metabolite profile separation patterns between the three IR time point groups and the untreated group in both HILIC and RP phases (Fig. 3.2A,B). The heatmaps of all identified metabolites at each time point in HILIC and RP phases display a pattern of increased metabolite levels for each IR group compared to untreated (Fig. 3.2C,D). Differential intensity analysis identifies 507 metabolites in HILIC phase and 976 in RP phase with P_{adj} <0.05 between the day 3 IR group and the untreated group (Table S1), 407 metabolites in HILIC phase and 901 metabolites in RP phase between the day 14 IR group and the untreated group (Table S2), and 276 metabolites in HILIC phase and 504 metabolites in RP phase between the day 30 IR group and the untreated group (Table S3). The significant differentially expressed metabolites with P_{adj} < 0.05 are shown in the heatmaps for each IR group compared to untreated in HILIC and RP phases (Fig. 3.2E,F).

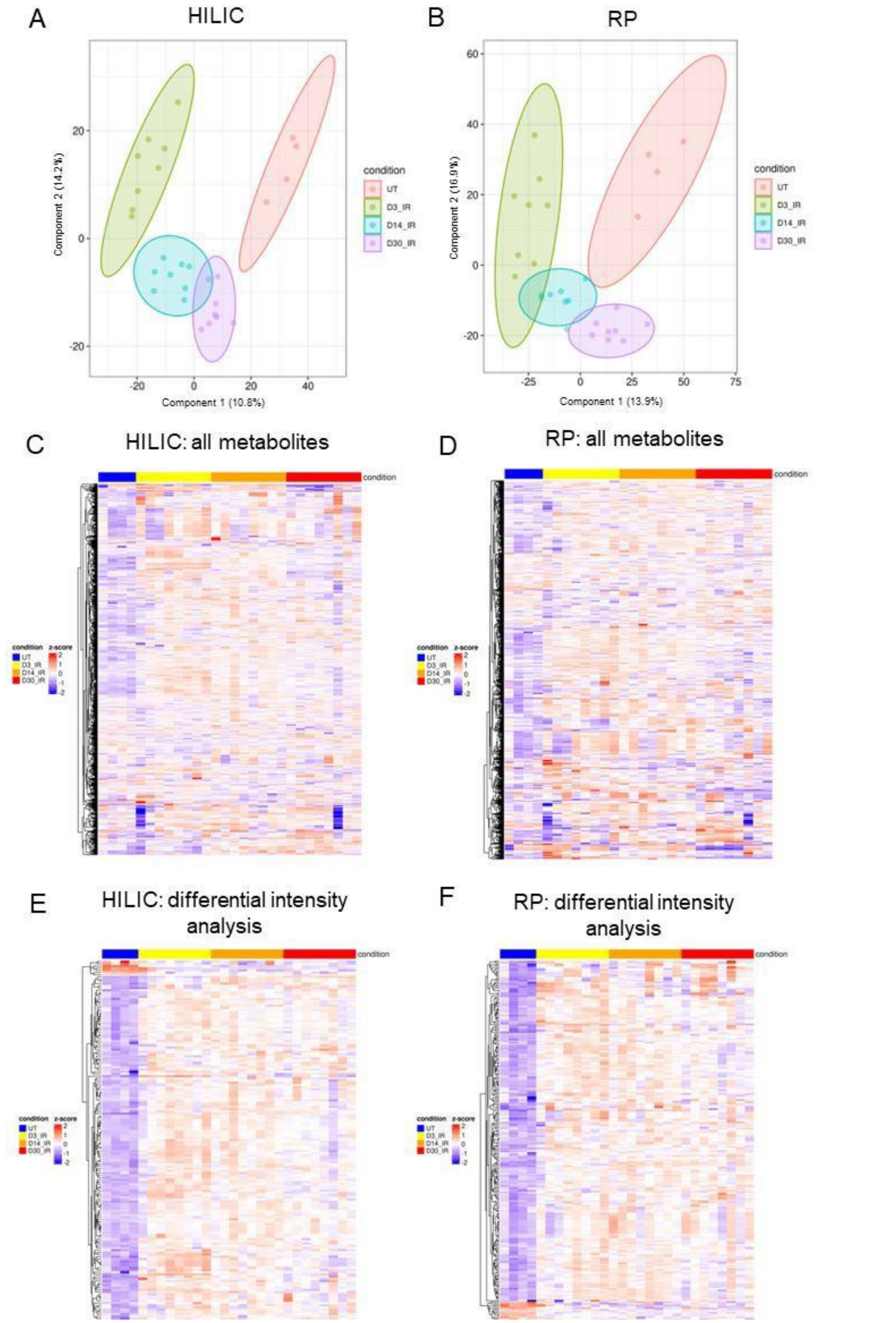
A
HILIC
B
RP
Component 1 (10.8%)
Component 2 (14.2%)
Component 1 (13.9%)
Component 2 (16.9%)
condition
UT
D3_IR
D14_IR
D30_IR
C
HILIC: all metabolites
D
RP: all metabolites
E
HILIC: differential intensity analysis
F
RP: differential intensity analysis
condition
z-score

Figure 3.2. Metabolomic profiling of irradiated parotid salivary glands at days 3 (N=8), 14 (N=8), and 30 (N=8) compared to untreated (N=4) reveals separation.

A) PLS-DA plot of HILIC phase data. B) PLS-DA plot of RP phase data. C) Heatmap of all metabolites identified in HILIC phase. D) Heatmap of all metabolites identified in RP phase. E) Heatmap of differentially expressed metabolites in HILIC phase (P_{adj}<0.05). F) Heatmap of differentially expressed metabolites in RP phase (P_{adj}<0.05). Abbreviations: IR=radiation, HILIC= hydrophilic interaction liquid chromatography, RP=reverse phase chromatography.

We next annotated the top 100 significant metabolites by class (day 3 IR is Table S4, day 14 IR is Table S5, and day 30 IR is Table S6). Table 3.1 presents a summary of the most commonly-observed metabolite classes for all IR time points compared to untreated in HILIC and RP phases. We observe across all IR time points that the majority of significant metabolites (P_{adj} < 0.01) are upregulated, with the highest percentage of upregulated metabolites observed at day 14 IR and the lowest percentage of upregulated metabolites observed at day 30 IR (Table 3.1, Tables S4, S5, S6). Across the 3 IR time points and 2 detection phases, alpha amino acids, carboxylic acids, peptides, and alcohol derivatives are upregulated in response to IR, while most of the significant downregulated metabolites are unidentified, with the few identified downregulated metabolites annotated to amino sugars and organonitrogen compounds (Table 3.1).

Table 3.1. Summary of the top 100 significant metabolites (Padj<0.05) annotated with metabolite class information at day 3, day 14, and day 30 IR compared to untreated in HILIC and RP phases.

Abbreviations: =radiation, HILIC= hydrophilic interaction liquid chromatography, RP=reverse phase chromatography, padj=a Benjamini Hochberg adjusted p-value.

IR Time Point	**HILIC: number of significant metabolites (padj<0.01)**	**HILIC: significant upregulated metabolites by class**	**HILIC: significant downregulated metabolites by class**	**RP: number of significant metabolites (padj<0.01)**	**RP: significant upregulated metabolites by class**	**RP: significant downregulated metabolites by class**
Day 3 IR	315 (94% upregulated, 6% downregulated)	alpha amino acids, peptides, azoles, carboxylic acids, 1,2-amino alcohols	unidentified, amino sugars, biotin and derivatives	615 (92% upregulated, 8% downregulated)	prenol lipids, benzene and derivatives, carboxylic acids, diazines, peptides	unidentified, organonitrogen compounds, diazines, phosphocholines
Day 14 IR	271 (96% upregulated, 4% downregulated)	alkaloids, alpha amino acids, n-acylethanolamines, phosphosphingolipids, carboxylic acids, secondary alcohols	unidentified, amino sugars, amines	503 (96% upregulated, 4% downregulated)	fatty acyls, carboxylic acids, piperidines, benzene and derivatives, peptides and dipeptides	unidentified, steroids and derivatives, organonitrogen compounds, diazines
Day 30 IR	139 (91% upregulated, 9% downregulated)	azoles, alpha amino acids, fatty amides, 1,2-amino alcohols, phosphocholines, alkaloids	unidentified, amino sugars, guanines, phosphocholines, pyridines and derivatives	229 (79% upregulated, 21% downregulated)	quinolines, piperidines, benzene and derivatives, fatty acyls, carboxylic acids	unidentified, organonitrogen compounds, diazines, steroids and derivatives, phosphocholines

Pathway enrichment analysis identifies significant enrichment at days 3 and 14 following radiation

We performed enrichment analysis on the metabolites with associated KEGG IDs using gene set enrichment analysis (GSEA) with KEGG pathways and the top 10 enriched pathways at each IR time point are presented in Table 3.2. We observe 16 significant pathways using P_{adj} < 0.25 at day 3 IR in HILIC phase and 3 significant pathways in RP phase (full set of enriched pathways for D3 IR presented in Table S7). The top 3 enriched pathways in day 3 IR HILIC phase are glutathione metabolism, aminoacyl-tRNA biosynthesis, and protein digestion and absorption, and the 3 significant pathways in RP phase are cysteine and methionine metabolism, central carbon metabolism in cancer, and glutathione metabolism (Table 3.2). At day 14 IR, 11 pathways are significantly enriched in HILIC phase and 10 pathways are significantly enriched in RP phase (full set of enriched pathways for D14 IR presented in Table S8). The top 3 enriched pathways in day 14 IR HILIC phase are ferroptosis, aminoacyl-tRNA biosynthesis, and protein digestion and absorption, and the top 3 enriched pathways in RP phase are central carbon metabolism in cancer, phenylalanine metabolism, and aminoacyl-tRNA biosynthesis (Table 3.2). At day 30 IR, no pathways reached significance at $P_{adj} < 0.25$ in HILIC phase, but the top enriched pathways are ferroptosis, diabetic cardiomyopathy, and glutathione metabolism (full set of enriched pathways for D30 IR presented in Table S9). In RP phase at day 30 IR, no pathways reached significance at $P_{adj} < 0.25$, with the top listed pathways being tryptophan metabolism, glutathione metabolism, and ubiquinone and other terpenoid-quinone biosynthesis (Table 3.2). The leading edge metabolites within the enriched pathways observed at each IR time point compared to untreated are shown in Supplemental Table S10. The leading edge metabolites are the metabolites with the highest contribution to the enrichment signal for the enriched pathway, which is comparable to leading edge genes in gene set enrichment analysis (GSEA) [323].

Table 3.2. Gene set enrichment analysis (GSEA) of top 3 pathways enriched at day 3, day 14, and day 30 IR compared to untreated in HILIC and RP phases using (Padj<0.05) for statistical significance.

No significant enrichment was observed at day 30 IR. Abbreviations: IR=radiation, HILIC= hydrophilic interaction liquid chromatography, RP=reverse phase chromatography, pval=an enrichment p-value, padj=a Benjamini Hochberg adjusted p-value, log2err=the expected error for the standard deviation of the p-value logarithm, ES=enrichment score, NES=enrichment score normalized to mean enrichment of random samples of the same size.

Day 3 IR - HILIC						**Day 3 IR - RP**					
Pathway	**pval**	**padj**	**log2err**	**ES**	**NES**	**Pathway**	**pval**	**padj**	**log2err**	**ES**	**NES**
Glutathione metabolism - Homo sapiens (human)	0.001	0.013	0.139	0.792	1.648	Cysteine and methionine metabolism - Homo sapiens (human)	0.008	0.222	0.052	0.698	1.523
Aminoacyl-tRNA biosynthesis - Homo sapiens (human)	0.001	0.013	0.129	0.735	1.607	Central carbon metabolism in cancer - Homo sapiens (human)	0.011	0.221	0.044	0.686	1.497
Protein digestion and absorption - Homo sapiens (human)	0.001	0.013	0.129	0.735	1.607	Glutathione metabolism - Homo sapiens (human)	0.013	0.222	0.043	0.793	1.524
Day 14 IR - HILIC						**Day 14 IR - RP**					
Pathway	**pval**	**padj**	**log2err**	**ES**	**NES**	**Pathway**	**pval**	**padj**	**log2err**	**ES**	**NES**
Ferroptosis - Homo sapiens (human)	0.002	0.022	0.113	0.799	1.665	Central carbon metabolism in cancer - Homo sapiens (human)	0.001	0.025	0.171	0.754	1.640
Aminoacyl-tRNA biosynthesis - Homo sapiens (human)	0.002	0.022	0.100	0.708	1.624	Phenylalanine metabolism - Homo sapiens (human)	0.002	0.025	0.117	0.800	1.638
Protein digestion and absorption - Homo sapiens (human)	0.002	0.022	0.100	0.708	1.624	Aminoacyl-tRNA biosynthesis - Homo sapiens (human)	0.002	0.025	0.105	0.730	1.589

Network analysis identifies the highest number of significant metabolites at day 3 following radiation

To further investigate metabolite interactions in the context of biological reactions, we implemented a network analysis of the metabolites based on structural annotation information in addition to metabolite level information. MetaMapp visualizes networks based on both chemical and biochemical similarity between metabolites, thus providing improved functional characterization of all metabolites, not just the small fraction that have KEGG IDs [324]. Figure 3.3A (HILIC) and 3.3B (RP) illustrate metabolomics networks from day 3 IR constructed using MetaMapp. Day 3 IR MetaMapp networks has the greatest number of significant metabolites relative to day 14 and day 30 IR (see Figure S1 for day 14 IR MetaMapp networks and Figure S2 for day 30 IR MetaMapp networks). At day 3 IR HILIC phase, we observe a cluster of 120 metabolites with 42 of them being differentially expressed (identified as Community 2 in the MetaMapp network), annotated to arginine biosynthesis as the top pathway (Fig. 3.3A). Communities are defined as clusters of metabolites detected using the Louvain method [325]. Most of the metabolites annotated to Community 2 are upregulated at day 3 IR compared to untreated. This is the only significant community using a hypergeometric p-value cutoff of 0.05 at this time point in HILIC phase (see Table S11 for full list of identified metabolite communities, see Table S12 for full list of pathways annotated to significant metabolite communities). At day 14 arginine biosynthesis remains the only significant pathway at day 14. At day 30, however, Community 1, consisting of 65 metabolites (25 are differentially expressed) is annotated to purine metabolism as the top pathway (Table 3.3, Table S12). In summary, for HILIC phase network analysis across the 3 IR time points, arginine biosynthesis is annotated as a significant metabolite community at day 3 and day 14 IR but not at day 30 IR, whereas lysine degradation and purine metabolism are significant metabolite communities at day 30 IR.

For the RP phase, we observe two significant communities identified as Communities 6 and 14 at day 3 IR (Fig. 3.3B). Community 6 is a cluster of 138 metabolites with 30 significant metabolites annotated to phenylalanine metabolism as the top pathway and Community 14 is a cluster of metabolites with 31 significant metabolites annotated to alanine, aspartate, and glutamate metabolism as the top pathways (Table 3.3, Table S12). Again, most of the significant metabolites are upregulated at day 3 IR compared to untreated. At day 14 IR RP phase, Community 14 remains significant, but not Community 6. Community 2, however, is detected as significant and consists of 182 metabolites (30 are significant) with tyrosine metabolism as the top annotated pathway (Table 3.3, Table S12). Community 2 remains significant at day 30 IR RP phase. Additionally, Communities 5 and 9 are significant (Table 3.3). Community 5 consists of 123 metabolites (30 are significant) with tryptophan metabolism annotated as the top pathway. Community 9 consists of 50 metabolites (25 are significant) with diabetic cardiomyopathy as the top annotated pathway (Table 3.3). In summary for RP phase network analysis across the 3 IR time points, alanine, aspartate, and glutamate metabolism is a significant metabolite community at day 3 and day 14 IR but not at day 30 IR. At day 30 IR RP phase, tryptophan metabolism, diabetic cardiomyopathy, and tyrosine metabolism are the significant metabolite communities.

A

Day 3 IR - HILIC

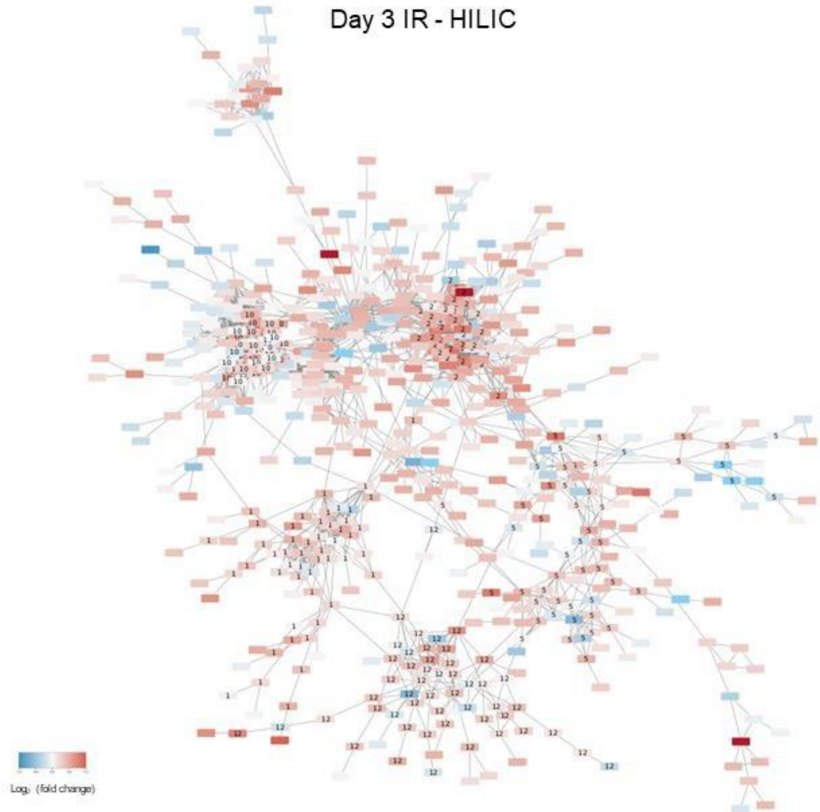

B

Day 3 IR - RP

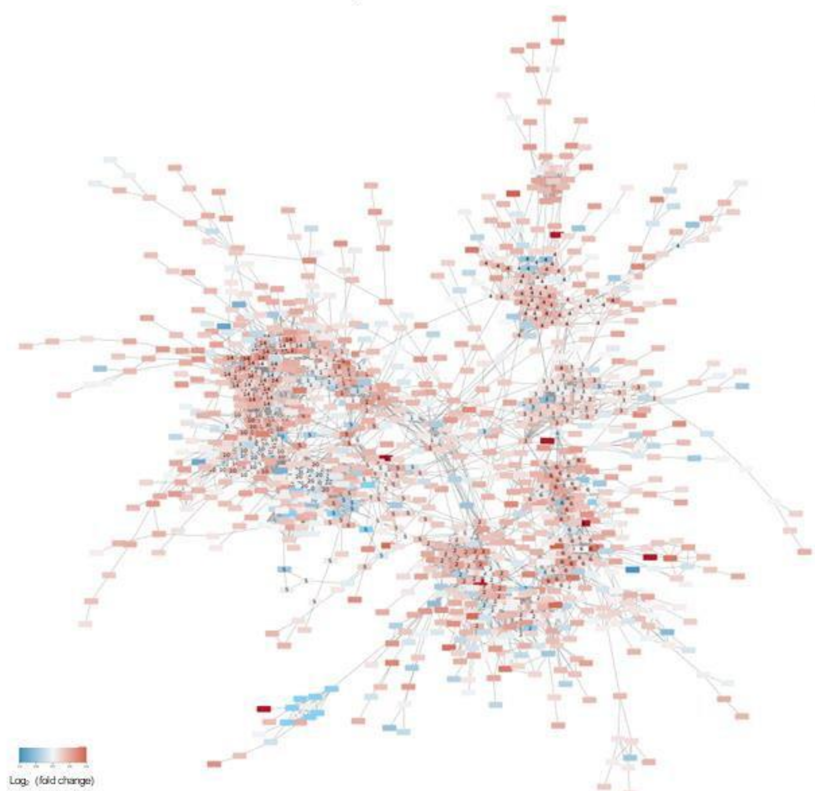

Figure 3.3. MetaMapp network analysis identifies significant metabolite clusters at day 3 IR.

A) HILIC phase. B) RP phase. Rectangles correspond to individual metabolites, edges denote chemical reactions between the metabolites, and numbers denote the communities that clusters of metabolites belong to. Color indicates Log2 (fold change) - red denotes upregulated metabolite levels versus untreated and blue denotes downregulated metabolite levels versus untreated. Abbreviations: IR=radiation, HILIC= hydrophilic interaction liquid chromatography, RP=reverse phase chromatography.

Table 3.3. Significant (Hypergeometric P-value <0.05) MetaMapp metabolite communities at day 3, day 14, and day 30 IR compared to untreated in HILIC and RP phases.

Abbreviations: IR=radiation, HILIC=hydrophilic interaction liquid chromatography, RP=reverse phase chromatography.

IR Time Point	**Community**	**Cluster Size**	**Number of Significant Metabolites**	**Pathway**	**Pathway P-value**	**Hypergeometric P-value**
HILIC Day 3 IR	2	120	42	Arginine biosynthesis - Homo sapiens (human)	2.97E-05	2.16E-08
HILIC Day 14 IR	2	120	33	Arginine biosynthesis - Homo sapiens (human)	2.97E-05	0.0017
HILIC Day 30 IR	2	104	31	Lysine degradation - Homo sapiens (human)	0.0004	7.39E-05
HILIC Day 30 IR	1	65	25	Purine metabolism - Homo sapiens (human)	1.72E-07	0.0212
RP Day 3 IR	14	124	31	Alanine, aspartate and glutamate metabolism - Homo sapiens (human)	1	0.0240
RP Day 3 IR	6	138	30	Phenylalanine metabolism - Homo sapiens (human)	0.0236	0.0459
RP Day 14 IR	14	116	31	Alanine, aspartate and glutamate metabolism - Homo sapiens (human)	1	0.0060
RP Day 14 IR	2	182	30	Tyrosine metabolism - Homo sapiens (human)	0.0002	0.0131
RP Day 30 IR	5	123	30	Tryptophan metabolism - Homo sapiens (human)	6.98E-05	4.53E-05
RP Day 30 IR	9	50	25	Diabetic cardiomyopathy - Homo sapiens (human)	0.0672	0.0068
RP Day 30 IR	2	181	24	Tyrosine metabolism - Homo sapiens (human)	0.0002	0.0147

Weighted gene correlation network analysis (WGCNA) shows amino acid metabolism enrichment at all radiation time points

We used a complementary approach, weighted gene correlation network analysis (WGCNA), to investigate correlations between metabolite networks and radiation damage. WGCNA does not use information about chemical structure or KEGG pathways, but instead is a completely data-driven method to identify networks of correlated metabolites, the functional modules active in the network, and the “hub” nodes (metabolites in our study) that may drive those biological functions [326]. Thus, WGCNA can incorporate all data from the platform, regardless of whether they have known chemical structures or pathway annotations. After identifying the WGCNA modules, over-representation analysis was performed to obtain pathway enrichment results using KEGG IDs (see Supplemental Table S13 for day 3 IR, S14 for day 14 IR, and S15 for day 30 IR). At day 3 IR HILIC phase, 6 metabolite correlation-based modules are identified (Table S13) and using a $P_{adj} < 0.25$ cutoff, we observe significant enrichment of purine metabolism (Table 3.4). The hub, or central metabolite, in purine metabolism is 6-Methoxyquinoline (Table 3.4). At day 14 IR HILIC phase, 8 metabolite correlation-based modules are detected (Table S14) and we observe significant enrichment for histidine metabolism and mineral absorption (Table 3.4). At day 30 IR, 8 modules are identified in HILIC phase (Table S15) with significant pathway enrichment only observed for arginine biosynthesis (Table 3.4). At day 3 IR RP phase, 9 modules are identified (Table S13) and we observe significant enrichment of glyoxylate and dicarboxylate metabolism and purine metabolism with the metabolite hub 3'-Adenosine monophosphate (3'-AMP) (Table 3.4). At day 14 IR RP phase, 13 modules are identified (Table S14) and we observe significant enrichment for phenylalanine metabolism and steroid hormone biosynthesis (Table 3.4). At day 30 IR, 12 modules are identified in RP phase

(Table S15) and no significant enrichment is observed (Table 3.4). When comparing the top pathway enrichment results for the detection phases across IR time points regardless of statistical significance, phenylalanine metabolism and lysine degradation are common to all IR time points (Tables S13,S14,S15). Glyoxylate and dicarboxylate metabolism is specific to day 3 IR, sphingolipid signaling pathway and thermogenesis are specific to day 14 IR, and ABC transporters and biosynthesis of unsaturated fatty acids are specific to day 30 IR (Tables S13,S14,S15).

Table 3.4. Significant (Padj<0.05) weighted gene correlation network analysis (WGCNA) metabolite modules with pathway enrichment annotation at day 3, day 14, and day 30 IR compared to untreated in HILIC and RP phases.

No significant enrichment was observed at day 30 IR RP phase. Abbreviations: IR=radiation, HILIC= hydrophilic interaction liquid chromatography, RP=reverse phase chromatography, Padj=a Benjamini Hochberg adjusted p-value.

Day 3 IR HILIC						
Module	**Top module pathway**	**Padj**	**Pathway size**	**Overlap metabolites**	**Module hub metabolite**	**Hub metabolite name**
green	Purine metabolism - Homo sapiens (human)	0.2043	10	6: Guanine, Adenine, GMP, Hypoxanthine, Adenosine, IMP	C10 H9 N O	6-Methoxyquinoline
Day 14 IR HILIC						
Module	**Top module pathway**	**Padj**	**Pathway size**	**Overlap metabolites**	**Module hub metabolite**	**Hub metabolite name**
blue	Histidine metabolism - Homo sapiens (human)	0.0660	9	6: 3-Methylhistidine, L-Aspartate, L-Glutamate, L-Histidinol, Urocanate, L-Histidine	C17 H11 Cl N2 O S	4-{2-[(2-chlorophenoxy)methyl]-1,3-thiazol-4-yl}benzonitrile
green yellow	Mineral absorption - Homo sapiens (human)	0.1186	11	3: L-Threonine, L-Asparagine, L-Serine	C25 H43 N3 O6	NA
Day 30 IR HILIC						
Module	**Top module pathway**	**Padj**	**Pathway size**	**Overlap metabolites**	**Module hub metabolite**	**Hub metabolite name**

red	Arginine biosynthesis - Homo sapiens (human)	0.1441	6	4: L-Aspartate, L-Glutamine, L-Ornithine, N-Acetylornithine	C41 H71 N3 O7	NA
Day 3 IR RP						
Module	**Top module pathway**	**Padj**	**Pathway size**	**Overlap metabolites**	**Module hub metabolite**	**Hub metabolite name**
green yellow	Glyoxylate and dicarboxylate metabolism - Homo sapiens (human)	0.0302	6	3: L-Serine, Glycine, 2-Oxoglutarate	C6 H5 N8 O16 P3 S5	NA
cyan	Purine metabolism - Homo sapiens (human)	0.1309	12	7: Guanine, Adenine, Hypoxanthine, Guanosine, 3'-AMP, 5'-AMP, Adenosine	C10 H14 N5 O7 P	3'-Adenosine monophosphate (3'-AMP)
Day 14 IR RP						
Module	**Top module pathway**	**Padj**	**Pathway size**	**Overlap metabolites**	**Module hub metabolite**	**Hub metabolite name**
light yellow	Phenylalanine metabolism - Homo sapiens (human)	0.0890	10	3: Benzoate, L-Tyrosine, 2-Phenylacetamide	C30 H56 N4 O3 P2 S	NA
purple	Steroid hormone biosynthesis - Homo sapiens (human)	0.1841	7	3: Pregnenolone, Pregnanediol, Allopregnanolone	C8 H2 Cl N2 O10 P3 S3	NA

Intersection of amino acids within mitochondrial metabolic pathways

Table S16 presents a summary of the significant metabolite classes, GSEA pathways and their associated leading-edge metabolites, MetaMapp community pathways, and WGCNA module pathways observed at day 3, day 14, and day 30 IR. We observe the highest number of significant metabolites and the highest number of significant enriched pathways at day 3 IR, and this significance decreases with increasing time as zero significant enriched pathways were observed at day 30 IR from the GSEA analysis. Common enriched pathways at day 3 and day 14 IR are glutathione metabolism, aminoacyl-tRNA biosynthesis, central carbon metabolism, and several types of amino acid pathways. Due to the high prevalence of enrichment for amino acid metabolism and significance for amino acids at all IR time points (Figure 3.4), we decided to further investigate amino acid metabolism as an application of this data by interpreting the results in a biological context (see Discussion). Figure 3.4A displays individual amino acid level changes in response to radiation over time, which are further grouped together based on where they interact with mitochondrial metabolic pathways. Figure 3.4B shows where the grouped amino acids feed into the tricarboxylic acid (TCA) cycle, central carbon metabolism in cancer, and one-carbon metabolism.

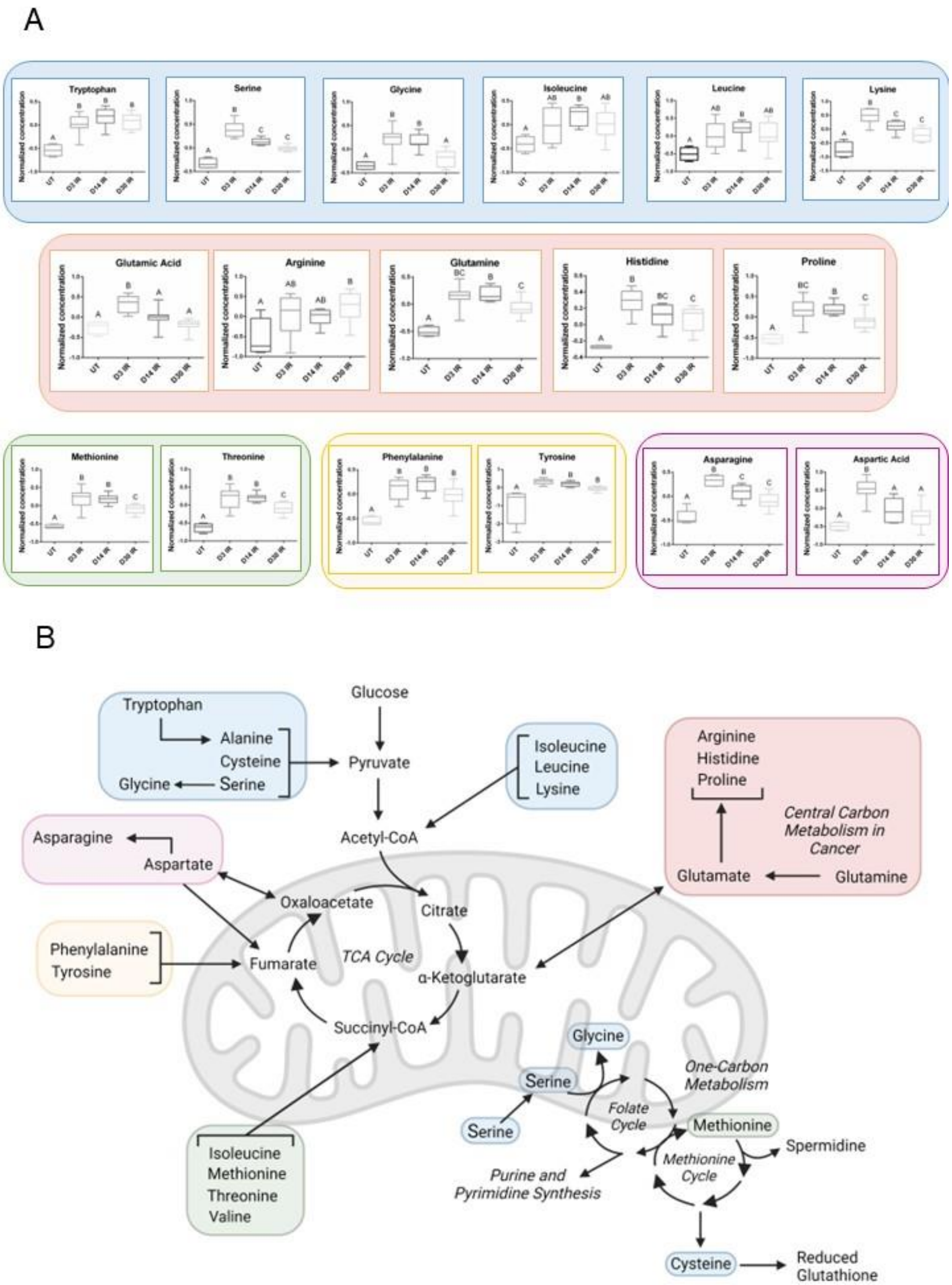
A
Tryptophan
Serine
Glycine
Isoleucine
Leucine
Lysine
Glutamic Acid
Arginine
Glutamine
Histidine
Proline
Methionine
Threonine
Phenylalanine
Tyrosine
Asparagine
Aspartic Acid
Normalized concentration
UT
D3 IR
D14 IR
D30 IR
B
Tryptophan
Alanine
Cysteine
Glycine
Serine
Glucose
Pyruvate
Isoleucine
Leucine
Lysine
Arginine
Histidine
Proline
Central Carbon Metabolism in Cancer
Glutamate
Glutamine
Acetyl-CoA
Asparagine
Aspartate
Oxaloacetate
Citrate
Phenylalanine
Tyrosine
Fumarate
TCA Cycle
α-Ketoglutarate
Succinyl-CoA
Glycine
Serine
One-Carbon Metabolism
Folate Cycle
Methionine
Serine
Spermidine
Methionine Cycle
Purine and Pyrimidine Synthesis
Isoleucine
Methionine
Threonine
Valine
Cysteine
Reduced Glutathione

Figure 3.4. Amino acids connected to mitochondrial metabolism.

A) Individual amino acids analyzed by one-way ANOVA with post-hoc Tukey's test for multiple comparisons. Letters denote statistical significance between groups, $P<0.05$. Box plots display the upper quartile, median, and lower quartile with the maximum and minimum values denoted by the whiskers. N=4 for untreated (UT), N=8 for day 3 (D3) IR, N=8 for day 14 (D14) IR, and N=8 for day 30 (D30) IR. Alanine, cysteine and valine were not detected in our data set. B) Overview of pathways related to amino acid metabolism. Created in BioRender.com. Abbreviations: TCA = tricarboxylic acid.

Discussion

This study utilized a metabolomics approach to identify metabolites and pathways altered in the salivary gland in response to IR over time. The results from the current study provide mechanistic insight into the different stages (acute, intermediate, and chronic) of salivary gland dysfunction following IR. While we identified the greatest number of significant enriched pathways at the acute damage stage, the metabolites and pathways still altered at the chronic damage timepoint most likely reflect the pathways of interest to develop targeted interventions against persistent xerostomia. We observed conservation of enriched pathways across the three time points: glutathione metabolism, aminoacyl-tRNA biosynthesis, central carbon metabolism in cancer, ferroptosis, and various amino acid metabolism pathways. These findings suggest targeting the enriched metabolic pathways conserved across the acute and chronic damage response stages may ameliorate chronic loss of salivary gland function following radiation treatment. Our group's previous study [315] combined a transcriptomics and metabolomics approach to identify metabolic changes in the salivary gland at day 5 IR, which is when increased compensatory proliferation and decreased apical/basal polarity are observed as the damage state transitions from the acute to the chronic responses (Figure 3.1) [153], [150]. Our previous study identified coordinated changes in glutathione metabolism, peroxisomal lipid metabolism, bile acid production, and energy metabolism pathways (TCA cycle and thermogenesis) at day 5 IR [315]. In the current study, peroxisomal lipid metabolism, bile acid production, and the TCA cycle and thermogenesis were not identified as significant pathways, and this is most likely due to the MS detection settings not selecting for bile acids and certain TCA cycle intermediates in positive ion mode. Another factor contributing to this discrepancy might be the absence of combinatorial transcriptomic analysis in the present study [315].

In our current study, glutathione metabolism was identified as a significant enriched pathway at day 3 and day 14 IR using GSEA, and as a significant enriched pathway at all three IR timepoints using MetaMapp network analysis (Table S16). Interestingly, reduced glutathione levels were lower in IR vs control at day 5 IR in our previous study [315] while reduced glutathione levels were significantly higher in IR vs control at day 3 in RP phase and at day 14 in HILIC and RP phases in the current study (Tables S1,S2). At day 30 IR, reduced glutathione levels were higher compared to control in RP phase although statistical significance was not reached (Table S3). A metabolomics analysis of liver tissue in mice exposed to 3 Gy and 11 Gy gamma IR to compare metabolic effects of low versus high dose IR exposure showed significantly higher levels of reduced glutathione levels at both day 4 and day 11 IR compared to untreated tissue, with the highest reduced glutathione levels observed at day 4 compared to day 11 in both the 3 Gy and 11 Gy treatment groups [197], thus supporting the results from our current study. It is well established that glutathione is one of the most prominent radioprotectors in cells as it scavenges free radicals produced from DNA damage [275], which would be a possible explanation for why we observed decreased reduced glutathione at day 5 IR previously as it was utilized to scavenge reactive oxygen species (ROS) that remain elevated in the salivary gland following IR (Figure 3.1) [170]. The elevation of reduced glutathione observed in the current study and in the metabolomics analysis of IR liver tissue could occur due to the increased synthesis of reduced glutathione from glutamine to fuel protection of the salivary gland tissue from the increase in ROS, which has been previously demonstrated in cancer cells as a protective mechanism against increased oxidative stress [327], [328]. Thus, the mixed results for reduced glutathione observed in our current and previous study may be attributed to flux of the metabolite as it scavenges ROS in the damaged salivary gland tissue over time.

Amino acid metabolic pathways were prominently enriched in the present study across all three IR time points in the GSEA, MetaMapp network modules, and WGCNA module results and include arginine biosynthesis, lysine degradation, histidine metabolism, cysteine and methionine metabolism, phenylalanine, tyrosine and tryptophan biosynthesis, and alanine, aspartate, and glutamate metabolism (Table S16). We investigated the levels of the detected amino acids that compose these pathways and discovered upon further analysis that all are significantly increased in at least one IR time point compared to untreated (Fig. 3.4A). Multiple studies observed increases in amino acid metabolites in response to IR acutely and chronically. Twelve hours following exposure to total body 6 Gy gamma IR in a mouse model, glutamate and glutamine were increased in the ileum, glutamate was increased in the liver, and phenylalanine in the muscle [271]. At 1, 2, and 3 days following exposure to 2 or 6 Gy x-ray IR in a rat model, phenylalanine was increased in the jejunum, phenylalanine, glutamine, serine, and lysine were elevated in the spleen, and glutamine and serine were increased in the liver [329]. At two months following exposure to 1.6 or 2 Gy gamma IR in a mouse model, histidine, glutamine, and phenylalanine were elevated in intestinal tissue at both IR doses [330]. Thus, it is established that amino acids increase in tissue exposed to IR, but the involvement of these amino acids in various metabolic pathways is not clearly understood.

Amino acid metabolism feeds into many different pathways, several of which were identified as significant enriched pathways in the current study: central carbon metabolism, glutathione metabolism, and purine metabolism. Central carbon metabolism in cancer refers to various pathways that increase energy production and macromolecule synthesis to sustain tumor growth [331], [332]. There are two main ways that cells accomplish this increase in energy and growth. One method is increasing glucose uptake and the rate of glycolytic flux to increase ATP production quickly, which also increases nucleotide production through the pentose phosphate pathway [331], [332]. A second method is increasing glutamine uptake, which is converted to glutamate and subsequently to other amino acids to synthesize proteins or it feeds into the TCA cycle to increase ATP production [331], [332]. Our previous study identified increased levels of the glutamine transporter transcript *SLC38A1* as well as increased levels of glutamine at day 5 IR in the salivary gland [315]. We observed an increase in glutamine levels at day 3, day 14, and day 30 IR in our current study, and a significant increase in glutamate (glutamic acid) levels at day 3 IR (Tables S1,S2,S3). The leading-edge metabolites in GSEA results for central carbon metabolism in cancer (across all three IR timepoints) include glutamate, asparagine, aspartate, methionine, phenylalanine, proline, serine, tryptophan, and tyrosine, which suggests increased glutamine levels fueling synthesis of these other amino acids (Table S10). These results support the hypothesis that IR increases glutamine levels, and subsequently other amino acid levels, potentially to rebuild the damaged salivary gland tissue, similar to what is observed in cancer cells by increasing central carbon metabolism to support tumor growth (Fig. 3.4B). However, the accumulation of amino acids following IR may have a detrimental effect on the function of the salivary gland. Autophagy maintains cellular homeostasis by recycling damaged proteins and is necessary for normal salivary gland function. Morgan-Bathke and colleagues previously demonstrated that administration of the rapalogue CCI-779, an autophagy activator, post-IR treatment significantly improved salivary flow rates at days 30, 60, and 90 post IR compared to mice that only received IR [125]. Therefore, the observed increases in amino acid levels in our current study may be reflective of impaired autophagy in the salivary gland following IR treatment.

Amino acid metabolism is closely linked to glutathione metabolism and purine metabolism through one-carbon metabolism. One-carbon metabolism refers to various anabolic reactions in both the cytoplasm and mitochondria that are responsible for nucleotide synthesis, methylation reactions that affect gene expression, amino acid homeostasis, and reductive/oxidative (redox) defense (Fig. 3.4B) [333], [334]. The methionine cycle is a component of one-carbon metabolism [333], and in our present study we observed significant increases in methionine at all 3 IR time points and significant increases in an intermediate in the methionine cycle, S-Adenosylhomocysteine (SAH), at day 3 and day 14 IR (Tables S1,S2). The methionine cycle synthesizes cysteine and reduced glutathione, and our study identified significant increases in reduced glutathione at day 3 and day 14 IR (Tables S1,S2). A leading-edge metabolite annotated to glutathione metabolism, which was significantly enriched in our GSEA output at all IR time points, was spermidine (Table S10), which is a by-product of the methionine cycle and was increased at all IR time points (Fig. 3.4B), (Tables S1,S2,S3). We observed increases in glycine, serine, and threonine levels at all IR timepoints in our study, and these three amino acids feed into the folate cycle, which generates purines and pyrimidines (Fig. 3.4A,B). Upon further investigation, the detected leading-edge metabolites (Table S10) for purine metabolism were increased at all IR time points (hypoxanthine was the one exception and was slightly downregulated at day 14 IR, although not significantly) and the leading-edge metabolites for pyrimidine metabolism were also increased at all IR time points (Tables S1,S2,S3). Collectively, the increase of cysteine, methionine, glycine, serine and threonine observed in response to IR over time may be linked to the increase in reduced glutathione and purine/pyrimidine levels in the salivary gland through elevated one-carbon metabolism. Previous research has demonstrated that 2, 5, and 7 Gy gamma IR alters one-carbon metabolism in murine liver at days 1, 2, 3, 4, 5, and 8 by shifting priority to nucleotide synthesis at the expense of transmethylation reactions, which can further exacerbate DNA damage [335]. Further investigation of transmethylation products and enzyme levels and activity in the folate and methionine cycles (specifically S-adenosylmethionine) would need to be evaluated to test if the results from our study in the salivary gland support the one-carbon metabolism alteration observed in previous IR research in the liver. Prior research has manipulated the supply of methyl group donors to mitigate the IR response in different model systems, with animal studies displaying significant increases in animal survival, bone marrow health, and intestinal integrity following low- and high-dose IR after receiving glycine betaine as a pre-treatment [336], [337], providing support for further pursuit of this mechanism in IR-induced salivary gland dysfunction as a possible therapeutic target.

This study has several strengths. A major strength is the use of multiple IR time points and multiple analytical methods at each timepoint, thus increasing the confidence in our identified pathways. Using the network-based analysis in our study aided in creating a biological context for the metabolomics output. The animal model is also a strength as it has previously been demonstrated that FVB mice treated with 5 Gy radiation experience a 40-50% reduction in stimulated salivary flow rates beginning at day 3 and continuing through days 30, 60, and 90 following IR treatment [154]. The use of salivary gland tissue instead of serum, blood, or urine for the metabolomics analysis was a strength as it reduced the influence of metabolites released from other tissues and organs on the metabolomics output. Future studies can use isotope tracing to confirm the directionality of metabolic reactions of interest. This data set is a useful resource for salivary gland biologists investigating mechanisms correlated with radiation-induced disfunction as they can mine the data for metabolic pathways related to their studied mechanism.

An inherent challenge in metabolomics is metabolite annotation. Metabolites vary in structure and lack a common building block, making the synthesis of reference standards for identification challenging despite utilization of several databases including KEGG, HMDB, ChemSpider, or PubChem [177], [338]. Thus, the majority of detected signals in untargeted mass spectrometry runs remain unidentified [339]. Another limitation of using solely metabolomics analysis is the biological interpretation of the alterations in individual metabolite levels because the metabolites are not identified as reactants or products in a biochemical reaction. For example, increased levels of glutamine could indicate increased output of glutamine, decreased consumption of glutamine, or increased synthesis of glutamine via shunting from another pathway. Due to the complex interplay of metabolic reactions, metabolic flux cannot be simplified to a unidirectional linear model, thus several biological interpretations of the data are possible.

This study incorporated both structural annotation and metabolite level data to identify metabolic pathways altered in the salivary gland at acute, intermediate, and chronic time points following radiation treatment, with the highest number of metabolic changes observed at the acute damage stage. Further investigation of metabolic changes in glutathione metabolism, amino acid metabolism, and central carbon metabolism in cancer may yield promising therapeutic targets to restore loss of tissue function after radiation treatment during the acute damage response to prevent chronic loss of function in the salivary gland.

IV. Energy Metabolism Alterations in Irradiated Salivary Glands

Authors: Lauren Buss[1], Kirsten H. Limesand[1,2*]

Affiliations:
[1]School of Nutritional Sciences and Wellness, University of Arizona, Tucson, AZ, United States of America
[2]University of Arizona Cancer Center, Tucson, AZ, United States of America

* Corresponding Author
Kirsten H. Limesand
1177 E 4th St, Shantz Building Room 421
Tucson, AZ 85719
limesank@arizona.edu
(520) 626-4517

Keywords: glycolysis, oxidative phosphorylation, ATP production, salivary gland, γ-radiation

Funding: This work was supported in part by NIH R01 grants DE023534 and DE029166 to KHL and NIH F31 grant DE030663-01 to LM.

Conflict of interests: No conflicts of interest, financial or otherwise, were declared by the authors.

Introduction

According to the National Cancer Institute's Unites States (US) Cancer Statistics data, the prevalence of oropharyngeal cancer has increased over the past 20 years in the US with the highest increases observed in older males [340], [341]. With the prevalence rate increasing, the quality of life of head and neck cancer (HNC) patients is becoming increasingly important to address as the number of cancer survivors continues to grow due to improvements in diagnosis and treatment [342], [343]. Human papillomavirus (HPV)-associated HNC cases have increased as smoking-associated HNC cases have decreased, and HPV-associated HNC patients display significantly increased progression-free survival compared to smoking-associated HNC cancer patients [344], [343], [3]. Although HPV-associated HNC patients exhibit increased long-term survival, they still experience adverse side effects associated with radiation therapy (IR), which is the standard of care for approximately 80% of HNC patients [345], [44]. The salivary gland is a nearby organ in HNC patients that is damaged by IR, resulting in hyposalivation, mucositis, xerostomia, malnutrition, and dental caries [13], [12], [346]. The majority of HNC patients exhibit xerostomia (70-80%) that lasts chronically, which negatively affects their quality of life [13], [12], [346]. Xerostomia is typically managed with topical saliva substitutes or cholinergic drugs that stimulate saliva production such as pilocarpine and cevimeline, but they only temporarily manage the symptoms and cholinergic agents have been reported to produce unpleasant side effects such as sweating and gastrointestinal distress [345], [12], [347]. Treatments are needed to restore function to the salivary gland itself to treat xerostomia in HNC patients, therefore more mechanistic understanding of radiation-induced salivary gland damage is needed to identify therapeutic drug targets to restore tissue function.

Energy metabolism is a well-studied mechanism that is necessary to produce ATP, amino acids, and fatty acid intermediates to fuel biosynthetic processes within cells to restore damaged tissue. The association between aberrant energy metabolism and disease has been established in type II diabetes mellitus, cancer, aging, and organ fibrosis [348], [349], [350], [351]. The classic example of metabolic reprogramming in cancer cells, termed the Warburg effect, is an increase in anaerobic ATP production through glycolysis instead of an increase in aerobic oxidative phosphorylation due to impaired mitochondrial function [352]. In HNC, glycolysis is elevated to fuel tumor cell proliferation and glycolytic inhibition leads to increased radiosensitivity of the tumor cells [353]. In the wound-healing response, glycolytic activity is observed to increase quickly to synthesize ATP and generate carbon backbones for macromolecule synthesis in stem cells, muscle tendons, endothelial cells, and epithelial cells [354], [355], [356], [357]. We previously integrated transcriptomic and metabolomic analysis and identified enrichment of energy metabolism at day 5 post-radiation treatment in the parotid gland of mice [315], however, the effect of IR on glycolysis in the salivary gland has not been studied, which may uncover a new mechanism for restoring tissue function. Following IR treatment, the acinar cells in the parotid salivary gland increase compensatory proliferation starting at day 5 and this increase is sustained chronically [117], [153], [11]. The significance of this compensatory proliferation is that it is correlated with loss of function of the tissue [11], therefore it is essential to investigate if glycolysis is a mechanism driving this sustained compensatory proliferation.

Investigating the role of glycolysis in IR-induced salivary gland dysfunction necessitates the exploration of the role of mitochondrial function in this damaged state. Historically, the focus of IR effects has been on the nucleus for DNA damage as the primary detrimental contributor [358], [359]. The mitochondrion is the only other organelle that contains coding DNA, and control of mitochondrial DNA (mtDNA) copy number, the number of multiple copies of mtDNA in each cell, is essential for normal cell function [360], [361]. An increase in mtDNA copy number (polyploidization) was observed in the brain and spleen cells of mice exposed to 3 Gy IR, and this increase in mtDNA copy number following IR is believed to be an adaptive repair response when mitochondrial function is reduced due to reactive oxygen species (ROS) damage [362]. It has been established that ROS increases acutely in the mitochondria of irradiated salivary gland acinar cells [170], but the effect of IR on mtDNA copy number in salivary glands is not established. Although mtDNA copy number polyploidization has been observed following IR, the effects of this process are not understood, specifically on mitochondrial oxidative phosphorylation. Improper electron transport chain function in the mitochondria is an indicator of mitochondrial dysfunction [289], [290], [291]. In our previous work, we identified reductions in NAD+, UQCR, NDUF, COX, ATP5, and MT-ND family members in the salivary gland five days following 5 Gy IR targeted to the head and neck region, and the products of these genes function within complexes I, III, IV, and V of the electron transport chain [315]. The purpose of this study was to investigate changes in energy metabolism and mitochondrial function over time in the parotid salivary glands of mice following a single 5 Gy dose targeted to the head and neck region. We hypothesized that IR would increase glycolysis and decrease mitochondrial oxidative phosphorylation as a response to mitochondrial damage, and that this modulation may be a factor contributing to the radiosensitivity of the salivary gland.

Materials and Methods

Mice and ethics statement

Female FVB/NJ mice (wild type; stock no. 001800) were purchased from Jackson Laboratories (Bar Harbor, ME). No differences in phenotype have been observed between sexes [153], [124]. All mice were housed and maintained in accordance with the University of Arizona Institutional Animal Care and Use Committee. All protocols were approved by the Institutional Animal Care and Use Committee.

Radiation treatment

Mice: Four- to eight-week-old female FVB mice were sedated via intraperitoneal injection of a ketamine-xylazine mixture (70 mg/kg-10 mg/ml) before irradiation. Mice were then constrained in 50-ml conical tubes and shielded with >6 mm lead with only their head and neck region exposed to a single dose of 5 Gy irradiation (X-ray, RS 2000 Small Animal Irradiator, Rad Source).

Primary cells: Primary cells isolated from parotid salivary glands were plated on an Agilent Seahorse XF96 Cell Culture Microplate (Part No. 101085-004, Agilent Technologies, Cedar Creek, TX) and cultured prior to irradiation at 24 hours or 48 hours before running the Seahorse ATP Rate Assay. Cells were exposed to a single dose of 5 Gy irradiation (X-ray, RS 2000 Small Animal Irradiator, Rad Source). The untreated cells were shielded with >6 mm lead.

Primary cell culture

Parotid glands were removed from four-eight-week-old female FVB mice, minced for 2 minutes, and added to a siliconized Erlenmeyer flask with 30 mL dispersion media (Hank's salt solution, 1 mg/ml collagenase, and 1mg/ml hyaluronidase, pH 7.4). Cells were incubated in a shaking water bath at 37°C for 1 hour with mechanical agitation at 40, 45, 50, 55, and 60 min. Cells were then centrifuged, resuspended in wash media [modified Hank's solution containing CaCl2 and 0.2% (wt/vol) BSA], recentrifuged, and resuspended again. The suspension was run through a sterile funnel filter, recentrifuged, and suspended in primary cell culture media: DMEM/F12 containing (in wt/vol except where noted) gentamycin (0.5%; Fisher Scientific), fungizone (0.2%; Invitrogen), hydrocortisone (0.04%; Sigma-Aldrich), EGF (0.4%; Fisher Scientific), insulin (0.125%; Invitrogen), transferrin (0.125%, Invitrogen), retinoic acid (0.05%; Sigma-Aldrich), glutamine (1.25%; Invitrogen), nonessential amino acids (1%; Invitrogen), trace elements (1%; Fisher Scientific), and fetal bovine serum (5% vol/vol; Fisher Scientific). Cells were plated on an Agilent Seahorse XF96 Cell Culture Microplate (Part No. 101085-004, Agilent Technologies, Cedar Creek, TX) that was manually coated with 50 ug/mL rat tail collagen I (Ref. no. A10483-01, Gibco, Grand Island, NY) prior to cell plating. The cells sat for 1 hour at room temperature prior to placement in the 37°C/5% CO_2 incubator for culture. Three mice supply an adequate number of cells for a single treatment group on one Seahorse microplate, with 1-3 treatment groups on a single microplate. One microplate from each independent primary cell culture preparation is considered a replicate for Seahorse assays involving the use of primary cells.

Seahorse XF Real-Time ATP Rate Assay

Acute IR time points: Primary acinar cells were isolated (see previous methods) from parotid salivary glands of untreated female FVB mice (n=6/plate) and plated on a 96-well collagen-coated Seahorse microplate at a seeding density of 150K/well. Optimization of seeding density and time in culture was performed prior to experimental runs. The effect of collagen on total protein concentration was determined as this was the normalization method for the extracellular acidification rate (ECAR) and oxygen consumption rate (OCR) data and showed to be non-significant (Supplemental Figure S1; for all supplemental material, use the Zenodo link provided in the Supplemental Data section of the Methods). Cells were cultured for 5 days and irradiated at 24 and 48 hours prior to the assay (Supplemental Figure S2). Cell culture media was removed and replaced with fresh media every 48 hours. One hour prior to running the assay, cell culture media was replaced with assay media (Seahorse XF DMEM medium pH 7.4, Cat. No. 103575-100, Agilent Technologies, Cedar Creek, TX, supplemented with 1 mM pyruvate, 2 mM glutamine, and 10 mM glucose) and incubated at 37°C. The XF Real-Time ATP Rate Assay Kit (Cat. No. 103592-100, Agilent Technologies, Cedar Creek, TX) was performed according to the manufacturer's protocol using the Seahorse XF96 Analyzer (Agilent Technologies, Cedar Creek, TX). Optimization of drug concentrations was performed prior to experimental runs. Oligomycin (2uM) was injected into the cell media to inhibit ATP synthase and a mixture of rotenone and antimycin A (0.5uM) was injected into the cell media to inhibit Complex I and III, respectively, of the electron transport chain. Basal ATP production rates were calculated using the Seahorse XF Real-Time ATP Rate Assay Kit Report Generator (Wave Desktop Software, Agilent Technologies, Cedar Creek, TX). Briefly, glycolytic ATP production is calculated from the glycolytic proton efflux rate (PER), which is calculated from the ECAR data, while mitochondrial ATP production is calculated from the OCR data [363]. Data are presented as ECAR, OCR, and basal ATP production rate normalized to protein concentration. Protein content was determined using the bicinchoninic acid (BCA) assay.

Day 5 and chronic IR time points: Female FVB mice received 5 Gy IR targeted to the head and neck region (n=3/group) and primary acinar cells were isolated from parotid salivary glands of UT and IR mice at day 5, day 30, and day 60 post-IR. Cells were seeded on a 96-well collagen-coated Seahorse microplate at a seeding density of 150K/well and cultured for 2 days (optimization of time in culture was determined prior to experimental assays). On day 2 the XF Real-Time ATP Rate Assay Kit (Cat. No. 103592-100, Agilent Technologies, Cedar Creek, TX) was run following the manufacturer's protocol using the Seahorse XF96 Analyzer as described above.

Western Blotting

Whole protein lysates from parotid glands of female FVB mice were harvested and processed for immunoblotting as previously described [153], [148]. The Coomassie Plus-The Better Bradford Assay (Thermo) was used to determine protein concentrations and 50ug total lysate was loaded onto a 10% polyacrylamide gel, transferred to an Immobilon PDVF membrane (Millipore, Bedford, MA), and blocked in 5% nonfat milk in Tris-buffered saline-Tween 20 (1X TBST). The following antibodies were used: anti-hexokinase isoform 1 (HK1) (Product no. C35C4, Cell Signaling), anti-muscle phosphofructokinase (PFKM) (Cat. No. 55028-1-AP, Proteintech), anti-muscle pyruvate kinase isoform 1 (PKM1) (Product no. D30G6, Cell Signaling), anti-complex I – 75 kDa subunit (ABN302, EMD Millipore), anti-complex III ubiquinol-cytochrome C reductase core protein 2 (UQCRC2) subunit (Cat. No. 14742-1-AP, Proteintech), and anti-extracellular signal-regulated protein kinases 1/2 (ERK1/2) (p44/42 MAPK, Cell Signaling). For detection, ECL substrate (Thermo Scientific) or SuperSignal West Pico Chemiluminescent Substrate (Thermo Scientific) was used. Restore Western Blotting Stripping Buffer (Fisher) was used to strip the membrane, re-block with 5% nonfat milk in 1X TBST, and re-probe for the loading control ERK1/2. Densitometry was performed using ImageJ software (NIH).

Enzyme Activity Assays

A split-sample approach was used for the enzyme activity assays. From the same mouse sample, one parotid salivary gland was analyzed using the hexokinase assay kit (ab136957, Abcam, Cambridge, UK) and the second parotid salivary gland was analyzed using the pyruvate kinase activity assay kit (cat. No. MAK072, Sigma-Aldrich, St. Louis, MO). For both activity assays, the samples were plated on a 96-well plate at a concentration of 10 ng/uL/well. Luminescence readings were measured every 5 minutes for a total period of 60 minutes to calculate enzymatic activity following the manufacturer's protocols.

Lactate Assay

A pair of parotid salivary glands were harvested from each mouse and directly placed in 500 uL of Lactate Assay Buffer from the L-Lactate Assay Kit (ab65331, Abcam, Cambridge, UK), 10 uL of protease inhibitor (PI) cocktail for mammalian cells (cat # P8340, Sigma-Aldrich, St. Louis, MO) and 5 uL of 100 mM phenylmethylsulfonyl fluoride (PMSF). Samples were homogenized and deproteinated prior to the assay following the manufacturer's protocol. For the assay, 30 uL of sample was added to a well for a single replicate. Lactate concentration was measured following the manufacturer's protocol (ab65331, Abcam, Cambridge, UK).

Quantitative real-time polymerase chain reaction (qRT-PCR)

Parotid glands were removed from mice and total DNA was immediately isolated using the DNeasy Blood & Tissue Kit (Ref. No. 69504, Qiagen, Hilden, Germany). DNA samples were diluted with nuclease-free water to a concentration of 10 ng/uL. For quantitative (q) PCR, samples were analyzed in triplicate for each DNA sample (five mice per condition) with an iQ5 Real-Time PCR Detection System (Bio-Rad). Master mixes were prepared as follows: 5 μl of diluted DNA, 2 μl of the forward and reverse primers, 7.5 μl of SYBR Green (Qiagen), and 0.5

μl nuclease-free water to a final volume of 15 μl. Forty cycles of PCR were performed (95°C for 15 s, 54°C for 30 s, 72°C for 30 s); fluorescence detection occurred during the 72°C step at each cycle. The data were analyzed using the 2-ΔΔCT method [364]. Results were normalized to S15, which remains unchanged in response to treatment, and graphed as fold change in comparison to untreated. The following primers were purchased from Integrated DNA Technologies (Coralville, IA): *S15* (ribosomal protein S15; Forward: 5′-ACT ATT CTG CCC GAG ATG GTG-3′; Reverse: 5′-TGC TTT ACG GGC TTG TAG GTG-3′), *COX2* (cyclooxygenase-2; Forward: 5′-ATA ACC GAG TCG TTC TGC CAA T-3′; Reverse: 5′-TTT CAG AGC ATT GGC CAT AGA A-3′), *Rsp18* (ribosomal protein S18; Forward: 5′-TGT GTT AGG GGA CTG GTG GAC A-3′; Reverse: 5′-CAT CAC CCA CTT ACC CCC AAA A-3′), *HK2* (hexokinase 2; Forward: 5′-GCC AGC CTC TCC TGA TTT TAG TGT-3′; Reverse: 5′-GGG AAC ACA AAA GAC CTC TTC TGG-3′), and *ND1* (NADH:Ubiquinone Oxidoreductase Core Subunit 1; Forward: 5′-CTA GCA GAA ACA AAC CGG GC-3′; Reverse: 5′-CCG GCT GCG TAT TCT ACG TT-3′.

Mitochondrial DNA (mtDNA) Copy Number

Total DNA was extracted from mouse parotid gland tissue following the manufacturer’s protocol for DNeasy Blood & Tissue Kit (Ref. No. 69504, Qiagen, Hilden, Germany). Mitochondrial DNA (mtDNA) copy number was measured by assessing the relative levels of mitochondrial gene targets *COX2* and *ND1* to genomic DNA (gDNA) targets *Rsp18* and *HK2* [365], [366] in extracts of total DNA using qRT-PCR analysis as described above.

Seahorse XF Mito Fuel Flex Test and Cell Mito Stress Test

Female FVB mice received 5 Gy IR targeted to the head and neck region (n=3/group) and primary acinar cells were isolated from parotid salivary glands of UT and IR mice at day 5 post-

IR. Cells were seeded on a 96-well collagen-coated Seahorse plate at a seeding density of 150K/well and cultured for 2 days. One hour prior to running the assay, cell culture media was replaced with assay media (Seahorse XF DMEM medium pH 7.4, Cat. No. 103575-100, Agilent Technologies, Cedar Creek, TX, supplemented with 1 mM pyruvate, 2 mM glutamine, and 10 mM glucose) and incubated at 37°C.

Mito Fuel Flex Test: The Seahorse XF Mito Fuel Flex Test Kit (Cat. No. 103260-100, Agilent Technologies, Cedar Creek, TX) was performed according to the manufacturer's protocol using the Seahorse XF96 Analyzer (Agilent Technologies, Cedar Creek, TX). UK5099 (2 uM) was injected into the cell media to inhibit glucose oxidation, BPTES (3 uM) was injected into the cell media to inhibit glutamine oxidation, and Etomoxir (4 uM) was injected into the cell media to inhibit long-chain fatty acid oxidation. The order of inhibitor injections and inhibitor combinations allowed the calculation of fuel dependency (glucose, glutamine, and long-chain fatty acids) and the calculation of the capability of the cells to use alternate fuel sources. Fuel flexibility was calculated using the Seahorse XF Mito Fuel Flex Test Report Generator (Wave Desktop Software, Agilent Technologies, Cedar Creek, TX) and data is presented as oxygen consumption rate (OCR) normalized to protein concentration. Protein content was determined using the BCA assay.

Cell Mito Stress Test: The Seahorse XF Cell Mito Stress Test Kit (Cat. No. 103015-100, Agilent Technologies, Cedar Creek, TX was performed according to the manufacturer's protocol using the Seahorse XF96 Analyzer (Agilent Technologies, Cedar Creek, TX). FCCP concentration was optimized prior to the experimental runs. Oligomycin (2uM) was injected into the cell media to inhibit ATP synthase, carbonyl cyanide-4 (trifluoromethoxy) phenylhydrazone (FCCP) (2uM) was injected into the cell media to uncouple electron transport from ATP production in the electron transport chain, and a mixture of rotenone and antimycin A (0.5uM) was injected into the cell media to inhibit Complex I and III, respectively, of the electron transport chain. Spare respiratory capacity was calculated using the Seahorse XF Cell Mito Stress Test Report Generator (Wave Desktop Software, Agilent Technologies, Cedar Creek, TX) and data is presented as oxygen consumption rate (OCR) normalized to protein concentration. Protein content was determined using the BCA assay.

Statistics

Data were analyzed using Prism 6.04 (GraphPad, La Jolla, CA). All values are reported as means ± standard error (SE) of at least three independent experiments unless denoted otherwise. Statistical tests were two-sided and differences between more than two group means were evaluated using the one-way analysis of variance (ANOVA) test and Bonferroni post-hoc multiple comparison test with significant differences at $p < 0.05$. Differences between two group means were evaluated using two-sided unpaired T-tests with significant differences at $p < 0.05$. Treatment groups with the same letter are not statistically different from each other.

Supplemental Data

All supplemental data can be accessed using the following link to Zenodo; https://doi.org/10.5281/zenodo.7776238.

Results

Cellular bioenergetics of acute irradiated salivary gland acinar cells

Measurements of the extracellular acidification rate (ECAR) and oxygen consumption rate (OCR) of live cells qualitatively reflects glycolysis and mitochondrial respiration, respectively [367], [368], [369]. To understand the effect of radiation on cellular energy production in the salivary gland, the Seahorse XF Real-Time ATP Rate Assay Kit [363] was performed to collect ECAR and OCR data in salivary gland primary acinar cells and calculate baseline ATP production rates at acute (24 and 48 hours) radiation (IR) time points. The use of primary cells is necessary as immortalized cells disrupt p53 function and it has previously been established that increased apoptosis in parotid acinar cells following radiation is p53 dependent [114], [115]. Therefore, we need p53 signaling to remain intact to study the radiation-damage response. Between 8-72 hours following IR, apoptosis of acinar cells occurs with a peak occurring at 24 hours post-IR, and reactive oxygen species levels increase starting at 24 hours post-IR [114], [320], [170], therefore 24 and 48 hours post-IR were chosen as acute IR time points in this study. Basal ECAR and OCR data was first collected, and then oligomycin was injected into the cell media to inhibit mitochondrial ATP production and allow the ATP production rate attributed to mitochondrial oxidative phosphorylation production to be quantified [363]. Injection of rotenone plus antimycin A completely inhibits mitochondrial respiration, which accounts for mitochondrial-associated acidification, and is used with ECAR to calculate the ATP production rate attributed to glycolysis [363].

At baseline readings, 24-hour IR ECAR measurements are significantly higher compared to untreated and 48-hour IR (Fig. 4.1A,B). Following oligomycin and rotenone/antimycin A injections, 24-hour IR ECAR measurements remain significantly higher compared to untreated and 48-hour IR, with the 48-hour IR readings decreasing slightly compared to untreated (Fig. 4.1A,B). At baseline readings, 24-hour IR OCR measurements are significantly higher than untreated and 48-hour IR OCR measurements are significantly lower compared to untreated (Fig. 4.1C,D). Following oligomycin and rotenone/antimycin A injections, the 24-hour IR OCR measurements decrease but are still higher compared to the 48-hour IR and untreated OCR measurements and the 48-hour IR and untreated OCR readings are not significantly different from each other (Fig. 4.1C,D). Calculation of the basal ATP production rates reveals a significantly higher ATP production rate in the 24-hour IR group compared to untreated and 48-hour IR groups (Fig. 4.1E), with the 24-hour IR group displaying a higher glycolytic ATP production compared to both the untreated and 48-hour IR groups (Fig.4.1F). Acutely, we observe an increase in ECAR, OCR, and ATP production rate at 24 hours post-IR that is attenuated at 48 hours post-IR.

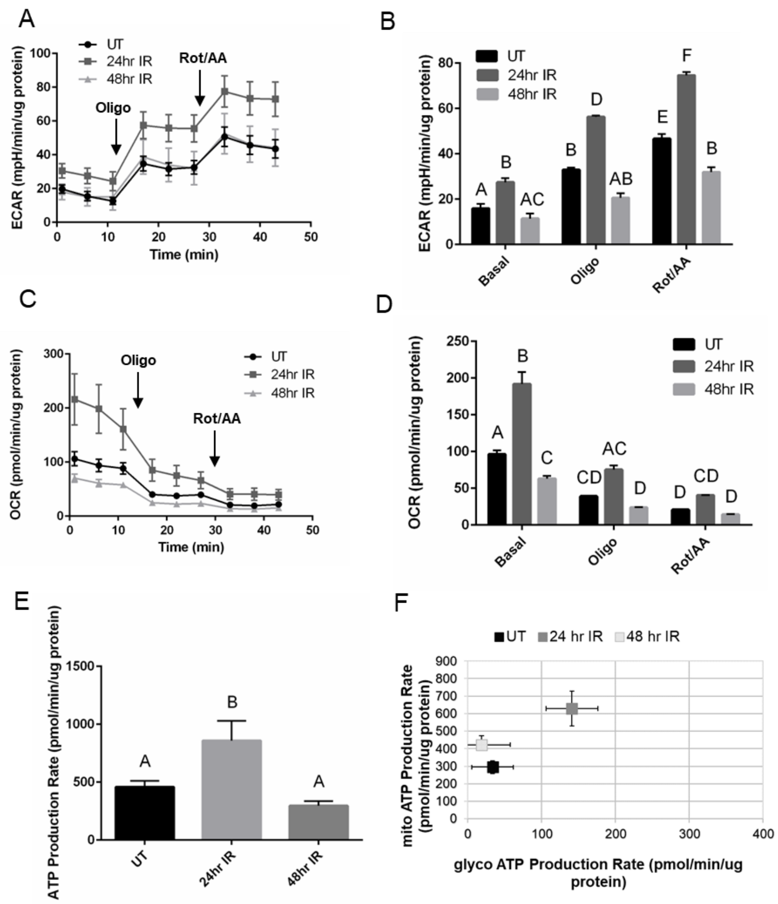

Figure 4.1. ECAR, OCR, and ATP production rate increase acutely at 24-hours following radiation in salivary acinar cells.

Primary acinar cells were isolated from parotid salivary glands of untreated female FVB mice (n=6/plate) and plated on a 96-well collagen-coated Seahorse microplate at a seeding density of 150K/well. Cells were cultured for 5 days and irradiated at 24 and 48 hours prior to the assay. The Seahorse XF Real-Time ATP Rate Assay Kit was performed using the Seahorse XF96 Analyzer. A) Individual ECAR readings for untreated (UT), 24-hour IR (24hr IR), and 48-hour IR (48hr IR) groups with the responses to 2.0uM oligomycin (oligo) injection and 0.5uM rotenone/antimycin A (rot/AA) injection shown. B) Average basal, oligo, and rot/AA ECAR readings for UT, 24hr IR, and 48hr IR. C) Individual OCR readings for UT, 24hr IR, and 48hr IR groups with the responses to 2.0uM oligomycin (oligo) injection and 0.5uM rotenone/antimycin A (rot/AA) injection shown. D) Average basal, oligo, and rot/AA OCR readings for UT, 24hr IR, and 48hr IR. E) Basal ATP production rates of UT, 24hr IR, and 48hr IR groups. F) The proportion of mitochondrial (mito) ATP production rate and glycolytic (glyco) ATP production rate for UT, 24hr IR, and 48hr IR groups. Each panel is representative of 3 independent assays (n=3/group). Significant differences were determined using one-way ANOVA and Bonferroni post-hoc test, $p<0.05$. Treatment groups with the same letter are not significantly different from each other.

Cellular bioenergetics of transitional and chronic irradiated salivary gland acinar cells

Due to the observed changes in ECAR, OCR, and basal ATP production at acute time points following IR, we decided to further investigate acinar cell bioenergetics at day 5, day 30, and day 60 following IR. Day 5 post-IR was chosen as a transitional time point where increased compensatory proliferation and decreased apical/basolateral polarity in the acinar compartment of the salivary gland begins following loss of function starting at day 3 post-IR [153], [154], [157], [125]. We have previously observed chronic loss of salivary gland function correlated with decreased acinar cell differentiation markers and continued compensatory proliferation at days 30, 60, and 90 post-IR [136], [154], [153], therefore days 30 and 60 were chosen as representative chronic IR time points. At baseline readings, day 5 IR ECAR measurements are higher compared to untreated (Fig. 4.2A,B), and following rotenone/antimycin A injection the increase becomes statistically significant (Fig. 4.2A,B). At baseline readings, day 5 IR OCR measurements are significantly higher than untreated (Fig. 4.2C,D). Following oligomycin and rotenone/antimycin A injections, day 5 IR OCR measurements remain higher compared to untreated (Fig. 4.2C,D). Calculation of the basal ATP production rates shows a significantly higher ATP production rate in the day 5 IR group compared to untreated (Fig. 4.2E), with the day 5 IR group displaying a higher mitochondrial ATP production rate compared to the untreated group (Fig.4.2F).

Cellular bioenergetics change sharply at chronic IR time points. At baseline readings, day 30 and day 60 IR ECAR measurements are lower compared to untreated with the day 30 IR group showing a statistically significant decrease (Fig. 4.2G,H). Following oligomycin and rotenone/antimycin A injections, day 30 and day 60 IR ECAR readings continue to remain lower compared to untreated (Fig. 4.2G,H). At baseline readings, day 30 and day 60 OCR measurements are significantly decreased compared to untreated and remain significantly decreased following oligomycin and rotenone/antimycin A injections (Fig. 4.2I,J). Visual inspection of the cells prior to running the assay confirmed viability to ensure that the low OCR cell readings are not due to cell death (Supplemental Figure S3; for all supplemental material, use the Zenodo link provided in the Supplemental Data section of the Methods). Calculation of the basal ATP production rates reveals a significantly lower ATP production rate in the day 30 and day 60 IR groups compared to untreated (Fig. 4.2K), with the day 30 and day 60 IR groups displaying a lower mitochondrial ATP production rate compared to the untreated group (Fig.4.2L). Thus, ECAR, OCR, and ATP production rate increase at day 5 IR and then subsequently decrease chronically following radiation.

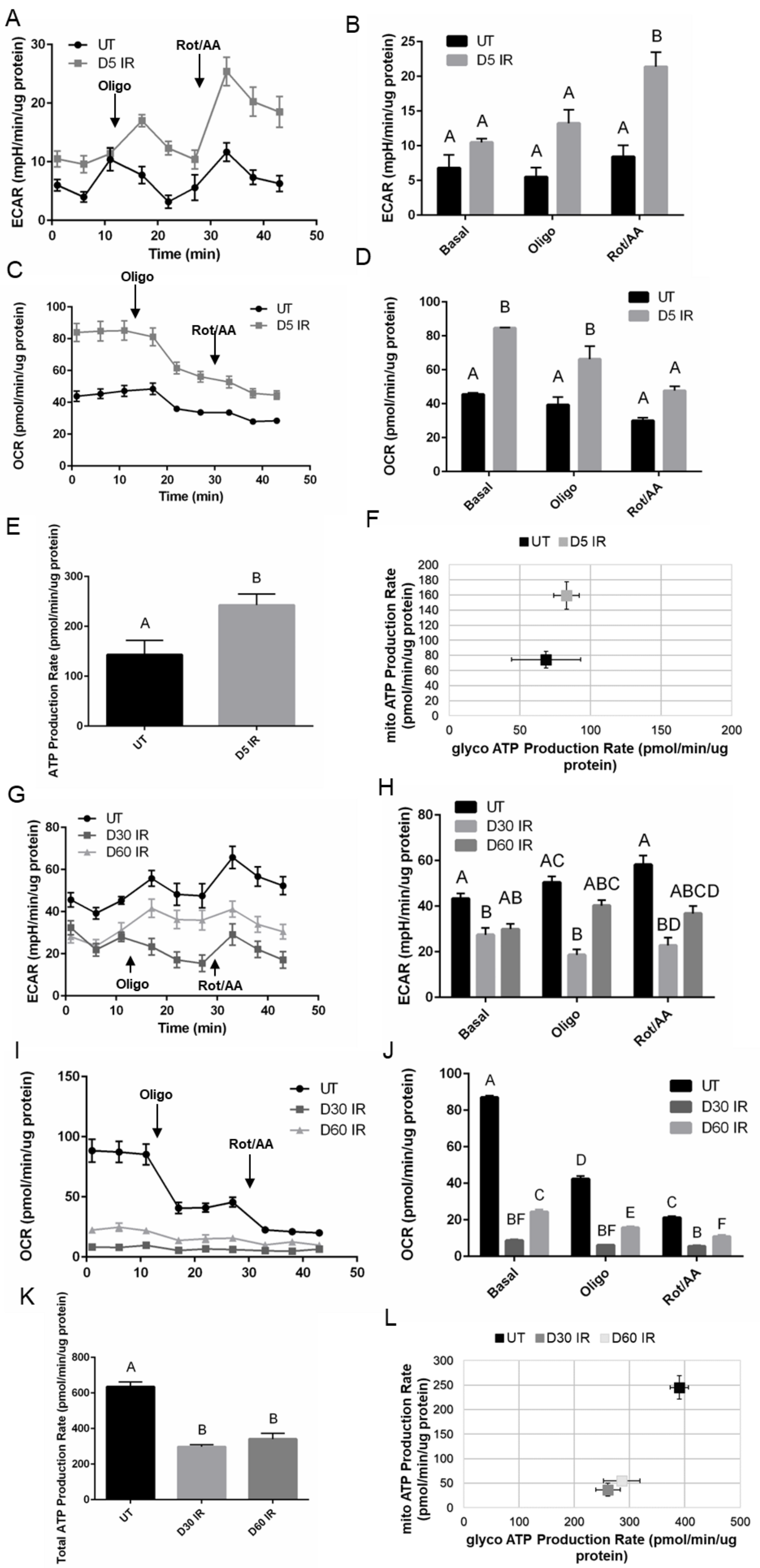
A
UT
D5 IR
Oligo
Rot/AA
ECAR (mpH/min/ug protein)
Time (min)
B
UT
D5 IR
ECAR (mpH/min/ug protein)
Basal
Oligo
Rot/AA
C
Oligo
Rot/AA
UT
D5 IR
OCR (pmol/min/ug protein)
Time (min)
D
UT
D5 IR
OCR (pmol/min/ug protein)
Basal
Oligo
Rot/AA
E
ATP Production Rate (pmol/min/ug protein)
UT
D5 IR
F
UT
D5 IR
mito ATP Production Rate (pmol/min/ug protein)
glyco ATP Production Rate (pmol/min/ug protein)
G
UT
D30 IR
D60 IR
Oligo
Rot/AA
ECAR (mpH/min/ug protein)
Time (min)
H
UT
D30 IR
D60 IR
ECAR (mpH/min/ug protein)
Basal
Oligo
Rot/AA
I
Oligo
Rot/AA
UT
D30 IR
D60 IR
OCR (pmol/min/ug protein)
J
UT
D30 IR
D60 IR
OCR (pmol/min/ug protein)
Basal
Oligo
Rot/AA
K
Total ATP Production Rate (pmol/min/ug protein)
UT
D30 IR
D60 IR
L
UT
D30 IR
D60 IR
mito ATP Production Rate (pmol/min/ug protein)
glyco ATP Production Rate (pmol/min/ug protein)

Figure 4.2. ECAR, OCR, and ATP production increase at 5 days and decrease chronically following radiation in salivary acinar cells.

Female FVB mice received 5 Gy IR targeted to the head and neck region (n=3/group) and primary acinar cells were isolated from parotid salivary glands of untreated (UT) and IR mice at day 5, day 30, and day 60 post-IR. Cells were seeded on a 96-well collagen-coated Seahorse microplate at a seeding density of 150K/well and cultured for 2 days. On day 2 of culture the Seahorse XF Real-Time ATP Rate Assay Kit was run using the Seahorse XF96 Analyzer. A) Individual ECAR readings for untreated UT and day 5 IR (D5 IR) groups with the responses to 2.0uM oligomycin (oligo) injection and 0.5uM rotenone/antimycin A (rot/AA) injection shown. B) Average basal, oligo, and rot/AA ECAR readings for UT and D5 IR. C) Individual OCR readings for UT and D5 IR groups with the responses to 2.0uM oligomycin (oligo) injection and 0.5uM rotenone/antimycin A (rot/AA) injection shown. D) Average basal, oligo, and rot/AA OCR readings for UT and D5 IR. E) Basal ATP production rates of UT and D5 IR groups. F) The proportion of mitochondrial (mito) ATP production rate and glycolytic (glyco) ATP production rate for UT and D5 IR groups. G) Individual ECAR readings for UT, day 30 IR (D30 IR), and day 60 IR (D60 IR) groups with the responses to 2.0uM oligomycin (oligo) injection and 0.5uM rotenone/antimycin A (rot/AA) injection shown. H) Average basal, oligo, and rot/AA ECAR readings for UT, D30 IR, and D60 IR. I) Individual OCR readings for UT, D30 IR, and D60 IR groups with the responses to 2.0uM oligomycin (oligo) injection and 0.5uM rotenone/antimycin A (rot/AA) injection shown. J) Average basal, oligo, and rot/AA OCR readings for UT, D30 IR, and D60 IR. K) Basal ATP production rates of UT, D30 IR, and D60 IR groups. L) The proportion of mitochondrial (mito) ATP production rate and glycolytic (glyco) ATP production rate for UT and D5 IR groups. Each panel is representative of 3 independent assays (n=3/group). Significant differences were determined using one-way ANOVA and Bonferroni post-hoc test, $p<0.05$. Treatment groups with the same letter are not significantly different from each other.

Glycolytic enzyme levels and activity in irradiated salivary glands

After identifying changes in cellular ECAR both acutely and chronically in response to radiation treatment, we sought to further investigate glycolytic flux in salivary gland tissue at multiple IR time points. To investigate the key metabolic enzymes that drive glycolysis, protein levels and enzymatic activity of rate-limiting enzymes were measured in salivary gland tissue as enzymatic activity is an established technique to assess glycolysis [370]. Western blot analysis of the first glycolytic enzyme, hexokinase (HK1-isoform found in the salivary glands), reveals statistically higher levels of the protein at day 3 IR compared to untreated, day 5 IR, and day 30 IR (Fig. 4.3A,B). No differences in protein levels of phosphofructokinase (PFKM-isoform found in salivary glands) and pyruvate kinase (PKM1-isoform found in salivary glands) are observed between the untreated and IR groups. The enzymatic activity of hexokinase measured over 60 minutes is higher in the day 3 IR group compared to untreated, day 5 IR, day 14 IR, and day 30 IR groups (Fig. 4.3C). The enzymatic activity of pyruvate kinase measured over 60 minutes is higher in the day 30 IR group compared to all other groups but is not statistically significant (Fig. 4.3D). Lactate is produced from pyruvate, the end product of glycolysis, under anaerobic conditions when pyruvate is not transported into the mitochondria to proceed to aerobic mitochondrial respiration [371]. The lactate concentration of irradiated salivary gland tissue reveals significantly higher levels at day 5 IR and day 14 IR compared to untreated (Fig. 4.3E).

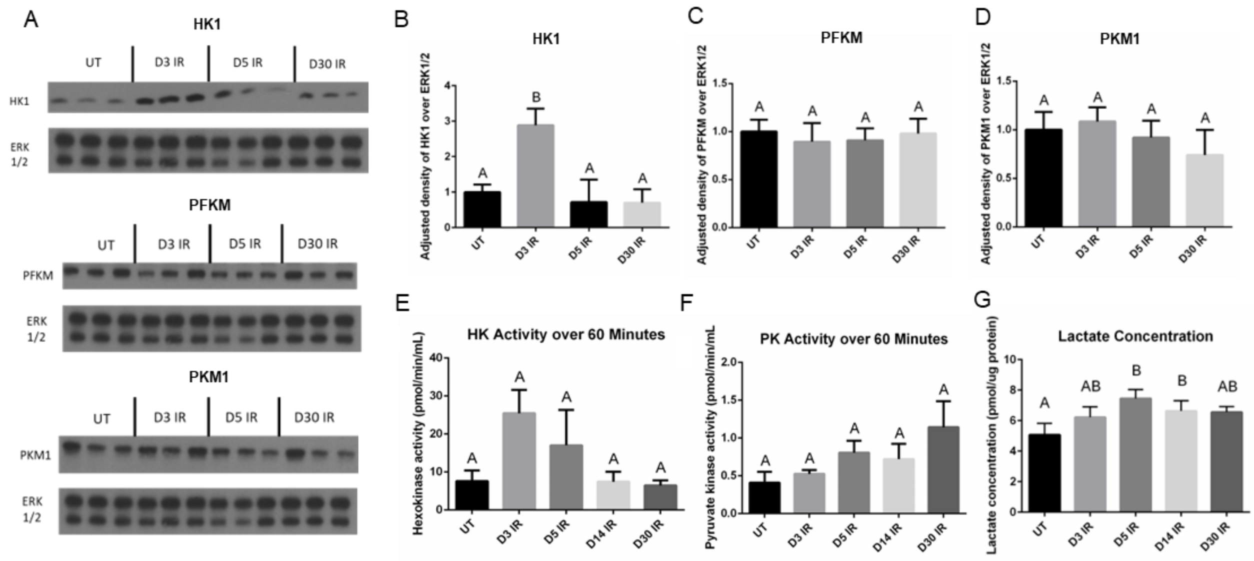

Figure 4.3. Glycolytic hexokinase protein levels and enzymatic activity increase at day 3 following radiation and lactate concentration increases at day 5 and day 14 following radiation in the salivary gland.

Female FVB mice were untreated (UT) or exposed to IR and parotid salivary glands were removed at 3 (D3 IR), 5 (D5 IR), 14 (D14 IR), and 30 (D30 IR) days after radiation treatment. A) Representative western blots probing for hexokinase 1 (HK1), phosphofructokinase-muscle (PFKM), and pyruvate kinase muscle isozyme-1 (PKM1) using untreated, D3 IR, D5 IR, and D30 tissue samples (n=3/group). Extracellular signal-regulated kinase 1/2 (ERK 1/2) was used as a loading control. B-D) Quantification of (A). E) A hexokinase enzyme activity assay was performed on tissue samples (n=4/group) and activity was measured over 60 minutes. F) A pyruvate kinase enzyme activity assay was performed on tissue samples (n=4/group) and activity was measured over 60 minutes. G) A lactate assay kit was used to measure lactate concentration in tissue samples (n=5/group). Data are presented as mean ± standard error of the mean (SEM). Significant differences were determined using one-way ANOVA and Bonferroni post-hoc test, $p<0.05$. Treatment groups with the same letter are not significantly different from each other.

Mitochondrial function in irradiated salivary glands

Due to the observed changes in OCR at acute and chronic time points in irradiated salivary gland acinar cells, we further investigated mitochondrial function in salivary gland tissue. In our previous work, we observed significant decreases in transcript families belonging to the core subunit of Complex I in the mitochondrial electron transport chain (*NDUF* and *MT-ND*), and in transcript families belonging to various subunits of Complex III (*UQCR*, *CYC1*, and *MT-CYB*) at day 5 IR in parotid salivary gland tissue [315]. Therefore, we measured protein levels of Complex I-75 kDa subunit and of UQCRC2, a subunit of Complex III. We observe a significant decrease in Complex I-75 kDa subunit at day 5-IR compared to untreated (Fig. 4.4A,B), and we observe a significant decrease in Complex III-UQCRC2 subunit at day 3 IR and day 5 IR (Fig. 4.4C,D). The data suggests a decrease in mitochondrial respiration at day 3 IR and day 5 IR in parotid salivary gland tissue. To further explore the effects of irradiation on mitochondrial function, we measured mitochondrial DNA (mtDNA) copy number. Mitochondrial DNA copy number partially regulates mitochondrial biogenesis, and research has shown increased mtDNA copy number following radiation treatment, which is hypothesized to be an adaptive response to help the remaining cells in the irradiated tissue survive [372], [373], [374]. Although this increase may appear beneficial, it can lead to the overproduction of mitochondrially encoded subunits, which can lead to mitochondrial dysfunction [361]. The relative ratio of a mitochondrial DNA target to a nuclear DNA target gives an estimate of mtDNA copy number. We utilized two different mitochondrial DNA and nuclear DNA targets to increase the reproducibility of our results. Looking at the relative ratio of *COX2* mitochondrial gene target to *Rsp18* genomic gene target, we see a significant increase in the relative ratio of *COX2/Rsp 18* at day 5 IR and day 30 IR compared to untreated, with no significant difference observed at day 3 IR (Fig. 4.4E). Looking at the relative ratio of *ND1* mitochondrial gene target to *HK2* genomic gene target, we observe a significant increase in the relative ratio of *ND1/HK2* at day 30 IR compared to untreated (Fig. 4.4F). At day 3 IR the *ND1/HK2* relative ratio appears to slightly decrease compared to untreated, although this decrease is not significant (Fig. 4.4F). The observed increase in mtDNA copy number suggests mitochondrial dysfunction chronically following radiation in the salivary gland.

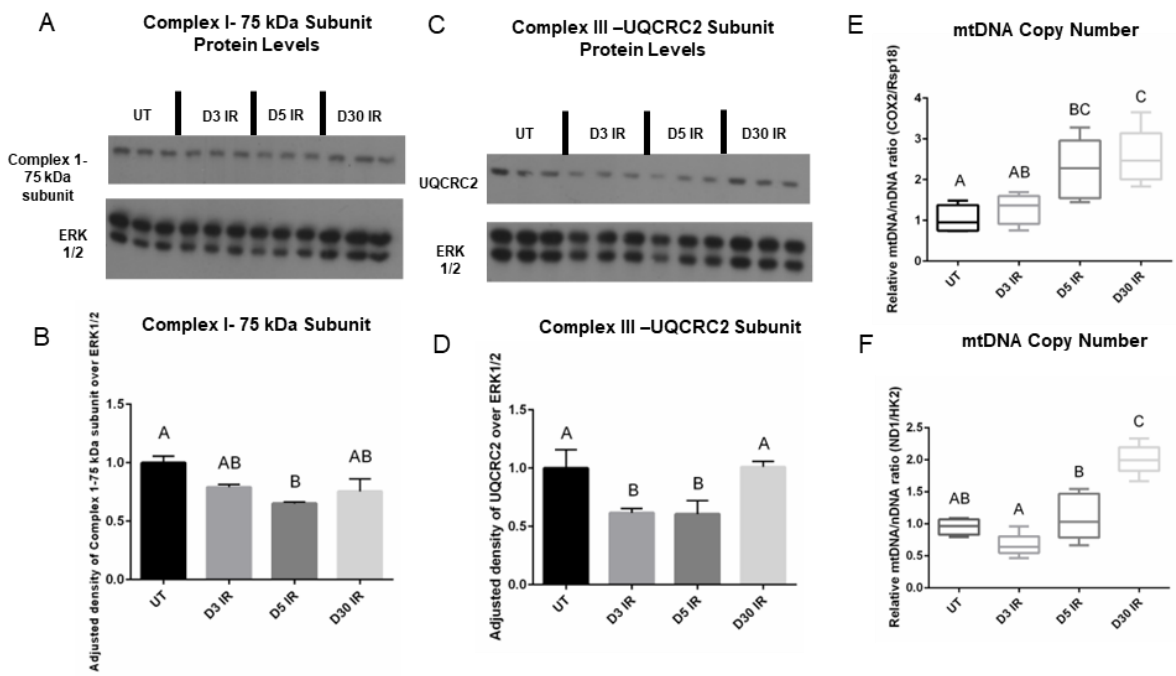

Figure 4.4. Mitochondrial complex I and III protein subunit levels decrease at day 5 following radiation and mitochondrial DNA copy number increases chronically following radiation in the salivary gland.

Female FVB mice were untreated (UT) or exposed to IR and parotid salivary glands were removed at 3 (D3 IR), 5 (D5 IR), and 30 (D30 IR) days after radiation treatment. A) Representative western blot probing for complex I-75 kDa subunit using tissue samples (n=3/group). Extracellular signal-regulated kinase 1/2 (ERK 1/2) was used as a loading control. B) Quantification of (A). Data are presented as mean ± standard error of the mean (SEM). C) Representative western blot probing for ubiquinol-cytochrome-C reductase complex core protein 2 (UQCRC2) using tissue samples (n=3/group). ERK 1/2 was used as a loading control. D) Quantification of (C). Data are presented as mean ± standard error of the mean (SEM). E-F) DNA was isolated from tissue samples (n=5/group) and RT-qPCR was performed with primers specific for the mitochondrial gene cyclooxygenase-2 (*COX2*) and the ribosomal gene ribosomal protein S18 (*Rsp18*) (E), and primers specific for the mitochondrial gene NADH:ubiquinone oxidoreductase core subunit 1 (*ND1*) and the nuclear gene hexokinase 2 (*HK2*) in (F). Data were normalized to 15S ribosomal protein as an internal control and fold change was calculated relative to DNA content in UT mice. Mitochondrial DNA (mtDNA) copy number was estimated using the ratio of *COX2/Rsp18* DNA content (E) and the ratio of *ND1/HK2* DNA content (F). Data are presented as the interquartile range of the data with the median indicated by the line ± standard error of the mean (SEM). Significant differences were determined using one-way ANOVA and Bonferroni post-hoc test, $p<0.05$. Treatment groups with the same letter are not significantly different from each other.

Mitochondrial function was also assessed in primary salivary gland acinar cells by performing the Seahorse XF Cell Mito Stress Test Kit [375] to measure spare respiratory capacity, which is the ability of the cells to respond to increased energy demand due to IR damage. The Seahorse XF Cell Mito Stress Test has been used to assess mitochondrial dysfunction in a number of disease models [376], [377], [378]. Due to the increased OCR and ATP production observed at day 5 IR and the decrease in mitochondrial complex protein I and III subunits, we chose day 5 IR as the time point to investigate spare respiratory capacity. Spare respiratory capacity is calculated as the difference between maximal respiration and basal respiration, and maximal respiration is induced by injecting the drug carbonyl cyanide-4 (trifluoromethoxy) phenylhydrazone (FCCP) into the cell media, which uncouples electron transport from ATP synthesis in oxidative phosphorylation, allowing unlimited electron transport and maximal OCR [375]. Following FCCP injection, OCR is significantly higher in the untreated group compared to day 5 IR, indicating a higher maximal respiration without radiation treatment (Fig. 4.5A,B). The spare respiratory capacity of the untreated group is significantly higher compared to the day 5 IR group (Fig. 4.5C), suggesting that day 5 IR salivary acinar cells have a reduced ability to respond to increased energy demand under stress, which is reflective of mitochondrial dysfunction.

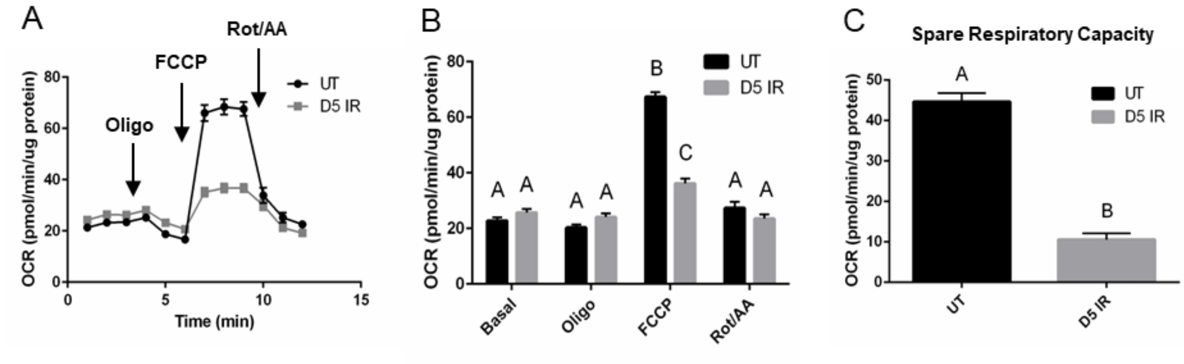

Figure 4.5. Spare respiratory capacity decreases at day 5 following radiation compared to untreated in salivary acinar cells.

Female FVB mice received 5 Gy IR targeted to the head and neck region (n=3/group) and primary acinar cells were isolated from parotid salivary glands of untreated (UT) and IR mice at day 5. Cells were seeded on a 96-well collagen-coated Seahorse microplate at a seeding density of 150K/well and cultured for 2 days. On day 2 of culture the Seahorse XF Cell Mito Stress Test Kit was run using the Seahorse XF96 Analyzer. A) Individual OCR readings for untreated UT and day 5 IR (D5 IR) groups with the responses to 2.0uM oligomycin (oligo) injection, 2.0uM FCCP injection, and 0.5uM rotenone/antimycin A (rot/AA) injection shown. B) Average basal, oligo, FCCP, and rot/AA OCR readings for UT and D5 IR. C) Spare respiratory capacity of untreated and day 5 IR groups. Each panel is representative of 2 independent assays (n=3/group). Significant differences were determined using one-way ANOVA and Bonferroni post-hoc test, $p<0.05$ in panel B. Significant differences were determined using the two-tailed unpaired T-test, $p<0.05$ in panel C. Treatment groups with the same letter are not significantly different from each other.

Mitochondrial energy substrate utilization following radiation in salivary gland acinar cells

Due to the observed increase in ATP production and reduced spare respiratory capacity at day 5 IR, we investigated the fuel preference of day 5 IR salivary acinar cells using the Seahorse XF Mito Fuel Flex Test Kit [379]. The fuel dependency of acinar cells to oxidize glucose, glutamine, and long-chain fatty acids was assessed by measuring OCR in response to the following fuel inhibitors: UK5099 inhibits the transport of pyruvate from glycolysis into the mitochondria for oxidation, BPTES inhibits the conversion of glutamine to glutamate so that it cannot enter the Kreb's cycle for oxidation, and etomoxir inhibits carnitine palmitoyl-transferase 1A (CPT1A), which inhibits the transport of long chain fatty acids into the mitochondria for oxidation (Fig. 4.6A). Untreated salivary acinar cells appear highly flexible in their use of fuel for energy production and show a low amount of dependency on glutamine (Fig. 4.6B,C,D). The day 5 IR group shows less dependency on glutamine and more dependency on long chain fatty acids as a fuel source in comparison to the untreated group (Fig. 4.6C,D). Radiation treatment does not appear to affect glucose dependency (Fig. 4.6B).

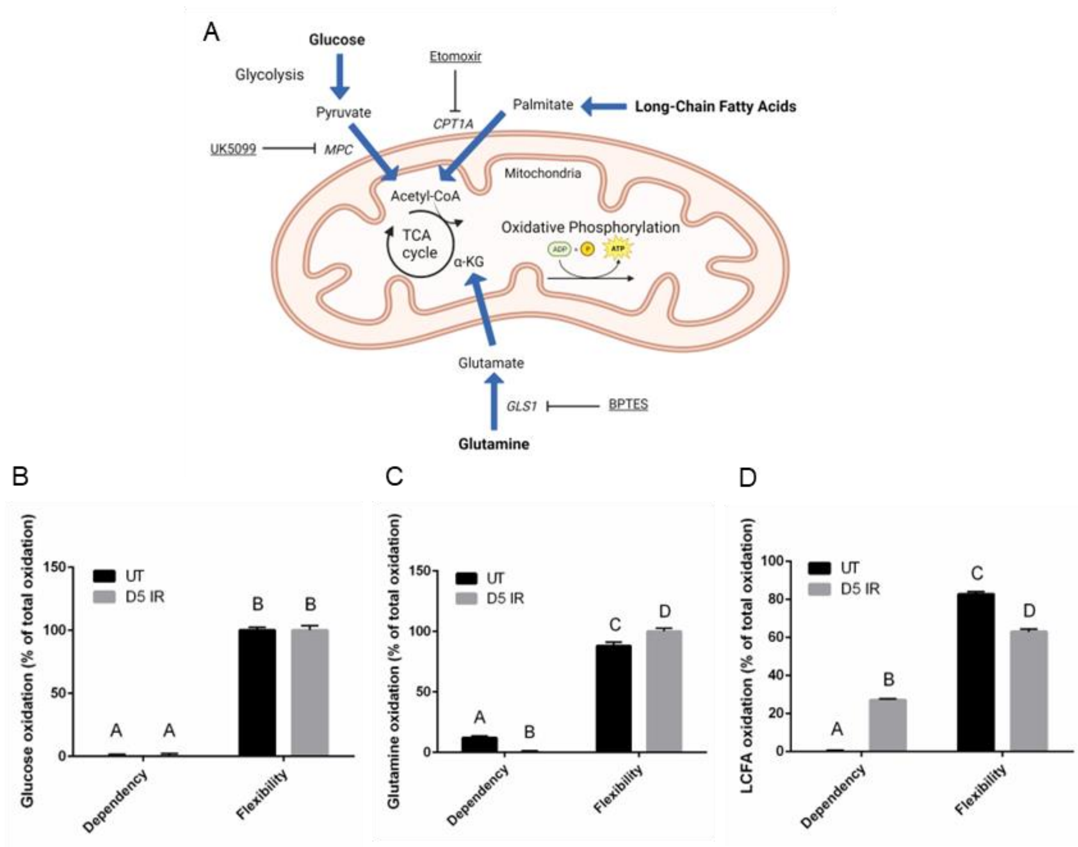

Figure 4.6. Dependency on long-chain fatty acids as a fuel source increases at day 5 following radiation treatment compared to untreated in salivary acinar cells.

Female FVB mice received 5 Gy IR targeted to the head and neck region (n=3/group) and primary acinar cells were isolated from parotid salivary glands of untreated (UT) and IR mice at day 5. Cells were seeded on a 96-well collagen-coated Seahorse microplate at a seeding density of 150K/well and cultured for 2 days. On day 2 of culture the Seahorse XF Mito Fuel Flex Test Kit was run using the Seahorse XF96 Analyzer. A) Schematic diagram of glucose, glutamine, and long-chain fatty acid metabolism and where the assay inhibitors block fuel oxidation. Image created in Biorender.com. B) Glucose dependency and flexibility in untreated and day 5 IR (D5 IR) groups. C) Glutamine dependency and flexibility in untreated and D5 IR groups. D) Long-chain fatty acid (LCFA) dependency and flexibility in untreated and D5 IR groups. Data is expressed as % of total oxidation of glucose, glutamine, and long-chain fatty acids ± standard error of the mean (SEM). Significant differences were determined using two-way ANOVA and Bonferroni post-hoc test, $p<0.05$. Treatment groups with the same letter are not significantly different from each other. Abbreviations: *MPC* = mitochondrial pyruvate carrier complex, *CPT1A* = carnitine palmitoyltransferase 1A, TCA cycle = tricarboxylic acid cycle, α-KG = alpha-ketoglutarate, *GLS1* = glutaminase-1, BPTES = (bis-2-(5-phenylacetamido-1,3,4-thiadiazol-2-yl)ethyl sulfide).

Discussion

Due to the ongoing need to identify therapeutic targets for restoring salivary gland function following radiation (IR) treatment clinically, mechanistic research is essential for providing new insight. In this study, we employed a variety of techniques to investigate how energy metabolism and mitochondrial function are altered in the irradiated salivary gland using both primary acinar cells and parotid gland tissue. We observed energy production variation over time in response to IR in the salivary gland. Acutely, we observed an increase in glycolysis assessed by extracellular acidification rate (ECAR), oxidative phosphorylation assessed by oxygen consumption rate (OCR), and energy (ATP) production rate at 24 hours post-IR in acinar cells that was attenuated at 48 hours post-IR. At day 5 post-IR when the transition to the chronic damage stage begins, ECAR, OCR, and ATP production rate increased. Energy metabolism reprogramming significantly changed chronically as displayed by decreased ECAR, OCR, and ATP production rate compared to untreated, suggesting changes in energy metabolism underlie the different stages of IR-induced damage in the salivary gland.

The reprogramming of energy metabolism and mitochondrial function has been assessed in different IR damage models, most notably the heart and skeletal muscle as these are highly metabolic tissues [380], [381], [349], [361], [382]. A study locally irradiated the heart (2 Gy) of mice and detected decreased activity of Complex I and Complex III in the electron transport chain of isolated mitochondria, decreased oxidative phosphorylation, and increased ROS levels at 4 weeks post-IR, indicating mitochondrial dysfunction [380]. The same group performed a follow-up study analyzing irradiated cardiac tissue collected at a more chronic time point, 40 weeks post-IR, and noted the same indicators of mitochondrial dysfunction observed in their previous study, demonstrating the non-transient effects of radiation on cardiac mitochondria

[381]. In our study, we observed decreased protein levels of Complex I and Complex III at days 3 and 5 post-IR in parotid tissue and decreased oxidative phosphorylation at days 30 and 60 post-IR. Although we observed increased OCR, ECAR, and ATP production at day 5 post-IR, we discovered a 76% decrease in spare respiratory capacity at day 5 post-IR, indicating a reduced ability of the mitochondria to overcome the stress induced by radiation, which is supported by OCR and ATP production significantly decreasing after the day 5 IR time point and Complex I and III protein subunit levels decreasing at day 5 IR. Together, the data suggests mitochondrial impairment at day 5 and chronically post-IR. Additional data to support this conclusion is the increase in mitochondrial DNA (mtDNA) copy number at day 5 and chronically post-IR in parotid tissue, which is hypothesized to be an adaptive response to maintain function following damage [374], [373].

Our results both support and contradict IR-induced metabolic reprogramming in skeletal muscle, although skeletal muscle and salivary gland exocrine tissue are not comparable in terms of function. One study exposed mice to whole-body 6 Gy IR and observed reduced skeletal muscle mitochondrial fatty acid beta-oxidation, reduced mitochondrial enzymatic activity, and impaired glucose uptake at 5 weeks post-IR [382]. In our previous work, we overlaid gene expression and metabolite data in the context of human biological networks and identified fatty acid degradation as an enriched metabolic pathway at day 5 post-radiation, with downregulation of metabolites and genes annotated to mitochondrial beta-oxidation of fatty acids and peroxisomal lipid metabolism observed [315], which supports the reduction in mitochondrial fatty acid beta-oxidation observed in irradiated skeletal muscle [382]. In our current study, we observed decreased protein levels of mitochondrial electron transport chain proteins and reduced ECAR, which suggests reduced glucose uptake chronically post-IR and supports observations observed in skeletal muscle [382]. A different group exposed mice to whole-body 6 Gy IR and discovered decreased ATP production, increased spare respiratory capacity, and increased fatty acid and amino acid metabolism through the TCA cycle at 24 hours post-IR in skeletal muscle mitochondria [361]. In contrast, we observed an increase in ATP production at 24 hours post-IR in salivary acinar cells and reduced spare respiratory capacity at day 5 post-IR, displaying time- and tissue-dependent differences in metabolic reprogramming following radiation exposure.

It is well established that radiation exposure acutely results in DNA damage and reactive oxygen species (ROS) production [105], [106], [107], [170], [383], and that mitochondria are the main source of ROS production [384], [385]. In our salivary gland radiation-damage model, apoptosis peaks at 24 hours post-radiation, and ROS production by mitochondria has been shown to mediate apoptosis [114], [320], [386]. A study investigated the mechanisms underlying radiation inducing mitochondrial ROS production using a human lung carcinoma cell line exposed to 10 Gy radiation (IR) and observed an acute increase in mitochondrial oxidative phosphorylation at 12 and 24 hours post-IR that corresponded to increased mitochondrial ROS production [387], which supports the observed increase in OCR and ATP production at 24 hours post-IR shown in our study and suggests a relationship between increased mitochondrial OCR and ROS production acutely following radiation in the salivary gland, which may mediate apoptosis and contribute to tissue dysfunction. Targeting the acute increase in OCR and ATP production observed in this study may be a mechanism to reduce mitochondrial ROS production and apoptosis and restore function to the salivary gland following IR.

The increase in OCR and mitochondrial ATP production observed in day 5 post-IR acinar cells in this study corroborates the enrichment of respiratory electron transport and the tricarboxylic acid (TCA) cycle identified in our previous work where we integrated transcriptomics and metabolomics analysis to identify pathway-level enrichment at day 5 post-IR in the salivary gland [315]. This observed metabolic reprogramming at day 5 post-IR is of interest due to the transition from the acute radiation damage response to the chronic damage response, which is associated with increased compensatory proliferation and mechanistic Target of Rapamycin (mTOR) pathway hyperactivation suggesting autophagy reduction. [153], [150], [125]. The increase in ECAR and total ATP production observed at day 5 IR in this study may facilitate the increase in compensatory proliferation within the salivary gland to quickly increase the level of carbon backbones for macromolecule synthesis for sustaining growth, as has been observed in other wound healing models [354], [355], [356], [357]. This proposed increase in glycolysis at day 5 IR is supported by increased lactate concentration observed in the parotid tissue compared to untreated, which is reflective of rapidly proliferating cells performing aerobic glycolysis and accumulating lactate [388], [355]. Hyperactivation of mTOR has been demonstrated to increase glycolysis in many diseases through the hypoxia inducible factor-1 alpha (HIF-1α), including breast cancer [389], lung fibrosis [390], Alzheimer's disease [391], and colorectal cancer [392], and targeting this pathway has demonstrated efficacy as a therapeutic mechanism for these diseases. Our lab previously demonstrated that post-IR treatment with the mTOR inhibitor, the rapalogue CCI-779, improves salivary gland function chronically post 5 Gy IR and restores proliferation levels in the gland of mice to untreated levels following IR [125]. A reduction in glycolysis may be a mechanism by which mTOR inhibition reduces compensatory proliferation and restores salivary gland function chronically following IR.

This paper demonstrates that primary acinar cells are flexible in their choice of fuel for energy production, with day 5 irradiated cell displaying a 27% increase in long-chain fatty acid

(LCFA) dependency for fuel oxidation. Interestingly, increased parotid gland fat content in head and neck cancer patients prior to beginning radiotherapy and chemotherapy treatments was shown to correlate with chronic radiation-induced xerostomia at 12 months post-treatment [393], but it is unknown how radiation affects the fat content of parotid glands and whether fat content in the gland influences the usage of fat as a preferred fuel source in response to radiation. Additionally, it has repeatedly been shown in Sjögren's syndrome (SS) patients that fat deposition is a biomarker of the disease and positively correlates with the level of salivary flow reduction [394], [395], [396], [397]. A microarray analysis on salivary glands from primary SS (pSS) patients showed enrichment for genes annotated to adipose tissue development and reduced mitochondrial fatty acid beta-oxidation, with interleukin (IL) 17 positive adipocytes observed in the salivary glands of pSS patients compared to healthy controls, suggesting that adipocyte deposition is involved in the immune response of the disease, but whether this phenomenon is part of disease progression or the repair process is unknown [398]. In the irradiated salivary gland, we don't know if adipocyte deposition occurs as part of the inflammatory repair process or damage response, and whether this will lead to increased salivary acinar cell dependency on fatty acids as a fuel source and contribute to metabolic reprogramming underlying IR-induced dysfunction.

Due to the complexity of cellular energy metabolism and mitochondrial function, this study used several techniques to help gain knowledge of these mechanisms in response to IR in the salivary gland and optimized primary acinar cells for OCR and ECAR measurements with the Seahorse XF96 Analyzer. It is important to note that OCR and ECAR measured in this study only constitute the metabolism of cells in the acinar compartment of the salivary gland and do not reflect the entire salivary gland (striated ductal cells, intercalated ductal cells, and granular ductal cells). Therefore, the measurements of glycolytic enzyme protein levels and activity, lactate concentration, mitochondrial complex I and III protein subunit levels, and mitochondrial DNA (mtDNA) copy number are reflective of a combination of cell types. To improve the assessment of mitochondrial function, isolating mitochondria from the parotid gland would improve the specificity of the assays measuring OCR and ATP production rate. The use of non-radioactive stable isotope tracing to track the flow of carbon from glycolysis, fatty acid beta-oxidation, and glutaminolysis into the TCA cycle would provide great insight into fuel dependency and metabolic flux in response to IR. This study helped elucidate the energy metabolism profile of the salivary gland, which is an understudied area of research, and demonstrated how IR reprograms energy metabolism in the salivary gland at different stages of damage following IR. Future research can test targeting enzymes within the altered metabolic pathways to reverse the changes observed following IR with the goal of restoring salivary gland function to improve the quality of life of head and neck cancer patients.

V. Conclusions

The American Cancer Society estimates over 54,000 new cases of head and neck cancer (HNC) annually in the United States [1], and the standard of care includes surgical removal of the tumor if operable followed by radiation (IR) treatment. Salivary glands are indirect targets of radiation treatment due to their adjacent location to HNC tumors, resulting in loss of tissue function. Loss of salivary gland function results in decreased saliva flow, which diminishes the quality of life of HNC patients and can lead to xerostomia, oral infections, periodontal disease, and even malnutrition [12]. Treatment options for xerostomia are limited and palliative, with certain drug treatments being associated with unpleasant side effects [13]. Therefore, mechanistic research of IR-induced salivary gland dysfunction is needed to identify drug targets that can restore tissue function and decrease the unpleasant side effects associated with current treatment options.

Metabolomics is a useful platform that reflects an organism's phenotype and has been utilized to identify mechanisms underlying IR-induced damage in various tissue types. Furthermore, drug targeting to reverse the observed radiation-induced metabolic alterations has been demonstrated to restore function in mouse testicular tissue [196], which paves the way for investigating metabolic alterations in irradiated salivary gland tissue to identify therapeutic targets to reverse IR-induced damage. Adding different "omics" data platforms can provide a deeper understanding of the metabolic reactions occurring in irradiated salivary glands. We integrated transcriptomic and metabolomic data and identified significant gene-metabolite interactions at day 5 post-IR in the parotid gland (Chapter II). Using integrated pathway enrichment analysis and network analysis, we identified changes in glutathione metabolism, energy metabolism (TCA cycle and thermogenesis), peroxisomal lipid metabolism, and bile acid production at day 5 post-IR (Chapter II). These metabolic changes may be related to previously identified increased compensatory proliferation and decreased apical/basolateral polarity beginning at this IR time point, which is correlated with reduced saliva flow [153], [150].

Due to day 5 post-IR marking the transitional beginning between the acute and chronic phases of the IR-damage response, with loss of salivary function beginning at day 3 and continuing chronically [321], we evaluated the effects of IR on the metabolic profile temporally at an acute (day 3), intermediate (day 14), and chronic (day 30) time point after radiation treatment in the salivary gland (Chapter III). The highest pathway-level enrichment occurred acutely at 3-days post-IR with a subsequent decrease at 14- and 30-days post-IR (Chapter III). Multiple amino acid metabolism pathways, glutathione metabolism, and central carbon metabolism in cancer were significantly enriched at all three IR time points (Chapter III), suggesting that these pathways underlie the damage response contributing to loss of salivary gland function.

We further investigated the enrichment of energy metabolism observed in Chapter II by measuring glycolytic flux and oxidative phosphorylation in primary acinar cells and parotid gland tissue exposed to IR at multiple time points (Chapter IV). Extracellular acidification rate (ECAR; reflective of glycolysis), oxygen consumption rate (OCR; reflective of oxidative phosphorylation), and ATP production rate increased at 24 hours and 5 days post-IR and then decreased at chronic time points (Chapter IV). Hexokinase protein levels and activity increased at 3 days post-IR, suggesting an increase in glycolysis at this time point (Chapter IV). Complex I and III subunit protein levels decreased at days 3 and 5 post-IR while mitochondrial DNA copy number increased chronically post-IR (Chapter IV), which may reflect adaptive responses of dysfunctional mitochondria. Primary acinar cells were more dependent on long-chain fatty acids for fuel at day 5 post-IR (Chapter IV), showing that IR changes fuel preference in primary acinar cells.

The presented research helps elucidate understanding of the metabolic response to IR at acute, intermediate, and chronic damage stages and provides novel insight into energy metabolism reprogramming in the salivary gland. Previous work has shown that glycolysis increases during tumor growth and that glycolytic inhibition reduces tumor cell proliferation [399], [400], [401], suggesting that inhibiting the observed increase in glycolysis at day 5 post-IR may reduce compensatory proliferation and prevent chronic salivary gland hypofunction. Changes in reduced glutathione levels observed at day 3, 5, 14, and 30 post-IR in Chapters II and III may be reflective of reduced antioxidant capacity in the salivary gland, which may be correlated with previously identified increased reactive oxygen species (ROS) production [170] and decreased oxygen consumption rate and increased mitochondrial DNA copy number reflective of chronic mitochondrial dysfunction presented in Chapter IV. Further investigation of mitochondrial function following IR exposure in the salivary gland is needed to understand the relationship between metabolic reprogramming and salivary gland hypofunction and test druggable targets for restoring chronic loss of function in HNC patients.

References

1. Siegel RL, Miller KD, Fuchs HE, Jemal A. Cancer statistics, 2022. CA Cancer J Clin 2022;**72**(1):7-33 doi: 10.3322/caac.21708 [published Online First: 20220112].
2. Chow LQM. Head and Neck Cancer. N Engl J Med 2020;**382**(1):60-72 doi: 10.1056/NEJMra1715715.
3. Nogues JC, Fassas S, Mulcahy C, Zapanta PE. Human Papillomavirus-Associated Head and Neck Cancer. J Am Board Fam Med 2021;**34**(4):832-37 doi: 10.3122/jabfm.2021.04.200588.
4. Berman TA, Schiller JT. Human papillomavirus in cervical cancer and oropharyngeal cancer: One cause, two diseases. Cancer 2017;**123**(12):2219-29 doi: 10.1002/cncr.30588 [published Online First: 20170327].
5. Mehanna H, Beech T, Nicholson T, et al. Prevalence of human papillomavirus in oropharyngeal and nonoropharyngeal head and neck cancer--systematic review and meta-analysis of trends by time and region. Head Neck 2013;**35**(5):747-55 doi: 10.1002/hed.22015 [published Online First: 20120120].
6. Miller KD, Nogueira L, Mariotto AB, et al. Cancer treatment and survivorship statistics, 2019. CA Cancer J Clin 2019;**69**(5):363-85 doi: 10.3322/caac.21565 [published Online First: 20190611].
7. Kaidar-Person O, Gil Z, Billan S. Precision medicine in head and neck cancer. Drug Resist Updat 2018;**40**:13-16 doi: 10.1016/j.drup.2018.09.001 [published Online First: 20180925].
8. Mallick I, Waldron JN. Radiation therapy for head and neck cancers. Semin Oncol Nurs 2009;**25**(3):193-202 doi: 10.1016/j.soncn.2009.05.002.
9. Thariat J, Bruchon Y, Bonnetain F, et al. Conservative treatment of early glottic carcinomas with exclusive radiotherapy. Cancer Radiother 2004;**8**(5):288-96 doi: 10.1016/j.canrad.2004.08.003.
10. Kim JK, Leeman JE, Riaz N, McBride S, Tsai CJ, Lee NY. Proton Therapy for Head and Neck Cancer. Curr Treat Options Oncol 2018;**19**(6):28 doi: 10.1007/s11864-018-0546-9 [published Online First: 20180509].
11. Grundmann O, Mitchell GC, Limesand KH. Sensitivity of salivary glands to radiation: from animal models to therapies. J Dent Res 2009;**88**(10):894-903 doi: 10.1177/0022034509343143.
12. Jensen SB, Vissink A, Limesand KH, Reyland ME. Salivary Gland Hypofunction and Xerostomia in Head and Neck Radiation Patients. J Natl Cancer Inst Monogr 2019;**2019**(53) doi: 10.1093/jncimonographs/lgz016.
13. Jasmer KJ, Gilman KE, Munoz Forti K, Weisman GA, Limesand KH. Radiation-Induced Salivary Gland Dysfunction: Mechanisms, Therapeutics and Future Directions. J Clin Med 2020;**9**(12) doi: 10.3390/jcm9124095 [published Online First: 20201218].
14. Jensen SB, Pedersen AM, Vissink A, et al. A systematic review of salivary gland hypofunction and xerostomia induced by cancer therapies: management strategies and economic impact. Support Care Cancer 2010;**18**(8):1061-79 doi: 10.1007/s00520-010-0837-6 [published Online First: 20100325].
15. Grewal AS, Jones J, Lin A. Palliative Radiation Therapy for Head and Neck Cancers. Int J Radiat Oncol Biol Phys 2019;**105**(2):254-66 doi: 10.1016/j.ijrobp.2019.05.024 [published Online First: 20190522].

16. Ghaderi N, Jung J, Bruningk SC, Subramanian A, Nassour L, Peacock J. A Century of Fractionated Radiotherapy: How Mathematical Oncology Can Break the Rules. Int J Mol Sci 2022;**23**(3) doi: 10.3390/ijms23031316 [published Online First: 20220124].
17. Porcheri C, Mitsiadis TA. Physiology, Pathology and Regeneration of Salivary Glands. Cells 2019;**8**(9) doi: 10.3390/cells8090976 [published Online First: 20190826].
18. Lee SW, Kang KW, Wu HG. Prospective investigation and literature review of tolerance dose on salivary glands using quantitative salivary gland scintigraphy in the intensity-modulated radiotherapy era. Head Neck 2016;**38 Suppl 1**:E1746-55 doi: 10.1002/hed.24310 [published Online First: 20160215].
19. Lacas B, Bourhis J, Overgaard J, et al. Role of radiotherapy fractionation in head and neck cancers (MARCH): an updated meta-analysis. Lancet Oncol 2017;**18**(9):1221-37 doi: 10.1016/S1470-2045(17)30458-8 [published Online First: 20170727].
20. Caudell JJ, Ward MC, Riaz N, et al. Volume, Dose, and Fractionation Considerations for IMRT-based Reirradiation in Head and Neck Cancer: A Multi-institution Analysis. Int J Radiat Oncol Biol Phys 2018;**100**(3):606-17 doi: 10.1016/j.ijrobp.2017.11.036 [published Online First: 20171201].
21. Mackie TR, Kapatoes J, Ruchala K, et al. Image guidance for precise conformal radiotherapy. Int J Radiat Oncol Biol Phys 2003;**56**(1):89-105 doi: 10.1016/s0360-3016(03)00090-7.
22. Bucci MK, Bevan A, Roach M, 3rd. Advances in radiation therapy: conventional to 3D, to IMRT, to 4D, and beyond. CA Cancer J Clin 2005;**55**(2):117-34 doi: 10.3322/canjclin.55.2.117.
23. Bortfeld T. IMRT: a review and preview. Phys Med Biol 2006;**51**(13):R363-79 doi: 10.1088/0031-9155/51/13/R21 [published Online First: 20060620].
24. Moon SH, Cho KH, Lee CG, et al. IMRT vs. 2D-radiotherapy or 3D-conformal radiotherapy of nasopharyngeal carcinoma : Survival outcome in a Korean multi-institutional retrospective study (KROG 11-06). Strahlenther Onkol 2016;**192**(6):377-85 doi: 10.1007/s00066-016-0959-y [published Online First: 20160314].
25. Eisbruch A, Harris J, Garden AS, et al. Multi-institutional trial of accelerated hypofractionated intensity-modulated radiation therapy for early-stage oropharyngeal cancer (RTOG 00-22). Int J Radiat Oncol Biol Phys 2010;**76**(5):1333-8 doi: 10.1016/j.ijrobp.2009.04.011 [published Online First: 20090618].
26. Sultanem K, Shu HK, Xia P, et al. Three-dimensional intensity-modulated radiotherapy in the treatment of nasopharyngeal carcinoma: the University of California-San Francisco experience. Int J Radiat Oncol Biol Phys 2000;**48**(3):711-22 doi: 10.1016/s0360-3016(00)00702-1.
27. Kam MK, Teo PM, Chau RM, et al. Treatment of nasopharyngeal carcinoma with intensity-modulated radiotherapy: the Hong Kong experience. Int J Radiat Oncol Biol Phys 2004;**60**(5):1440-50 doi: 10.1016/j.ijrobp.2004.05.022.
28. Parliament MB, Scrimger RA, Anderson SG, et al. Preservation of oral health-related quality of life and salivary flow rates after inverse-planned intensity- modulated radiotherapy (IMRT) for head-and-neck cancer. Int J Radiat Oncol Biol Phys 2004;**58**(3):663-73 doi: 10.1016/S0360-3016(03)01571-2.
29. Kam MK, Leung SF, Zee B, et al. Prospective randomized study of intensity-modulated radiotherapy on salivary gland function in early-stage nasopharyngeal carcinoma patients. J Clin Oncol 2007;**25**(31):4873-9 doi: 10.1200/JCO.2007.11.5501.

30. Teoh M, Clark CH, Wood K, Whitaker S, Nisbet A. Volumetric modulated arc therapy: a review of current literature and clinical use in practice. Br J Radiol 2011;**84**(1007):967-96 doi: 10.1259/bjr/22373346.
31. Buciuman N, Marcu LG. Is there a dosimetric advantage of volumetric modulated arc therapy over intensity modulated radiotherapy in head and neck cancer? Eur Arch Otorhinolaryngol 2022;**279**(11):5311-21 doi: 10.1007/s00405-022-07452-1 [published Online First: 20220522].
32. Dursun P, Zarepisheh M, Jhanwar G, Deasy JO. Solving the volumetric modulated arc therapy (VMAT) problem using a sequential convex programming method. Phys Med Biol 2021;**66**(8) doi: 10.1088/1361-6560/abee58 [published Online First: 20210414].
33. Johnston M, Clifford S, Bromley R, Back M, Oliver L, Eade T. Volumetric-modulated arc therapy in head and neck radiotherapy: a planning comparison using simultaneous integrated boost for nasopharynx and oropharynx carcinoma. Clin Oncol (R Coll Radiol) 2011;**23**(8):503-11 doi: 10.1016/j.clon.2011.02.002 [published Online First: 20110311].
34. Lu SH, Cheng JC, Kuo SH, et al. Volumetric modulated arc therapy for nasopharyngeal carcinoma: a dosimetric comparison with TomoTherapy and step-and-shoot IMRT. Radiother Oncol 2012;**104**(3):324-30 doi: 10.1016/j.radonc.2011.11.017 [published Online First: 20120109].
35. Hommadi M, N'da G, Bertrand C, et al. Volumetric modulated arctherapy for locally advanced nasopharyngeal carcinoma: Clinical efficacy and late toxicity. Cancer Radiother 2022;**26**(3):433-39 doi: 10.1016/j.canrad.2021.05.006 [published Online First: 20210805].
36. Poon WY, Thomson M, McLoone P, et al. Comparative cohort study of volumetric modulated arc therapy for squamous cell cancer of unknown primary in the head and neck-Involved neck only versus mucosal irradiation. Clin Otolaryngol 2020;**45**(6):847-52 doi: 10.1111/coa.13593 [published Online First: 20200917].
37. Moreno AC, Frank SJ, Garden AS, et al. Intensity modulated proton therapy (IMPT) - The future of IMRT for head and neck cancer. Oral Oncol 2019;**88**:66-74 doi: 10.1016/j.oraloncology.2018.11.015 [published Online First: 20181121].
38. Kandula S, Zhu X, Garden AS, et al. Spot-scanning beam proton therapy vs intensity-modulated radiation therapy for ipsilateral head and neck malignancies: a treatment planning comparison. Med Dosim 2013;**38**(4):390-4 doi: 10.1016/j.meddos.2013.05.001 [published Online First: 20130802].
39. Stromberger C, Cozzi L, Budach V, et al. Unilateral and bilateral neck SIB for head and neck cancer patients : Intensity-modulated proton therapy, tomotherapy, and RapidArc. Strahlenther Onkol 2016;**192**(4):232-9 doi: 10.1007/s00066-016-0945-4 [published Online First: 20160206].
40. Mock U, Georg D, Bogner J, Auberger T, Potter R. Treatment planning comparison of conventional, 3D conformal, and intensity-modulated photon (IMRT) and proton therapy for paranasal sinus carcinoma. Int J Radiat Oncol Biol Phys 2004;**58**(1):147-54 doi: 10.1016/s0360-3016(03)01452-4.
41. Cao J, Zhang X, Jiang B, et al. Intensity-modulated proton therapy for oropharyngeal cancer reduces rates of late xerostomia. Radiother Oncol 2021;**160**:32-39 doi: 10.1016/j.radonc.2021.03.036 [published Online First: 20210408].
42. Placidi L, Bolsi A, Lomax AJ, et al. Effect of Anatomic Changes on Pencil Beam Scanned Proton Dose Distributions for Cranial and Extracranial Tumors. Int J Radiat Oncol Biol

Phys 2017;**97**(3):616-23 doi: 10.1016/j.ijrobp.2016.11.013 [published Online First: 20161116].
43. Gu W, O'Connor D, Nguyen D, et al. Integrated beam orientation and scanning-spot optimization in intensity-modulated proton therapy for brain and unilateral head and neck tumors. Med Phys 2018;**45**(4):1338-50 doi: 10.1002/mp.12788 [published Online First: 20180301].
44. Alterio D, Marvaso G, Ferrari A, Volpe S, Orecchia R, Jereczek-Fossa BA. Modern radiotherapy for head and neck cancer. Semin Oncol 2019;**46**(3):233-45 doi: 10.1053/j.seminoncol.2019.07.002 [published Online First: 20190726].
45. Xiang M, Colevas AD, Holsinger FC, Le QX, Beadle BM. Survival After Definitive Chemoradiotherapy With Concurrent Cisplatin or Carboplatin for Head and Neck Cancer. J Natl Compr Canc Netw 2019;**17**(9):1065-73 doi: 10.6004/jnccn.2019.7297.
46. Bonner JA, Harari PM, Giralt J, et al. Radiotherapy plus cetuximab for squamous-cell carcinoma of the head and neck. N Engl J Med 2006;**354**(6):567-78 doi: 10.1056/NEJMoa053422.
47. Concu R, Cordeiro M. Cetuximab and the Head and Neck Squamous Cell Cancer. Curr Top Med Chem 2018;**18**(3):192-98 doi: 10.2174/1568026618666180112162412.
48. Gillison ML, Trotti AM, Harris J, et al. Radiotherapy plus cetuximab or cisplatin in human papillomavirus-positive oropharyngeal cancer (NRG Oncology RTOG 1016): a randomised, multicentre, non-inferiority trial. Lancet 2019;**393**(10166):40-50 doi: 10.1016/S0140-6736(18)32779-X [published Online First: 20181115].
49. Mehanna H, Robinson M, Hartley A, et al. Radiotherapy plus cisplatin or cetuximab in low-risk human papillomavirus-positive oropharyngeal cancer (De-ESCALaTE HPV): an open-label randomised controlled phase 3 trial. Lancet 2019;**393**(10166):51-60 doi: 10.1016/S0140-6736(18)32752-1 [published Online First: 20181115].
50. Vermorken JB, Mesia R, Rivera F, et al. Platinum-based chemotherapy plus cetuximab in head and neck cancer. N Engl J Med 2008;**359**(11):1116-27 doi: 10.1056/NEJMoa0802656.
51. de Mello RA, Geros S, Alves MP, Moreira F, Avezedo I, Dinis J. Cetuximab plus platinum-based chemotherapy in head and neck squamous cell carcinoma: a retrospective study in a single comprehensive European cancer institution. PLoS One 2014;**9**(2):e86697 doi: 10.1371/journal.pone.0086697 [published Online First: 20140206].
52. Depenni R, Cossu Rocca M, Ferrari D, et al. Clinical outcomes and prognostic factors in recurrent and/or metastatic head and neck cancer patients treated with chemotherapy plus cetuximab as first-line therapy in a real-world setting. Eur J Cancer 2019;**115**:4-12 doi: 10.1016/j.ejca.2019.03.022 [published Online First: 20190510].
53. Han Y, Liu D, Li L. PD-1/PD-L1 pathway: current researches in cancer. Am J Cancer Res 2020;**10**(3):727-42 [published Online First: 20200301].
54. Cramer JD, Burtness B, Ferris RL. Immunotherapy for head and neck cancer: Recent advances and future directions. Oral Oncol 2019;**99**:104460 doi: 10.1016/j.oraloncology.2019.104460 [published Online First: 20191101].
55. Burtness B, Harrington KJ, Greil R, et al. Pembrolizumab alone or with chemotherapy versus cetuximab with chemotherapy for recurrent or metastatic squamous cell carcinoma of the head and neck (KEYNOTE-048): a randomised, open-label, phase 3 study. Lancet 2019;**394**(10212):1915-28 doi: 10.1016/S0140-6736(19)32591-7 [published Online First: 20191101].

56. Ferris RL, Blumenschein G, Jr., Fayette J, et al. Nivolumab for Recurrent Squamous-Cell Carcinoma of the Head and Neck. N Engl J Med 2016;**375**(19):1856-67 doi: 10.1056/NEJMoa1602252 [published Online First: 20161008].
57. Doki Y, Ueno M, Hsu CH, et al. Tolerability and efficacy of durvalumab, either as monotherapy or in combination with tremelimumab, in patients from Asia with advanced biliary tract, esophageal, or head-and-neck cancer. Cancer Med 2022;**11**(13):2550-60 doi: 10.1002/cam4.4593 [published Online First: 20220524].
58. Koukourakis MI. Amifostine in clinical oncology: current use and future applications. Anticancer Drugs 2002;**13**(3):181-209 doi: 10.1097/00001813-200203000-00001.
59. Sodicoff M, Conger AD, Pratt NE, Trepper P. Radioprotection by WR-2721 against long-term chronic damage to the rat parotid gland. Radiat Res 1978;**76**(1):172-9.
60. Ito H, Meistrich ML, Barkley HT, Jr., Thames HD, Jr., Milas L. Protection of acute and late radiation damage of the gastrointestinal tract by WR-2721. Int J Radiat Oncol Biol Phys 1986;**12**(2):211-9 doi: 10.1016/0360-3016(86)90096-9.
61. Geng L, Hanson WR, Malkinson FD. Topical or systemic 16, 16 dm prostaglandin E2 or WR-2721 (WR-1065) protects mice from alopecia after fractionated irradiation. Int J Radiat Biol 1992;**61**(4):533-7 doi: 10.1080/09553009214551291.
62. Sigdestad CP, Treacy SH, Knapp LA, Grdina DJ. The effect of 2-[(aminopropyl)amino] ethanethiol (WR-1065) on radiation induced DNA double strand damage and repair in V79 cells. Br J Cancer 1987;**55**(5):477-82 doi: 10.1038/bjc.1987.97.
63. Treskes M, Nijtmans LG, Fichtinger-Schepman AM, van der Vijgh WJ. Effects of the modulating agent WR2721 and its main metabolites on the formation and stability of cisplatin-DNA adducts in vitro in comparison to the effects of thiosulphate and diethyldithiocarbamate. Biochem Pharmacol 1992;**43**(5):1013-9 doi: 10.1016/0006-2952(92)90607-k.
64. Orditura M, De Vita F, Roscigno A, et al. Amifostine: A selective cytoprotective agent of normal tissues from chemo-radiotherapy induced toxicity (Review). Oncol Rep 1999;**6**(6):1357-62 doi: 10.3892/or.6.6.1357.
65. Capizzi RL. The preclinical basis for broad-spectrum selective cytoprotection of normal tissues from cytotoxic therapies by amifostine (Ethyol). Eur J Cancer 1996;**32A Suppl 4**:S5-16 doi: 10.1016/s0959-8049(96)00333-4.
66. Brizel DM, Wasserman TH, Henke M, et al. Phase III randomized trial of amifostine as a radioprotector in head and neck cancer. J Clin Oncol 2000;**18**(19):3339-45 doi: 10.1200/JCO.2000.18.19.3339.
67. Veerasarn V, Phromratanapongse P, Suntornpong N, et al. Effect of Amifostine to prevent radiotherapy-induced acute and late toxicity in head and neck cancer patients who had normal or mild impaired salivary gland function. J Med Assoc Thai 2006;**89**(12):2056-67.
68. Jellema AP, Slotman BJ, Muller MJ, et al. Radiotherapy alone, versus radiotherapy with amifostine 3 times weekly, versus radiotherapy with amifostine 5 times weekly: A prospective randomized study in squamous cell head and neck cancer. Cancer 2006;**107**(3):544-53 doi: 10.1002/cncr.22020.
69. Buentzel J, Micke O, Adamietz IA, Monnier A, Glatzel M, de Vries A. Intravenous amifostine during chemoradiotherapy for head-and-neck cancer: a randomized placebo-controlled phase III study. Int J Radiat Oncol Biol Phys 2006;**64**(3):684-91 doi: 10.1016/j.ijrobp.2005.08.005 [published Online First: 20051021].

70. Rades D, Fehlauer F, Bajrovic A, Mahlmann B, Richter E, Alberti W. Serious adverse effects of amifostine during radiotherapy in head and neck cancer patients. Radiother Oncol 2004;**70**(3):261-4 doi: 10.1016/j.radonc.2003.10.005.
71. King M, Joseph S, Albert A, et al. Use of Amifostine for Cytoprotection during Radiation Therapy: A Review. Oncology 2020;**98**(2):61-80 doi: 10.1159/000502979 [published Online First: 20191217].
72. Singh A, Rosen EB, Randazzo JD, Estilo CL, Gelblum DY, Huryn JM. Intraoral radiation stents-Primer for clinical use in head and neck cancer therapy. Head Neck 2021;**43**(12):4010-17 doi: 10.1002/hed.26848 [published Online First: 20210904].
73. Goel A, Tripathi A, Chand P, Singh SV, Pant MC, Nagar A. Use of positioning stents in lingual carcinoma patients subjected to radiotherapy. Int J Prosthodont 2010;**23**(5):450-2.
74. Rocha BA, Lima LMC, Paranaiba LMR, et al. Intraoral stents in preventing adverse radiotherapeutic effects in lip cancer patients. Rep Pract Oncol Radiother 2017;**22**(6):450-54 doi: 10.1016/j.rpor.2017.08.003 [published Online First: 20170901].
75. Li LX, Tian G, He J. The standardization of acupuncture treatment for radiation-induced xerostomia: A literature review. Chin J Integr Med 2016;**22**(7):549-54 doi: 10.1007/s11655-015-2145-y [published Online First: 20150826].
76. Cho JH, Chung WK, Kang W, Choi SM, Cho CK, Son CG. Manual acupuncture improved quality of life in cancer patients with radiation-induced xerostomia. J Altern Complement Med 2008;**14**(5):523-6 doi: 10.1089/acm.2007.0793.
77. Simcock R, Fallowfield L, Monson K, et al. ARIX: a randomised trial of acupuncture v oral care sessions in patients with chronic xerostomia following treatment of head and neck cancer. Ann Oncol 2013;**24**(3):776-83 doi: 10.1093/annonc/mds515 [published Online First: 20121025].
78. Garcia MK, Meng Z, Rosenthal DI, et al. Effect of True and Sham Acupuncture on Radiation-Induced Xerostomia Among Patients With Head and Neck Cancer: A Randomized Clinical Trial. JAMA Netw Open 2019;**2**(12):e1916910 doi: 10.1001/jamanetworkopen.2019.16910 [published Online First: 20191202].
79. Deng G, Hou BL, Holodny AI, Cassileth BR. Functional magnetic resonance imaging (fMRI) changes and saliva production associated with acupuncture at LI-2 acupuncture point: a randomized controlled study. BMC Complement Altern Med 2008;**8**:37 doi: 10.1186/1472-6882-8-37 [published Online First: 20080707].
80. Fernandez E, Morillo V, Salvador M, et al. Hyperbaric oxygen and radiation therapy: a review. Clin Transl Oncol 2021;**23**(6):1047-53 doi: 10.1007/s12094-020-02513-5 [published Online First: 20201118].
81. Thom SR. Hyperbaric oxygen: its mechanisms and efficacy. Plast Reconstr Surg 2011;**127 Suppl 1**(Suppl 1):131S-41S doi: 10.1097/PRS.0b013e3181fbe2bf.
82. Sherlock S, Way M, Tabah A. Hyperbaric oxygen treatment for the management of radiation-induced xerostomia. J Med Imaging Radiat Oncol 2018;**62**(6):841-46 doi: 10.1111/1754-9485.12789 [published Online First: 20180816].
83. Fox NF, Xiao C, Sood AJ, et al. Hyperbaric oxygen therapy for the treatment of radiation-induced xerostomia: a systematic review. Oral Surg Oral Med Oral Pathol Oral Radiol 2015;**120**(1):22-8 doi: 10.1016/j.oooo.2015.03.007 [published Online First: 20150325].
84. Warde P, Kroll B, O'Sullivan B, et al. A phase II study of Biotene in the treatment of postradiation xerostomia in patients with head and neck cancer. Support Care Cancer 2000;**8**(3):203-8 doi: 10.1007/s005200050286.

85. Tsibouklis J, Middleton AM, Patel N, Pratten J. Toward mucoadhesive hydrogel formulations for the management of xerostomia: the physicochemical, biological, and pharmacological considerations. J Biomed Mater Res A 2013;**101**(11):3327-38 doi: 10.1002/jbm.a.34626 [published Online First: 20130325].
86. Barbe AG, Ludwar L, Hamacher S, Noack MJ. Efficacy of a newly developed mouth gel for xerostomia relief-A randomized double-blind trial. Oral Dis 2019;**25**(6):1519-29 doi: 10.1111/odi.13105 [published Online First: 20190503].
87. Epstein JB, Stevenson-Moore P. A clinical comparative trial of saliva substitutes in radiation-induced salivary gland hypofunction. Spec Care Dentist 1992;**12**(1):21-3 doi: 10.1111/j.1754-4505.1992.tb00401.x.
88. Wan H, Vissink A, Sharma PK. Enhancement in Xerostomia Patient Salivary Lubrication Using a Mucoadhesive. J Dent Res 2020;**99**(8):914-21 doi: 10.1177/0022034520917675 [published Online First: 20200506].
89. Kapourani A, Kontogiannopoulos KN, Manioudaki AE, et al. A Review on Xerostomia and Its Various Management Strategies: The Role of Advanced Polymeric Materials in the Treatment Approaches. Polymers (Basel) 2022;**14**(5) doi: 10.3390/polym14050850 [published Online First: 20220222].
90. Laffleur F, Rottges S. Buccal adhesive chitosan conjugate comprising pilocarpine for xerostomia. Int J Biol Macromol 2019;**135**:1043-51 doi: 10.1016/j.ijbiomac.2019.05.219 [published Online First: 20190531].
91. Treijtel N, Groenendaal-van de Meent D, Michon I, et al. Pilocarpine-Induced Effects on Salivary Secretion as a Pharmacological Biomarker for Cholinergic Parasympathetic Activation. Clin Pharmacol Drug Dev 2022;**11**(1):25-33 doi: 10.1002/cpdd.1048 [published Online First: 20211126].
92. Horiot JC, Lipinski F, Schraub S, et al. Post-radiation severe xerostomia relieved by pilocarpine: a prospective French cooperative study. Radiother Oncol 2000;**55**(3):233-9 doi: 10.1016/s0167-8140(99)00018-3.
93. Haddad P, Karimi M. A randomized, double-blind, placebo-controlled trial of concomitant pilocarpine with head and neck irradiation for prevention of radiation-induced xerostomia. Radiother Oncol 2002;**64**(1):29-32 doi: 10.1016/s0167-8140(02)00104-4.
94. Warde P, O'Sullivan B, Aslanidis J, et al. A Phase III placebo-controlled trial of oral pilocarpine in patients undergoing radiotherapy for head-and-neck cancer. Int J Radiat Oncol Biol Phys 2002;**54**(1):9-13 doi: 10.1016/s0360-3016(02)02890-0.
95. Kapourani A, Kontogiannopoulos KN, Barmpalexis P. A Review on the Role of Pilocarpine on the Management of Xerostomia and the Importance of the Topical Administration Systems Development. Pharmaceuticals (Basel) 2022;**15**(6) doi: 10.3390/ph15060762 [published Online First: 20220618].
96. Motamed B, Alaee A, Azizi A, Jahandar H, Fard MJK, Jafari A. Comparison of the 1 and 2% pilocarpine mouthwash in a xerostomic population: a randomized clinical trial. BMC Oral Health 2022;**22**(1):548 doi: 10.1186/s12903-022-02576-6 [published Online First: 20221201].
97. Chambers MS, Posner M, Jones CU, et al. Cevimeline for the treatment of postirradiation xerostomia in patients with head and neck cancer. Int J Radiat Oncol Biol Phys 2007;**68**(4):1102-9 doi: 10.1016/j.ijrobp.2007.01.019 [published Online First: 20070326].
98. Chambers MS, Jones CU, Biel MA, et al. Open-label, long-term safety study of cevimeline in the treatment of postirradiation xerostomia. Int J Radiat Oncol Biol Phys

2007;**69**(5):1369-76 doi: 10.1016/j.ijrobp.2007.05.024 [published Online First: 20070912].
99. Brimhall J, Jhaveri MA, Yepes JF. Efficacy of cevimeline vs. pilocarpine in the secretion of saliva: a pilot study. Spec Care Dentist 2013;**33**(3):123-7 doi: 10.1111/scd.12010 [published Online First: 20130107].
100. Nanni JM, Nguyen KH, Alford CE, et al. Assessment of bromhexine as a treatment regimen in Sjogren's syndrome-like disease in the NOD (non-obese diabetic) mouse. Clin Exp Rheumatol 1997;**15**(5):515-21.
101. Adachi K, Ono M, Kawamura A, Yuki M, Fujishiro H, Kinoshita Y. Nizatidine and cisapride enhance salivary secretion in humans. Aliment Pharmacol Ther 2002;**16**(2):297-301 doi: 10.1046/j.1365-2036.2002.01159.x.
102. de Almeida Pdel V, Gregio AM, Machado MA, de Lima AA, Azevedo LR. Saliva composition and functions: a comprehensive review. J Contemp Dent Pract 2008;**9**(3):72-80 [published Online First: 20080301].
103. Kondo Y, Nakamoto T, Jaramillo Y, Choi S, Catalan MA, Melvin JE. Functional differences in the acinar cells of the murine major salivary glands. J Dent Res 2015;**94**(5):715-21 doi: 10.1177/0022034515570943 [published Online First: 20150213].
104. Roukema PA, Oderkerk CH, Salkinoga-Salonen MS. The murine sublingual and submandibular mucins. Their isolation and characterization. Biochim Biophys Acta 1976;**428**(2):432-40 doi: 10.1016/0304-4165(76)90051-9.
105. Duncan Lyngdoh RH, Schaefer HF, 3rd. Elementary lesions in DNA subunits: electron, hydrogen atom, proton, and hydride transfers. Acc Chem Res 2009;**42**(4):563-72 doi: 10.1021/ar800077q.
106. Reisz JA, Bansal N, Qian J, Zhao W, Furdui CM. Effects of ionizing radiation on biological molecules--mechanisms of damage and emerging methods of detection. Antioxid Redox Signal 2014;**21**(2):260-92 doi: 10.1089/ars.2013.5489 [published Online First: 20140221].
107. Zhang C, Xiang B. The underlying mechanisms and strategies of DNA damage and repair in radiation sialadenitis. Oral Dis 2021 doi: 10.1111/odi.14078 [published Online First: 20211112].
108. Meyer S, Chibly AM, Burd R, Limesand KH. Insulin-Like Growth Factor-1-Mediated DNA Repair in Irradiated Salivary Glands Is Sirtuin-1 Dependent. J Dent Res 2017;**96**(2):225-32 doi: 10.1177/0022034516677529 [published Online First: 20161116].
109. Finkel T, Deng CX, Mostoslavsky R. Recent progress in the biology and physiology of sirtuins. Nature 2009;**460**(7255):587-91 doi: 10.1038/nature08197.
110. Limesand KH, Avila JL, Victory K, et al. Insulin-like growth factor-1 preserves salivary gland function after fractionated radiation. Int J Radiat Oncol Biol Phys 2010;**78**(2):579-86 doi: 10.1016/j.ijrobp.2010.03.035 [published Online First: 20100716].
111. Barnum KJ, O'Connell MJ. Cell cycle regulation by checkpoints. Methods Mol Biol 2014;**1170**:29-40 doi: 10.1007/978-1-4939-0888-2_2.
112. Mitchell GC, Fillinger JL, Sittadjody S, Avila JL, Burd R, Limesand KH. IGF1 activates cell cycle arrest following irradiation by reducing binding of DeltaNp63 to the p21 promoter. Cell Death Dis 2010;**1**(6):e50 doi: 10.1038/cddis.2010.28.
113. Martin KL, Hill GA, Klein RR, Arnett DG, Burd R, Limesand KH. Prevention of radiation-induced salivary gland dysfunction utilizing a CDK inhibitor in a mouse model. PLoS

One 2012;**7**(12):e51363 doi: 10.1371/journal.pone.0051363 [published Online First: 20121207].
114. Limesand KH, Schwertfeger KL, Anderson SM. MDM2 is required for suppression of apoptosis by activated Akt1 in salivary acinar cells. Mol Cell Biol 2006;**26**(23):8840-56 doi: 10.1128/MCB.01846-05 [published Online First: 20060918].
115. Avila JL, Grundmann O, Burd R, Limesand KH. Radiation-induced salivary gland dysfunction results from p53-dependent apoptosis. Int J Radiat Oncol Biol Phys 2009;**73**(2):523-9 doi: 10.1016/j.ijrobp.2008.09.036.
116. Arany S, Benoit DS, Dewhurst S, Ovitt CE. Nanoparticle-mediated gene silencing confers radioprotection to salivary glands in vivo. Mol Ther 2013;**21**(6):1182-94 doi: 10.1038/mt.2013.42 [published Online First: 20130319].
117. Bralic M, Muhvic-Urek M, Stemberga V, et al. Cell death and cell proliferation in mouse submandibular gland during early post-irradiation phase. Acta Med Okayama 2005;**59**(4):153-9 doi: 10.18926/AMO/31948.
118. Ogawara Y, Kishishita S, Obata T, et al. Akt enhances Mdm2-mediated ubiquitination and degradation of p53. J Biol Chem 2002;**277**(24):21843-50 doi: 10.1074/jbc.M109745200 [published Online First: 20020328].
119. Verheij M, Bartelink H. Radiation-induced apoptosis. Cell Tissue Res 2000;**301**(1):133-42 doi: 10.1007/s004410000188.
120. Choi JS, Shin HS, An HY, Kim YM, Lim JY. Radioprotective effects of Keratinocyte Growth Factor-1 against irradiation-induced salivary gland hypofunction. Oncotarget 2017;**8**(8):13496-508 doi: 10.18632/oncotarget.14583.
121. Humphries MJ, Limesand KH, Schneider JC, Nakayama KI, Anderson SM, Reyland ME. Suppression of apoptosis in the protein kinase Cdelta null mouse in vivo. J Biol Chem 2006;**281**(14):9728-37 doi: 10.1074/jbc.M507851200 [published Online First: 20060201].
122. Wie SM, Adwan TS, DeGregori J, Anderson SM, Reyland ME. Inhibiting tyrosine phosphorylation of protein kinase Cdelta (PKCdelta) protects the salivary gland from radiation damage. J Biol Chem 2014;**289**(15):10900-08 doi: 10.1074/jbc.M114.551366 [published Online First: 20140225].
123. Fimia GM, Piacentini M. Regulation of autophagy in mammals and its interplay with apoptosis. Cell Mol Life Sci 2010;**67**(10):1581-8 doi: 10.1007/s00018-010-0284-z [published Online First: 20100218].
124. Morgan-Bathke M, Hill GA, Harris ZI, et al. Autophagy correlates with maintenance of salivary gland function following radiation. Sci Rep 2014;**4**:5206 doi: 10.1038/srep05206 [published Online First: 20140606].
125. Morgan-Bathke M, Harris ZI, Arnett DG, et al. The Rapalogue, CCI-779, improves salivary gland function following radiation. PLoS One 2014;**9**(12):e113183 doi: 10.1371/journal.pone.0113183 [published Online First: 20141201].
126. Orhon I, Rocchi C, Villarejo-Zori B, et al. Autophagy induction during stem cell activation plays a key role in salivary gland self-renewal. Autophagy 2022;**18**(2):293-308 doi: 10.1080/15548627.2021.1924036 [published Online First: 20210519].
127. Marmary Y, Adar R, Gaska S, et al. Radiation-Induced Loss of Salivary Gland Function Is Driven by Cellular Senescence and Prevented by IL6 Modulation. Cancer Res 2016;**76**(5):1170-80 doi: 10.1158/0008-5472.CAN-15-1671 [published Online First: 20160112].

128. Hu L, Du C, Yang Z, et al. Transient Activation of Hedgehog Signaling Inhibits Cellular Senescence and Inflammation in Radiated Swine Salivary Glands through Preserving Resident Macrophages. Int J Mol Sci 2021;**22**(24) doi: 10.3390/ijms222413493 [published Online First: 20211216].
129. Peng X, Wu Y, Brouwer U, et al. Cellular senescence contributes to radiation-induced hyposalivation by affecting the stem/progenitor cell niche. Cell Death Dis 2020;**11**(10):854 doi: 10.1038/s41419-020-03074-9 [published Online First: 20201014].
130. Hai B, Zhao Q, Deveau MA, Liu F. Delivery of Sonic Hedgehog Gene Repressed Irradiation-induced Cellular Senescence in Salivary Glands by Promoting DNA Repair and Reducing Oxidative Stress. Theranostics 2018;**8**(4):1159-67 doi: 10.7150/thno.23373 [published Online First: 20180113].
131. Wang XY, Yu J, Zhang FY, Liu KJ, Xiang B. Phenylephrine Alleviates (131)I Radiation Damage in Submandibular Gland Through Maintaining Mitochondrial Homeostasis. Int J Radiat Oncol Biol Phys 2019;**104**(3):644-55 doi: 10.1016/j.ijrobp.2019.02.048 [published Online First: 20190304].
132. Liu X, Subedi KP, Zheng C, Ambudkar I. Mitochondria-targeted antioxidant protects against irradiation-induced salivary gland hypofunction. Sci Rep 2021;**11**(1):7690 doi: 10.1038/s41598-021-86927-3 [published Online First: 20210408].
133. Ren J, Huang R, Li Y, Chen R, Tian H, Liu C. Radioprotective effects and mechanism of HL-003 on radiation-induced salivary gland damage in mice. Sci Rep 2022;**12**(1):8419 doi: 10.1038/s41598-022-12581-y [published Online First: 20220519].
134. Sun YM, Wang XY, Zhou XR, et al. Salidroside Ameliorates Radiation Damage by Reducing Mitochondrial Oxidative Stress in the Submandibular Gland. Antioxidants (Basel) 2022;**11**(7) doi: 10.3390/antiox11071414 [published Online First: 20220721].
135. Gilman KE, Camden JM, Klein RR, Zhang Q, Weisman GA, Limesand KH. P2X7 receptor deletion suppresses gamma-radiation-induced hyposalivation. Am J Physiol Regul Integr Comp Physiol 2019;**316**(5):R687-R96 doi: 10.1152/ajpregu.00192.2018 [published Online First: 20190320].
136. Gilman KE, Camden JM, Woods LT, Weisman GA, Limesand KH. Indomethacin Treatment Post-irradiation Improves Mouse Parotid Salivary Gland Function via Modulation of Prostaglandin E(2) Signaling. Front Bioeng Biotechnol 2021;**9**:697671 doi: 10.3389/fbioe.2021.697671 [published Online First: 20210721].
137. Proctor GB, Carpenter GH. Regulation of salivary gland function by autonomic nerves. Auton Neurosci 2007;**133**(1):3-18 doi: 10.1016/j.autneu.2006.10.006 [published Online First: 20061206].
138. Knox SM, Lombaert IM, Reed X, Vitale-Cross L, Gutkind JS, Hoffman MP. Parasympathetic innervation maintains epithelial progenitor cells during salivary organogenesis. Science 2010;**329**(5999):1645-7 doi: 10.1126/science.1192046.
139. Knox SM, Lombaert IM, Haddox CL, et al. Parasympathetic stimulation improves epithelial organ regeneration. Nat Commun 2013;**4**:1494 doi: 10.1038/ncomms2493.
140. Heuckeroth RO, Enomoto H, Grider JR, et al. Gene targeting reveals a critical role for neurturin in the development and maintenance of enteric, sensory, and parasympathetic neurons. Neuron 1999;**22**(2):253-63 doi: 10.1016/s0896-6273(00)81087-9.
141. Ferreira JNA, Zheng C, Lombaert IMA, et al. Neurturin Gene Therapy Protects Parasympathetic Function to Prevent Irradiation-Induced Murine Salivary Gland

Hypofunction. Mol Ther Methods Clin Dev 2018;**9**:172-80 doi: 10.1016/j.omtm.2018.02.008 [published Online First: 20180223].
142. Lombaert IMA, Patel VN, Jones CE, et al. CERE-120 Prevents Irradiation-Induced Hypofunction and Restores Immune Homeostasis in Porcine Salivary Glands. Mol Ther Methods Clin Dev 2020;**18**:839-55 doi: 10.1016/j.omtm.2020.07.016 [published Online First: 20200731].
143. Paris F, Fuks Z, Kang A, et al. Endothelial apoptosis as the primary lesion initiating intestinal radiation damage in mice. Science 2001;**293**(5528):293-7 doi: 10.1126/science.1060191.
144. Cotrim AP, Sowers A, Mitchell JB, Baum BJ. Prevention of irradiation-induced salivary hypofunction by microvessel protection in mouse salivary glands. Mol Ther 2007;**15**(12):2101-6 doi: 10.1038/sj.mt.6300296 [published Online First: 20070828].
145. Mizrachi A, Cotrim AP, Katabi N, Mitchell JB, Verheij M, Haimovitz-Friedman A. Radiation-Induced Microvascular Injury as a Mechanism of Salivary Gland Hypofunction and Potential Target for Radioprotectors. Radiat Res 2016;**186**(2):189-95 doi: 10.1667/RR14431.1 [published Online First: 20160726].
146. Lombaert IM, Brunsting JF, Wierenga PK, Kampinga HH, de Haan G, Coppes RP. Cytokine treatment improves parenchymal and vascular damage of salivary glands after irradiation. Clin Cancer Res 2008;**14**(23):7741-50 doi: 10.1158/1078-0432.CCR-08-1449.
147. Davis MA, Reynolds AB. Blocked acinar development, E-cadherin reduction, and intraepithelial neoplasia upon ablation of p120-catenin in the mouse salivary gland. Dev Cell 2006;**10**(1):21-31 doi: 10.1016/j.devcel.2005.12.004.
148. Wong WY, Pier M, Limesand KH. Persistent disruption of lateral junctional complexes and actin cytoskeleton in parotid salivary glands following radiation treatment. Am J Physiol Regul Integr Comp Physiol 2018;**315**(4):R656-R67 doi: 10.1152/ajpregu.00388.2017 [published Online First: 20180613].
149. Yao QT, Wu YH, Liu SH, et al. Pilocarpine improves submandibular gland dysfunction in irradiated rats by downregulating the tight junction protein claudin-4. Oral Dis 2022;**28**(6):1528-38 doi: 10.1111/odi.13870 [published Online First: 20210423].
150. Wong WY, Allie S, Limesand KH. PKCzeta and JNK signaling regulate radiation-induced compensatory proliferation in parotid salivary glands. PLoS One 2019;**14**(7):e0219572 doi: 10.1371/journal.pone.0219572 [published Online First: 20190709].
151. Peter B, Van Waarde MA, Vissink A, s-Gravenmade EJ, Konings AW. Radiation-induced cell proliferation in the parotid and submandibular glands of the rat. Radiat Res 1994;**140**(2):257-65.
152. Friedrich RE, Hieke N, Stern C, et al. DNA-flow cytometry, DNA-image cytometry and proliferation index (MIB-5) in irradiated rat salivary glands and salivary gland tumors. In Vivo 2004;**18**(2):213-22.
153. Chibly AM, Wong WY, Pier M, et al. aPKCzeta-dependent Repression of Yap is Necessary for Functional Restoration of Irradiated Salivary Glands with IGF-1. Sci Rep 2018;**8**(1):6347 doi: 10.1038/s41598-018-24678-4 [published Online First: 20180420].
154. Grundmann O, Fillinger JL, Victory KR, Burd R, Limesand KH. Restoration of radiation therapy-induced salivary gland dysfunction in mice by post therapy IGF-1 administration. BMC Cancer 2010;**10**:417 doi: 10.1186/1471-2407-10-417 [published Online First: 20100810].

155. Lombaert IM, Brunsting JF, Wierenga PK, Kampinga HH, de Haan G, Coppes RP. Keratinocyte growth factor prevents radiation damage to salivary glands by expansion of the stem/progenitor pool. Stem Cells 2008;**26**(10):2595-601 doi: 10.1634/stemcells.2007-1034 [published Online First: 20080731].
156. Kowalczyk-Quintas C, Schneider P. Ectodysplasin A (EDA) - EDA receptor signalling and its pharmacological modulation. Cytokine Growth Factor Rev 2014;**25**(2):195-203 doi: 10.1016/j.cytogfr.2014.01.004 [published Online First: 20140123].
157. Hill G, Headon D, Harris ZI, Huttner K, Limesand KH. Pharmacological activation of the EDA/EDAR signaling pathway restores salivary gland function following radiation-induced damage. PLoS One 2014;**9**(11):e112840 doi: 10.1371/journal.pone.0112840 [published Online First: 20141119].
158. Emmerson E, Knox SM. Salivary gland stem cells: A review of development, regeneration and cancer. Genesis 2018;**56**(5):e23211 doi: 10.1002/dvg.23211 [published Online First: 20180504].
159. Lombaert I, Movahednia MM, Adine C, Ferreira JN. Concise Review: Salivary Gland Regeneration: Therapeutic Approaches from Stem Cells to Tissue Organoids. Stem Cells 2017;**35**(1):97-105 doi: 10.1002/stem.2455 [published Online First: 20160715].
160. Emmerson E, May AJ, Berthoin L, et al. Salivary glands regenerate after radiation injury through SOX2-mediated secretory cell replacement. EMBO Mol Med 2018;**10**(3) doi: 10.15252/emmm.201708051.
161. Pringle S, Van Os R, Coppes RP. Concise review: Adult salivary gland stem cells and a potential therapy for xerostomia. Stem Cells 2013;**31**(4):613-9 doi: 10.1002/stem.1327.
162. Aure MH, Konieczny SF, Ovitt CE. Salivary gland homeostasis is maintained through acinar cell self-duplication. Dev Cell 2015;**33**(2):231-7 doi: 10.1016/j.devcel.2015.02.013 [published Online First: 20150402].
163. Yoshida S, Ohbo K, Takakura A, et al. Sgn1, a basic helix-loop-helix transcription factor delineates the salivary gland duct cell lineage in mice. Dev Biol 2001;**240**(2):517-30 doi: 10.1006/dbio.2001.0473.
164. Kimoto M, Yura Y, Kishino M, Toyosawa S, Ogawa Y. Label-retaining cells in the rat submandibular gland. J Histochem Cytochem 2008;**56**(1):15-24 doi: 10.1369/jhc.7A7269.2007 [published Online First: 20070917].
165. Chibly AM, Querin L, Harris Z, Limesand KH. Label-retaining cells in the adult murine salivary glands possess characteristics of adult progenitor cells. PLoS One 2014;**9**(9):e107893 doi: 10.1371/journal.pone.0107893 [published Online First: 20140919].
166. Kim YJ, Kwon HJ, Shinozaki N, et al. Comparative analysis of ABCG2-expressing and label-retaining cells in mouse submandibular gland. Cell Tissue Res 2008;**334**(1):47-53 doi: 10.1007/s00441-008-0667-8 [published Online First: 20080808].
167. Nguyen VT, Dawson P, Zhang Q, Harris Z, Limesand KH. Administration of growth factors promotes salisphere formation from irradiated parotid salivary glands. PLoS One 2018;**13**(3):e0193942 doi: 10.1371/journal.pone.0193942 [published Online First: 20180328].
168. Ambudkar I. Calcium signaling defects underlying salivary gland dysfunction. Biochim Biophys Acta Mol Cell Res 2018;**1865**(11 Pt B):1771-77 doi: 10.1016/j.bbamcr.2018.07.002 [published Online First: 20180710].

169. Liu X, Cotrim A, Teos L, et al. Loss of TRPM2 function protects against irradiation-induced salivary gland dysfunction. Nat Commun 2013;**4**:1515 doi: 10.1038/ncomms2526.
170. Liu X, Gong B, de Souza LB, et al. Radiation inhibits salivary gland function by promoting STIM1 cleavage by caspase-3 and loss of SOCE through a TRPM2-dependent pathway. Sci Signal 2017;**10**(482) doi: 10.1126/scisignal.aal4064 [published Online First: 20170606].
171. Sperber H, Mathieu J, Wang Y, et al. The metabolome regulates the epigenetic landscape during naive-to-primed human embryonic stem cell transition. Nat Cell Biol 2015;**17**(12):1523-35 doi: 10.1038/ncb3264 [published Online First: 20151116].
172. Li X, Gianoulis TA, Yip KY, Gerstein M, Snyder M. Extensive in vivo metabolite-protein interactions revealed by large-scale systematic analyses. Cell 2010;**143**(4):639-50 doi: 10.1016/j.cell.2010.09.048 [published Online First: 20101028].
173. Wellen KE, Hatzivassiliou G, Sachdeva UM, Bui TV, Cross JR, Thompson CB. ATP-citrate lyase links cellular metabolism to histone acetylation. Science 2009;**324**(5930):1076-80 doi: 10.1126/science.1164097.
174. Zhao J, Xie C, Wang K, et al. Comprehensive analysis of transcriptomics and metabolomics to understand triptolide-induced liver injury in mice. Toxicol Lett 2020;**333**:290-302 doi: 10.1016/j.toxlet.2020.08.007 [published Online First: 20200821].
175. Nowinski SM, Solmonson A, Rusin SF, et al. Mitochondrial fatty acid synthesis coordinates oxidative metabolism in mammalian mitochondria. Elife 2020;**9** doi: 10.7554/eLife.58041 [published Online First: 20200817].
176. Rinschen MM, Ivanisevic J, Giera M, Siuzdak G. Identification of bioactive metabolites using activity metabolomics. Nat Rev Mol Cell Biol 2019;**20**(6):353-67 doi: 10.1038/s41580-019-0108-4.
177. Schrimpe-Rutledge AC, Codreanu SG, Sherrod SD, McLean JA. Untargeted Metabolomics Strategies-Challenges and Emerging Directions. J Am Soc Mass Spectrom 2016;**27**(12):1897-905 doi: 10.1007/s13361-016-1469-y [published Online First: 20160913].
178. Zhou B, Xiao JF, Tuli L, Ressom HW. LC-MS-based metabolomics. Mol Biosyst 2012;**8**(2):470-81 doi: 10.1039/c1mb05350g [published Online First: 20111101].
179. Emwas AH. The strengths and weaknesses of NMR spectroscopy and mass spectrometry with particular focus on metabolomics research. Methods Mol Biol 2015;**1277**:161-93 doi: 10.1007/978-1-4939-2377-9_13.
180. Lapa B, Goncalves AC, Jorge J, et al. Acute myeloid leukemia sensitivity to metabolic inhibitors: glycolysis showed to be a better therapeutic target. Med Oncol 2020;**37**(8):72 doi: 10.1007/s12032-020-01394-6 [published Online First: 20200728].
181. Boroughs LK, DeBerardinis RJ. Metabolic pathways promoting cancer cell survival and growth. Nat Cell Biol 2015;**17**(4):351-9 doi: 10.1038/ncb3124 [published Online First: 20150316].
182. Fujii T, Khawaja MR, DiNardo CD, Atkins JT, Janku F. Targeting isocitrate dehydrogenase (IDH) in cancer. Discov Med 2016;**21**(117):373-80.
183. Johnson CH, Ivanisevic J, Siuzdak G. Metabolomics: beyond biomarkers and towards mechanisms. Nat Rev Mol Cell Biol 2016;**17**(7):451-9 doi: 10.1038/nrm.2016.25 [published Online First: 20160316].

184. Masoodi M, Gastaldelli A, Hyotylainen T, et al. Metabolomics and lipidomics in NAFLD: biomarkers and non-invasive diagnostic tests. Nat Rev Gastroenterol Hepatol 2021;**18**(12):835-56 doi: 10.1038/s41575-021-00502-9 [published Online First: 20210910].
185. Gramatyka M, Boguszewicz Ł, Ciszek M, Gabrys D, Kulik R, Sokol M. Metabolic changes in mice cardiac tissue after low-dose irradiation revealed by 1H NMR spectroscopy. J Radiat Res 2020;**61**(1):14-26 doi: 10.1093/jrr/rrz079.
186. Tyburski JB, Patterson AD, Krausz KW, et al. Radiation metabolomics. 2. Dose- and time-dependent urinary excretion of deaminated purines and pyrimidines after sublethal gamma-radiation exposure in mice. Radiat Res 2009;**172**(1):42-57 doi: 10.1667/RR1703.1.
187. Mak TD, Tyburski JB, Krausz KW, Kalinich JF, Gonzalez FJ, Fornace AJ, Jr. Exposure to ionizing radiation reveals global dose- and time-dependent changes in the urinary metabolome of rat. Metabolomics 2015;**11**(5):1082-94 doi: 10.1007/s11306-014-0765-4 [published Online First: 20141220].
188. Laiakis EC, Mak TD, Anizan S, et al. Development of a metabolomic radiation signature in urine from patients undergoing total body irradiation. Radiat Res 2014;**181**(4):350-61 doi: 10.1667/RR13567.1 [published Online First: 20140327].
189. Pannkuk EL, Laiakis EC, Authier S, Wong K, Fornace AJ, Jr. Global Metabolomic Identification of Long-Term Dose-Dependent Urinary Biomarkers in Nonhuman Primates Exposed to Ionizing Radiation. Radiat Res 2015;**184**(2):121-33 doi: 10.1667/rr14091.1 [published Online First: 20150731].
190. Chen C, Brenner DJ, Brown TR. Identification of urinary biomarkers from X-irradiated mice using NMR spectroscopy. Radiat Res 2011;**175**(5):622-30 doi: 10.1667/RR2388.1 [published Online First: 20110221].
191. Wang Q, Gao P, Wang X, Duan Y. Investigation and identification of potential biomarkers in human saliva for the early diagnosis of oral squamous cell carcinoma. Clin Chim Acta 2014;**427**:79-85 doi: 10.1016/j.cca.2013.10.004 [published Online First: 20131019].
192. Maan K, Tyagi R, Dutta A, Bakhshi R, Rana P. Comparative metabolic profiles of total and partial body radiation exposure in mice using an untargeted metabolomics approach. Metabolomics 2020;**16**(12):124 doi: 10.1007/s11306-020-01742-7 [published Online First: 20201127].
193. Tyagi R, Maan K, Khushu S, Rana P. Urine metabolomics based prediction model approach for radiation exposure. Sci Rep 2020;**10**(1):16063 doi: 10.1038/s41598-020-72426-4 [published Online First: 20200930].
194. Maan K, Baghel R, Bakhshi R, Dhariwal S, Tyagi R, Rana P. An integrative chemometric approach and correlative metabolite networking of LC-MS and (1)H NMR based urine metabolomics for radiation signatures. Mol Omics 2022;**18**(3):214-25 doi: 10.1039/d1mo00399b [published Online First: 20220328].
195. Laiakis EC, Strawn SJ, Brenner DJ, Fornace AJ, Jr. Assessment of Saliva as a Potential Biofluid for Biodosimetry: A Pilot Metabolomics Study in Mice. Radiat Res 2016;**186**(1):92-7 doi: 10.1667/RR14433.1 [published Online First: 20160622].
196. Haritwal T, Maan K, Rana P, et al. Trichostatin A, an epigenetic modifier, mitigates radiation-induced androphysiological anomalies and metabolite changes in mice as evident from NMR-based metabolomics. Int J Radiat Biol 2019;**95**(4):443-51 doi: 10.1080/09553002.2018.1524989 [published Online First: 20181011].

197. Xiao X, Hu M, Zhang X, Hu JZ. NMR-based Metabolomics Analysis of Liver from C57BL/6 Mouse Exposed to Ionizing Radiation. Radiat Res 2017;**188**(1):44-55 doi: 10.1667/RR14602.1 [published Online First: 20170502].
198. Kurland IJ, Broin PO, Golden A, et al. Integrative Metabolic Signatures for Hepatic Radiation Injury. PLoS One 2015;**10**(6):e0124795 doi: 10.1371/journal.pone.0124795 [published Online First: 20150605].
199. Salah M, Osuga S, Nakahana M, et al. Elucidation of gastrointestinal dysfunction in response to irradiation using metabolomics. Biochem Biophys Rep 2020;**23**:100789 doi: 10.1016/j.bbrep.2020.100789 [published Online First: 20200729].
200. Hafner L, Walsh L, Schneider U. Cancer incidence risks above and below 1 Gy for radiation protection in space. Life Sci Space Res (Amst) 2021;**28**:41-56 doi: 10.1016/j.lssr.2020.09.001 [published Online First: 20200914].
201. Laiakis EC, Shuryak I, Deziel A, et al. Effects of Low Dose Space Radiation Exposures on the Splenic Metabolome. Int J Mol Sci 2021;**22**(6) doi: 10.3390/ijms22063070 [published Online First: 20210317].
202. Vigneulle RM, Rao S, Fasano A, MacVittie TJ. Structural and functional alterations of the gastrointestinal tract following radiation-induced injury in the rhesus monkey. Dig Dis Sci 2002;**47**(7):1480-91 doi: 10.1023/a:1015846514471.
203. MacVittie TJ, Farese AM, Bennett A, et al. The acute gastrointestinal subsyndrome of the acute radiation syndrome: a rhesus macaque model. Health Phys 2012;**103**(4):411-26 doi: 10.1097/HP.0b013e31826525f0.
204. van Kleef EM, Zurcher C, Oussoren YG, et al. Long-term effects of total-body irradiation on the kidney of Rhesus monkeys. Int J Radiat Biol 2000;**76**(5):641-8 doi: 10.1080/095530000138303.
205. Johnson CH, Patterson AD, Krausz KW, et al. Radiation metabolomics. 5. Identification of urinary biomarkers of ionizing radiation exposure in nonhuman primates by mass spectrometry-based metabolomics. Radiat Res 2012;**178**(4):328-40 doi: 10.1667/rr2950.1 [published Online First: 20120906].
206. Crook A, De Lima Leite A, Payne T, et al. Radiation exposure induces cross-species temporal metabolic changes that are mitigated in mice by amifostine. Sci Rep 2021;**11**(1):14004 doi: 10.1038/s41598-021-93401-7 [published Online First: 20210707].
207. Pannkuk EL, Laiakis EC, Garcia M, Fornace AJ, Jr., Singh VK. Nonhuman Primates with Acute Radiation Syndrome: Results from a Global Serum Metabolomics Study after 7.2 Gy Total-Body Irradiation. Radiat Res 2018;**190**(6):576-83 doi: 10.1667/RR15167.1 [published Online First: 20180905].
208. Pannkuk EL, Laiakis EC, Gill K, et al. Liquid Chromatography-Mass Spectrometry-Based Metabolomics of Nonhuman Primates after 4 Gy Total Body Radiation Exposure: Global Effects and Targeted Panels. J Proteome Res 2019;**18**(5):2260-69 doi: 10.1021/acs.jproteome.9b00101 [published Online First: 20190318].
209. Pannkuk EL, Laiakis EC, Mak TD, et al. A Lipidomic and Metabolomic Serum Signature from Nonhuman Primates Exposed to Ionizing Radiation. Metabolomics 2016;**12**(5) doi: 10.1007/s11306-016-1010-0 [published Online First: 20160315].
210. Kumar P, Wang P, Farese AM, MacVittie TJ, Kane MA. Metabolomics of Multiorgan Radiation Injury in Non-human Primate Model Reveals System-wide Metabolic Perturbations. Health Phys 2021;**121**(4):395-405 doi: 10.1097/HP.0000000000001472.

211. Boguszewicz L, Bielen A, Mrochem-Kwarciak J, et al. NMR-based metabolomics in real-time monitoring of treatment induced toxicity and cachexia in head and neck cancer: a method for early detection of high risk patients. Metabolomics 2019;**15**(8):110 doi: 10.1007/s11306-019-1576-4 [published Online First: 20190816].
212. Boguszewicz L, Bielen A, Ciszek M, et al. NMR-Based Metabolomics in Investigation of the Radiation Induced Changes in Blood Serum of Head and Neck Cancer Patients and Its Correlation with the Tissue Volumes Exposed to the Particulate Doses. Int J Mol Sci 2021;**22**(12) doi: 10.3390/ijms22126310 [published Online First: 20210611].
213. Hansen TV, Simonsen MK, Nielsen FC, Hundrup YA. Collection of blood, saliva, and buccal cell samples in a pilot study on the Danish nurse cohort: comparison of the response rate and quality of genomic DNA. Cancer Epidemiol Biomarkers Prev 2007;**16**(10):2072-6 doi: 10.1158/1055-9965.EPI-07-0611.
214. Rathnayake N, Akerman S, Klinge B, et al. Salivary biomarkers for detection of systemic diseases. PLoS One 2013;**8**(4):e61356 doi: 10.1371/journal.pone.0061356 [published Online First: 20130424].
215. Pernot E, Cardis E, Badie C. Usefulness of saliva samples for biomarker studies in radiation research. Cancer Epidemiol Biomarkers Prev 2014;**23**(12):2673-80 doi: 10.1158/1055-9965.EPI-14-0588.
216. Zhang A, Sun H, Wang X. Saliva metabolomics opens door to biomarker discovery, disease diagnosis, and treatment. Appl Biochem Biotechnol 2012;**168**(6):1718-27 doi: 10.1007/s12010-012-9891-5 [published Online First: 20120913].
217. Moore HD, Ivey RG, Voytovich UJ, et al. The human salivary proteome is radiation responsive. Radiat Res 2014;**181**(5):521-30 doi: 10.1667/RR13586.1 [published Online First: 20140410].
218. Laiakis EC, Nishita D, Bujold K, et al. Salivary Metabolomics of Total Body Irradiated Nonhuman Primates Reveals Long-Term Normal Tissue Responses to Radiation. Int J Radiat Oncol Biol Phys 2019;**105**(4):843-51 doi: 10.1016/j.ijrobp.2019.07.017 [published Online First: 20190725].
219. Herrala M, Mikkonen JJW, Pesonen P, et al. Variability of salivary metabolite levels in patients with Sjogren's syndrome. J Oral Sci 2020;**63**(1):22-26 doi: 10.2334/josnusd.19-0504 [published Online First: 20201029].
220. Ishikawa S, Sugimoto M, Kitabatake K, et al. Effect of timing of collection of salivary metabolomic biomarkers on oral cancer detection. Amino Acids 2017;**49**(4):761-70 doi: 10.1007/s00726-017-2378-5 [published Online First: 20170118].
221. Toan NK, Tai NC, Kim SA, Ahn SG. Choline Acetyltransferase Induces the Functional Regeneration of the Salivary Gland in Aging SAMP1/Kl -/- Mice. Int J Mol Sci 2021;**22**(1) doi: 10.3390/ijms22010404 [published Online First: 20210102].
222. Kageyama G, Saegusa J, Irino Y, et al. Metabolomics analysis of saliva from patients with primary Sjogren's syndrome. Clin Exp Immunol 2015;**182**(2):149-53 doi: 10.1111/cei.12683 [published Online First: 20150915].
223. Li Z, Mu Y, Guo C, et al. Analysis of the saliva metabolic signature in patients with primary Sjogren's syndrome. PLoS One 2022;**17**(6):e0269275 doi: 10.1371/journal.pone.0269275 [published Online First: 20220602].
224. Wu M, Li B, Zhang X, Sun G. Serum metabolomics reveals an innovative diagnostic model for salivary gland tumors. Anal Biochem 2022;**655**:114853 doi: 10.1016/j.ab.2022.114853 [published Online First: 20220812].

225. Liebsch C, Pitchika V, Pink C, et al. The Saliva Metabolome in Association to Oral Health Status. J Dent Res 2019;**98**(6):642-51 doi: 10.1177/0022034519842853 [published Online First: 20190426].
226. Ishikawa S, Sugimoto M, Edamatsu K, Sugano A, Kitabatake K, Iino M. Discrimination of oral squamous cell carcinoma from oral lichen planus by salivary metabolomics. Oral Dis 2020;**26**(1):35-42 doi: 10.1111/odi.13209 [published Online First: 20191113].
227. Toan NK, Kim SA, Ahn SG. Ascorbic acid induces salivary gland function through TET2/acetylcholine receptor signaling in aging SAMP1/Klotho (-/-) mice. Aging (Albany NY) 2022;**14**(15):6028-46 doi: 10.18632/aging.204213 [published Online First: 20220811].
228. Picard M, Scott-Boyer MP, Bodein A, Perin O, Droit A. Integration strategies of multi-omics data for machine learning analysis. Comput Struct Biotechnol J 2021;**19**:3735-46 doi: 10.1016/j.csbj.2021.06.030 [published Online First: 20210622].
229. Gerassy-Vainberg S, Blatt A, Danin-Poleg Y, et al. Radiation induces proinflammatory dysbiosis: transmission of inflammatory susceptibility by host cytokine induction. Gut 2018;**67**(1):97-107 doi: 10.1136/gutjnl-2017-313789 [published Online First: 20170424].
230. Guo H, Chou WC, Lai Y, et al. Multi-omics analyses of radiation survivors identify radioprotective microbes and metabolites. Science 2020;**370**(6516) doi: 10.1126/science.aay9097.
231. Li Y, Yan H, Zhang Y, et al. Alterations of the Gut Microbiome Composition and Lipid Metabolic Profile in Radiation Enteritis. Front Cell Infect Microbiol 2020;**10**:541178 doi: 10.3389/fcimb.2020.541178 [published Online First: 20201021].
232. Lewis JE, Kemp ML. Integration of machine learning and genome-scale metabolic modeling identifies multi-omics biomarkers for radiation resistance. Nat Commun 2021;**12**(1):2700 doi: 10.1038/s41467-021-22989-1 [published Online First: 20210511].
233. Ren S, Shao Y, Zhao X, et al. Integration of Metabolomics and Transcriptomics Reveals Major Metabolic Pathways and Potential Biomarker Involved in Prostate Cancer. Mol Cell Proteomics 2016;**15**(1):154-63 doi: 10.1074/mcp.M115.052381 [published Online First: 20151106].
234. Meller S, Meyer HA, Bethan B, et al. Integration of tissue metabolomics, transcriptomics and immunohistochemistry reveals ERG- and gleason score-specific metabolomic alterations in prostate cancer. Oncotarget 2016;**7**(2):1421-38 doi: 10.18632/oncotarget.6370.
235. Tan SK, Mahmud I, Fontanesi F, et al. Obesity-Dependent Adipokine Chemerin Suppresses Fatty Acid Oxidation to Confer Ferroptosis Resistance. Cancer Discov 2021;**11**(8):2072-93 doi: 10.1158/2159-8290.CD-20-1453 [published Online First: 20210323].
236. Yang F, Xiao Y, Ding JH, et al. Ferroptosis heterogeneity in triple-negative breast cancer reveals an innovative immunotherapy combination strategy. Cell Metab 2023;**35**(1):84-100 e8 doi: 10.1016/j.cmet.2022.09.021 [published Online First: 20221017].
237. da Silveira WA, Fazelinia H, Rosenthal SB, et al. Comprehensive Multi-omics Analysis Reveals Mitochondrial Stress as a Central Biological Hub for Spaceflight Impact. Cell 2020;**183**(5):1185-201 e20 doi: 10.1016/j.cell.2020.11.002.
238. Siegel RL, Miller KD, Jemal A. Cancer statistics, 2019. CA Cancer J Clin 2019;**69**(1):7-34 doi: 10.3322/caac.21551 [published Online First: 20190108].

239. Hammerlid E, Silander E, Hornestam L, Sullivan M. Health-related quality of life three years after diagnosis of head and neck cancer--a longitudinal study. Head Neck 2001;**23**(2):113-25 doi: 10.1002/1097-0347(200102)23:2<113::aid-hed1006>3.0.co;2-w.
240. Epstein JB, Robertson M, Emerton S, Phillips N, Stevenson-Moore P. Quality of life and oral function in patients treated with radiation therapy for head and neck cancer. Head Neck 2001;**23**(5):389-98 doi: 10.1002/hed.1049.
241. Pinna R, Campus G, Cumbo E, Mura I, Milia E. Xerostomia induced by radiotherapy: an overview of the physiopathology, clinical evidence, and management of the oral damage. Ther Clin Risk Manag 2015;**11**:171-88 doi: 10.2147/TCRM.S70652 [published Online First: 20150204].
242. Bockel S, Vallard A, Levy A, et al. Pharmacological modulation of radiation-induced oral mucosal complications. Cancer Radiother 2018;**22**(5):429-37 doi: 10.1016/j.canrad.2017.11.006 [published Online First: 20180526].
243. Goudarzi M, Mak TD, Chen C, Smilenov LB, Brenner DJ, Fornace AJ. The effect of low dose rate on metabolomic response to radiation in mice. Radiat Environ Biophys 2014;**53**(4):645-57 doi: 10.1007/s00411-014-0558-1 [published Online First: 20140722].
244. Subramanian A, Tamayo P, Mootha VK, et al. Gene set enrichment analysis: a knowledge-based approach for interpreting genome-wide expression profiles. Proc Natl Acad Sci U S A 2005;**102**(43):15545-50 doi: 10.1073/pnas.0506580102 [published Online First: 20050930].
245. Xia J, Wishart DS. MSEA: a web-based tool to identify biologically meaningful patterns in quantitative metabolomic data. Nucleic Acids Res 2010;**38**(Web Server issue):W71-7 doi: 10.1093/nar/gkq329 [published Online First: 20100510].
246. Ideker T, Ozier O, Schwikowski B, Siegel AF. Discovering regulatory and signalling circuits in molecular interaction networks. Bioinformatics 2002;**18 Suppl 1**:S233-40 doi: 10.1093/bioinformatics/18.suppl_1.s233.
247. Evans AM, DeHaven CD, Barrett T, Mitchell M, Milgram E. Integrated, nontargeted ultrahigh performance liquid chromatography/electrospray ionization tandem mass spectrometry platform for the identification and relative quantification of the small-molecule complement of biological systems. Anal Chem 2009;**81**(16):6656-67 doi: 10.1021/ac901536h.
248. Nieman DC, Shanely RA, Gillitt ND, Pappan KL, Lila MA. Serum metabolic signatures induced by a three-day intensified exercise period persist after 14 h of recovery in runners. J Proteome Res 2013;**12**(10):4577-84 doi: 10.1021/pr400717j [published Online First: 20130913].
249. Chong J, Wishart DS, Xia J. Using MetaboAnalyst 4.0 for Comprehensive and Integrative Metabolomics Data Analysis. Curr Protoc Bioinformatics 2019;**68**(1):e86 doi: 10.1002/cpbi.86.
250. Aittokallio T. Dealing with missing values in large-scale studies: microarray data imputation and beyond. Brief Bioinform 2010;**11**(2):253-64 doi: 10.1093/bib/bbp059 [published Online First: 20091204].
251. Liu D, Peck I, Dangi S, Schwarz KQ, Linte CA. A Statistical Shape Model Approach for Computing Left Ventricle Volume and Ejection Fraction Using Multi-plane Ultrasound Images. VipIMAGE 2019 (2019) 2019;**34**:540-50 doi: 10.1007/978-3-030-32040-9_55 [published Online First: 20190928].

252. Thevenot EA, Roux A, Xu Y, Ezan E, Junot C. Analysis of the Human Adult Urinary Metabolome Variations with Age, Body Mass Index, and Gender by Implementing a Comprehensive Workflow for Univariate and OPLS Statistical Analyses. J Proteome Res 2015;**14**(8):3322-35 doi: 10.1021/acs.jproteome.5b00354 [published Online First: 20150702].
253. Ito K, Murphy D. Application of ggplot2 to Pharmacometric Graphics. CPT Pharmacometrics Syst Pharmacol 2013;**2**(10):e79 doi: 10.1038/psp.2013.56 [published Online First: 20131016].
254. Caspi R, Billington R, Fulcher CA, et al. The MetaCyc database of metabolic pathways and enzymes. Nucleic Acids Res 2018;**46**(D1):D633-D39 doi: 10.1093/nar/gkx935.
255. Wishart DS, Jewison T, Guo AC, et al. HMDB 3.0--The Human Metabolome Database in 2013. Nucleic Acids Res 2013;**41**(Database issue):D801-7 doi: 10.1093/nar/gks1065 [published Online First: 20121117].
256. Kind T, Scholz M, Fiehn O. How large is the metabolome? A critical analysis of data exchange practices in chemistry. PLoS One 2009;**4**(5):e5440 doi: 10.1371/journal.pone.0005440 [published Online First: 20090505].
257. Ritchie ME, Phipson B, Wu D, et al. limma powers differential expression analyses for RNA-sequencing and microarray studies. Nucleic Acids Res 2015;**43**(7):e47 doi: 10.1093/nar/gkv007 [published Online First: 20150120].
258. Gu Z, Hubschmann D. Make Interactive Complex Heatmaps in R. Bioinformatics 2022;**38**(5):1460-62 doi: 10.1093/bioinformatics/btab806.
259. Bolger AM, Lohse M, Usadel B. Trimmomatic: a flexible trimmer for Illumina sequence data. Bioinformatics 2014;**30**(15):2114-20 doi: 10.1093/bioinformatics/btu170 [published Online First: 20140401].
260. de Sena Brandine G, Smith AD. Falco: high-speed FastQC emulation for quality control of sequencing data. F1000Res 2019;**8**:1874 doi: 10.12688/f1000research.21142.2 [published Online First: 20191107].
261. Kim D, Paggi JM, Park C, Bennett C, Salzberg SL. Graph-based genome alignment and genotyping with HISAT2 and HISAT-genotype. Nat Biotechnol 2019;**37**(8):907-15 doi: 10.1038/s41587-019-0201-4 [published Online First: 20190802].
262. Anders S, Pyl PT, Huber W. HTSeq--a Python framework to work with high-throughput sequencing data. Bioinformatics 2015;**31**(2):166-9 doi: 10.1093/bioinformatics/btu638 [published Online First: 20140925].
263. Love MI, Huber W, Anders S. Moderated estimation of fold change and dispersion for RNA-seq data with DESeq2. Genome Biol 2014;**15**(12):550 doi: 10.1186/s13059-014-0550-8.
264. Gu Z, Eils R, Schlesner M. Complex heatmaps reveal patterns and correlations in multidimensional genomic data. Bioinformatics 2016;**32**(18):2847-9 doi: 10.1093/bioinformatics/btw313 [published Online First: 20160520].
265. Cavill R, Kamburov A, Ellis JK, et al. Consensus-phenotype integration of transcriptomic and metabolomic data implies a role for metabolism in the chemosensitivity of tumour cells. PLoS Comput Biol 2011;**7**(3):e1001113 doi: 10.1371/journal.pcbi.1001113 [published Online First: 20110331].
266. Ghosh D. Wavelet-based Benjamini-Hochberg procedures for multiple testing under dependence. Math Biosci Eng 2019;**17**(1):56-72 doi: 10.3934/mbe.2020003.

267. Platig J, Castaldi PJ, DeMeo D, Quackenbush J. Bipartite Community Structure of eQTLs. PLoS Comput Biol 2016;**12**(9):e1005033 doi: 10.1371/journal.pcbi.1005033 [published Online First: 20160912].
268. Sergushichev AA, Loboda AA, Jha AK, et al. GAM: a web-service for integrated transcriptional and metabolic network analysis. Nucleic Acids Res 2016;**44**(W1):W194-200 doi: 10.1093/nar/gkw266 [published Online First: 20160420].
269. Brunk E, Sahoo S, Zielinski DC, et al. Recon3D enables a three-dimensional view of gene variation in human metabolism. Nat Biotechnol 2018;**36**(3):272-81 doi: 10.1038/nbt.4072 [published Online First: 20180219].
270. Kuhn M, von Mering C, Campillos M, Jensen LJ, Bork P. STITCH: interaction networks of chemicals and proteins. Nucleic Acids Res 2008;**36**(Database issue):D684-8 doi: 10.1093/nar/gkm795 [published Online First: 20071215].
271. Golla S, Golla JP, Krausz KW, et al. Metabolomic Analysis of Mice Exposed to Gamma Radiation Reveals a Systemic Understanding of Total-Body Exposure. Radiat Res 2017;**187**(5):612-29 doi: 10.1667/RR14592.1 [published Online First: 20170309].
272. Rubin P, Casarett GW. Clinical radiation pathology as applied to curative radiotherapy. Cancer 1968;**22**(4):767-78 doi: 10.1002/1097-0142(196810)22:4<767::aid-cncr2820220412>3.0.co;2-7.
273. Tilton SC, Matzke MM, Sowa MB, et al. Data integration reveals key homeostatic mechanisms following low dose radiation exposure. Toxicol Appl Pharmacol 2015;**285**(1):1-11 doi: 10.1016/j.taap.2015.01.019 [published Online First: 20150202].
274. Su LJ, Zhang JH, Gomez H, et al. Reactive Oxygen Species-Induced Lipid Peroxidation in Apoptosis, Autophagy, and Ferroptosis. Oxid Med Cell Longev 2019;**2019**:5080843 doi: 10.1155/2019/5080843 [published Online First: 20191013].
275. Chatterjee A. Reduced glutathione: a radioprotector or a modulator of DNA-repair activity? Nutrients 2013;**5**(2):525-42 doi: 10.3390/nu5020525 [published Online First: 20130207].
276. Grabon A, Bankaitis VA, McDermott MI. The interface between phosphatidylinositol transfer protein function and phosphoinositide signaling in higher eukaryotes. J Lipid Res 2019;**60**(2):242-68 doi: 10.1194/jlr.R089730 [published Online First: 20181130].
277. Ramos AR, Elong Edimo W, Erneux C. Phosphoinositide 5-phosphatase activities control cell motility in glioblastoma: Two phosphoinositides PI(4,5)P2 and PI(3,4)P2 are involved. Adv Biol Regul 2018;**67**:40-48 doi: 10.1016/j.jbior.2017.09.001 [published Online First: 20170905].
278. Iwakawa M, Hamada N, Imadome K, et al. Expression profiles are different in carbon ion-irradiated normal human fibroblasts and their bystander cells. Mutat Res 2008;**642**(1-2):57-67 doi: 10.1016/j.mrfmmm.2008.04.007 [published Online First: 20080502].
279. Lupia E, Goffi A, De Giuli P, et al. Ablation of phosphoinositide 3-kinase-gamma reduces the severity of acute pancreatitis. Am J Pathol 2004;**165**(6):2003-11 doi: 10.1016/s0002-9440(10)63251-8.
280. Kolesnick R, Fuks Z. Radiation and ceramide-induced apoptosis. Oncogene 2003;**22**(37):5897-906 doi: 10.1038/sj.onc.1206702.
281. Obinata H, Hla T. Sphingosine 1-phosphate and inflammation. Int Immunol 2019;**31**(9):617-25 doi: 10.1093/intimm/dxz037.
282. Cheng JC, Chang HM, Liu PP, Leung PC. Sphingosine-1-phosphate induces COX-2 expression and PGE2 production in human granulosa cells through a S1P1/3-mediated

YAP signaling. Cell Signal 2016;**28**(6):643-51 doi: 10.1016/j.cellsig.2016.03.006 [published Online First: 20160317].
283. Olesch C, Ringel C, Brune B, Weigert A. Beyond Immune Cell Migration: The Emerging Role of the Sphingosine-1-phosphate Receptor S1PR4 as a Modulator of Innate Immune Cell Activation. Mediators Inflamm 2017;**2017**:6059203 doi: 10.1155/2017/6059203 [published Online First: 20170807].
284. Fransen M, Lismont C, Walton P. The Peroxisome-Mitochondria Connection: How and Why? Int J Mol Sci 2017;**18**(6) doi: 10.3390/ijms18061126 [published Online First: 20170524].
285. Lodhi IJ, Semenkovich CF. Peroxisomes: a nexus for lipid metabolism and cellular signaling. Cell Metab 2014;**19**(3):380-92 doi: 10.1016/j.cmet.2014.01.002 [published Online First: 20140206].
286. Su AI, Wiltshire T, Batalov S, et al. A gene atlas of the mouse and human protein-encoding transcriptomes. Proc Natl Acad Sci U S A 2004;**101**(16):6062-7 doi: 10.1073/pnas.0400782101 [published Online First: 20040409].
287. Waterham HR, Ferdinandusse S, Wanders RJ. Human disorders of peroxisome metabolism and biogenesis. Biochim Biophys Acta 2016;**1863**(5):922-33 doi: 10.1016/j.bbamcr.2015.11.015 [published Online First: 20151122].
288. Hunt MC, Siponen MI, Alexson SE. The emerging role of acyl-CoA thioesterases and acyltransferases in regulating peroxisomal lipid metabolism. Biochim Biophys Acta 2012;**1822**(9):1397-410 doi: 10.1016/j.bbadis.2012.03.009 [published Online First: 20120323].
289. Andreasson C, Ott M, Buttner S. Mitochondria orchestrate proteostatic and metabolic stress responses. EMBO Rep 2019;**20**(10):e47865 doi: 10.15252/embr.201947865 [published Online First: 20190918].
290. Cogliati S, Lorenzi I, Rigoni G, Caicci F, Soriano ME. Regulation of Mitochondrial Electron Transport Chain Assembly. J Mol Biol 2018;**430**(24):4849-73 doi: 10.1016/j.jmb.2018.09.016 [published Online First: 20181004].
291. Nicolson GL. Mitochondrial Dysfunction and Chronic Disease: Treatment With Natural Supplements. Integr Med (Encinitas) 2014;**13**(4):35-43.
292. Stein A, Sia EA. Mitochondrial DNA repair and damage tolerance. Front Biosci (Landmark Ed) 2017;**22**(5):920-43 doi: 10.2741/4525 [published Online First: 20170101].
293. Vanella A, Russo A, Acquaviva R, et al. L -propionyl-carnitine as superoxide scavenger, antioxidant, and DNA cleavage protector. Cell Biol Toxicol 2000;**16**(2):99-104 doi: 10.1023/a:1007638025856.
294. Goetzman ES, Prochownik EV. The Role for Myc in Coordinating Glycolysis, Oxidative Phosphorylation, Glutaminolysis, and Fatty Acid Metabolism in Normal and Neoplastic Tissues. Front Endocrinol (Lausanne) 2018;**9**:129 doi: 10.3389/fendo.2018.00129 [published Online First: 20180412].
295. Siegel RL, Miller KD, Fuchs HE, Jemal A. Cancer Statistics, 2021. CA Cancer J Clin 2021;**71**(1):7-33 doi: 10.3322/caac.21654 [published Online First: 20210112].
296. Poole ME, Sailer SL, Rosenman JG, et al. Chemoradiation for locally advanced squamous cell carcinoma of the head and neck for organ preservation and palliation. Arch Otolaryngol Head Neck Surg 2001;**127**(12):1446-50 doi: 10.1001/archotol.127.12.1446.
297. Davy C, Heathcote S. A systematic review of interventions to mitigate radiotherapy-induced oral mucositis in head and neck cancer patients. Support Care Cancer

2021;**29**(4):2187-202 doi: 10.1007/s00520-020-05548-0 [published Online First: 20200905].
298. Hoebers FJ, Kartachova M, de Bois J, et al. 99mTc Hynic-rh-Annexin V scintigraphy for in vivo imaging of apoptosis in patients with head and neck cancer treated with chemoradiotherapy. Eur J Nucl Med Mol Imaging 2008;**35**(3):509-18 doi: 10.1007/s00259-007-0624-x [published Online First: 20071110].
299. Epstein JB, Thariat J, Bensadoun RJ, et al. Oral complications of cancer and cancer therapy: from cancer treatment to survivorship. CA Cancer J Clin 2012;**62**(6):400-22 doi: 10.3322/caac.21157 [published Online First: 20120912].
300. Sullivan CA, Haddad RI, Tishler RB, Mahadevan A, Krane JF. Chemoradiation-induced cell loss in human submandibular glands. Laryngoscope 2005;**115**(6):958-64 doi: 10.1097/01.MLG.0000163340.90211.87.
301. van der Laan HP, Bijl HP, Steenbakkers RJ, et al. Acute symptoms during the course of head and neck radiotherapy or chemoradiation are strong predictors of late dysphagia. Radiother Oncol 2015;**115**(1):56-62 doi: 10.1016/j.radonc.2015.01.019 [published Online First: 20150316].
302. Sroussi HY, Epstein JB, Bensadoun RJ, et al. Common oral complications of head and neck cancer radiation therapy: mucositis, infections, saliva change, fibrosis, sensory dysfunctions, dental caries, periodontal disease, and osteoradionecrosis. Cancer Med 2017;**6**(12):2918-31 doi: 10.1002/cam4.1221 [published Online First: 20171025].
303. Dirix P, Nuyts S, Van den Bogaert W. Radiation-induced xerostomia in patients with head and neck cancer: a literature review. Cancer 2006;**107**(11):2525-34 doi: 10.1002/cncr.22302.
304. Spirk C, Hartl S, Pritz E, et al. Comprehensive investigation of saliva replacement liquids for the treatment of xerostomia. Int J Pharm 2019;**571**:118759 doi: 10.1016/j.ijpharm.2019.118759 [published Online First: 20191014].
305. Fox PC. Salivary enhancement therapies. Caries Res 2004;**38**(3):241-6 doi: 10.1159/000077761.
306. Holmes E, Loo RL, Stamler J, et al. Human metabolic phenotype diversity and its association with diet and blood pressure. Nature 2008;**453**(7193):396-400 doi: 10.1038/nature06882 [published Online First: 20080420].
307. Chan Q, Loo RL, Ebbels TM, et al. Metabolic phenotyping for discovery of urinary biomarkers of diet, xenobiotics and blood pressure in the INTERMAP Study: an overview. Hypertens Res 2017;**40**(4):336-45 doi: 10.1038/hr.2016.164 [published Online First: 20161222].
308. Licha D, Vidali S, Aminzadeh-Gohari S, et al. Untargeted Metabolomics Reveals Molecular Effects of Ketogenic Diet on Healthy and Tumor Xenograft Mouse Models. Int J Mol Sci 2019;**20**(16) doi: 10.3390/ijms20163873 [published Online First: 20190808].
309. Barry EL, Fedirko V, Uppal K, et al. Metabolomics Analysis of Aspirin's Effects in Human Colon Tissue and Associations with Adenoma Risk. Cancer Prev Res (Phila) 2020;**13**(10):863-76 doi: 10.1158/1940-6207.CAPR-20-0014 [published Online First: 20200712].
310. Yin G, Huang J, Guo W, Huang Z. Metabolomics of Oral/Head and Neck Cancer. Adv Exp Med Biol 2021;**1280**:277-90 doi: 10.1007/978-3-030-51652-9_19.

311. Lu J, Guo Y, Lu Y, et al. Untargeted lipidomics reveals specific lipid abnormalities in Sjogren's syndrome. Rheumatology (Oxford) 2021;**60**(3):1252-59 doi: 10.1093/rheumatology/keaa456.
312. Piraino LR, Benoit DSW, DeLouise LA. Salivary Gland Tissue Engineering Approaches: State of the Art and Future Directions. Cells 2021;**10**(7) doi: 10.3390/cells10071723 [published Online First: 20210708].
313. Wang K, Li J, Meng D, Zhang Z, Liu S. Machine learning based on metabolomics reveals potential targets and biomarkers for primary Sjogren's syndrome. Front Mol Biosci 2022;**9**:913325 doi: 10.3389/fmolb.2022.913325 [published Online First: 20220905].
314. Hynne H, Sandas EM, Elgstoen KBP, et al. Saliva Metabolomics in Dry Mouth Patients with Head and Neck Cancer or Sjogren's Syndrome. Cells 2022;**11**(3) doi: 10.3390/cells11030323 [published Online First: 20220119].
315. Meeks L, De Oliveira Pessoa D, Martinez JA, Limesand KH, Padi M. Integration of metabolomics and transcriptomics reveals convergent pathways driving radiation-induced salivary gland dysfunction. Physiol Genomics 2021;**53**(3):85-98 doi: 10.1152/physiolgenomics.00127.2020 [published Online First: 20210201].
316. Najdekr L, Blanco GR, Dunn WB. Collection of Untargeted Metabolomic Data for Mammalian Urine Applying HILIC and Reversed Phase Ultra Performance Liquid Chromatography Methods Coupled to a Q Exactive Mass Spectrometer. Methods Mol Biol 2019;**1996**:1-15 doi: 10.1007/978-1-4939-9488-5_1.
317. Zeidan YH, Xiao N, Cao H, Kong C, Le QT, Sirjani D. Botulinum Toxin Confers Radioprotection in Murine Salivary Glands. Int J Radiat Oncol Biol Phys 2016;**94**(5):1190-7 doi: 10.1016/j.ijrobp.2015.12.371 [published Online First: 20151229].
318. Timiri Shanmugam PS, Dayton RD, Palaniyandi S, et al. Recombinant AAV9-TLK1B administration ameliorates fractionated radiation-induced xerostomia. Hum Gene Ther 2013;**24**(6):604-12 doi: 10.1089/hum.2012.235.
319. Victory K, Burd R, Fribley A, et al. Head and neck tumor cell radiation response occurs in the presence of IGF1. J Dent Res 2011;**90**(3):347-52 doi: 10.1177/0022034510388037 [published Online First: 20101112].
320. Matassa AA, Carpenter L, Biden TJ, Humphries MJ, Reyland ME. PKCdelta is required for mitochondrial-dependent apoptosis in salivary epithelial cells. J Biol Chem 2001;**276**(32):29719-28 doi: 10.1074/jbc.M100273200 [published Online First: 20010521].
321. Limesand KH, Said S, Anderson SM. Suppression of radiation-induced salivary gland dysfunction by IGF-1. PLoS One 2009;**4**(3):e4663 doi: 10.1371/journal.pone.0004663 [published Online First: 20090302].
322. Reinke JM, Sorg H. Wound repair and regeneration. Eur Surg Res 2012;**49**(1):35-43 doi: 10.1159/000339613 [published Online First: 20120711].
323. Fleming DS, Miller LC. Leading edge analysis of transcriptomic changes during pseudorabies virus infection. Genom Data 2016;**10**:104-06 doi: 10.1016/j.gdata.2016.09.014 [published Online First: 20160930].
324. Barupal DK, Haldiya PK, Wohlgemuth G, et al. MetaMapp: mapping and visualizing metabolomic data by integrating information from biochemical pathways and chemical and mass spectral similarity. BMC Bioinformatics 2012;**13**:99 doi: 10.1186/1471-2105-13-99 [published Online First: 20120516].

325. Rahiminejad S, Maurya MR, Subramaniam S. Topological and functional comparison of community detection algorithms in biological networks. BMC Bioinformatics 2019;**20**(1):212 doi: 10.1186/s12859-019-2746-0 [published Online First: 20190427].
326. Niu X, Zhang J, Zhang L, et al. Weighted Gene Co-Expression Network Analysis Identifies Critical Genes in the Development of Heart Failure After Acute Myocardial Infarction. Front Genet 2019;**10**:1214 doi: 10.3389/fgene.2019.01214 [published Online First: 20191126].
327. Fath MA, Ahmad IM, Smith CJ, Spence J, Spitz DR. Enhancement of carboplatin-mediated lung cancer cell killing by simultaneous disruption of glutathione and thioredoxin metabolism. Clin Cancer Res 2011;**17**(19):6206-17 doi: 10.1158/1078-0432.CCR-11-0736 [published Online First: 20110815].
328. Scarbrough PM, Mapuskar KA, Mattson DM, Gius D, Watson WH, Spitz DR. Simultaneous inhibition of glutathione- and thioredoxin-dependent metabolism is necessary to potentiate 17AAG-induced cancer cell killing via oxidative stress. Free Radic Biol Med 2012;**52**(2):436-43 doi: 10.1016/j.freeradbiomed.2011.10.493 [published Online First: 20111104].
329. Jang WG, Park JY, Lee J, et al. Investigation of relative metabolic changes in the organs and plasma of rats exposed to X-ray radiation using HR-MAS (1)H NMR and solution (1)H NMR. NMR Biomed 2016;**29**(4):507-18 doi: 10.1002/nbm.3485 [published Online First: 20160212].
330. Cheema AK, Suman S, Kaur P, Singh R, Fornace AJ, Jr., Datta K. Long-term differential changes in mouse intestinal metabolomics after gamma and heavy ion radiation exposure. PLoS One 2014;**9**(1):e87079 doi: 10.1371/journal.pone.0087079 [published Online First: 20140127].
331. Li Z, Zhang H. Reprogramming of glucose, fatty acid and amino acid metabolism for cancer progression. Cell Mol Life Sci 2016;**73**(2):377-92 doi: 10.1007/s00018-015-2070-4 [published Online First: 20151023].
332. Wong TL, Che N, Ma S. Reprogramming of central carbon metabolism in cancer stem cells. Biochim Biophys Acta Mol Basis Dis 2017;**1863**(7):1728-38 doi: 10.1016/j.bbadis.2017.05.012 [published Online First: 20170511].
333. Rosenzweig A, Blenis J, Gomes AP. Beyond the Warburg Effect: How Do Cancer Cells Regulate One-Carbon Metabolism? Front Cell Dev Biol 2018;**6**:90 doi: 10.3389/fcell.2018.00090 [published Online First: 20180815].
334. Ducker GS, Rabinowitz JD. One-Carbon Metabolism in Health and Disease. Cell Metab 2017;**25**(1):27-42 doi: 10.1016/j.cmet.2016.08.009 [published Online First: 20160915].
335. Batra V, Kesavan V, Mishra KP. Modulation of enzymes involved in folate dependent one-carbon metabolism by gamma-radiation stress in mice. J Radiat Res 2004;**45**(4):527-33 doi: 10.1269/jrr.45.527.
336. Monobe M, Uzawa A, Hino M, Ando K, Kojima S. Glycine betaine, a beer component, protects radiation-induced injury. J Radiat Res 2005;**46**(1):117-21 doi: 10.1269/jrr.46.117.
337. Monobe M, Hamano N, Sumi M, et al. Effects of glycine betaine on bone marrow death and intestinal damage by gamma rays and carbon ions. Radiat Prot Dosimetry 2006;**122**(1-4):494-7 doi: 10.1093/rpd/ncl390 [published Online First: 20061204].

338. Chen L, Lu W, Wang L, et al. Metabolite discovery through global annotation of untargeted metabolomics data. Nat Methods 2021;**18**(11):1377-85 doi: 10.1038/s41592-021-01303-3 [published Online First: 20211028].
339. Mahieu NG, Patti GJ. Systems-Level Annotation of a Metabolomics Data Set Reduces 25 000 Features to Fewer than 1000 Unique Metabolites. Anal Chem 2017;**89**(19):10397-406 doi: 10.1021/acs.analchem.7b02380 [published Online First: 20170915].
340. Damgacioglu H, Sonawane K, Zhu Y, et al. Oropharyngeal Cancer Incidence and Mortality Trends in All 50 States in the US, 2001-2017. JAMA Otolaryngol Head Neck Surg 2022;**148**(2):155-65 doi: 10.1001/jamaoto.2021.3567.
341. Liao CI, Francoeur AA, Kapp DS, Caesar MAP, Huh WK, Chan JK. Trends in Human Papillomavirus-Associated Cancers, Demographic Characteristics, and Vaccinations in the US, 2001-2017. JAMA Netw Open 2022;**5**(3):e222530 doi: 10.1001/jamanetworkopen.2022.2530 [published Online First: 20220301].
342. Miller KD, Nogueira L, Devasia T, et al. Cancer treatment and survivorship statistics, 2022. CA Cancer J Clin 2022;**72**(5):409-36 doi: 10.3322/caac.21731 [published Online First: 20220623].
343. Kreimer AR, Chaturvedi AK, Alemany L, et al. Summary from an international cancer seminar focused on human papillomavirus (HPV)-positive oropharynx cancer, convened by scientists at IARC and NCI. Oral Oncol 2020;**108**:104736 doi: 10.1016/j.oraloncology.2020.104736 [published Online First: 20200602].
344. Lechner M, Liu J, Masterson L, Fenton TR. HPV-associated oropharyngeal cancer: epidemiology, molecular biology and clinical management. Nat Rev Clin Oncol 2022;**19**(5):306-27 doi: 10.1038/s41571-022-00603-7 [published Online First: 20220201].
345. Strojan P, Hutcheson KA, Eisbruch A, et al. Treatment of late sequelae after radiotherapy for head and neck cancer. Cancer Treat Rev 2017;**59**:79-92 doi: 10.1016/j.ctrv.2017.07.003 [published Online First: 20170718].
346. Hamilton SN, Mahdavi S, Martinez IS, et al. A cross-sectional assessment of long-term effects in adolescent and young adult head and neck cancer survivors treated with radiotherapy. J Cancer Surviv 2022;**16**(5):1117-26 doi: 10.1007/s11764-021-01103-w [published Online First: 20210920].
347. Malallah OS, Garcia CMA, Proctor GB, Forbes B, Royall PG. Buccal drug delivery technologies for patient-centred treatment of radiation-induced xerostomia (dry mouth). Int J Pharm 2018;**541**(1-2):157-66 doi: 10.1016/j.ijpharm.2018.02.004 [published Online First: 20180206].
348. Rabbani N, Xue M, Thornalley PJ. Hexokinase-2-Linked Glycolytic Overload and Unscheduled Glycolysis-Driver of Insulin Resistance and Development of Vascular Complications of Diabetes. Int J Mol Sci 2022;**23**(4) doi: 10.3390/ijms23042165 [published Online First: 20220216].
349. Xu P, Yi Y, Luo Y, et al. Radiation-induced dysfunction of energy metabolism in the heart results in the fibrosis of cardiac tissues. Mol Med Rep 2021;**24**(6) doi: 10.3892/mmr.2021.12482 [published Online First: 20211011].
350. Pavlova NN, Zhu J, Thompson CB. The hallmarks of cancer metabolism: Still emerging. Cell Metab 2022;**34**(3):355-77 doi: 10.1016/j.cmet.2022.01.007 [published Online First: 20220204].

351. Azzu V, Valencak TG. Energy Metabolism and Ageing in the Mouse: A Mini-Review. Gerontology 2017;**63**(4):327-36 doi: 10.1159/000454924 [published Online First: 20170125].
352. Liu X, Wang X, Zhang J, et al. Warburg effect revisited: an epigenetic link between glycolysis and gastric carcinogenesis. Oncogene 2010;**29**(3):442-50 doi: 10.1038/onc.2009.332 [published Online First: 20091102].
353. Raj S, Kumar A, Kumar D. Regulation of Glycolysis in Head and Neck Cancer. Adv Exp Med Biol 2021;**1280**:219-30 doi: 10.1007/978-3-030-51652-9_15.
354. Chen F, Zhou J, Li Y, et al. YY1 regulates skeletal muscle regeneration through controlling metabolic reprogramming of satellite cells. EMBO J 2019;**38**(10) doi: 10.15252/embj.201899727 [published Online First: 20190412].
355. Porporato PE, Payen VL, De Saedeleer CJ, et al. Lactate stimulates angiogenesis and accelerates the healing of superficial and ischemic wounds in mice. Angiogenesis 2012;**15**(4):581-92 doi: 10.1007/s10456-012-9282-0 [published Online First: 20120603].
356. Sun CM, Xiong DB, Yan Y, Geng J, Liu M, Yao XD. Genetic alteration in phosphofructokinase family promotes growth of muscle-invasive bladder cancer. Int J Biol Markers 2016;**31**(3):e286-93 doi: 10.5301/jbm.5000189 [published Online First: 20160730].
357. Zhang K, Hast MW, Izumi S, et al. Modulating Glucose Metabolism and Lactate Synthesis in Injured Mouse Tendons: Treatment With Dichloroacetate, a Lactate Synthesis Inhibitor, Improves Tendon Healing. Am J Sports Med 2018;**46**(9):2222-31 doi: 10.1177/0363546518778789 [published Online First: 20180621].
358. Harper JW, Elledge SJ. The DNA damage response: ten years after. Mol Cell 2007;**28**(5):739-45 doi: 10.1016/j.molcel.2007.11.015.
359. Jackson SP, Bartek J. The DNA-damage response in human biology and disease. Nature 2009;**461**(7267):1071-8 doi: 10.1038/nature08467.
360. Clay Montier LL, Deng JJ, Bai Y. Number matters: control of mammalian mitochondrial DNA copy number. J Genet Genomics 2009;**36**(3):125-31 doi: 10.1016/S1673-8527(08)60099-5.
361. Kim EJ, Lee M, Kim DY, Kim KI, Yi JY. Mechanisms of Energy Metabolism in Skeletal Muscle Mitochondria Following Radiation Exposure. Cells 2019;**8**(9) doi: 10.3390/cells8090950 [published Online First: 20190821].
362. Malakhova L, Bezlepkin VG, Antipova V, et al. The increase in mitochondrial DNA copy number in the tissues of gamma-irradiated mice. Cell Mol Biol Lett 2005;**10**(4):721-32.
363. Mookerjee SA, Gerencser AA, Nicholls DG, Brand MD. Quantifying intracellular rates of glycolytic and oxidative ATP production and consumption using extracellular flux measurements. J Biol Chem 2018;**293**(32):12649-52 doi: 10.1074/jbc.AAC118.004855.
364. Livak KJ, Schmittgen TD. Analysis of relative gene expression data using real-time quantitative PCR and the 2(-Delta Delta C(T)) Method. Methods 2001;**25**(4):402-8 doi: 10.1006/meth.2001.1262.
365. Zhao M, Wang Y, Li L, et al. Mitochondrial ROS promote mitochondrial dysfunction and inflammation in ischemic acute kidney injury by disrupting TFAM-mediated mtDNA maintenance. Theranostics 2021;**11**(4):1845-63 doi: 10.7150/thno.50905 [published Online First: 20210101].

366. Quiros PM, Goyal A, Jha P, Auwerx J. Analysis of mtDNA/nDNA Ratio in Mice. Curr Protoc Mouse Biol 2017;**7**(1):47-54 doi: 10.1002/cpmo.21 [published Online First: 20170302].
367. Plitzko B, Loesgen S. Measurement of Oxygen Consumption Rate (OCR) and Extracellular Acidification Rate (ECAR) in Culture Cells for Assessment of the Energy Metabolism. Bio Protoc 2018;**8**(10):e2850 doi: 10.21769/BioProtoc.2850 [published Online First: 20180520].
368. Zhang J, Zhang Q. Using Seahorse Machine to Measure OCR and ECAR in Cancer Cells. Methods Mol Biol 2019;**1928**:353-63 doi: 10.1007/978-1-4939-9027-6_18.
369. Decleer M, Jovanovic J, Vakula A, et al. Oxygen Consumption Rate Analysis of Mitochondrial Dysfunction Caused by Bacillus cereus Cereulide in Caco-2 and HepG2 Cells. Toxins (Basel) 2018;**10**(7) doi: 10.3390/toxins10070266 [published Online First: 20180702].
370. TeSlaa T, Teitell MA. Techniques to monitor glycolysis. Methods Enzymol 2014;**542**:91-114 doi: 10.1016/B978-0-12-416618-9.00005-4.
371. Rabinowitz JD, Enerback S. Lactate: the ugly duckling of energy metabolism. Nat Metab 2020;**2**(7):566-71 doi: 10.1038/s42255-020-0243-4 [published Online First: 20200720].
372. Chen J, Zheng Q, Peiffer LB, et al. An in Situ Atlas of Mitochondrial DNA in Mammalian Tissues Reveals High Content in Stem and Proliferative Compartments. Am J Pathol 2020;**190**(7):1565-79 doi: 10.1016/j.ajpath.2020.03.018 [published Online First: 20200415].
373. Nugent S, Mothersill CE, Seymour C, McClean B, Lyng FM, Murphy JE. Altered mitochondrial function and genome frequency post exposure to γ-radiation and bystander factors. Int J Radiat Biol 2010;**86**(10):829-41 doi: 10.3109/09553002.2010.486019.
374. Kam WW, Banati RB. Effects of ionizing radiation on mitochondria. Free Radic Biol Med 2013;**65**:607-19 doi: 10.1016/j.freeradbiomed.2013.07.024 [published Online First: 20130726].
375. Gu X, Ma Y, Liu Y, Wan Q. Measurement of mitochondrial respiration in adherent cells by Seahorse XF96 Cell Mito Stress Test. STAR Protoc 2021;**2**(1):100245 doi: 10.1016/j.xpro.2020.100245 [published Online First: 20201230].
376. Przystal JM, Cianciolo Cosentino C, Yadavilli S, et al. Imipridones affect tumor bioenergetics and promote cell lineage differentiation in diffuse midline gliomas. Neuro Oncol 2022;**24**(9):1438-51 doi: 10.1093/neuonc/noac041.
377. Xie W, Guo D, Li J, et al. CEND1 deficiency induces mitochondrial dysfunction and cognitive impairment in Alzheimer's disease. Cell Death Differ 2022;**29**(12):2417-28 doi: 10.1038/s41418-022-01027-7 [published Online First: 20220622].
378. Fao L, Coelho P, Duarte L, et al. Restoration of c-Src/Fyn Proteins Rescues Mitochondrial Dysfunction in Huntington's Disease. Antioxid Redox Signal 2023;**38**(1-3):95-114 doi: 10.1089/ars.2022.0001 [published Online First: 20220805].
379. Numa K, Ueno M, Fujita T, et al. Mitochondria as a Platform for Dictating the Cell Fate of Cultured Human Corneal Endothelial Cells. Invest Ophthalmol Vis Sci 2020;**61**(14):10 doi: 10.1167/iovs.61.14.10.
380. Barjaktarovic Z, Schmaltz D, Shyla A, et al. Radiation-induced signaling results in mitochondrial impairment in mouse heart at 4 weeks after exposure to X-rays. PLoS One

2011;**6**(12):e27811 doi: 10.1371/journal.pone.0027811 [published Online First: 20111208].
381. Barjaktarovic Z, Shyla A, Azimzadeh O, et al. Ionising radiation induces persistent alterations in the cardiac mitochondrial function of C57BL/6 mice 40 weeks after local heart exposure. Radiother Oncol 2013;**106**(3):404-10 doi: 10.1016/j.radonc.2013.01.017 [published Online First: 20130320].
382. Amorim NML, Kee A, Coster ACF, et al. Irradiation impairs mitochondrial function and skeletal muscle oxidative capacity: significance for metabolic complications in cancer survivors. Metabolism 2020;**103**:154025 doi: 10.1016/j.metabol.2019.154025 [published Online First: 20191122].
383. Yahyapour R, Motevaseli E, Rezaeyan A, et al. Reduction-oxidation (redox) system in radiation-induced normal tissue injury: molecular mechanisms and implications in radiation therapeutics. Clin Transl Oncol 2018;**20**(8):975-88 doi: 10.1007/s12094-017-1828-6 [published Online First: 20180109].
384. Boveris A, Chance B. The mitochondrial generation of hydrogen peroxide. General properties and effect of hyperbaric oxygen. Biochem J 1973;**134**(3):707-16 doi: 10.1042/bj1340707.
385. Cadenas E, Davies KJ. Mitochondrial free radical generation, oxidative stress, and aging. Free Radic Biol Med 2000;**29**(3-4):222-30 doi: 10.1016/s0891-5849(00)00317-8.
386. Sidoti-de Fraisse C, Rincheval V, Risler Y, Mignotte B, Vayssiere JL. TNF-alpha activates at least two apoptotic signaling cascades. Oncogene 1998;**17**(13):1639-51 doi: 10.1038/sj.onc.1202094.
387. Yamamori T, Yasui H, Yamazumi M, et al. Ionizing radiation induces mitochondrial reactive oxygen species production accompanied by upregulation of mitochondrial electron transport chain function and mitochondrial content under control of the cell cycle checkpoint. Free Radic Biol Med 2012;**53**(2):260-70 doi: 10.1016/j.freeradbiomed.2012.04.033 [published Online First: 20120508].
388. Vander Heiden MG, Cantley LC, Thompson CB. Understanding the Warburg effect: the metabolic requirements of cell proliferation. Science 2009;**324**(5930):1029-33 doi: 10.1126/science.1160809.
389. Holloway RW, Marignani PA. Targeting mTOR and Glycolysis in HER2-Positive Breast Cancer. Cancers (Basel) 2021;**13**(12) doi: 10.3390/cancers13122922 [published Online First: 20210611].
390. Hu X, Xu Q, Wan H, et al. PI3K-Akt-mTOR/PFKFB3 pathway mediated lung fibroblast aerobic glycolysis and collagen synthesis in lipopolysaccharide-induced pulmonary fibrosis. Lab Invest 2020;**100**(6):801-11 doi: 10.1038/s41374-020-0404-9 [published Online First: 20200212].
391. Baik SH, Kang S, Lee W, et al. A Breakdown in Metabolic Reprogramming Causes Microglia Dysfunction in Alzheimer's Disease. Cell Metab 2019;**30**(3):493-507 e6 doi: 10.1016/j.cmet.2019.06.005 [published Online First: 20190627].
392. Weng ML, Chen WK, Chen XY, et al. Fasting inhibits aerobic glycolysis and proliferation in colorectal cancer via the Fdft1-mediated AKT/mTOR/HIF1alpha pathway suppression. Nat Commun 2020;**11**(1):1869 doi: 10.1038/s41467-020-15795-8 [published Online First: 20200420].
393. van Dijk LV, Thor M, Steenbakkers R, et al. Parotid gland fat related Magnetic Resonance image biomarkers improve prediction of late radiation-induced xerostomia. Radiother

Oncol 2018;**128**(3):459-66 doi: 10.1016/j.radonc.2018.06.012 [published Online First: 20180626].
394. Izumi M, Eguchi K, Nakamura H, Nagataki S, Nakamura T. Premature fat deposition in the salivary glands associated with Sjogren syndrome: MR and CT evidence. AJNR Am J Neuroradiol 1997;**18**(5):951-8.
395. Takagi Y, Sumi M, Sumi T, Ichikawa Y, Nakamura T. MR microscopy of the parotid glands in patients with Sjogren's syndrome: quantitative MR diagnostic criteria. AJNR Am J Neuroradiol 2005;**26**(5):1207-14.
396. Skarstein K, Aqrawi LA, Oijordsbakken G, Jonsson R, Jensen JL. Adipose tissue is prominent in salivary glands of Sjogren's syndrome patients and appears to influence the microenvironment in these organs. Autoimmunity 2016;**49**(5):338-46 doi: 10.1080/08916934.2016.1183656 [published Online First: 20160520].
397. Skarstein K, Jensen JL, Galtung H, Jonsson R, Brokstad K, Aqrawi LA. Autoantigen-specific B cells and plasma cells are prominent in areas of fatty infiltration in salivary glands of patients with primary Sjogren's syndrome. Autoimmunity 2019;**52**(7-8):242-50 doi: 10.1080/08916934.2019.1684475 [published Online First: 20191030].
398. Aqrawi LA, Jensen JL, Oijordsbakken G, et al. Signalling pathways identified in salivary glands from primary Sjogren's syndrome patients reveal enhanced adipose tissue development. Autoimmunity 2018;**51**(3):135-46 doi: 10.1080/08916934.2018.1446525 [published Online First: 20180305].
399. Chen HL, Ma P, Chen YL, et al. [Effect of Metformin on Proliferation Capacity, Apoptosis and Glycolysis in K562 Cells]. Zhongguo Shi Yan Xue Ye Xue Za Zhi 2019;**27**(5):1387-94 doi: 10.19746/j.cnki.issn.1009-2137.2019.05.006.
400. Li T, Sun X, Jiang X. UCA1 involved in the metformin-regulated bladder cancer cell proliferation and glycolysis. Tumour Biol 2017;**39**(6):1010428317710823 doi: 10.1177/1010428317710823.
401. Wang Z, Xiao X, Ge R, et al. Metformin inhibits the proliferation of benign prostatic epithelial cells. PLoS One 2017;**12**(3):e0173335 doi: 10.1371/journal.pone.0173335 [published Online First: 20170302].